


Summer 2008

Reflection High-Energy Electron Diffraction Studies of Indium Phosphide (100) and Growth on Indium and Indium Nitride on Silicon (100)

Mohamed Abd-Elsattar Hafez
Old Dominion University

Follow this and additional works at: https://digitalcommons.odu.edu/ece_etds

 Part of the [Condensed Matter Physics Commons](#), [Electrical and Computer Engineering Commons](#), and the [Materials Science and Engineering Commons](#)

Recommended Citation

Hafez, Mohamed A.. "Reflection High-Energy Electron Diffraction Studies of Indium Phosphide (100) and Growth on Indium and Indium Nitride on Silicon (100)" (2008). Doctor of Philosophy (PhD), dissertation, Electrical/Computer Engineering, Old Dominion University, DOI: 10.25777/215y-zh41
https://digitalcommons.odu.edu/ece_etds/77

This Dissertation is brought to you for free and open access by the Electrical & Computer Engineering at ODU Digital Commons. It has been accepted for inclusion in Electrical & Computer Engineering Theses & Dissertations by an authorized administrator of ODU Digital Commons. For more information, please contact digitalcommons@odu.edu.

**REFLECTION HIGH-ENERGY ELECTRON DIFFRACTION
STUDIES OF INDIUM PHOSPHIDE (100) AND GROWTH
OF INDIUM AND INDIUM NITRIDE ON SILICON (100)**

by

Mohamed Abd-Elsattar Hafez

M.Sc. July 1998, Cairo University, Egypt

B.Sc. May 1991, Cairo University, Egypt

A Dissertation Submitted to the Faculty of Old Dominion University in
Partial Fulfillment of the Requirement for the Degree of

DOCTOR OF PHILOSOPHY

ELECTRICAL AND COMPUTER ENGINEERING

OLD DOMINION UNIVERSITY

August 2008

Approved by:

Hani Elsayed-Ali (Director)

Sacharia Albin (Member)

Julie Hao (Member)

Tamer Refaat (Member)

ABSTRACT

REFLECTION HIGH-ENERGY ELECTRON DIFFRACTION STUDIES OF INDIUM PHOSPHIDE (100) AND GROWTH OF INDIUM AND INDIUM NITRIDE ON SILICON (100)

Mohamed Abd-Elsattar Hafez
Old Dominion University, 2008
Director: Dr. Hani E. Elsayed-Ali

Study of the effects of atomic hydrogen exposure on structure and morphology of semiconductor surfaces is important for fundamental properties and applications. In this dissertation, the electron yield of a hydrogen-cleaned indium phosphide (InP) surface was measured and correlated to the development of the surface morphology, which was monitored by in situ reflection high-energy electron diffraction (RHEED). Atomic hydrogen treatment produced a clean, well-ordered, and (2×4)-reconstructed InP(100) surface. The quantum efficiency, after activation to negative electron affinity, and the secondary electron emission were shown to increase with hydrogen cleaning time. RHEED patterns of low-index InP(100) surface were modified by the step structure and resulted in splitting of the specular beam at the out-of-phase diffraction condition. Quantitative RHEED showed reduction in the average terrace width and a decrease of the adatom-vacancy density with hydrogen exposure. This suggests that atomic hydrogen etching occurs preferentially at terrace edges, and thermal diffusion on the surface causes changes in the terrace edge morphology, which result in the observed decrease in the average terrace width. The results show that the decrease in the surface disorder, measured from the RHEED intensity-to-background ratio, correlated with the increased quantum efficiency.

The growth of group-III metals on Si surfaces has become an attractive area of research because of its scientific importance and great potential in technological applications. In this work, the growth dynamics, structure, and morphology of indium (In) on a vicinal Si(100)-(2×1) surface by femtosecond pulsed laser deposition (fsPLD) were studied using in situ RHEED and ex situ atomic force microscopy. Indium was found to grow on Si(100) by the Stranski-Krastanov mode. At room temperature, the initial growth formed strained two-dimensional (2D) layers in the In(2×1) structure followed by growth of three-dimensional islands. During the 2D growth, the surface diffusion coefficient of deposited In on the In(2×1) layer was estimated to be in the order of 10^{-14} cm²/s, from recovery of the RHEED intensity. This was attributed to surface diffusion of In clusters by step flow mode. The results suggest that fsPLD of In removed the reconstruction of the Si(100)-(2×1) surface in the early growth and resulted in the initial In(2×1) structure. Next, growth of In on Si(100)-(2×1) was studied at temperature of 350-420 °C and showed formation of In(4×3) structure. The growth stages, probed by RHEED intensity relaxation, proceed in a two-step process, formation of small In clusters and surface diffusion to the terrace step edges with activation energy of 1.4 ± 0.2 eV and diffusion rate constant of $1.0 \pm 0.1 \times 10^{11}$ s⁻¹. The terrace width dynamics and the related surface processes were studied during growth of the In(4×3) phase with increase in film coverage. Finally, the fsPLD was used to grow nitride films of InN on Si(100) substrates. A buffer layer of In was grown on Si(100) by fsPLD prior to growth of InN and different nitridation procedures were used.

This dissertation is dedicated to my parents and my brothers.

ACKNOWLEDGMENTS

I would like to express my gratitude and thanks to my dissertation advisor, Dr. Hani Elsayed-Ali, for his supervision, help, and support. His scientific intuition, great knowledge, and invaluable guidance assisted me much to perform this research. I would also like to thank Dr. Sacharia Albin of the Department of Electrical and Computer Engineering, Dr. Julie Hao of the Department of Mechanical Engineering, and Dr. Tamer Refaat of the NASA Langley Research Center for serving on my Ph.D. committee.

Many thanks to the Department of Electrical and Computer Engineering and the Applied Research Center of Old Dominion University for their support. I am grateful to the laboratory managers at the Norfolk State University and the College of William and Mary for assisting and permitting me to use their equipment during my research work. My appreciations go to my laboratory mate Mohammed Hegazy for his cooperation and help. I would like to thank Theresa Dettmer for her help and for reviewing the final parts of the dissertation.

I am very thankful and grateful to all the members of my family: my father, Abd-Elstatar Hafez; my mother, Samiha Mohamed; and my brother, Gamal Hafez; back home in Egypt for their encouragement, support, and patience for all the time that I spent studying and working on my dissertation. I dedicate the work of this dissertation to the memory of my brother Ahmed Abd-Elstatar Hafez.

TABLE OF CONTENTS

	Page
LIST OF FIGURES.....	x
CHAPTER I. INTRODUCTION.....	1
I.1. References.....	11
CHAPTER II. REFLECTION HIGH-ENERGY ELECTRON DIFFRACTION: THEORY AND APPLICATIONS.....	26
II.1. Introduction.....	26
II.2. RHEED set-up and techniques.....	28
II.3. RHEED theoretical models.....	31
II.3.1. Geometrical model.....	31
II.3.2. Kinematical and dynamical models.....	35
II.4. Diffraction features from surfaces.....	38
II.4.1. Surface reconstruction.....	38
II.4.2. Kikuchi patterns and resonance reflections.....	40
II.4.3. RHEED rocking curves.....	40
II.5. RHEED from vicinal surfaces.....	42
II.6. RHEED and thin film growth.....	47
II.6.1. RHEED and growth modes.....	47
II.6.2. RHEED intensity oscillations.....	49
II.7. References.....	57
CHAPTER III. ELECTRON YIELD AND SURFACE MORPHOLOGY STUDY OF HYDROGEN-CLEANED InP(100).....	67
III.1. Introduction.....	67
III.2. Experiment.....	71
III.3. RHEED calculations.....	74
III.3.1. Real and reciprocal lattices.....	74
III.3.2. Terrace width and misorientation angle.....	76
III.4. Results and discussion.....	79
III.4.1. Quantum efficiency and secondary electron emission.....	79
III.4.2. RHEED study of surface morphology.....	87
III.5. Conclusion.....	98
III.6. References.....	100

CHAPTER IV. GROWTH OF INDIUM ON Si(100)-(2×1) BY FEMTOSECOND PULSED LASER DEPOSITION.....	104
IV.1. Introduction.....	104
IV.2. Thin film nucleation and growth.....	109
IV.3. Femtosecond pulsed laser deposition.....	113
IV.4. Experiment.....	115
IV.5. Results and discussion.....	118
IV.5.1. Growth of In on Si(100)-(2×1) at room temperature	118
IV.5.1.1. Growth mode and morphology.....	118
IV.5.1.1.1. General observations by RHEED.....	118
IV.5.1.1.2. Film in-plane lattice spacing.....	121
IV.5.1.1.3. FWHM of the RHEED specular beam.....	123
IV.5.1.1.4. Morphology of In film on Si(100).....	125
IV.5.1.2. Growth kinetics of the initial In(2×1) layer and the In islands.....	131
IV.5.1.2.1. RHEED intensity recovery and growth kinetics...	131
IV.5.1.2.2. Island growth and morphology.....	140
IV.5.1.2.3. fsPLD effects.....	149
IV.5.2. Growth of In on Si(100)-(2×1) at high temperature.....	153
IV.5.2.1. Growth of In(4×3) on Si(100).....	153
IV.5.2.2. RHEED intensity relaxation and activation energy..	159
IV.5.2.3. Terrace width growth dynamics.....	165
IV.6. Conclusion.....	172
IV.7. References.....	174
CHAPTER V. FEMTOSECOND PULSED LASER DEPOSITION OF INDIUM NITRIDE ON Si(100).....	188
V.1. Introduction.....	188
V.2. Crystal structure.....	196
V.3. Experiment.....	198
V.4. Results and discussion.....	200
V.5. Conclusion.....	215
V.6. References.....	216
CHAPTER VI. SUMMARY.....	226
APPENDICES	
A. Pulsed laser deposition system.....	231
B. Femtosecond laser system.....	254

C. RHEED and imaging system.....	266
D. List of manufacturer contacts.....	274
VITA.....	276

LIST OF FIGURES

Figure		Page
2.1	Schematic diagram of RHEED geometry. The parameters λ , θ_i , and ϕ are the electron wavelength, incident angle, and azimuthal angle. The transmitted (000) corresponds to the primary electron beam.	27
2.2	Schematic diagrams and corresponding RHEED patterns of two possible modes of electron diffraction. (a) Reflection diffraction from Si(100)-(2×1) reconstructed surface. (b) Transmission diffraction from InP(100) surface.	27
2.3	Ewald sphere construction and diffraction geometry of RHEED according to the geometrical model. Ewald sphere radius is $k = 2\pi/\lambda$. The conditions for constructive interference of the elastically scattered electrons inferred using the Ewald construction in the reciprocal lattice (modified from Braun [2]).	32
2.4	(a) Top view of reciprocal lattice points and Ewald sphere. Ewald sphere is determined by the conservation of energy and conservation of momentum by a reciprocal lattice vector $\Delta\mathbf{k}$. (b) Schematic diagram of intersection of Ewald sphere with reciprocal lattice rods of same zone.	32
2.5	The lateral spacing a^* of the reciprocal lattice rods in (a) is related to the streak spacing W between the integral order of the diffracted beams in the Si(100)-(1×1) RHEED pattern in (b).	34
2.6	Schematic diagrams of (2×1) surface reconstruction in real space (a) and in reciprocal space (b). (c) RHEED pattern of reconstructed Si(100)-(2×1) surface.	39
2.7	Ewald sphere intersection with broadened reciprocal lattice rod. The broadening along the diffracted beam appears as a streak in the RHEED patterns. $S_{//}$ and S_{\perp} are the components of the momentum transfer parallel and perpendicular to the incident electron beam, respectively.	44
2.8	Schematic of the vicinal surface with the relevant dimensions in real lattice (a) and in reciprocal lattice (b). Depending on the electron beam incident angle θ_i down the staircase and the terrace width L , the reflected electrons will maximize or broaden the specular beam profile.	44
2.9	(a) Schematic of InP(100) vicinal surface and the related crystal directions. The electron beam is incident down the staircase in the [031] azimuth. Ewald construction, RHEED pattern, and intensity profile along the specular beam are shown for: (b) out-of-phase condition and (c) in-	46

phase condition. The splitting quantity of the specular beam is related to the misorientation angle θ_m .

- 2.10 Schematic diagrams of film growth modes and corresponding RHEED patterns represented in: (a) Si(100)-(2×1) substrate surface; (b) growth of 2D In layers on Si(100)-(2×1); (c) growth of 3D In islands on preceding 2D layers (lattice mismatch between In and Si account for this mixed growth SK mode); and (d) 3D islands growth of InP on GaAs(100) surface.

48
- 2.11 (a) RHEED intensity oscillations during growth of In on Si(100)-(2×1) by PLD at ~145 °C. From the intensity oscillations, a growth rate of ~0.05 monolayer/s is estimated. (b) Oscillatory behavior of the RHEED intensity between laser pulses taken during growth of In on Si(100)-(2×1) at ~400 °C. The oscillation of the specular beam matches the pulsed deposition rate. This feature is a characteristic of PLD growth.

51
- 2.12 (a) Phase shift in the RHEED intensity of the (20) and ($\bar{2}0$) beams during growth of In on Si(100)-(2×1) at ~145 °C. The arrows indicate that the laser was turned on at 21 s and turned off at 100 s. (b) Magnified scale of graph (a) showing oscillations have cycled out of phase. (c) RHEED tracking scan of the (20) beam showing pulsing in brightness corresponding to the intensity in (b).

54
- 3.1 Energy band diagrams. (a) Semiconductor band structure showing the conduction band minimum E_c , the valence band maximum E_v , the Fermi level E_f , the band-gap energy E_g , and the vacuum level E_o . The electron affinity χ is the energy required to remove an electron from the lowest conduction band level and place it in a vacuum. Typically, χ is 3 to 4 eV [21]. For InP, $E_g = 1.35$ eV and $\chi = 4.38$ eV. (b) Negative electron affinity achieved by band bending in a surface depletion region on a p-type semiconductor. The diagram shows conditions in relation to E_g and work function Φ . The diffusion lengths of the electrons thermalized to E_c are several orders of magnitude longer than the escape depths for conventional emitters. Emission efficiency increased as the number of electrons diffused to the NEA surface increased.

70
- 3.2 Experimental set up for preparation and study of NEA photocathode. The sample is electrically insulated from the chamber. The UHV system consists of an ion pump (220 l/s), titanium sublimation pump, turbomolecular pump (60 l/s), and mechanical pump. An electro-pneumatic valve was used to separate the chamber from the turbomolecular and mechanical pumps. During hydrogen cleaning, the chamber is filled to $1-5 \times 10^{-6}$ Torr hydrogen as measured using the ion pump controller. For photocurrent measurement, an accelerating voltage of negative bias is applied to the sample and a He-Ne laser beam, $\lambda = 632$

73

nm, is used as a light source. The operating current to heat the cesium source depends on the cesium deposition rate and the distance between the sample and the source. The activation procedure is performed by applying cesium and oxygen in an alternative way. When cesiation is started, the photocurrent increases from zero to maximum value and then goes down. When the photocurrent is dropped to ~90 % of its maximum value, the cesium current is dropped, which effectively terminates cesiation, and the oxygen leak valve is opened. This step increases the pressure and reduces the photocurrent. When the photocurrent reaches ~10 % of its maximum value, the oxygen valve is closed and the cesium is evaporated again. This procedure is repeated until the photocurrent measurements reach the highest value.

- | | | |
|-----|---|----|
| 3.3 | Real lattice of InP(100) surface. | 74 |
| 3.4 | Reciprocal lattice of InP(100) surface and unit mesh corresponding to the real lattice in the Fig. 3.3(a). RHEED patterns taken for a cleaned-surface are shown. | 75 |
| 3.5 | RHEED from InP(100) vicinal surface. (a) Schematic diagram of vicinal surface. The splitting of specular beam can be observed at different azimuth angles ϕ . (b) Illustration of a geometrical method used to determine the angle of incidence and splitting of the electron diffraction in case of the out-of-phase condition. $S_{//}$ and S_{\perp} are the components of the momentum transfer parallel and perpendicular to the incident electron beam, respectively. (c) Corresponding RHEED pattern of InP(100) for incident electron beam down the staircase along the [031] azimuth. | 77 |
| 3.6 | RHEED patterns of InP(100) surface after heat cleaning at 370 °C showing a strong background due to contaminants. | 80 |
| 3.7 | The quantum efficiency and secondary electron emission ratios were measured for a (2×4)-reconstructed InP surface. At each cleaning cycle, the InP sample was cleaned for three hours and the measurements were taken at room temperature. | 81 |
| 3.8 | RHEED patterns of InP(100) surface after atomic hydrogen cleaning. (a) After hydrogen cleaning at ~ 370 °C, the RHEED streaks are visible along with a strong background. The electron beam was incident along the [031] direction. (b) After hydrogen cleaning at 385-400 °C, a clear (2×4)-reconstructed surface is obtained. The electron beam was incident along the $[0\bar{1}\bar{1}]$ direction. | 83 |
| 3.9 | After activating the surface with cesium and oxygen, the secondary electron emission increased with the incident electron energy. The secondary-electron yield is higher for a surface that produces higher | 84 |

quantum efficiency.

- | | | |
|------|---|----|
| 3.10 | The decrease of secondary electron emission with time after InP(100) surface activation to negative electron affinity. The measurement was taken after atomic hydrogen cleaning at $\sim 370^\circ\text{C}$. | 85 |
| 3.11 | After several hydrogen cleanings at $\sim 385\text{--}400^\circ\text{C}$, spotty and streaky RHEED patterns were observed at different locations as shown in (a) and (b), respectively. The electron beam was incident along the $[031]$ direction. | 86 |
| 3.12 | Intensity profiles along the specular RHEED spot showing the in-phase and out-of-phase conditions. The electron beam was incident along the $[031]$ azimuth. | 89 |
| 3.13 | RHEED rocking curve of the peak intensity of the specular spot for the heat-cleaned vicinal InP(100) surface at $\sim 300^\circ\text{C}$. The intensity profile was obtained close to room temperature in the $[0\bar{1}3]$ azimuth. The intensity peaked at in-phase angles while it reached minimum at out-of-phase angle as indicated by the arrows. | 90 |
| 3.14 | The RHEED intensity profiles of the split specular beam taken in the out-of-phase condition were obtained after heat cleaning at $\sim 300^\circ\text{C}$ (—) and atomic hydrogen cleaning at $\sim 380^\circ\text{C}$; (— · —), (— — —) and (——) denote the second, fourth, and sixth cleaning cycles. The split peak spacing increases with hydrogen cleaning, indicating the decrease in the average terrace width. The inset is the RHEED pattern at the out-of-phase condition after hydrogen cleaning. | 92 |
| 3.15 | (a) The average terrace width decreases with atomic hydrogen cleaning from $301 \pm 42 \text{ \AA}$ after heat cleaning to $229 \pm 20 \text{ \AA}$ after the sixth hydrogen cleaning cycle. Cycle 0 is heat cleaned at $\sim 300^\circ\text{C}$; 1-6 are hydrogen cleaned at $\sim 380^\circ\text{C}$. The inset gives a sketch of the terrace width of a vicinal surface. (b) The measured FWHM along the specular beam ($S_{//}$ direction). | 94 |
| 3.16 | (a) Linescans across the specular beam at the out of phase condition; (— · —), (——), and (— — —) denotes to the profiles after heat cleaning, second and sixth hydrogen cleaning cycles. (b) The measured FWHM across the specular beam (S_{\perp} direction). | 94 |
| 3.17 | Hydrogen cleaning increases the ratio $R = (I_p - I_b)/I_b$, where I_p and I_b are the RHEED peak and background intensities, respectively, measured at the out-of-phase condition. After activation to NEA, the QE correlates with the ratio R measured before activation. | 96 |

- 4.1 TSK model showing atomic sites and defects on a surface of a simple cubic crystal. Each atom in the lattice is represented by a cube and has a certain number of nearest neighbors (its coordination numbers). The TSK model is based upon the idea that the energy of an atom on the surface is determined by its bonding to the neighboring atoms and that transition involves the counting of broken and formed bonds [61]. 109
- 4.2 (a) Surface processes involved in 3D nucleation and film growth. The incoming flux of film species first thermally accommodated with the substrate. The adatoms then diffuse on the surface to interact with adatoms or re-evaporate. Surface diffusion leads to nucleation of clusters, such as metastable and critical size clusters, and continue to grow in size and became islands and film growth. (b) Growth on vicinal surface. Surface steps can act as a sink for deposits where the adatoms are incorporated under the step flow growth mode. Adatom can move on the terrace through a horizontal jump or move from terrace to a lower level through a vertical jump. 112
- 4.3 Schematic diagram of the PLD experimental set up and components arrangement. 117
- 4.4 RHEED patterns of the Si substrate and In film. (a) RHEED pattern of the Si(100)-(2×1) surface before deposition taken in the [011] azimuth direction. (b) RHEED pattern of the In film after deposition time of 60 s taken in the [011] azimuth direction. Deposition conditions were 2-Hz laser repetition rate and 0.5 J/cm² laser energy density. (c) and (d) RHEED patterns of the substrate before and after deposition time of 400 s, respectively, taken in the [013] azimuth direction. Deposition conditions were 1-Hz laser repetition rate and 0.3 J/cm² laser energy density. 119
- 4.5 (a) The behavior of the strain during the deposition of In on Si(100)-(2×1) surface at RT in the first 70 s of the deposition time. The in-plane lattice parameter is calculated from the spacing between the ($\bar{1}0$) and (10) diffraction RHEED streaks ([011] azimuth). At the beginning of the indium deposition, instant relaxation of ~2 % after 2 sec occurred. (b) RHEED intensities of the (00), ($\bar{1}0$), and ($\bar{3}/2$ 0) beams taken in the [011] azimuth direction. Deposition conditions were 2-Hz laser repetition rate and 0.5 J/cm² laser energy density. 122
- 4.6 The FWHM_{//} taken along the (00) specular beam. The electron beam was incident in the [011] azimuth direction down the staircase of the vicinal Si surface. Deposition conditions were 2-Hz laser repetition rate and 0.5 J/cm² laser energy density. As deposition started, the FWHM_{//} decreased for the first 240 s, indicating an increase of In islands size. The top inset figure shows the line track of the (00) beam width during the film growth. 124

The FWHM_{\perp} across the (00) shows the same behavior as FWHM_{\parallel} , as seen in the inset figure. After a deposition time of 240 s, the FWHM_{\parallel} started to increase, indicating an increase of surface roughness. RHEED patterns taken in the [011] direction at time sequences of 5 s, 100 s, 296 s, and after terminating the deposition, are shown on top.

- 4.7 (a) EDX spectrum showing peak of the resultant In film deposited by fsPLD on Si. AFM images of the grown In film on Si(100)-(2×1) substrate after deposition at RT by the fsPLD (corresponding to the post deposition RHEED pattern in Fig. 4.6): (b) AFM image of size $4\text{ }\mu\text{m} \times 4\text{ }\mu\text{m}$ showing In islands located close to the middle of the sample; (c) magnified AFM image with size of $1.5\text{ }\mu\text{m} \times 1.5\text{ }\mu\text{m}$ showing the indium islands have approximately similar hexagonal shapes; (d) elongated In islands found at different sample locations exhibiting preferential growth orientation; and (e) hemispherical islands were found close to the sample edges. 126
- 4.8 In islands' shape and height profiles measured by the AFM: (a) An area histogram of hexagonal islands is shown. A line scan taken over an island shows a flat top plane with diameter of $\sim 70\text{ nm}$ and inclined planes at the sidewalls, indicating formation of faceted In islands. The island has a height of $\sim 5\text{ nm}$ and width of $\sim 220\text{ nm}$; (b) Three-dimensional image of the elongated islands. A line scan along an elongated island shows a height and length of $\sim 4.5\text{ nm}$ and $\sim 200\text{ nm}$, respectively. The island has a width of $\sim 60\text{ nm}$. The lateral sizes of the hexagonal and elongated islands are larger with respect to their heights. (c) Three-dimensional image of the hemispherical islands. The corresponding line profile over a hemispherical island shows a radius of $\sim 50\text{ nm}$ and height of $\sim 6\text{ nm}$. The root-mean-square surface roughness along the line profile is 0.9 nm . 129
- 4.9 Specular beam RHEED intensity after deposition of: (a) $\sim 0.5\text{ ML}$ on an initial $\sim 1.5\text{ ML}$ In(2×1), (b) an additional $\sim 1\text{ ML}$ giving a total coverage of $\sim 3\text{ ML}$, and (c) $\sim 4\text{ ML}$ on an initial $\sim 5\text{ ML}$ of In. The deposition was performed with the laser operated at 2-Hz laser repetition rate and 0.5 J/cm^2 laser energy density. The RHEED electron beam was incident along the [011] azimuth down the vicinal Si surface. The initial 2D layer formed in the In(2×1) structure. 132
- 4.10 RHEED intensity of the (20) diffraction beam as a function of In deposition time on Si(100)-(2×1) at a substrate temperature of $\sim 145\text{ }^{\circ}\text{C}$. The laser was operated at 1 Hz repetition rate with an energy density of 0.5 J/cm^2 on the In target. Relaxation of the RHEED intensity was observed during In deposition after each laser pulse as seen in the inset figure, which displays the RHEED intensity for laser pulse numbers 2 to 5 from starting the deposition. 134

- 4.11 (a) Recovery of the RHEED specular beam intensity after deposition of In at RT and coverage of ~ 2 ML. (b) Recovery of the RHEED (20) beam intensity after deposition of In at a substrate temperature of ~ 145 °C performed on initially ~ 2.7 ML of In. The RHEED intensity shows an initial fast increase and then a slow recovery, characterized by two exponential recovery times τ_1 and τ_2 , respectively. The x-axis start with 0 in (a) and (b) for curves fit. The inset in (b) shows a decrease and then a relaxation of the RHEED intensity after and before the second and third deposition laser pulses, respectively. 136
- 4.12 RHEED pattern of the Si(100)-(2 \times 1) vicinal surface taken at the out-of-phase condition corresponding to $\theta_{inc.}$ of ~ 65 mrad. The primary electron energy of 8.6 keV was incident down the staircase of the vicinal surface along the [011] azimuth. $S_{//}$ and S_{\perp} are the components of the momentum transfer parallel and perpendicular to the electron beam, respectively. The specular beam is split in the $S_{//}$ direction into two peaks around a central part, which is located within the RHEED zeroth Laue zone. 138
- 4.13 RHEED intensity of the specular beam was monitored with deposition time. The electron beam was incident with $\theta_{inc.}$ of ~ 68 mrad along the [011] substrate azimuth. The deposition conditions were 2 Hz laser repetition rate and 0.5 J/cm² laser energy density. RHEED patterns taken in the [011] azimuth of the Si(100)-(2 \times 1) substrate and of the grown In film at 100 s, 296 s, and post-deposition are shown in the inset. The In(2 \times 1) structure was preserved during the initial growth. The final film shows wide faint rings on a high background, indicating random in-plane crystallographic orientation. 141
- 4.14 (a) RHEED intensity profiles of the specular beam at film coverage of ~ 7 and ~ 14 ML versus the momentum transfer S_{\perp} parallel to the substrate surface. (b) FWHM of specular RHEED intensity profile as a function of the deposition time taking into account an instrumental response of 0.30 ± 0.015 Å⁻¹ in the S_{\perp} direction. The FWHM decreased from ~ 0.22 Å⁻¹ to 0.04 Å⁻¹. The spot intensity-to-background ratio of I_{spec}/I_{back} (open squares) during film deposition is shown, where I_{spec} and I_{back} are the specular peak and RHEED background intensities, respectively. 143
- 4.15 (a)-(d) AFM images taken after deposition of In on Si(100)-(2 \times 1) substrate at RT by fsPLD (corresponding to the post-deposition RHEED pattern in Fig. 4.13). The 3D islands in (b)-(d) show elongated, circular, and triangular shapes, respectively. The elongated and triangular islands are highly oriented towards [011] and $[01\bar{1}]$ azimuths of the Si(100)-(2 \times 1) surface. (d) Hexagonal-shaped In island. 146
- 4.16 (a) 3D AFM image of an elongated In island oriented toward the [011] substrate azimuth. (b) and (c) are line profiles taken along and across the 147

- elongated island in (a), respectively.
- 4.17 (a) 3D AFM image of a circular In island. (b) Line profile across center of the island in (a) showing a higher edge surrounding a flat central part as indicated by arrows. 147
- 4.18 STM 3D scans of an In circular island (a) and small In clusters (b). 148
- 4.19 Structure model proposed for the In(2×1) grown on the Si(100) surface by fsPLD. (a) Top view showing In first layer on Si terminated surface with In dimer along [011] direction. (b) Side view of the In(2×1) model showing top dimers bonded to the Si atoms in the second layer. (c) The reciprocal lattice with its coordinates determined in term of the measured in-plane lattice parameter $a = 3.65 \pm 0.36 \text{ \AA}$, where a^* and b^* are reciprocal lattice axes. 151
- 4.20 (a) and (b) RHEED patterns of Si(100)-(2×1) surface before In deposition taken along the [011] and $[0\bar{1}\bar{1}]$ azimuths, respectively. (c) and (d) RHEED patterns of In(4×3) grown on Si(100)-(2×1) by fsPLD taken along the [011] and $[0\bar{1}\bar{1}]$ azimuths, respectively. The laser was operated at 2 Hz repetition rate with an energy density of 0.50 J/cm^2 on the In target. 154
- 4.21 RHEED intensity of the specular beam during growth of In at a substrate temperature of 400°C . The laser was operated at 50 Hz repetition rate and 0.07 J/cm^2 laser energy density on the In target. The surface structure changed successively from (2×1) to (4×3) to (1×1) after ~1500 laser shots as shown in the inset RHEED patterns. The RHEED patterns are taken in the [011] azimuth before and during In deposition for 33 s and 100 s. The arrows indicate the time at which the ablating laser was turned on and off. 156
- 4.22 (a) AFM image of the grown In film on Si(100)-(2×1) at 386°C for an In coverage of ~38 ML. The laser was operated at 2 Hz repetition rate and the laser energy density was 0.50 J/cm^2 on the In target. (b) Line profile of an In island shows a rounded shape with height of ~1 nm and width of ~25 nm. (c) 3D STM image of the In film morphology showing grown islands. 157
- 4.23 RHEED intensity of the specular beam during growth of In on Si(100)-(2×1) by fsPLD. The In film was grown at a substrate temperature of 390°C using 2 Hz laser repetition rate and an energy density of 0.50 J/cm^2 on the In target. Specular beam intensity is shown in the inset for In film grown at 400°C using 2 Hz laser repetition rate and an energy density of 0.37 J/cm^2 on the In target. Recovery of the RHEED intensity occurred after termination of the deposition. The arrows indicate the time at which the ablating laser was turned on and off. 158

- 4.24 RHEED intensity of the specular beam was monitored during growth of In within the first ~ 2 ML at different substrate temperatures. The laser was operated at a 2 Hz repetition rate with an energy density of 0.50 J/cm^2 on the In target. The primary electron beam was incident along the $[011]$ azimuth down the staircase of the vicinal Si surface. The inset shows a magnified time scale of RHEED intensity relaxation observed after laser pulses during fsPLD of In on Si(100) at T_s of 390°C from the sixth to the eleventh laser pulse. 160
- 4.25 The RHEED intensity relaxation measured at different growth temperatures. The inset shows time dependence of the normalized RHEED intensity taken after the eighth laser deposition pulse, coverage of ~ 0.5 ML of In. The solid lines are exponential fit. The time constant τ has Arrhenius temperature dependence. The activation energy E_d and the diffusion frequency constant ν_0 of the surface diffusion are determined. 163
- 4.26 The average terrace width L during growth of In at T_s of 358°C on the vicinal Si(100)-(2 \times 1) surface. The laser was operated at a 2 Hz repetition rate and an energy density of 0.50 J/cm^2 on the In target. The primary electron energy of 8.6 keV was incident down the staircase along the $[011]$ azimuth of the Si surface. L was decreasing during growth of the first ~ 11 ML of In. RHEED intensity profiles taken across one of the split peaks, in S_\perp direction, before and during the deposition at ~ 1 ML and ~ 7.6 ML are shown in the inset. The FWHM is measured from a Lorentzian fit to the intensity profiles. A schematic diagram of a vicinal surface is shown in the inset. 167
- 4.27 The average terrace width L during fsPLD of In by two different laser energy densities of 0.25 J/cm^2 and 0.50 J/cm^2 (inset) for ablation of In target. The laser was operated at 2 Hz repetition rate and the growth temperature T_s was 400°C . The 8.6 keV electron beam was incident down the staircase along the $[011]$ azimuth of the Si surface. 168
- 4.28 The average terrace width L during growth of In by fsPLD at T_s of 405°C on the vicinal Si(100)-(2 \times 1) surface. The laser was operated at a 2 Hz repetition rate and an energy density of 0.50 J/cm^2 on the In target. The 8.6 keV electron beam was incident down the staircase along the $[011]$ azimuth of the Si surface. L decreased until an equilibrium reached after deposition of ~ 23 ML of In. The arrow indicates the equilibrium L . The In(4 \times 3) RHEED pattern remained observable during the deposition. In the inset, RHEED patterns of Si(100)-(2 \times 1) before deposition and In(4 \times 3) for In coverage of ~ 38 ML are shown. The splitting of the specular beam was along the $[011]$ azimuth of the vicinal Si(100) surface and parallel to the RHEED shadow edge. 171
- 5.1 (a) The hexagonal wurtzite structure. The parameter $a_1 = a_2 = a$ is the 196

- lattice constant. (b) Tetragonal bonding of In and N. The N atom sits downs the center of a triangle of In atoms and above an In atom of the next layer.
- 5.2 (a) The hexagonal unit cell of InN. a and c are the lattice constants. (b) The layer sequences in terms of the lattice constant c . 197
- 5.3 Schematic diagram of the geometry of PLD and the in situ components. 199
- 5.4 RGA spectra before and after thermal cracking of ammonia in (a) and (b), respectively. Atomic nitrogen resulted after dissociation of the ammonia molecules. 201
- 5.5 RHEED patterns of InN films grown on Si(100)-(1×1) substrates at room temperature. The growth was carried out by fsPLD of In target during thermal cracking of ammonia at pressure of $\sim 5 \times 10^{-6}$ Torr. Buffer layer of In was deposited on the substrate surface before growth of the InN film. The RHEED patterns were taken for two samples prepared at the same deposition conditions. 202
- 5.6 (a) Reflection RHEED pattern of Si(100)-(2×1) surface before deposition. (b) RHEED pattern after deposition of In for ~ 6 ML on Si(100)-(2×1) at substrate temperature of ~ 70 °C. (c) RHEED pattern after deposition of InN buffer layer at temperature of ~ 250 °C. (d) Transmission RHEED pattern after growth of the final InN film at temperature of ~ 350 °C. Thermal cracking of ammonia occurred at a pressure of $\sim 5 \times 10^{-6}$ Torr. 204
- 5.7 (a) Reflection RHEED pattern of Si(100)-(2×1) surface before deposition. (b) RHEED pattern shows In(2×1) structure after deposition of ~ 6 ML In. (c) RHEED patterns after growth of InN at temperature of ~ 100 °C at pressure of $\sim 2 \times 10^{-8}$ Torr taken at [011], $[0\bar{1}1]$, $[01\bar{1}]$ and azimuths of the Si(100) surface. The deposition of InN film on Si(100)-(2×1) surface was performed using a solid InN target made from powder sample. 205
- 5.8 Schematic diagram of the laser induced ammonia breakdown to assist PLD process for growth of InN film on the Si(100) substrate. Laser ablation and laser breakdown create high-density plasmas, which propagate towards the substrate surface where the energetic deposits took place. 207
- 5.9 RHEED patterns of the grown InN film on Si(100) substrate at a temperature of ~ 350 °C and pressure of ~ 2 Torr ammonia. Initially, buffer layers of In was grown on top of the Si(100). Then, laser induced ammonia breakdown performed at a substrate temperature of ~ 250 °C without fsPLD of In before the final film InN took place. RHEED patterns were taken at [011], [001], $[0\bar{1}0]$, and [031] azimuths of the 208

Si(100) surface are shown in (a), (b), (c), and (d), respectively.

- | | | |
|------|---|-----|
| 5.10 | Streaky RHEED patterns observed at $[001]$ and $[0\bar{1}0]$ azimuths of the Si(100) surface are shown in (a) and (b), respectively. Transmission and short streaks diffraction beams are overlapped in (b). | 208 |
| 5.11 | (a) and (b) are AFM images taken at different surface locations of the grown InN film on Si(100) at $\sim 350^\circ\text{C}$ by the fsPLD. (c) and (d) are SEM images taken at different surface locations of the grown film. | 210 |
| 5.12 | (a) RHEED pattern along the $[0\bar{1}0]$ azimuth of the Si(100) surface. (b) RHEED intensity profiles of the first-order peaks of the In and InN. The bright diffraction beams correspond to the 2D In initial layer and the faint beams corresponds to the InN lattice. The distance between the neighboring streaks is inversely proportional to the in-plane lattice parameter. | 211 |
| 5.13 | XRD profile of the epitaxial InN film grown on Si(100)-(2 \times 1) at temperature of $\sim 350^\circ\text{C}$. A buffer layer of In was deposited before growth of InN. Two peaks from InN $[10\bar{1}1]$ and InN $[10\bar{1}\bar{1}]$ are observed. The peak (400) is reflection from the Si substrate. | 213 |
| A.1 | Top view of the PLD system showing components arrangement: (1) chamber; (2) target holder; (3) shutter holder; (4) RHEED gun; (5) substrate holder; (6) laser window; (7) phosphor RHEED screen; (8) CCD camera; (9) and (10) thermal cracker sources; (11) RGA; and (12) UHV high precision leak valve. | 231 |
| A.2 | The target manipulator showing the target and the shutter holders on the 8" O.D. CF flange in (a) and magnified image in (b). | 234 |
| A.3 | (a) Substrate manipulator on the 4.5" O.D. CF flange: (1) power terminals and (2) thermocouple terminals. (b) Sample holder. | 235 |
| A.4 | Schematic diagram of the direct heating stage: (a) front view and (b) side view. | 236 |
| A.5 | Resistive heater stage: (a) image of front part and (b) schematic diagram of the stage and its components. | 238 |
| A.6 | (a) RGA 200: (1) control unit; (2) ion detector; (3) quadrupole filter, and (4) ionizer. The RGA spectrum in (b) and (c) are taken before and after heat cleaning the Si(00) sample for preparation of PLD of In/Si(00) thin films. | 243 |
| A.7 | (a) Schematic diagram of ammonia cracker source. (b) Thermal cracker | 244 |

dc power supply (0-10 V and 0-50 A).

- | | | |
|------|---|-----|
| A.8 | The mechanical pump: (1) forline trap; (2) exhaust line; (3) oil level, and (4) gas ballast. | 247 |
| A.9 | (a) Turbo pump connections; (1) power line; (2) rough pump connection; (3) manual vent valve, and (4) connection to UHV valve. (b) Turbo pump controller. | 248 |
| A.10 | (a) Ion pump components: (1) magnets; (2) bakeout line; (3) titanium filaments feedthrough; (4) manual gate valve, and (5) water cool line. (b) Ion pump control unit: (1) protect switch; (2) power switch, and (3) selector key to monitor pressure, voltage, and current. | 250 |
| A.11 | The pressure monitors of the ionization gauge (1) and the convector gauge (2) of the PLD system. | 252 |
| A.12 | An overview of the PLD system. | 253 |
| B.1 | The diode laser. (a) Remote control module. (b) The laser head: (1) emission indicator and (2) output laser window connected to the laser oscillator. | 255 |
| B.2 | The Ti:sapphire laser oscillator system. (a) The laser head: (1) high reflector; (2) prism dispersion micrometer; (3) slit wavelength micrometer; (4) output coupler, and (5) output laser window. (b) Electronics module: (1) photodiode signal strength indicator; (2) pulsing and enable mode locker indicators showing if the system is mode locked, and (3) fine phase control to adjust the phase relationship between the AOM signal and the photodiode signal to provide a pulse-locking mechanism. (c) Chiller. | 258 |
| B.3 | The Nd:YLF laser system. (a) The laser head: (1) emission indicators and (2) output laser widow connected to the laser amplifier. (b) Power supply: (1) key switch; (2) indicators of power, water level and flow, and temperature, and (3) operation hour counter of the arc flash lamps. (c) Remote control box; (1) Q-Switch on/off; (2) shutter key; (3) lamp enable, and (4) lamp power control and display (in kW). | 260 |
| B.4 | The Ti:sapphire amplifier system. (a) The amplifier laser head. (b) Synchronization and delay generator (SDG) which is used to control the precise timing necessary or a regenerative amplifier to operate: (1) laser output enable; (2) adjustable input divide to change the laser output frequency; (3) output 1 triggers the first Pockels cell driver used to set the timing of the input to the regenerative amplifier; (4) output 2 triggers the second Pockels cell driver used to set the timing of the output pulse | 262 |

from the regenerative amplifier, and (5) synchronization out. (c) Part of the front view of the laser amplifier: (1) LED indicator (Off if the SDG is in synchronization error) and (2) output laser window.

- C.1 The electron gun power supply is two-chassis units, 10 keV source and a control. (a) Front view: (1) power; (2) meter switch; (3) filament control keys; (4) beam energy control keys; (5) x-axis deflector; (6) y-axis deflector; (7) stigmator, and (8) objective, condenser, and extractor keys. (b) Rear view: (1) electron gun cable and (2) high voltage input. 267
- C.2 The electron gun source mounted on 4.5" CF on the vacuum chamber. It connected to the controller by two cables. 267

CHAPTER I

INTRODUCTION*

The study of solid surfaces and thin films growth is of great interest both from the fundamental physical and technological points of view [1-7]. Structural and electronic properties of surfaces or thin films are closely connected. Surface cleaning treatments or adsorption of deposits on a single crystal surface can cause structural changes at surfaces [1, 3, 5]. The surface can be modified with respect to the corresponding atomic planes in the bulk and result in a surface phenomenon such as surface reconstruction or relaxation. In thin films growth, deposits take place on a base material through surface processes [5]. The macroscopic properties are influenced by the kinetic mechanisms such as surface diffusion, nucleation of islands, and interlayer mass transport [4]. Epitaxial films can be produced with electrical properties different from substrates, either higher purity or with doped layers, which play a key role in device processing [6]. Study of nucleation and growth of thin films on single crystal surfaces is fundamental for understanding the crystal growth and for device applications [4, 5].

Preparation of clean and atomically ordered surfaces is an essential step for device fabrications, prior to epitaxial growth, and for high quality thin layers. In negative electron affinity (NEA) devices that are based on III-V semiconductor compounds, native oxides and carbons are tightly bound and thermally desorb above their congruent temperatures [8-13]. For indium phosphide (InP), such heat cleaning causes preferential desorption of phosphor atoms leaving an indium-rich rough surface. The NEA effect is

* The reference model of this dissertation follows the SPIE format.

observed on clean surfaces; after deposition a thin layer of cesium oxide to low the work function. When the vacuum level becomes lower than bulk conduction band minimum, on p-type III-V semiconductor surfaces, electrons excited across the band gap will escape into a vacuum [14-16]. Contaminants and rough crystal surfaces degrade the electrons emission and broaden the angular spread of the emitted electrons. In nanoscale device fabrication, concerns over changes in the dopant profile and damage to prefabricated structures limit the thermal and chemical surface treatments. Atomic hydrogen has been used for surface cleaning before film growth or activation to NEA [17-23]. The low temperature surface cleaning and interaction to the topmost layer make in situ atomic hydrogen an attractive technique to eliminate the drawbacks of other surface cleaning methods. Surfaces studies using in situ techniques such as reflection high-energy electron diffraction (RHEED) and scanning tunneling microscopy (STM) showed that atomic hydrogen cleaning is effective in surface cleaning [24-27]. The structural and optical properties of quantum dots grown on a hydrogen-cleaned surface were improved due to reduction of the interface defects [28]. The electronic properties of the NEA devices depend on the quality of the surface cleaning step. NEA cathodes have been used for spin-polarized electron emitters, electron beam lithography, high brightness electron sources, and vacuum microelectronic devices [14, 15, 29-31]. The performance of the photoelectrons in an ultrahigh vacuum is significant to produce high beam polarization and high quantum yield. The main barrier of NEA cathodes has been concern about their lifetime and stability. The low-energy spread, low emission noise, and picosecond-scale switching time make NEA materials as electron sources for a new generation of microscopy and further electron beam applications [32, 33]. InP based NEA have

recently been recognized as having important applications in near infrared transferred electron photocathodes and imaging systems [34-36]. The efficient surface cleaning and the activation layer are critical for a photocathode to achieve high quantum efficiency. Study of the effects of atomic hydrogen exposure on the surface structure and understanding the nature of its microscopic reactions with the surface can advance the surface electronic quality. In addition, formation mechanism and the structure of the activation layer need further study for stability of the NEA property of the surface.

Growth of group-III metals (Al, Ga, and In) on silicon surfaces has been the subject of theoretical and experimental studies due to its fundamental and technological interests. Most of the studies have been focused on the initial growth modes and on determination of the structures induced by adsorbate submonolayers of the group-III metals on Si crystalline surfaces. Indium was previously grown on Si(100)-(2×1) using molecular beam epitaxy (MBE) and conventional evaporation [37-41]. The nucleation and growth of In on Si(100) surfaces were studied by low-energy electron diffraction (LEED), RHEED, STM, time-of-flight impact collision ion scattering spectroscopy (ICISS), and Auger electron spectroscopy (AES) [37-41]. The growth mechanism of In on clean Si(100)-(2×1) surfaces was found to occur by the Stranski-Krastanov (SK) mode, with initial formation of two-dimensional (2D) layer followed by nucleation and growth of three-dimensional (3D) islands [37]. The structure of the initial 2D layer was dependent upon the film coverage and substrate temperature [37]. Results showed that the In(2×2) was the main structure of the 2D layer observed at room temperature. At low film coverage, STM studies showed that Al, Ga, and In initially form long one-dimensional ad-dimers on the Si(100)-(2×1) surface [42, 43]. This growth mode

continued until the (2×2) structure was completed at 0.5 monolayers (ML) [1 ML = 6.8×10^{14} atoms/cm² for unreconstructed Si(100) surface] [44-46]. The In(2×2) reconstruction consists of In dimers on a still-dimerized Si(100) substrate with orientation of In parallel to the Si dimers. Spontaneous formation of self-organized In nanowire arrays on Si(100), with a (2×2) structure, have been shown and were stable at temperatures up to 150 °C [47]. With increasing In coverage, 2D and 3D islands were observed with different morphologies [37, 39, 41, 48]. The difference in the islands' morphology was explained by the effect of the surface structure and the difference in the diffusion length of the deposited In on the surface. A completely different result occurs at high temperatures deposition, or when the Si surface is annealed: a well ordered In(4×3) superlattice is formed with In coverage of 0.5 ML [37, 49-51]. The In(4×3) surface phase was studied by AES, RHEED, LEED, STM, ICISS, and x-ray diffraction [37, 49-56]. The In(4×3) structural model has been a subject of debate. Theoretical and experimental studies using first principle total energy calculations, STM image simulations, and photoelectron holography were performed to solve the structural model of the In(4×3) on Si(100) [57-59]. Their results favored the x-ray diffraction analysis by Bunk et al. [55], in which the 4×3 unit cell comprises a stable pyramid-like Si₇In₆ cluster. Results showed that the initial structure is a mix of In(4×3) and Si(2×1) until the surface becomes fully In(4×3). It has been suggested that the growth of the In(4×3) at 0.5 ML In is accompanied by displacement of the underlying Si surface atoms [51]. The Si(100)-In(4×3) surface has been identified to be composed of nearly identical-size nanoclusters and shown to be prepared by spontaneous self-assembly [60-64]. The structural and electronic properties of these nanoclusters have the potential for future nanoscale and

electronic device applications. For In coverages > 2 ML, the (4×3) surface was decorated with 3D islands or replaced by a disordered phase [50]. This transition between the (4×3) + 3D islands morphology to a disordered 2D layer + 3D islands occurred as temperature was raised above ~ 450 °C [50]. Indium is an acceptor in Si and it has been observed to strongly surface segregate during Si MBE growth [65]. Study the growth dynamics of In on Si(100)- (2×1) in the early stages of growth and the following film morphology is useful such as in understanding In incorporation into Si as dopants during film growth or how III-V compound semiconductor materials grow on Si(100).

Indium nitride (InN) is an interesting material due to its excellent electrical properties predicted theoretically and for its potential device applications [66, 67]. The group III-nitrides have been considered a promising system for optoelectronic devices, especially for the development of high brightness light-emitting diodes (LEDs), laser diodes and optical detectors, and high frequency transistors operating at high powers and temperatures [68-72]. Among the group III-nitride semiconductors, InN has the lowest effective mass and highest carrier mobility [66]. Electron transport studies of InN indicate extremely high peak drift velocity at room temperature, which can be applied in high-speed electronic devices [66, 73, 74]. InN has received much attention in LEDs, field-effect transistors, terahertz emitters, and solar cells applications [66, 75-77]. For example, photovoltaic cells using InN/Si have been proposed for high-efficiency solar cells [78]. However, the fundamental parameters of the grown InN films, including the band gap, lattice constant and effective electron mass, have shown wide variation in measured values. With improvement in material quality, the band gap of InN was found to be 0.6-0.9 eV, much lower than the previously cited value of 1.9 eV [79-83].

Therefore, the use of InN and its alloys creates the possibility of band gap tuning and extension of the emission of nitride-based LEDs from ultraviolet to near infrared region [66]. The discrepancy in band gap could be attributed to low crystalline quality and defects and impurities present in the material. One of the main limitations to a proper understanding has been the difficulty in consistently applying standard measurement techniques developed for other III-V materials [67]. Suggestions for observations of a higher band gap have included the Moss-Burstein effect, oxygen inclusion, presence of metallic In and Mie scattering from such In droplets, quantum size effects and stoichiometry changes [67]. Growth of high quality InN films is known to be difficult due to a lack of suitable substrates, the low dissociation temperature, and the high equilibrium vapor pressure of nitrogen over the InN [84-88]. Nitridation of In is generally a problem since the sticking probability of nitrogen on its surface is very small [89, 90]. Studying the InN growth and improving the films' structural properties further advances the group III-nitrides devices.

Several techniques have been employed for the growth of thin films and multilayers. These include MBE, sputter deposition, chemical vapor deposition, and pulsed laser deposition (PLD). PLD has been applied for wide range of materials [91-93]. Lasers are unique energy sources characterized by their monochromatic light emission, spatial and temporal coherence, and high average and peak intensity [92]. Tuning these laser parameters has the ability to control the structural properties and growth mode of thin films. The PLD process can be considered in three stages: (i) the interaction of laser beam with the target material, which results in ablation of the surface layers, (ii) adiabatic expansion of the resultant plasma, and (iii) deposition of the ablated material on the

substrate surface. The high energetic species in the plasma plume increase sticking coefficients and surface mobilities of the deposits, which gives PLD the potential to assist in crystalline phase formation of thin films [92, 93]. The high instantaneous deposition rate leads to a high nucleation density and improves the layer-by-layer growth. The influences of these ablation characteristics on the film growth mechanism are complex due to the interaction between the incident particles and the surface atoms [91-95]. The growth by PLD and MBE often yields significantly different initial stages of growth and film morphology [93]. Growth of compound elements and semiconductors by PLD has been of interest due to stoichiometric transfer of material from bulk to film and the capability for reactive deposition in ambient gases [92]. However, the formation of large particulates and the angular distribution of ablated species are the main limitations of PLD for thin film growth. Experimental techniques have been developed to minimize the number and size of particulates [96-98]. The use of femtosecond lasers has been proposed as a possible solution to overcome the occurrence of droplets often observed in nanosecond PLD due to thermal effects at the target surface [99, 100]. In the femtosecond pulsed laser deposition (fsPLD), heat diffusion into the target material is negligible and the conventional thermal deposition is considerably limited, which results in a high efficiency of ablation [93]. Understanding the nucleation and growth dynamics in the PLD thin films, in particular for the first monolayers, can assist in developing the film structures' properties.

RHEED is an in situ analytical technique that is used to study surface structures and thin films growth [101-104]. A focused beam of high energy (10-30 keV) electrons is directed at grazing incidence onto the sample, making the probe highly surface sensitive.

Electrons diffracted from the surface are detected with a fluorescent screen placed opposite the RHEED gun. The geometry of RHEED indicates that a long mean-free path through the sample is associated with penetration normal to the surface of only a few atomic layers [101, 102]. The diffraction pattern will usually consist of streaks or spots depending on if the sample has a flat surface or there are crystalline islands on the surface, respectively. RHEED pattern can show development when surface oxide is removed and show improvements in surface ordering that occurs with the subsequent annealing. The fundamentals of RHEED and interpretation of measurements are typically described in the framework of the kinematical approaches. In the reciprocal lattice, the conditions of elastic scattering and constructive interference are combined to find the locations of intensity maxima in the diffraction pattern [105]. However, theoretical works are introduced to study the effects of multiple elastic and inelastic scattering on the RHEED analysis [101, 103, 106]. RHEED intensity oscillations, in the layer-by-layer growth mode, provide important information about the film growth in real time. It is used to control the film thickness on the order of a monolayer and is a powerful tool to assist in fabrication of complicated material structures. RHEED oscillations can detect the birth and spread of 2D nuclei under various growth conditions and used to study the growth dynamics [107]. The transition from layer-by-layer to step flow growth has been used to estimate the surface diffusion parameters [108]. RHEED technique has been extended to study the stress at the interface between the growing film and the substrate surface [109, 110], monitor fabrication of complex oxide materials [111, 112], reveal the surface texture of polycrystalline films [113, 114], and determine structural properties of nanostructures [115, 116].

In this work, studies of hydrogen-cleaned InP activated surfaces and two heteroepitaxial growth systems, namely In on Si(100) and InN on Si(100) by fsPLD, are presented. In the InP work, the objective is to study the effect of hydrogen exposure on the surface morphology of a semiconductor surface before activation to negative electron affinity. The methodology is to measure the electron yield with atomic hydrogen cleaning time and correlated to the development in surface morphology. Another objective is to monitor the surface preparation and the photocathode performance. In the fsPLD of In work, the first objective is to study the nucleation and growth of In on the Si(100)-(2×1) surface by fsPLD. The study is performed to determine the initial layer structure, the growth mode, and the film morphology; then it compares the results to the available previous work. Another aim of this work is to determine the deposition conditions of obtaining high quality In films and then employ them in fabrication of InN on Si(100). In the nitride film work, the objective was to grow InN on Si(100) surface using the fsPLD, which could possibly be used for device applications. The plan of work is to grow a buffer layer of In on the substrate before growing the final films and to use nitridation techniques such as thermal cracking and laser induced gas breakdown of ammonia. The growth and morphology of the InN films were investigated at different deposition conditions. The use of in situ RHEED investigating technique is to provide qualitative and quantitative analysis of treatment surfaces and during film growth. The film morphology is examined and analyzed using ex situ microscopic techniques including AFM, EDAX, SEM, and STM.

The thesis is organized after this introductory chapter as follows. Chapter II gives an overview of theoretical and basic fundamentals of RHEED. The experimental

procedures and applications of RHEED for studying vicinal surfaces and thin films are described. Chapter III presents a study of electron yield and surface morphology of negative electron affinity InP(100) activated surfaces. The effect of atomic hydrogen cleaning on surface morphology such as surface terrace width and vacancy-adatom density is studied. Chapter IV discusses the growth of In on vicinal Si(100)-(2×1) surface by fsPLD. The growth mode, in-plane lattice parameter, and film morphology are studied. The growth of the initial layer and the 3D islands are studied and related to the growth kinetics by fsPLD. RHEED intensity recovery and oscillations are used to determine the surface diffusion parameters. Activation energy of surface diffusion and terrace width dynamics during the growth of In on Si at high temperatures are studied. The morphology of the grown thin films is examined using ex situ AFM and STM. In chapter V, the fsPLD is used to grow InN on Si(100) surface. An additional purpose of this chapter is to study the effects of growing an initial In buffer layer and nitridation process on the properties of InN films. The growth and morphology of InN films are studied. Each chapter will be self-contained, having its own introduction, conclusion and list of references. The thesis is based on the published work in journals [22, 117-120]. Finally, chapter VI summarizes the main results of this work. Technical information about operation and maintenance of the ultrahigh vacuum PLD system, femtosecond laser system, and RHEED system are given in appendices A, B, and C.

I.1. References

- [1] M. Prutton, "*Surface physics*," Oxford University Press, Oxford (1983).
- [2] A. Zangwill, "*Physics at surfaces*," Cambridge University Press, Cambridge (1988).
- [3] W. Monch, "*Semiconductor surfaces and interfaces*," Springer-Verlag, Berlin Heidelberg (1993).
- [4] Z. Zhang and M. G. Lagally, "Atomic processes in the early stages of thin-film growth," *Science* **276**, 377-383 (1997).
- [5] J. A. Venables, "*Introduction to surface and thin film processes*," Cambridge University Press, Cambridge (2000).
- [6] J. R. Arthur, "*Molecular beam epitaxy*," *Surf. Sci.* **500**, 189-217 (2002).
- [7] K. Oura, V. G. Lifshits, A. A. Saranin, A. V. Zotov, and M. Katayama, "*Surface Science, An Introduction*," Springer-Verlag, Berlin (2003).
- [8] W. Ranke and K. Jacobi, "Structure and reactivity of GaAs surfaces," *Surf. Sci.* **10**, 1-52 (1981).
- [9] R. P. Vasquez, B. F. Lewis, and F. J. Grunthaner, "X-ray photoelectron spectroscopic study of the oxide removal mechanism of GaAs (100) molecular beam epitaxial substrates in in situ heating," *Appl. Phys. Lett.* **42**, 293-295 (1983).
- [10] N. Kobayashi and Y. Kobayashi, "As and P desorption from III-V semiconductor surface in metalorganic chemical vapor deposition studied by surface photo-absorption," *Jpn. J. Appl. Phys.* **30**, L1699-L1701 (1991).

- [11] T. V. Buuren, M. K. Weilmeier, I. Athwal, K. M. Colbow, and J. A. Mackenzie, "Oxide thickness effect and surface roughening in the desorption of the oxide from GaAs," *Appl. Phys. Lett.* **59**, 464-466 (1991).
- [12] W. M. Lau, R. N. S. Sodhi, and S. Ingre, "Thermal desorption of oxides on InP," *Appl. Phys. Lett.* **52**, 386-388 (1991).
- [13] R. Averbek, H. Riechert, H. Schlötterer, and G. Weimann, "Oxide desorption from InP under stabilizing pressures of P_2 or As_4 ," *Appl. Phys. Lett.* **59**, 1732-1734 (1991).
- [14] R. L. Bell, "*Negative electron affinity devices*," Clarendon Press, Oxford (1973).
- [15] R. U. Martinelli and D. G. Fisher, "The application of semiconductors with negative electron affinity surfaces to electron emission devices," *Proc. IEEE* **62**, 1339-1360 (1974).
- [16] W. E. Spicer, "Negative affinity 3-5 photocathodes: Their physics and technology," *Appl. Phys. A* **12**, 115-130 (1977).
- [17] C. M. Rouleau and R. M. Park, "GaAs substrate cleaning for epitaxy using a remotely generated atomic hydrogen beam," *J. Appl. Phys.* **73**, 4610-4613 (1993).
- [18] Y. Okada, T. Fujita, and M. Kawabe "Growth modes in atomic hydrogen-assisted molecular beam epitaxy of GaAs," *Appl. Phys. Lett.* **67**, 676-678 (1995).
- [19] Z. Yu, S. L. Buczkowski, N. C. Giles, and T. H. Myers, "Defect reduction in ZnSe grown by molecular beam epitaxy on GaAs substrates cleaned using atomic hydrogen," *Appl. Phys. Lett.* **69**, 82-84 (1996).

- [20] L. S. Hirsch, Z. Yu, S. L. Buczkowski, T. H. Myers, and M. R. Richards-Babb
“The use of atomic hydrogen for substrate cleaning for subsequent growth of II-VI semiconductors,” *Journal of Electronic Materials* **26**, 534-541 (1997).
- [21] K. A. Elamrawi and H. E. Elsayed-Ali, “Preparation and operation of hydrogen cleaned GaAs(100) negative electron affinity photocathodes,” *J. Vac. Sci. Technol. A* **17**, 823-831 (1999).
- [22] M. A. Hafez and H. E. Elsayed-Ali, “Atomic hydrogen cleaning of InP(100): Electron yield and surface morphology of negative electron affinity activated surfaces,” *J. Appl. Phys.* **91**, 1256-1264 (2002).
- [23] T. Maruyama, D.-A. Luh, A. Brachmann, J. E. Clendenin, E. L. Garwin, S. Harvey, R. E. Kirby, C. Y. Prescott, and R. Prepost, “Atomic hydrogen cleaning of polarized GaAs photocathodes,” *Appl. Phys. Lett.* **82**, 4184-4186 (2003).
- [24] T. Kikawa, I. Ochiai, and S. Takatani, “Atomic hydrogen cleaning of GaAs and InP surfaces studied by photoemission spectroscopy,” *Surf. Sci.* **316**, 238-246 (1992).
- [25] T. Muranaka, C. Jiang, A. Ito and H. Hasegawa “Characterization and optimization of atomic hydrogen cleaning of InP surface for selective molecular beam epitaxial growth of InGaAs quantum structure arrays,” *Jpn. J. Appl. Phys.* **40**, 1874-1877 (2001).
- [26] A. Khatiri, J. M. Ripalda, T. J. Krzyzewski, G. R. Bell, C. F. McConville, and T. S. Jones, “Atomic hydrogen cleaning of GaAs(001): A scanning tunnelling microscopy study,” *Surf. Sci.* **548**, L1-L6 (2004).

- [27] A. Khatiria, T. J. Krzyzewskia, C. F. McConvilleb, T. S. Jonesa “Atomic hydrogen cleaning of low-index GaAs surfaces,” *J. Cryst. Growth* **282**, 1-6 (2005).
- [28] J. S. Kim, M. Kawabe, N. Koguchi, D.-Y. Lee, J. S. Kim, and I.-H. Bae, “Structural and optical properties of InAs quantum dots regrown on atomic hydrogen-cleaned GaAs surface,” *Appl. Phys. Lett.* **87**, 261914-261916 (2005).
- [29] E. J. P. Santos and N. C. MacDonald, “Selective emission of electrons from patterned negative electron affinity cathodes,” *IEEE Trans. Electron Devices* **41**, 607-611 (1994).
- [30] F. Ciccacci, S. De Rossi, and D. M. Campbell, “Low energy Mott polarimetry of electrons from negative electron affinity photocathodes,” *Rev. Sci. Instrum.* **66**, 4161-4165 (1995).
- [31] F. R. Hughes, E. D. Savoye, and D. L. Thoman, “Application of negative electron affinity materials to imaging devices,” *J. Electronic Materials* **3**, 9-23 (2007).
- [32] A. Baum, P. Arcuni, V. Aebi, S. Presley, and M. Elder, “Prototype negative electron affinity-based multibeam electron gun for lithography and microscopy,” *J. Vac. Sci. Technol. B* **17**, 2819-2822 (1999).
- [33] P. Arcuni, S. Presley, V. Aebi, and W. E. Spicer, “Recent tests of negative electron affinity photocathodes as source for electron lithography and microscopy,” *J. Vac. Sci. Technol. B* **19**, 2585-2590 (2001).
- [34] J. Peretti, H.-J. Drouhin, and D. Paget, “High-resolution energy analysis of field-assisted photoemission: A spectroscopic image of hot-electron transport in semiconductors,” *Phys. Rev. B* **47**, 3603-3619 (1993).

- [35] D.-I. Lee, Y. Sun, Z. Liu, S. Sun, and P. Pianetta, "Angular dependence of the photoelectron energy distribution of InP(100) and GaAs(100) negative electron affinity photocathodes," *Appl. Phys. Lett.* **91**, 192101 (1-3) (2007).
- [36] Y. Sun, Z. Liu, P. Pianetta, and D.-I. Lee, "Formation of cesium peroxide and cesium superoxide on InP photocathode activated by cesium and oxygen," *J. Appl. Phys.* **102**, 074908 (1-6) (2007).
- [37] J. Knall, J.-E. Sundgren, G. V. Hansson, and J. E. Greene, "Indium overlayers on clean Si(100)-(2×1): surface structure, nucleation, and growth," *Surf. Sci.* **166**, 512-538 (1986).
- [38] M. M. R. Evans, J. C. Glueckstein, and J. Nogami, "Indium on Si(001): Growth beyond the first atomic layer," *Surf. Sci.* **406**, 246-253 (1998).
- [39] J.-T. Ryu, K. Kui, K. Noda, M. Katayama, and K. Oura, "The effect of hydrogen termination on In growth on Si(100) surface," *Surf. Sci.* **401**, L425-L431 (1998).
- [40] M. M. R. Evans and J. Nogami, "Indium and gallium on Si(001): A closer look at the parallel dimer structure," *Phys. Rev. B* **59**, 7644-7648 (1999).
- [41] J. T. Ryu, O. Kubo, H. Tani, T. Harada, M. Katayama, and K. Oura, "The growth of indium thin films on clean and hydrogen-terminated Si(100) surfaces," *Surf. Sci.* **433-435**, 575-580 (1999).
- [42] H. Itoh, J. Itoh, A. Schmid, and T. Ichinokawa, "Structures of low-coverage phases of Al on the Si(100) surface observed by scanning tunneling microscopy," *Phys. Rev. B* **48**, 14663-14666 (1993).

- [43] N. Takeuchi, "Adsorption of group III and group V metals on Si(001): One-dimensional versus two-dimensional growth," *Phys. Rev. B* **63**, 035311 (1-5) (2001).
- [44] A. A. Baski, J. Nogami, and C. F. Quate, "Gallium growth and reconstruction on the Si(100) surface," *J. Vac. Sci. Technol. A* **8**, 245-248 (1990).
- [45] J. Nogami, A. A. Baski, and C. F. Quate, "Aluminum on the Si(100) surface: Growth of the first monolayer," *Phys. Rev. B* **44**, 1415-1418 (1991).
- [46] A. A. Baski, J. Nogami, and C. F. Quate, "Evolution of the Si(100)-2×2-In reconstruction," *J. Vac. Sci. Technol. A* **9**, 1946-1950 (1991).
- [47] J.-L. Li, X.-J. Liang, J.-F. Jia, X. Liu, J.-Z. Wang, E.-G. Wang, and Q.-K. Xue, "Spontaneous formation of ordered indium nanowire array on Si(001)," *App. Phys. Lett.* **79**, 2826-2828 (2001).
- [48] O. Kubo, J. T. Ryu, H. Tani, T. Harada, M. Katayama, and K. Oura, "Direct observation of strained layer formation at the initial stage of In thin film growth on Si(100)," *Jpn. J. Appl. Phys.* **38**, 3849-3852 (1999).
- [49] N. Kuwata, T. Asai, K. Kimura, and M. Mannami, "Superlattice structures of Si(100) surfaces deposited with In and Sn atoms," *Surf. Sci.* **143**, L393-L397 (1984).
- [50] J. Knall, S. A. Barnett, J.-E. Sundgren, and J. E. Greene, "Adsorption and desorption kinetics of In on Si(100)," *Surf. Sci.* **209**, 314-334 (1989).
- [51] A. A. Baski, J. Nogami, and C. F. Quate, "Indium-induced reconstructions of the Si(100) surface," *Phys. Rev. B* **43**, 9316-9319 (1991).

- [52] A. V. Zotov, A. A. Saranin, V. G. Lifshits, J.-T. Ryu, O. Kubo, H. Tani, M. Katayama, and K. Oura, "Structural model for the Si(100)4×3-In surface phase," *Phys. Rev. B* **57**, 12492-12496 (1998).
- [53] A. A. Saranin, A. V. Zotov, V. G. Lifshits, J.-T. Ryu, O. Kubo, H. Tani, T. Harada, M. Katayama, and K. Oura, "Analysis of surface structures through determination of their composition using STM: Si(100)4×3-In and Si (111)4×1-In reconstructions," *Phys. Rev. B* **60**, 14372-14381 (1999).
- [54] B. E. Steele, D. M. Cornelison, L. Li, and I. S. T. Tsong, "The structure of the Si(100)-(4×3)In surface studied by STM and ICISS," *Nucl. Instr. and Meth. in Phys. Res. B* **85**, 414-419 (1994).
- [55] O. Bunk, G. Falkenberg, L. Seehofer, J. H. Zeysing, R. L. Johnson, M. Nielsen, R. Feidenhans'l, and E. Landemark, "Structure determination of the indium induced Si(001)-(4×3) reconstruction by surface X-ray diffraction and scanning tunneling microscopy," *Appl. Surf. Sci.* **123/124**, 104-110 (1998).
- [56] O. Bunk, G. Falkenberg, J. H. Zeysing, R. L. Johnson, M. Nielsen, and R. Feidenhans'l, "Comment on "Structural model for the Si(001) 4×3-In surface phase"," *Phys. Rev. B* **60**, 13905-13906 (1999).
- [57] N. Takeuchi, "First-principles calculations of the atomic structure of the In-induced Si(001)-(4×3) reconstruction," *Phys. Rev. B* **63**, 245325(1-7) (2001).
- [58] T. M. Schmidt, J. L. P. Castineira, and R. H. Miwa, "Solving the structural model for the Si(001)-In(4×3) surface," *Appl. Phys. Lett.* **79**, 203-205 (2001).
- [59] P. J. E. Reese, T. Miller, and T.-C. Chiang, "Photoelectron holography of the In-terminated Si(001)-(4×3) surface," *Phys. Rev. B* **64**, 233307(1-4) (2001).

- [60] V. G. Kotlyar, A. V. Zotov, A. A. Saranin, T. V. Kasyanova, M. A. Cherevik, O. V. Bekhtereva, M. Katayama, K. Oura, and V. G. Lifshits, "Magic nanoclusters of group III metals on Si(100) surface," *e-J. Surf. Sci. Nanotech.* **1**, 33-40 (2003).
- [61] V. G. Kotlyar, A. V. Zotov, A. A. Saranin, E. N. Chukurov, T. V. Kasyanova, M. A. Cherevik, I. V. Pisarenko, H. Okado, M. Katayama, K. Oura, and V. G. Lifshits, "Doping of magic nanoclusters in the submonolayer In/Si(100) system," *Phys. Rev. Lett.* **91**, 026104(1-4) (2003).
- [62] J. R. Ahn, J. H. Byun, W. H. Choi, H. W. Yeom, H. Jeong, and S. Jeong, "Nonmetallic nature of In-induced nanoclusters on Si(100)," *Phys. Rev. B* **70**, 113304(1-4) (2004).
- [63] A. A. Saranin, A. V. Zotov, V. G. Kotlyar, H. Okado, M. Katayama, and K. Oura, "Modified Si(100)4×3-In nanoclusters arrays," *Surf. Sci.* **598**, 136-143 (2005).
- [64] A. A. Saranin, A. V. Zotov, I. A. Kuyanov, M. Kishida, Y. Murata, S. Honda, M. Katayama, K. Oura, C. M. Wei, and Y. L. Wang, "Atomic dynamics of In nanoclusters on Si(100)," *Phys. Rev. B* **74**, 125304(1-4) (2006).
- [65] J. Knall, J.-E. Sundgren, J. E. Greene, A. Rockett, S. A. Barnett, "Indium incorporation during the growth of (100)Si by molecular beam epitaxy: Surface segregation and reconstruction," *Appl. Phys. Lett.* **45**, 689-691 (1984).
- [66] A. G. Bhuiyan, A. Hashimoto, and A. Yamamoto, "Indium nitride (InN): A review on growth, characterization, and properties," *J. Appl. Phys.* **94**, 2779-2808 (2003).
- [67] K. S. A. Butcher and T. L. Tansley, "InN, latest development and a review of the band-gap controversy," *Superlattices and Microstructures* **38**, 1-37 (2005).

- [68] S. Strite and H. Morkoc, "GaN, AlN, and InN: A review," J. Vac. Sci. Technol. B **10**, 1237-1266 (1992).
- [69] O. Ambacher, "Growth and applications of Group III-nitrides," J. Phys. D: Appl. Phys. **31**, 2653-2710 (1998).
- [70] S. C. Jain, M. Willander, J. Narayan, and R. Van Overstraeten, "III-nitrides: Growth, characterization, and properties," J. Appl. Phys. **87**, 965-1006 (2000).
- [71] S. Yoshida, "Growth of cubic III-nitride semiconductors for electronics and optoelectronics application," Physica E **7**, 907-914 (2000).
- [72] I. Akasaki, "Nitride semiconductors – impact on the future world," J. Cryst. Growth **237-239**, 905-911 (2002).
- [73] S. K. O'Leary, B. E. Foutz, M. S. Shur, U. V. Bhapkar, and L. F. Eastman "Electron transport in wurtzite indium nitride," J. Appl. Phys. **83**, 826-829 (1998).
- [74] E. Bellotti, B. K. Doshi, and K. F. Brennan, J. D. Albrecht and P. P. Ruden, "Ensemble Monte Carlo study of electron transport in wurtzite InN," J. Appl. Phys. **85**, 916-923 (1998).
- [75] S. Nakamura, M. Senoh, M. Iwara, S. Nagahama, T. Yamada, and T. Mukai, "Superbright green InGaN single-quantum-well-structure light-emitting diodes," Jpn. J. Appl. Phys. **34**, L1332-L1335 (1995).
- [76] H. Ahn, Y.-P. Ku, C.-H. Chuang, C.-L. Pan, H.-W. Lin, Y.-L. Hong, and S. Gwo, "Intense terahertz emission from *a*-plane InN surface," Appl. Phys. Lett. **92**, 102103 (1-3) (1985).
- [77] L.-C. Chen, "In₂O₃/Si heterojunction solar cells fabricated by InN oxidation," Eur. Phys. J. Appl. Phys. **40**, 145-148 (2007).

- [78] C. Morioka, T. Yamaguchi, H. Naoi, T. Araki, A. Suzuki, and Y. Nanishi
“Characterization of photovoltaic cells using n-InN/p-Si grown by RF-MBE,”
Mat. Res. Soc. Symp. Proc. **798**, Y10.71(1-6) (2004).
- [79] J. Wu, W. Walukiewicz, K. M. Yu, J. W. Ager III, E. E. Haller, H. Lu, W. J.
Schaff, Y. Saito, and Y. Nanishi, “Unusual properties of the fundamental band
gap of InN,” Appl. Phys. Lett. **80**, 3967-3969 (2002).
- [80] T. Matsuoka, H. Okamoto, M. Nakao, H. Harima, and E. Kurimoto, “Optical
bandgap energy of wurtzite InN,” Appl. Phys. Lett. **81**, 1246-1248 (2002).
- [81] M. Higashiwaki and T. Matsui, “Estimation of band-gap energy of intrinsic InN
from photoluminescence properties of undoped and Si-doped InN films grown by
plasma-assisted molecular-beam epitaxy,” J. Cryst. Growth **269**, 162-166 (2004).
- [82] T. V. Shubina, S. V. Ivanov, V. N. Jmerik, D. D. Solnyshkov, V. A. Vekshin, P.
S. Kop’ev, A. Vasson, J. Leymarie, A. Kavokin, H. Amano, K. Shimono, A.
Kasic, and B. Monemar, “Mie resonances, infrared emission, and the band gap of
InN,” Phys. Rev. Lett. **92**, 117407 (1-4) (2004).
- [83] K. M. Yu, Z. Liliental-Weber, W. Walukiewicz, W. Shan, J. W. Ager III, S. X. Li,
R. E. Jones, E. E. Haller, H. Lu, and W. J. Schaff, “On the crystalline structure,
stoichiometry and band gap of InN thin films,” Appl. Phys. Lett. **86**, 071910-
071912 (2005).
- [84] L. Liu and J. H. Edgar, “Substrates for gallium nitride epitaxy,” Mater. Sci. Eng.
R **37**, 61-127 (2002).
- [85] Q. Guo, O. Kato, and A. Yoshida, “Thermal stability of indium nitride single
crystal films,” J. Appl. Phys. **73**, 7969-7971 (1993).

- [86] Y. Nanishi, Y. Saito and T. Yamaguchi, "RF-molecular beam epitaxy growth and properties of InN and related alloys," Jpn. J. Appl. Phys. **42**, 2549-2559 (2003).
- [87] K. Xu and A. Yoshikawa, "Effects of film polarities on InN growth by molecular-beam epitaxy," Appl. Phys. Lett. **83**, 251-253 (2003).
- [88] E. Dimakis, E. Lliopoulos, K. Tsagaraki, Th. Kehagias, Ph. Komninou, and A. Georgakilas, "Heteroepitaxial growth of In-face InN on GaN (0001) by plasma-assisted molecular-beam epitaxy," J. Appl. Phys. **97**, 113520 (1-10) (2005).
- [89] M. E. Jones, J. R. Shealy, J. R. Engstrom, "Thermal and plasma-assisted nitridation of GaAs(100) using NH_3 ," Appl. Phys. Lett. **67**, 542-544 (1995).
- [90] S. Dhara, P. Magudapathy, R. Kesavamoorthy, S. Kalavathi, V. S. Sastry, K. G. M. Nair, G. M. Hsu, L. C. Chen, and K. H. Chen, K. Santhakumar and T. Soga, "Nitrogen ion beam synthesis of InN in InP(100) at elevated temperature," Appl. Phys. Lett. **88**, 241904 (1-3) (2006).
- [91] D. B. Chrisey and G. K. Hubler, "*Pulsed laser deposition of thin films*," John Wiley and Sons, New York (1994).
- [92] J. C. Miller and R. F. Haglund, "*Laser ablation and desorption*," Experimental Methods in the Physical Sciences **30**, Academic Press, Boston (1998).
- [93] J. Shen, Z. Gai, and J. Kirschner, "Growth and magnetism of metallic thin films and multilayers by pulsed-laser deposition," Surf. Sci. Reports **52**, 163-218 (2004).
- [94] D. M. Zhang, L. Guan, Z. H. Li, G. J. Pan, H. Z. Sun, X. Y. Tan, and L. Li, "Influence of kinetic energy and substrate temperature on thin film growth in pulsed laser deposition," Surf. Coat. Technol. **200**, 4027-4031 (2006).

- [95] J. Perriere, E. Millon, W. Seiler, C. Boulmer-Leborgne, V. Carciun, O. Albert, J. C. Loulergue, and J. Etchepare, "Comparison between ZnO films grown by femtosecond and nanosecond laser ablation," *J. Appl. Phys.* **91**, 690-696 (2002).
- [96] G. Koren, A. Gupta, R. J. Baseman, M. I. Lutwyche, and R. B. Laibowitz, "Laser wavelength dependent properties of $\text{Yb}_2\text{Cu}_3\text{O}_7$ - thin films deposited by laser ablation," *Appl. Phys. Lett.* **55**, 2450-2452 (1989).
- [97] D. Lubben, S. A. Barnett, K. Suzuki, S. Gorbatkin, and J. E. Greene, "Laser-induced plasmas for primary ion deposition of epitaxial Ge and Si films," *J. Vac. Sci. Technol. B* **3**, 968 (1985).
- [98] S. Witanachchi, K. Ahmed, P. Sakthivel, and P. Mukherjee, "Dual-laser ablation for particulate-free film growth," *Appl. Phys. Lett.* **66**, 1469-1471 (1995).
- [99] E.G. Gamaly, A.V. Rode, and B. Luther-Davies, "Ultrafast ablation with high-pulse-rate lasers. Part I: Theoretical considerations," *J. Appl. Phys.* **85**, 4213-4221 (1999).
- [100] E. G. Gamaly, A.V. Rode, V.T. Tikhonchuk, and B. Luther-Davies, "Electrostatic mechanism of ablation by femtosecond lasers," *Appl. Surf. Sci.* **197-198**, 699-704 (2002).
- [101] W. Braun, "*Applied RHEED, reflection high-energy electron diffraction during crystal growth*," Springer-Verlag, Berlin (1999).
- [102] A. Ichimiya and P. I. Cohen, "*Reflection high-energy electron diffraction*," Cambridge University Press, Cambridge (2004).
- [103] L. -M. Peng, S. L. Dudarev, and M. J. Whelan, "*High-energy electron diffraction and microscopy*," Oxford University Press (2004).

- [104] M. G. Lagally, D. E. Savage, and M. C. Tringides, “*Reflection high-energy electron diffraction and reflection electron imaging of surfaces*,” edited by P. K. Larson, and P. J. Dobson, Vol. 188, p. 139, Plenum Press, New York (1988).
- [105] J. E. Mahan, K. M. Geib, G. Y. Robinson, and R. G. Long, “A review of the geometrical fundamentals of reflection high-energy electron diffraction with application to silicon surfaces,” *J. Vac. Sci. Technol. A* **8**, 3692- 3700 (1990).
- [106] Z. L. Wang, “*Reflection electron microscopy and spectroscopy for surface analysis*,” Cambridge University Press, Cambridge (1996).
- [107] J. H. Neave, B. A. Joyce, P. J. Dobson, and N. Norton, “Dynamics of film growth of GaAs by MBE from RHEED observations,” *Appl. Phys. A: Solid Surf.* **31**, 1-8 (1983).
- [108] J. H. Neave, P. J. Dobson, B. A. Joyce, and J. Zhang, “Reflection high-energy electron diffraction oscillations from vicinal surfaces – a new approach to surface diffusion measurements,” *Appl. Phys. Lett.* **47**, 100-102 (1985).
- [109] J. Massies and N. Grandjean, “Oscillations of the lattice relaxation in layer-by-layer epitaxial growth of highly strained materials,” *Phys. Rev. Lett.* **71**, 1411-1414 (1993).
- [110] P. Turban, L. Hennet, and S. Andrieu “In-plane lattice spacing oscillatory behaviour during the two-dimensional hetero- and homoepitaxy of metals,” *Surface Science* **446**, 241-253 (2000).
- [111] N. Chandrasekhar, V. S. Achutharaman, V. Agrawal, and A. M. Goldman, “Reflection high-energy electron diffraction studies of the growth of $\text{YBa}_2\text{Cu}_3\text{O}_{7-x}$

- and $\text{DyBa}_2\text{Cu}_3\text{O}_{7-3}$ superconducting thin films,” *Phys. Rev. B* **46**, 8565-8572 (1992).
- [112] G. J. H. M. Rijnders, G. Koster, D. H. A. Blank, and H. Rogalla, “In situ monitoring during pulsed laser deposition of complex oxides using reflection high energy electron diffraction under high oxygen pressure,” *Appl. Phys. Lett.* **70**, 1888-1890 (1997).
- [113] S. Andrieu and P. Frechard, “What information can be obtained by RHEED applied on polycrystalline films?,” *Surf. Sci.* **360**, 289-296 (1996).
- [114] D. Litvinov, T. O'Donnell, and R. Clarke, “In situ thin-film texture determination,” *J. Appl. Phys.* **85**, 2151-2156 (2007).
- [115] H. Lee, R. Lowe-Webb, W. Yang, and P. C. Sercel, “Determination of the shape of self-organized InAs/GaAs quantum dots by reflection high energy electron diffraction,” *Appl. Phys. Lett.* **72**, 812-814 (1998).
- [116] A. Feltrin and A. Freundlich, “RHEED metrology of Stranski–Krastanov quantum dots,” *J. Crystal Growth* **301-302**, 38-41 (2007).
- [117] M. A. Hafez and H. E. Elsayed-Ali, “Indium growth on $\text{Si}(100)-(2\times 1)$ by femtosecond pulsed laser deposition,” *J. Vac. Sci. Technol. A* **23**, 1681-1686 (2005).
- [118] M. A. Hafez and H. E. Elsayed-Ali, “Formation of $\text{In}(2\times 1)$ and In islands on $\text{Si}(100)-(2\times 1)$ by femtosecond pulsed laser deposition,” *J. Appl. Phys.* **101**, 113515 (1-10) (2007).

- [119] M. A. Hafez and H. E. Elsayed-Ali, "Activation energy of surface diffusion and terrace width dynamics during the growth of In(4×3) on Si(100)-(2×1) by femtosecond pulsed laser deposition," J. Appl. Phys. **103**, 093510 (1-10) (2008).
- [120] M. A. Hafez and H. E. Elsayed-Ali, "Low temperature growth of high-quality InN on Si(100) by femtosecond pulsed laser deposition," to be published.

CHAPTER II

REFLECTION HIGH-ENERGY ELECTRON DIFFRACTION: THEORY AND APPLICATIONS

II.1. Introduction

Reflection high-energy electron diffraction (RHEED) has become an indispensable technique for studying surface structures and thin film growth [1, 2]. The grazing incidence of the primary electron beam makes RHEED highly sensitive to the surface structure [3]. Therefore, the high-energy electrons keep in the near surface region and the dominant diffraction effects take place a few atomic layers deep. For example, 50-100 keV electrons have a mean free path of about 1000 Å, and at an incident angle of about 1° penetrate to a depth of about 10 Å [4]. The geometry of a RHEED system consists of an accelerated electron beam incident on a sample surface; the reflected beams form a diffraction pattern on a fluorescent screen, Fig. 2.1. RHEED patterns can provide fundamental information about surface structure in both static and dynamic conditions. The symmetry and spacing of the diffraction beams in the RHEED patterns give information on the surface symmetry, real space lattice, and degree of perfection. In addition, RHEED is used for quantitative structural analysis of reconstructed surfaces and surface disorder [5]. Due to its high surface sensitivity and its compatibility with ultrahigh vacuum (UHV) systems, RHEED is used as an in situ technique to probe the growth of thin films in real time [2]. The film growth modes, the surface morphology, and the epitaxy film growth can be identified from the diffraction patterns. The features in the RHEED patterns depend on the structure and morphology of the probed surface.

Electron diffraction from a smooth 2D crystalline surface usually gives rise to a streaky pattern, reflection diffraction, while 3D islands or a rough surfaces result in a spotty pattern, transmission diffraction (see Fig. 2.2).

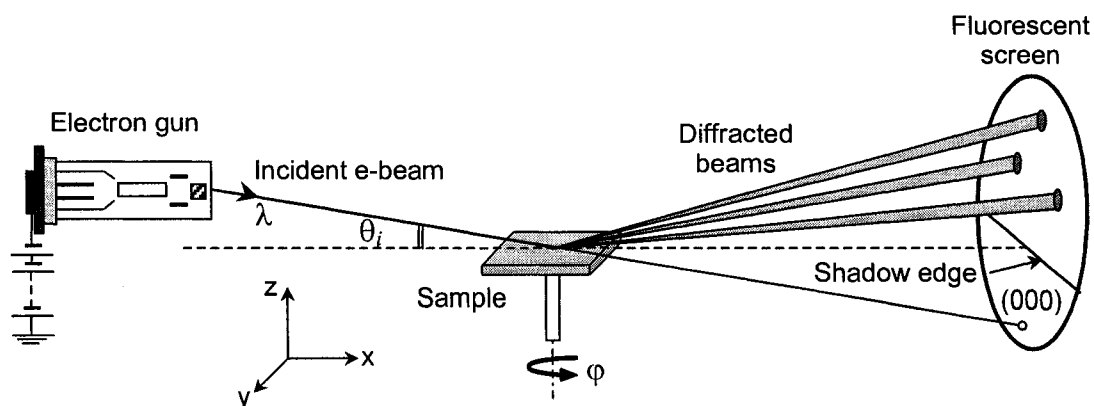


FIG. 2.1. Schematic diagram of RHEED geometry. The parameters λ , θ_i , and ϕ are the incident electron wavelength, incident angle, and azimuthal angle. The transmitted (000) corresponds to the primary electron beam.

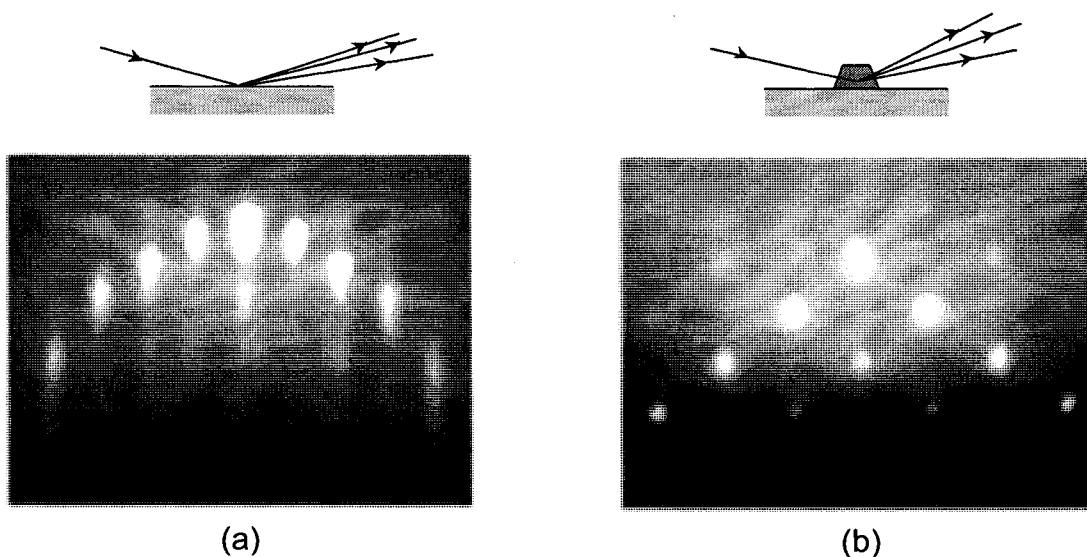


FIG. 2.2. Schematic diagrams and corresponding RHEED patterns of two possible modes of electron diffraction. (a) Reflection diffraction from Si(100)-(2 \times 1) reconstructed surface. (b) Transmission diffraction from InP(100) surface.

RHEED intensity oscillations are observed when the growth follows a layer-by-layer mode [2, 6]. The intensity period corresponds to the growth of one monolayer, which is used to determine the deposition rates and layer thickness. It provides a means to control the film growth and study the growth dynamics. Studies show that lattice relaxation is occurred as a result of oscillations of the in-plane lattice constant along with the oscillation of RHEED intensity [7, 8]. It is used to study the stress at the interface between the growing film and the substrate surface. RHEED technique has been extended to monitor fabrication of complex oxide materials [9-11], reveal the surface texture of polycrystalline films [12-15], and determine structural properties of nanostructures [16-19]. The fundamentals of RHEED and interpretation of measurements are typically described in the framework of the kinematic approaches. However, theoretical works are introduced to study the effects of multiple elastic and inelastic scattering on the RHEED analysis [1, 3, 20].

II.2. RHEED set-up and techniques

A typical RHEED set-up consists of an electron gun, a fluorescent screen, and an image processing system. A wide variety of electron guns are in use, from simple electrostatically focused guns, operating at 5-20 keV, to much more sophisticated guns that approach electron microscope quality (up to 100 keV). Sometimes magnetic lenses are used for focusing the beam and fine control of the beam trajectory. The sample holder is mounted in the manipulator stage to allow sample rotation about its surface normal to record the RHEED patterns at various azimuthal directions. Rotating substrates has been used to obtain RHEED analysis of azimuthal plots during thin layers growth [2]. The

fluorescent screen is often coated directly onto the inside of the viewport in the UHV system along with a transparent conducting film to avoid screen charging. The electron gun and the fluorescent screen are positioned far apart from the sample and do not interfere with the deposition flux for thin film growth. Some systems utilize energy filtering to separate the inelastic scattered background for quantitative RHEED analysis. To record and analyze the entire area of a RHEED pattern, a charge coupled device (CCD) camera is employed outside the UHV. The RHEED patterns observed on the fluorescent screen are stored and transferred to a computer for data analysis.

The angular and energy resolution of RHEED for beam profiles is determined by the transfer width, dynamic range, linearity, and signal to noise ratio [21]. The dynamic range and the resolution of the RHEED system are limited by the fluorescent screen and the detection system. Scanning of reflection profiles can be performed by either moving a detector across the phosphor screen or deflecting the RHEED pattern by means of magnetic or electric fields in the vacuum [2]. An instrument designed for spot profile analysis of diffracted electrons, which utilize a channeltron as the detector and a suppressor aperture as the energy filter element, has been reported [21]. The diffracted electron distribution is scanned across the aperture using electrostatic deflection. Energy filter apparatuses have been developed to study the inelastic scattering by measuring the energy loss spectra of RHEED beams [22, 23]. For RHEED oscillations, an energy loss spectroscopy detector is used to investigate the contribution of elastically and plasmon inelastically scattered electrons during film growth [22]. In this set-up, the RHEED screen and the grounded grid are fixed at zero potential, and the suppressor grid is kept at a variable potential close to primary beam energy. The RHEED system has been

developed to monitor film growth under high pressures [24, 25]. While typical pressures required for RHEED in high vacuum systems are $< 10^{-5}$ Torr, using two stage differential pumping systems allows operating pressures of several hundred millitorrs and maintains high vacuum (10^{-6} Torr) near the electron gun filament.

The geometry of RHEED set-up allows additional *in situ* techniques to join experiments for further measurements. Two RHEED guns have been mounted on the same MBE chamber to record diffraction patterns and RHEED dynamics in two azimuths simultaneously [26]. This set-up is used to study the growth modes and phase transitions on anisotropic surfaces. Compared with microscopy techniques, RHEED probes a large area, typically several square mm, and thus provides averaged information on structure and morphology [2]. It is beneficial to complement RHEED with a scanning microscopy technique, such as scanning electron microscope (SEM) and tunneling electron microscope (STM), to compare and establish a connection between microscopic surface structure and RHEED measurement [2]. Microprobe RHEED is a combination of SEM and RHEED, where an SEM gun is used as the electron source to image the real space of the surface with a spatial resolution of a few microns [27, 28]. It has been used to observe the epitaxial growth and surface diffusion length. An Experimental set-up has been performed for time-resolved RHEED of surface structural changes [29, 30]. In such a technique, an ultrashort laser pulse is split into two beams, one laser beam to heat a sample surface while the second beam irradiates a photocathode and generates an electron pulse. Synchronizing the electron pulse with the heating laser pulse, the temporal evolution of heat on a surface can be monitored by means of the transient surface Debye-Waller effect (i.e. intensity changes of RHEED peaks).

II.3. RHEED theoretical models

II.3.1. Geometrical model

The geometrical structure of a RHEED pattern is derived with kinematic approximation, i.e. the diffraction of a plane wave by a single crystal using only geometric considerations and neglecting the interaction mechanism between incident wave and scatterer [31]. Thus, the kinematic approach has come to mean single scattering analysis since in this view symmetry and energy conservation, and not the details of the potential, largely determines the diffraction pattern [3]. The conditions of elastic scattering and constructive interference are combined to determine the locations of intensity maxima in the diffraction pattern [32]. Because of the grazing incidence, most of the incident electrons are scattered elastically by atoms on the sample's surface. If k_0 and k are the wave vectors of the incident and diffracted beam, respectively, the elastic scattering obeys with the conservation of energy:

$$|k_0| = |k| = \frac{2\pi}{\lambda}. \quad (2.1)$$

If Δk is the difference vector between the incident and diffracted wave vectors, then,

$$k - k_0 = \Delta k. \quad (2.2)$$

Then the maximum intensity of the diffraction beam will be obtained when the Laue diffraction condition is satisfied

$$\Delta k = G_m, \quad (2.3)$$

where G_m is a vector of the reciprocal lattice; the subscript m refers to the m th diffracted beam. The intensity can be lowered rapidly for $\Delta k \neq G_m$. The diffraction condition (2.1) and (2.3) define Ewald sphere in reciprocal lattice. Figures 2.3 and 2.4 describe the diffraction geometry of RHEED and the Ewald sphere construction.

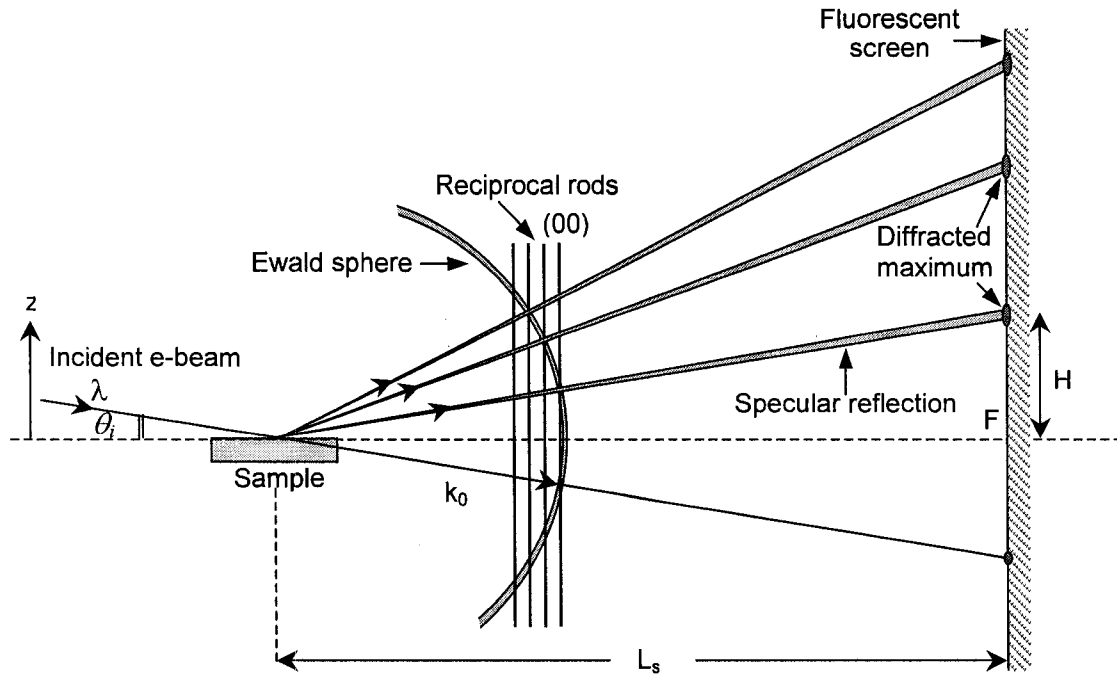


FIG. 2.3. Ewald sphere construction and diffraction geometry of RHEED according to the geometrical model. Ewald sphere radius is $k = 2\pi/\lambda$. L_s is the sample to RHEED screen distance. F is denoted to the location center where reflections occur on so called Laue rings and H is the distance from F to the specular reflection. The conditions for constructive interference of the elastically scattered electrons inferred using the Ewald construction in the reciprocal lattice (modified from Braun [2]).

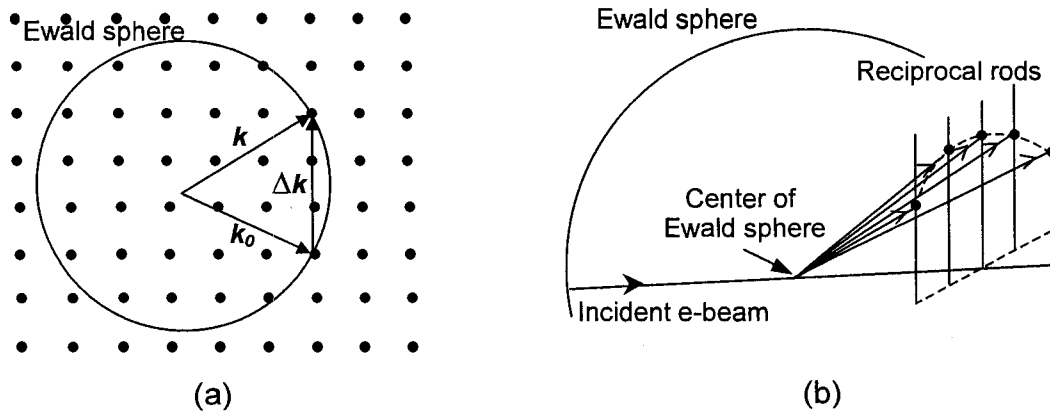


FIG. 2.4. (a) Top view of reciprocal lattice points and Ewald sphere. Ewald sphere is determined by the conservation of energy and conservation of momentum by a reciprocal lattice vector $\Delta\mathbf{k}$. (b) Schematic diagram of intersection of Ewald sphere with reciprocal lattice rods of same zone.

For low incident angles, the sampling depth of RHEED can be very small, and the incident electrons are reflected essentially from a 2D atomic net. Therefore, the construction of a reciprocal lattice for the sample's volume is approximated by a 2D layer [2]. The reciprocal lattice reduces in one-dimension rods along the z direction perpendicular to the surface. Generally, only a few angles yield the proper conditions for diffraction. In Ewald construction, the diffraction is determined by the conservation of energy and the conservation of parallel momentum [3]. Reflections can occur for all k connecting the origin of the sphere and reciprocal lattice points on the sphere. Fig. 2.4(b) is a schematic diagram of the intersection of the Ewald sphere with reciprocal lattice rods from the same zone order.

In RHEED experiment, diffraction maxima in the form of streaks are observed in the direction perpendicular to the surface [1, 32]. The streaking effect occurs due to small electron penetration depth into the surface [1]. In addition, the primary beam divergence, due to electrons energy and angular spread, produces smeared out of the Ewald sphere. Broadening of the reciprocal lattice rods, due to surface disorder, regular spaced surface steps, and inelastic scattering are other sources for producing spreading of intensity in RHEED. Therefore, the diffraction pattern will usually consist of streaks corresponding to the sections of reciprocal lattice rods intersected with Ewald sphere. In the ideal case, an extremely flat surface and very good instrumentation, sharp diffraction spots can be observed. The relation between the lateral spacing a^* of the reciprocal lattice rods of the zeroth zone and the streak spacing W of the observed RHEED streaks is given by [32]:

$$a^* = \frac{2\pi W}{\lambda L_s}. \quad (2.4)$$

Fig. 2.5 shows an example of reciprocal lattice spacing and streak spacing of a RHEED pattern. This can be used to calculate the in-plane lattice spacing. The Miller indices (hk) are given for the reciprocal lattice rods and to the spots or streaks that create in the RHEED pattern.

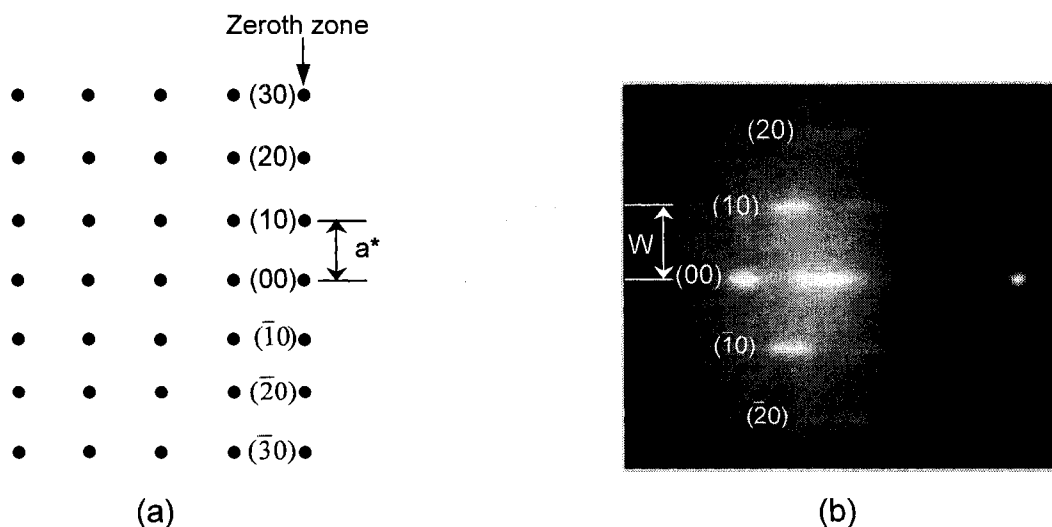


FIG. 2.5. The lateral spacing a^* of the reciprocal lattice rods in (a) is related to the streak spacing W between the integral order of the diffracted beams in the Si(100)-(1×1) RHEED pattern in (b).

Since the reciprocal lattice consists of continuous rods, every rod intersect Ewald sphere produces a reflection in the diffraction pattern [2]. The reflections occur on the so-called Laue rings centered at F , where the projection of the component parallel to the surface onto the screen, Fig. 2.3. The specular reflection is located at the intersection of the zeroth-order Laue ring and the (00) rod. The zeroth Laue ring could give rise to a streak in the pattern because its lattice rods are tangent to the Ewald sphere. For the idealized RHEED experiment, they lie in a straight line along the shadow edge of the pattern, rather than in a ring. However, for an angle of incidence of 1° , they form an

actual arc or ring on the screen [32], Fig. 2.4(b). Higher order rings consist of spots or short streaks. The angle of electron beam incidence θ_i is calculated from

$$\theta_i = \tan^{-1}\left(\frac{H}{L_s}\right), \quad (2.5)$$

where H is the distance of the specular spot from the shadow edge of the RHEED screen.

In RHEED, the Ewald sphere is much larger than the reciprocal lattice unit of the surface. Therefore, it produces an almost planar cut through the first few Brillouin zones of the reciprocal lattice [2]. This is achieved by using a high accelerating voltage and then the magnitude of the electron's wavelength λ is given by the relativistic expression of [1]:

$$\lambda = \frac{h}{\sqrt{2m_0qU_0\left(1 + \frac{qU_0}{2m_0c^2}\right)}}, \quad (2.6)$$

where h is the Planck's constant, m_0 is the electron rest mass, q is its charge, c is the speed of light, and U_0 is the accelerating potential of the electron gun. Expression (2.6) is sometimes written as:

$$\lambda = \frac{12.26}{\sqrt{U_0(1 + 0.9788 \times 10^{-6} U_0)}}, \quad (2.7)$$

where the wavelength λ is measured in Å, and U_0 is in volts. For typical electron energies used in RHEED (~10-30 keV) the wavelength of the electrons, λ (~0.1-0.2 Å) is $\ll a$ where a is the crystal lattice parameter [14].

II.3.2. Kinematical and dynamical models

The RHEED theory in terms of kinematical scattering can be described within the Born approximation. It assumes single scattering in which the electron scattered only

once [1]. The incident electron has a plane wave in the form of $e^{2\pi i \mathbf{k}_0 \cdot \mathbf{r}}$ with the wave vector \mathbf{k}_0 and is scattered due to its interaction with the electrostatic potential of the atom [1]. If the scattering potential $U(\mathbf{r})$ is weak and is distributed in a small region, then the wave observed at a large distance from the scattering zone is

$$\psi(\mathbf{r}) \approx e^{2\pi i \mathbf{k}_0 \cdot \mathbf{r}} + f(\theta) \frac{e^{2\pi i \mathbf{k} \cdot \mathbf{r}}}{r}, \quad (2.8)$$

where $f(\theta)$ is the amplitude of the scattered wave as a function of the scattering semi-angle (2θ is the scattering angle). The first Born approximation assumes that the scattering cross section of the whole scatterer is so small that the wave function everywhere in the scatterer can be approximated by the incident wave [31]. Therefore for the incident plane wave $e^{2\pi i \mathbf{k}_0 \cdot \mathbf{r}}$ scattered to an exit plane wave $e^{2\pi i \mathbf{k} \cdot \mathbf{r}}$, the amplitude of the scattered wave is calculated

$$f(\mathbf{u}) = -\frac{m_0}{2\pi\hbar^2} \int_{-\infty}^{\infty} e^{-2\pi i \mathbf{u} \cdot \mathbf{r}} U(\mathbf{r}) d\mathbf{r}, \quad (2.9)$$

where $\hbar \mathbf{u} = \hbar(\mathbf{k} - \mathbf{k}_0)$ is the momentum transfer of the incident electron. Equation (2.9) implies that the scattering amplitude under the single scattering approximation is proportional to the Fourier transform of the scattering object potential. If the atomic potential is spherically symmetric, i.e. $U(\mathbf{r}) = U(r)$, then the equation (2.9) becomes

$$f(\theta) = -\frac{2m_0}{\hbar^2} \int_0^{\infty} dr \frac{\sin(2\pi u r)}{2\pi u r} U(r) r^2, \quad (2.10)$$

From equation (2.9), the scattering power of the atom is determined by the Fourier transform (FT) of its electrostatic potential, thus the electron scattering factor is defined as

$$f^e(\mathbf{u}) = \int_{-\infty}^{\infty} d\mathbf{r} e^{-4\pi i \mathbf{s} \cdot \mathbf{r}} U(\mathbf{r}), \quad (2.11)$$

where the scattering vector is defined as $\mathbf{s} = \mathbf{u}/2$, with $s = \sin\theta/\lambda$ and \mathbf{u} a reciprocal space vector. Equation (2.11) is a quantity that characterizes the scattering power of an atom and is independent of the accelerating voltage.

Next, the kinematic theory is applied to the scattering amplitude from a crystal surface. For simplification, the contribution made by the top atomic layer of the surface is considered. Under the rigid-body approximation, the potential distribution in the surface can be written generally as a superposition of the potential distribution from each atom site \mathbf{r}_i ,

$$U_s(\mathbf{r}) = \sum_i U_i(\mathbf{r} - \mathbf{r}_i), \quad (2.12)$$

where i refers to the i th atom site on the surface. According to the first Born approximation, the scattering amplitude is a Fourier transform of U_s

$$U_s(\mathbf{u}) = \text{FT}[U_s(\mathbf{r})] = \sum_i f_i^e(\mathbf{u}) e^{-2\pi i \mathbf{u} \cdot \mathbf{r}_i}. \quad (2.13)$$

The kinematically diffracted intensity is thus [1]:

$$I_s(\mathbf{u}) = |U_s(\mathbf{u})|^2 = \sum_i \sum_j f_i^e(\mathbf{u}) f_j^{e*}(\mathbf{u}) e^{-2\pi i \mathbf{u} \cdot (\mathbf{r}_i - \mathbf{r}_j)}. \quad (2.14)$$

This is the general equation for RHEED. By knowing the distribution of the surface atoms, and hence the potential distribution, the diffracted intensity $I_s(\mathbf{u})$ can be predicted from different structure surfaces such as disordered surfaces, surfaces with islands, and stepped surfaces [1].

When the incident electron beam penetrates deeper into the solid, strong multiple scattering effects (dynamical effects) dominate the diffraction process. Multiple elastic

scattering generally complicates the analysis since the mutual interaction between incident wave and scatterer described by an effective potential $U(r)$ has to be taken into account [1, 31]. These dynamical processes transfer the scattered intensity between diffracted beams and can be observed in the RHEED patterns. Although the positions of RHEED beams can generally be predicted by kinematical scattering theory, quantitative analysis of RHEED patterns relies on dynamical calculations [1]. In the dynamical theory, the mutual interaction between the high-energy incident electron and the crystal atoms is taken into account for the scattered wave. It is based on the exact solution of the Schrodinger equation for scattered waves. Different methods are adopted to solve the problem of computing the full wave function inside the crystal using Fourier transformation to take advantage of the periodicity of the crystal potential [1-3, 20].

II.4. Diffraction features from surfaces

II.4.1. Surface reconstruction

When surface atoms can rearrange themselves into a net that is different from the corresponding face of the terminated bulk lattices, it results as either surface reconstruction or surface relaxation. Reconstruction changes the symmetry of the atomic arrangement parallel to the surface and leads to a unit mesh that is normally larger than the unit mesh cell of the bulk lattice. The unit mesh of the surface's reciprocal net is consequently reduced in size, and new features appear in the RHEED pattern, namely higher order streaks and higher orders Laue zones [1].

Fig. 2.6 (a) and (b) shows an example of a (2×1) reconstructed surface in real space and reciprocal space. What is known initially about the structure of the bulk crystal

is that its net is parallel to the surface and is the reference net. If \mathbf{a} and \mathbf{b} are two basis vectors for the reference net, and the surface mesh basis vectors are $a_s = \alpha a$ and $b_s = \beta b$, then a shorthand notation of the surface structure is denoted by $\alpha \times \beta$ reconstruction. In reciprocal lattice, the basis vectors of the surface and the reference are related by $\mathbf{a}_s^* = (1/\alpha) \mathbf{a}^*$ and $\mathbf{b}_s^* = (1/\beta) \mathbf{b}^*$. The type of reconstruction provides information on the surface termination as in the GaAs(100) surface. Figure 2.6 (c) shows a RHEED pattern of a reconstructed Si(100)-(2×1) surface. In the (2×1) surface, the Laue zone was divided into two subsections in the [011] azimuth due to the additional reflected RHEED beams, such as (0,1/2) and (0,-1/2) orders, which are corresponded to half-orders Laue zones. In the Si(100)-(2×1) surface, the surface atoms are paired to form dimers, thus reduction of the number of dangling bonds in rows and the surface has a (2×1) periodicity [33].

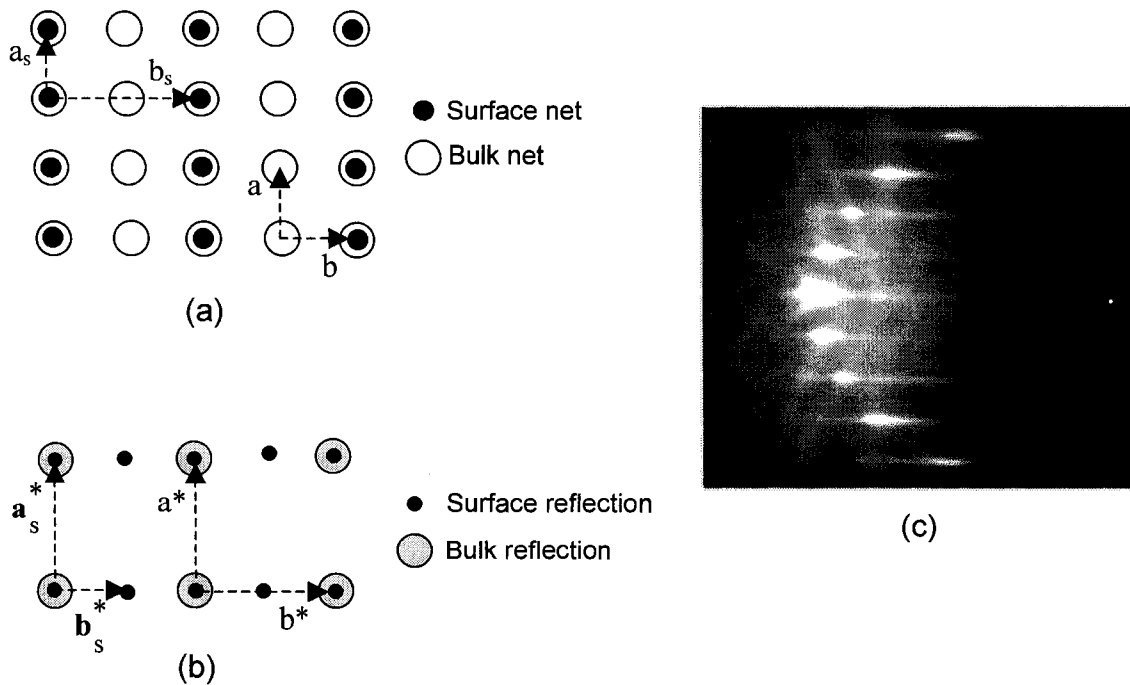


FIG. 2.6. Schematic diagrams of (2×1) surface reconstruction in real space (a) and in reciprocal space (b). (c) RHEED pattern of reconstructed Si(100)-(2×1) surface.

II.4.2. Kikuchi patterns and resonance reflections

Kikuchi patterns are formed in electron diffraction whenever the sample is a reasonably flat single crystal with good lattice perfection [31]. They consist of dark and light pairs, bands, and curved lines. The intensities of reflected RHEED beams are enhanced when the beams intersect the Kikuchi lines. Kikuchi patterns originate from inelastic scattering, which is responsible for scattering the electrons into a wide angular range. Therefore, the kinematic theory cannot be applied to the description of Kikuchi patterns. In RHEED, multiple scattering by the crystal produces a general diffuse background. The most important multiple scattering event is called surface resonance effect, which is characterized by a diffracted beam traveling parallel to the sample surface. In reciprocal space, this condition is met when the Laue ring tangentially touches a reciprocal lattice rod and causes transfer intensity to any of the reflections on the Laue rings [2]. In real space, Bragg reflections are generated by two processes. One is the scattering of the incident beam by the crystal surface directly toward the direction of the specularly reflected beam. In the other process, electrons are scattered to an intermediate state, finally ending with another Bragg scattering to join the specularly reflected wave and cause the resonance reflection [1].

II.4.3. RHEED rocking curves

RHEED rocking curves mean measurement of the variation of diffracted intensity in the specular beam in the (00) and other rods with the incident angle of the primary beam at some fixed azimuth [34]. In the interpretation of the RHEED intensity, it is important to understanding the conditions that lead to intensity variations of the RHEED

pattern features. A condition that can arise is the streaks or elongated spots that result from diffraction by the surface unit cell have their intensities modulated by the scattering of electrons from the underlying 3D lattice [34]. An additional, but often neglected complication is caused by refraction. As the electrons cross the surface potential barrier they gain energy by an amount V_0 , the inner potential, and are therefore refracted as they enter the solid. From conservation of energy, it follows that the angle between the surface and the incident beam in vacuum, θ_i , is related to the equivalent angle inside the solid, θ , by:

$$\cos \theta_i = \sqrt{\frac{1 - V_0}{E}} \cos \theta, \quad (2.15)$$

where E is the primary beam energy and the inner potential V_0 is negative, measured with respect to the vacuum level. The gain in energy is taken into account for the Ewald construction. The angles of the beam with respect to the surface, such as the (00) rod, can be estimated from equation (2.15). This condition gives a maximum in the intensity of the specular spot that is scattered at an angle θ_i with respect to the surface. This condition will also lead to secondary Bragg maxima in the intensity of diffracted beams as a result of dynamical coupling beams excited in the solid and the outgoing specular beam [34]. The process can be considered as a double diffraction involving the bulk and the surface of the crystal, which causes a similar refraction effect as that which occurred with primary Bragg diffraction. Maxima in the intensity of a specular beam may therefore be expected whenever a Bragg condition is met by a primary or secondary beam. Surface resonance is an additional condition, related to the surface region, which can give rise to maxima in the rocking curves.

II.5. RHEED from vicinal surfaces

A vicinal surface consists of terraces arranged in a periodic staircase formation due to misorientation from a low-index plane in a specific direction. The structure of terraces is composed of steps separated by an average width L and a step height. The RHEED pattern produced by an electron beam directed down the staircase will be modified by the periodic nature of the steps. Depending on the electron beam incident angle down the staircase, the reflected electrons will maximize or broaden the specular beam profile. When the reflected electrons from surface terraces interfere constructively, a maximum sharp specular beam profile is observed and θ_i will satisfy the Bragg equation

$$2d \sin \theta_i = n\lambda, \quad (2.16)$$

where d is the monolayer height, and n is an integer. This is called the in-phase condition, which is not sensitive to the steps. Qualitatively, diffraction from a vicinal surface at the in-phase angles gives a narrow profile. Conversely, when θ_i satisfies the equation

$$2d \sin \theta_i = (n+1/2)\lambda. \quad (2.17)$$

In the kinematic approach, the reflected electrons from regions differing in height by one monolayer are 180° out of phase and interfere destructively [35]. This is known as the out-of-phase condition, which results in splitting of the diffracted beam into two separate peaks. At the out-of-phase condition, the diffracted beam profile is most sensitive to the surface disorder. To observe the splitting peaks at the out-of-phase condition, the split distance should be within the resolving power of the RHEED. Surface disorder and step structures result in broadening and elongation of the diffracted beams. In the reciprocal space, the surface steps can be illustrated by domains of average width

L . The reciprocal space of one domain gives a (00) rod whose thickness is $2\pi/L$. The intersection of the broadened reciprocal lattice rod with the Ewald sphere explains the formation of RHEED streaks. Parallel to the surface, but normal to the beam direction, the diffracted streaks will have an angular thickness of

$$\Delta\phi_f = \frac{2\pi}{Lk \cos\theta_f}, \quad (2.18)$$

where θ_f is the final angle from the low-index plane. In contrast, in the direction normal to the surface, the diffracted streaks will have angular thickness of

$$\Delta\theta_f = \frac{2\pi}{Lk \sin\theta_f}. \quad (2.19)$$

The sensitivity of $\Delta\theta_f$ along the streak is related to the surface disorder and θ_f . Ewald construction that gives a streaked specular beam for a reciprocal lattice broadened by disorder is given in Fig. 2.7. For vicinal surfaces, the misorientation angle θ_m determines the average spacing between steps, where $\tan\theta_m = d/L$ and d is the step height. A vicinal surface can be viewed as the convolution of a single terrace of atoms and a periodic lattice of points, where each point represents a terrace location [36]. The reciprocal lattice construction of the vicinal surface is formed by the intersection of the reciprocal lattice rods of a single terrace with reciprocal lattice planes of the periodic step lattice (see Fig. 2.8).

RHEED patterns at different diffraction conditions can be recognized from the construction of the vicinal surface reciprocal lattice. If disorder is introduced into the terraces in the form of a width distribution about the mean terrace size, an edge roughness of terrace kinks, or a combination, the split peaks will broaden except at the in-phase condition [5]. The splitting space in the diffracted beam can disappear if enough disorder

is introduced either in the form of meandering step edges or in an increased randomness in the terrace width [37]. A previous study showed that RHEED characterization of the step period on vicinal Si surfaces could be deduced from the separation of the specular beam splitting at arbitrary azimuths [38].

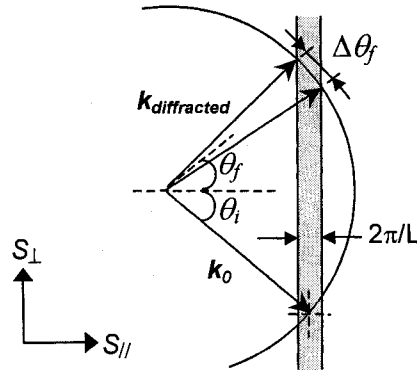


FIG. 2.7. Ewald sphere intersection with broadened reciprocal lattice rod. The broadening along the diffracted beam appears as a streak in the RHEED patterns. S_{\parallel} and S_{\perp} are the components of the momentum transfer parallel and perpendicular to the incident electron beam, respectively.

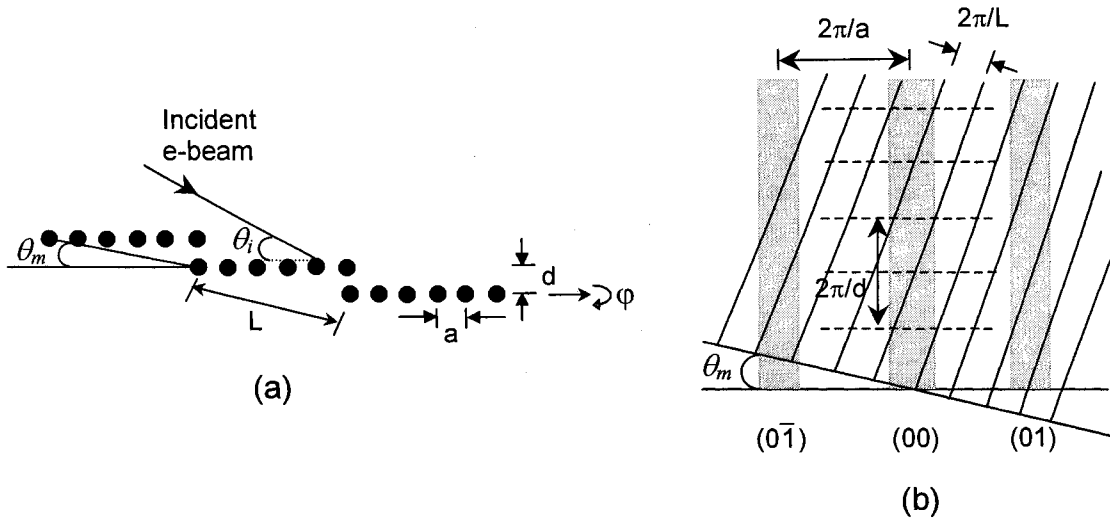


FIG. 2.8. Schematic of the vicinal surface with the relevant dimensions in real lattice (a) and in reciprocal lattice (b). Depending on the electron beam incident angle θ_i down the staircase and the terrace width L , the reflected electrons will maximize or broaden of the specular beam profile.

An example of RHEED patterns obtained at the out-of-phase and in-phase conditions for an InP(100) vicinal surface is shown in Fig. 2.9. In electron diffraction, the angular width of a reflected beam is a convolution of instrumental broadening and broadening in the reciprocal lattice rod. Therefore instrumental response, obtained from the full width at half maximum along the beam at the in-phase condition, should be taken into account when measuring the average terrace width L [39]. A quantitative determination of step density, average terrace width, terrace width distribution, and step edge roughness can be established by RHEED. It is found that the shape of split peaks produced with the incident electron beam normal to step edges of GaAs(100) vicinal surface is a measure of surface orientation over lengths on the order of terrace widths [35]. The resultant spot profile, when the electron beam incident parallel to step edges is sensitive to terrace roughness, can be used to measure string length, which is any line of atoms before an up or down step occurs [5, 35]. Changes in the average terrace width and the average string length at the step edge are studied using RHEED [40-42]. A study on a vicinal Si(100) surface showed that a profile measurement in an azimuth parallel to the step edges and integrating the profile in the splitting direction are distinguished edge roughness from variation in the average terrace size [37]. RHEED analysis showed that the intensity along the length of the RHEED streak near a surface wave resonance associated with the out-of-phase condition does not show changes in the splitting or streak asymmetry. In addition, no inner potential correction is needed since the phase advance at each terrace is identical and only the path length outside the crystal contributes [43]. Kinematical approaches were utilized for quantitative analysis of RHEED from regular and random steps [44-46].

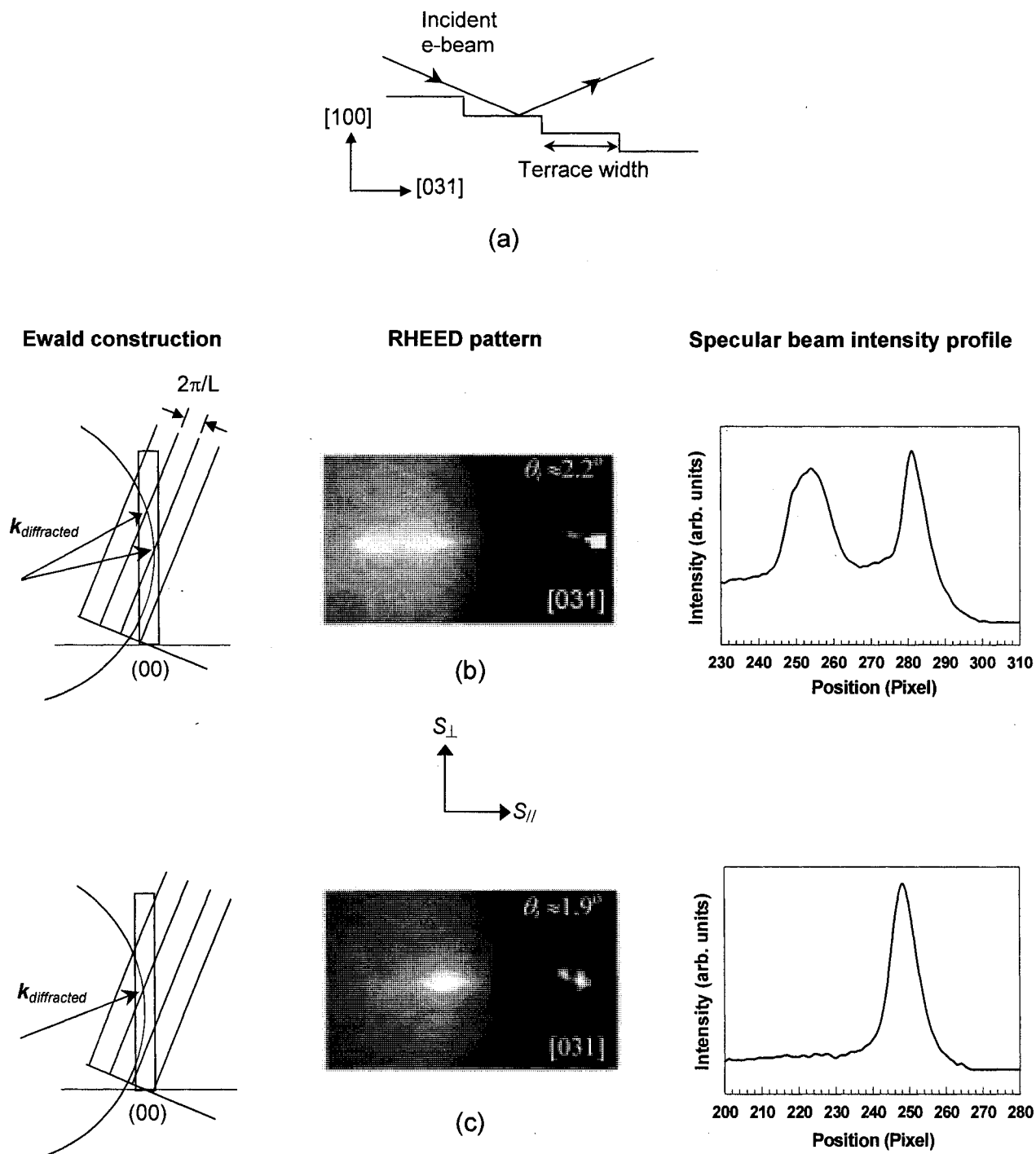


FIG. 2.9. (a) Schematic of InP(100) vicinal surface and the related crystal directions. The electron beam is incident down the staircase in the [031] azimuth. Ewald construction, RHEED pattern, and intensity profile along the specular beam are shown for: (b) out-of-phase condition and (c) in-phase condition [42]. The splitting quantity of the specular beam is related to the misorientation angle θ_m .

II.6. RHEED and thin film growth

II.6.1. RHEED and growth modes

The film growth modes can be identified experimentally by monitoring temporal variations of diffraction features in the RHEED patterns. Three principal modes of film growth are generally distinguished. The layer-by-layer growth mode (or Frank-van der Merwe, FM) refers to the case when the adatoms are more strongly attracted to the substrate than to each other. As a result, each layer is fully completed before the next layer starts to grow, i.e. strictly 2D growth takes place. The opposite case, where the adatoms are more strongly bound to each other than to the substrate, 3D islands (or Volmer-Weber, VW) growth mode results. The layer-plus-island (or Stranski-Krastanov, SK) is an intermediate case between FM and VW growth. In this case, layers form first, but then the growth of 3D islands takes place. Because of the small penetration depth, RHEED is primarily sensitive to the outermost few atomic layers and can probe changes in the growth mode. Figure 2.10 shows examples of real time RHEED observation during pulsed laser deposition (PLD) growth of thin films. RHEED patterns demonstrate streaks in the zeroth Laue zones, wide faint rings on a high background, and transmission spots resultant from different film growth modes. In homoepitaxy, RHEED intensity can determine if the 2D mode occurs by step-flow or layer-by layer growth, which depends on kinetics and growth conditions. If the terrace width exceeds the deposits' diffusion length, layer-by-layer growth, which results in RHEED oscillations, or multilayer growth takes place [4]. In heteroepitaxy, strain effects produce pseudomorphic growth or relaxed dislocated growth. These growth modes can be described from the diffracted beam profiles in the RHEED patterns.

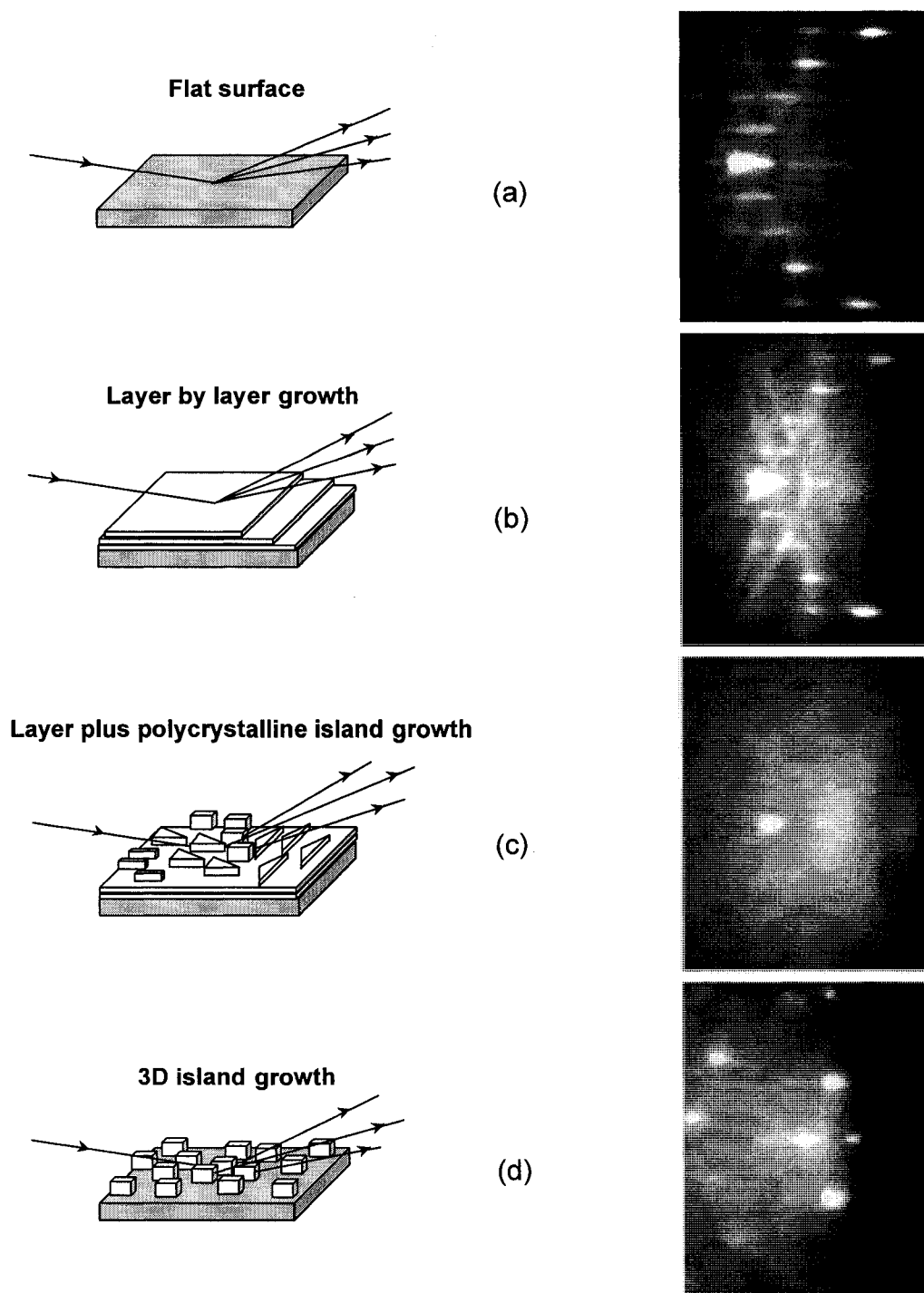


FIG. 2.10. Schematic diagrams of film growth modes and corresponding RHEED patterns represented [51] in: (a) Si(100)-(2×1) substrate surface; (b) growth of 2D In layers on Si(100)-(2×1); (c) growth of 3D In islands on preceding 2D layers (lattice mismatch between In and Si account for this mixed growth SK mode); and (d) 3D islands growth of InP on GaAs(100) surface.

II.6.2. RHEED intensity oscillations

The phenomenon of RHEED intensity oscillations was first reported by Harris et al. [47]. Interpretation of RHEED intensity oscillations is correlated to the electron diffraction and film growth conditions. During the layer-by-layer growth, the surface cycles between rough and smooth, with a period corresponding to the time to complete a monolayer of growth [48]. Since the layer thickness is much larger than the de Broglie wavelength of the electrons (for GaAs $0.283 \text{ nm} \gg 0.01 \text{ nm}$), the electrons are easily scattered out of the specular beam by the step edges [49]. As growth starts, the incident electron beam gets partially scattered by the island steps of the forming monolayer, thus reducing the reflected intensity. At coverage of half the monolayer, the scattering becomes maximum, leading to a decrease of the intensity to minimum. As the new monolayer completes, by coalescence of the islands, the reflected intensity of the specular spot will be relatively high. On vicinal surfaces, when the growth temperature is increased, a condition of decreasing of the amplitude of the RHEED oscillations can be reached. The oscillations disappear when the surface diffusion length is equal to the average terrace width at a transition temperature. The transition from layer-by-layer to step flow growth has been used to estimate the surface diffusion parameters [50].

RHEED intensity oscillations during growth of In on Si(100)-(2×1) by PLD are observed, Figure 2.11 (a) [51, 52]. In addition to oscillations with the monolayer period, the RHEED intensity is found to be modulated by pulsed deposition. During PLD growth, each deposition laser pulse modulates the RHEED intensity and an oscillatory behavior of the intensity is observed (an example is shown in Fig. 2.11 (b)). Periodic changes of the surface morphology, as a result of random distribution and surface

smoothness by energetic deposits after each laser pulse, caused the specularly reflected RHEED intensity to oscillate. In contrast, due to the continuous nature of molecular beam epitaxy (MBE), this feature does not appear. From these RHEED oscillations, qualitative and quantitative information can be extracted and analyzed. Among them are the period, amplitude, phase and damping of the oscillations, the behavior at the initial growth, the recovery after growth, and the frequency distribution in the Fourier spectrum of the oscillations [2, 34]. In favorable cases, a study of these parameters as a function of diffraction parameters allows the analysis of growth dynamics as well as the nature of the diffraction. The dependence of RHEED oscillations on MBE growth parameters is studied by measuring the angular profiles of the diffracted beam from misoriented surfaces [53-55]. In MBE growth of GaAs, RHEED oscillations are observed near the out-of-phase condition and stronger than near the Bragg condition [53]. It is concluded that the growth involved a competition between nucleation on terraces and step propagation; therefore, partially completed layers are grown with smaller average terrace lengths than a complete layer. Similarly, the width of the diffracted beams and the envelope of the oscillations are found to depend on the competition between diffusion to step edges and cluster formation [55]. Damping in oscillations is referred to a macroscopic spatial nonuniformity in the incident flux over the surface, which caused the diffracted amplitudes from different regions to add incoherently [53]. In another study, the damping effect in the layer-by-layer process is referred to the new layers that are able to start before the preceding one has been completed [6]. The persistence of RHEED oscillations can therefore be considered as a measure of the layer-by-layer epitaxial quality.

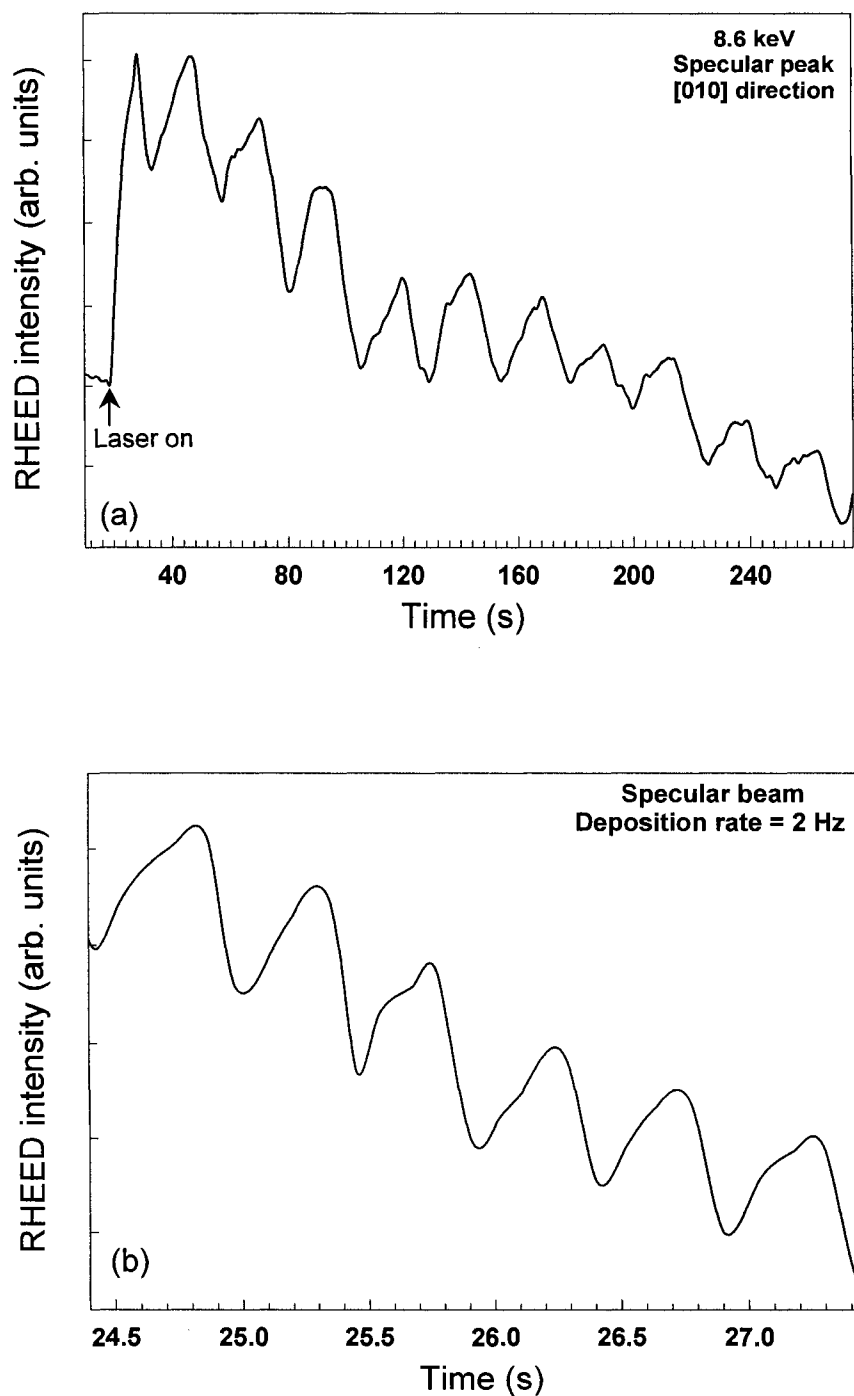


FIG. 2.11. (a) RHEED intensity oscillations during growth of In on Si(100)-(2 \times 1) by PLD at $\sim 145^\circ\text{C}$. From the intensity oscillations, a growth rate of ~ 0.05 monolayer/s is estimated. (b) Oscillatory behavior of the RHEED intensity between laser pulses taken during growth of In on Si(100)-(2 \times 1) at $\sim 400^\circ\text{C}$. The oscillation of the specular beam matches the pulsed deposition rate. This feature is a characteristic of PLD growth [51, 52].

Despite its popularity, the RHEED intensity oscillation is a complicated phenomenon and a lot of research work was devoted to understand its behavior and the driven processes. Some description of this phenomenon involves the origin of the oscillation, the initial behavior of the intensity, recovery effects, and the phase shift and differences of the specular and non-specular RHEED beams. Previous published work on RHEED oscillations showed an initial abrupt increase of intensity, which does not always fit in with the subsequent series of regular oscillations [53, 56]. Briones et al. [56] suggested that this transient increase is caused by an initial smoothing of steps already present on a GaAs(001)-(2×4) surface. In contrast, Dobson et al. [57] favored a model based on a transient change of surface reconstruction from (2×4) towards (3×1) structure, which led to a change in the specular beam intensity. The initial behavior for RHEED oscillations were observed to have a strong dependence on the diffraction conditions such as the angles of incident and azimuth [57]. Another feature observed by Joyce et al. [58] was the appearance of second harmonics in the oscillations in the specular beam. The authors suggested that the harmonics result from the superposition of the elastic specular scattered intensity and the diffuse scattering [58]. From this practical point of view, if conditions are chosen such that the diffuse scattering dominates over elastic specular scattering, the RHEED intensity will increase for the first half period and the peaks will make 180° out-of-phase with the more familiar case [34].

The phase of RHEED oscillations is analyzed using different approaches such as dynamical diffraction theory [59], reconstruction induced phase shifts [60], and change of surface coherence length [61]. An example of phase shift in the RHEED intensity during growth of In on Si(100)-(2×1) by femtosecond PLD is shown in Fig. 2.12 [51]. The

intensity of the reflected beams start and end up with an 180° phase difference. The intensity oscillations between the deposited laser pulses are cycled out of phase. This phenomenon of the phase shift is a complicated function of the diffraction conditions. A study of the RHEED intensity oscillations of growth of Ge(001) by MBE show that phase shift is caused by the overlap of the specular spot and Kikuchi line at high angle of the incident electron beam [62]. Phase differences in the RHEED oscillations between the intensities of specular and nonspecular beams are measured and found to vary with incident and azimuthal angle, regardless of the presence or absence of Kikuchi line crossing in the beams [63]. One should be careful that RHEED measurements be conducted under conditions where the influence of the dynamical nature of electron scattering, such as the Kikuchi features, is minimized. Braun et al. [64] observed energy filtered RHEED oscillations for several energy losses and concluded that the phase of the oscillation was not influenced by inelastic scattering and is determined by the surface reconstruction forming on top of the growing layer during crystal growth.

RHEED oscillations behavior in thin film growth is discussed theoretically and experimentally. Among the proposed models, the kinematic approximation [55, 65-68] and the step density model [6, 50, 69-71], which are applied to interpreting RHEED results. Both models assume that the RHEED intensity is determined by a single parameter of the evolving morphology such as layer coverage or step density. In the kinematic model, the oscillating coverage of a growing layer is the structural parameter and the interference of the electron beams reflected off terraces of different heights is reasoned to cause the RHEED intensity oscillations [55, 65, 66].

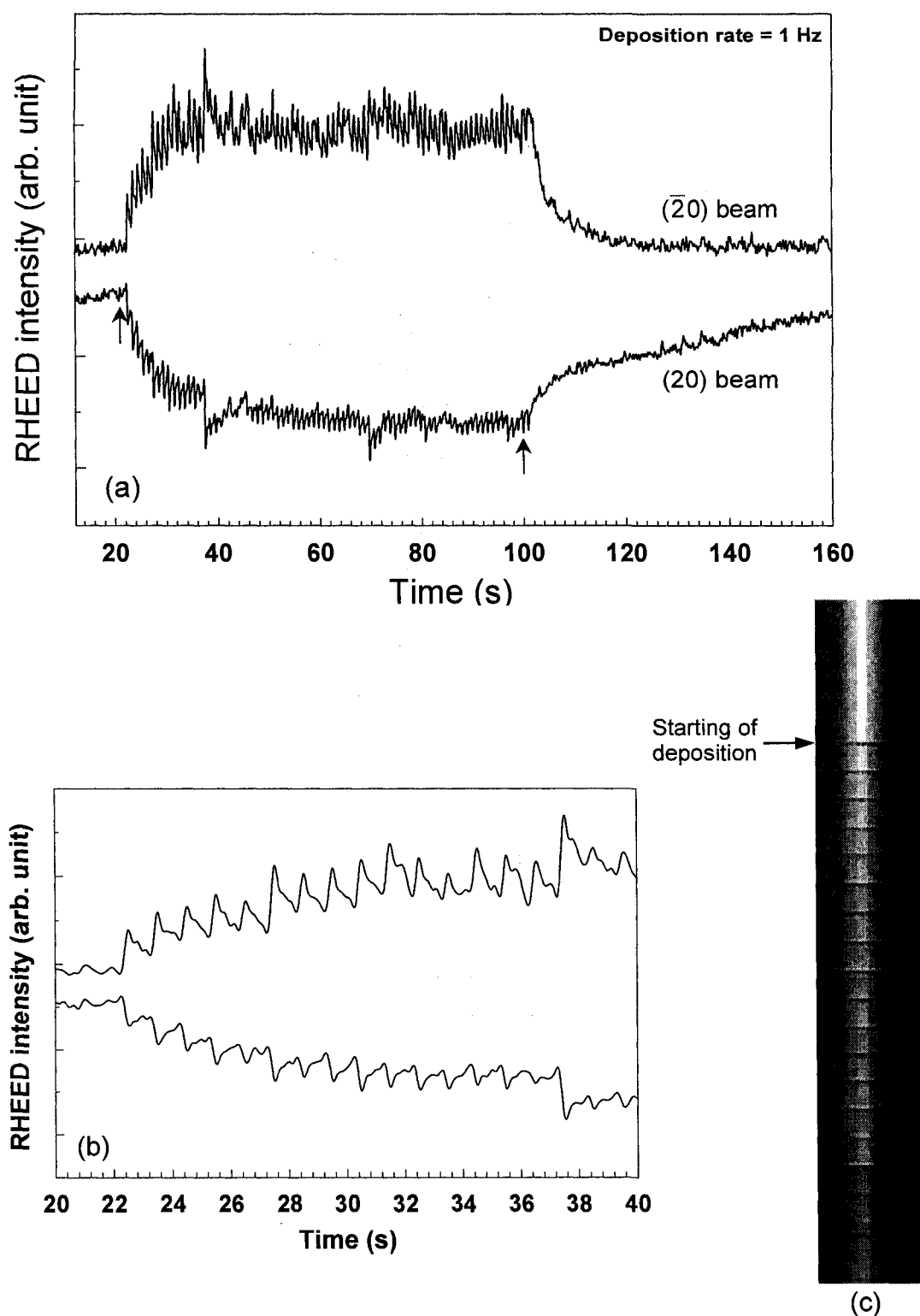


FIG. 2.12. (a) Phase shift in the RHEED intensity of the (20) and $(\bar{2}0)$ beams during femtosecond PLD growth of In on Si(100)-(2 \times 1) at $\sim 145^\circ\text{C}$ [51]. The arrows indicate that the laser was turned on at 21 s and turned off at 100 s. (b) Magnified scale of graph (a) showing oscillations have cycled out of phase. (c) RHEED tracking scan of the (20) beam showing pulsing in brightness corresponding to the intensity in (b).

In the step density model, RHEED oscillations are assumed to be composed of two contributions [2]. One is the coherent Bragg diffraction of the kinematic approach, which involves atoms at positions that define the long-range periodicity of the surface. The second contribution is defined as the incoherent scattering proportional to the step edge atoms or other defects that vary with the developing surface morphology. At the out-of-phase conditions, the diffracted intensity should be dominated by the destructive interference of the kinematic model, leading to minimum at half monolayer coverage. At the in-phase conditions, the coherent process should not produce any intensity variations. Instead, the incoherent process should dominate, producing an intensity minimum at half monolayer coverage, where the step density is largest. This model can explain the oscillatory behavior of the RHEED intensity during pulsed deposition in Fig. 2.11 (b). After deposited laser pulse, the surface has a large step density and results in minimizing the RHEED intensity. When the deposits arranged on the surface, the RHEED intensity increased. Therefore, the phase variation between incoherent and coherent diffraction contributions led to the observed RHEED oscillations between laser pulses. Studies based on the evaluation of STM images find a direct correspondence between step density and RHEED intensity for special cases during growth [71, 72]. The most basic features of the layer-by-layer growth process can be described by a basic rate equation in the so-called birth-death model, which explains the growth process in terms of the coverages [73]. This model does not describe the distribution of the atoms within any given layer and therefore contains limited information about the surface morphology [2]. In the dynamical diffraction approaches for the intensity oscillations, the main part of the scattering potential of a growing layer is assumed to vary linearly with the coverage. This causes a

periodic change in the refraction conditions for electrons entering the growing layer, which affects their reflection from the bottom boundary of the growing layer [59, 60, 64, 74]. The application of the current theoretical models to realistic RHEED oscillation experiments is at the stage of development [2].

II.7. References:

- [1] Z. L. Wang, "*Reflection electron microscopy and spectroscopy for surface analysis*," Cambridge University Press, Cambridge (1996).
- [2] W. Braun, "*Applied RHEED, Reflection High-Energy Electron Diffraction During Crystal Growth*," Springer-Verlag, Berlin (1999).
- [3] A. Ichimiya and P. I. Cohen, "*Reflection High Energy Electron Diffraction*," Cambridge University Press, Cambridge (2004).
- [4] K. Oura, V. G. Lifshits, A. A. Saranin, A. V. Zotov, and M. Katayama, "*Surface Science, An Introduction*," Springer-Verlag, Berlin (2003).
- [5] M. G. Lagally, D. E. Savage, and M. C. Tringides, "*Reflection high-energy electron diffraction and reflection electron imaging of surfaces*," edited by P. K. Larson, and P. J. Dobson, Vol. 188, p. 139, Plenum Press, New York (1988).
- [6] J. H. Neave, B. A. Joyce, P. J. Dobson, and N. Norton, "Dynamics of film growth of GaAs by MBE from RHEED observations," *Appl. Phys. A: Solid Surf.* **31**, 1-8 (1983).
- [7] J. Massies and N. Grandjean, "Oscillations of the Lattice Relaxation in Layer-by-Layer Epitaxial Growth of Highly Strained Materials," *Phys. Rev. Lett.* **71**, 1411-1414 (1993).
- [8] P. Turban, L. Hennet, and S. Andrieu "In-plane lattice spacing oscillatory behaviour during the two-dimensional hetero- and homoepitaxy of metals," *Surface Science* **446**, 241-253 (2000).
- [9] N. Chandrasekhar, V. S. Achutharaman, V. Agrawal, and A. M. Goldman, "Reflection high-energy electron diffraction studies of the growth of $\text{YBa}_2\text{Cu}_3\text{O}_{7-x}$

- and $\text{DyBa}_2\text{Cu}_3\text{O}_{7-3}$ superconducting thin films,” *Phys. Rev. B* **46**, 8565-8572 (1992).
- [10] G. J. H. M. Rijnders, G. Koster, D. H. A. Blank, and H. Rogalla, “In situ monitoring during pulsed laser deposition of complex oxides using reflection high energy electron diffraction under high oxygen pressure,” *Appl. Phys. Lett.* **70**, 1888-1890 (1997).
- [11] L. S.-J. Peng and B. H. Moeckly, “In situ composition monitoring using reflection high-energy electron diffraction for SrTiO_3 thin films grown by reactive coevaporation,” *J. Vac. Sci. Technol. A* **22**, 2437-2439 (2004).
- [12] S. Andrieu and P. Frechard, “What information can be obtained by RHEED applied on polycrystalline films?,” *Surf. Sci.* **360**, 289-296 (1996).
- [13] F. Tang, G.-C. Wang, and T.-M. Lu, “Surface pole figures by reflection high-energy electron diffraction,” *Appl. Phys. Lett.* **89**, 241903-241905 (2006).
- [14] D. Litvinov, T. O'Donnell, and R. Clarke, “In situ thin-film texture determination,” *J. Appl. Phys.* **85**, 2151-2156 (2007).
- [15] F. Tang, G.-C. Wang, and T.-M. Lu, “In situ reflection high energy electron diffraction surface pole figure study of biaxial texture evolution in anisotropic Mg nanoblades during shadowing growth,” *J. Appl. Phys.* **102**, 014306 (1-7) (2007).
- [16] H. Lee, R. Lowe-Webb, W. Yang, and P. C. Sercel, “Determination of the shape of self-organized InAs/GaAs quantum dots by reflection high energy electron diffraction,” *Appl. Phys. Lett.* **72**, 812-814 (1998).

- [17] J. T. Drotar, B. Q. Wei, Y.-P. Zhao, G. Ramanath, P. M. Ajayan, T.-M. Lu, and G.-C. Wang, "Reflection high-energy electron diffraction from carbon nanotubes," *Phys. Rev. B* **64**, 125417(1-6) (2001).
- [18] M. S. Hegazy and H. E. Elsayed-Ali, "Growth of Ge quantum dots on Si(100)-(2×1) by pulsed laser deposition," *J. Appl. Phys.* **99**, 054308(1-7) (2006).
- [19] A. Feltrin and A. Freundlich, "RHEED metrology of Stranski–Krastanov quantum dots," *J. Crystal Growth* **301-302**, 38-41 (2007).
- [20] L.-M. Peng, S. L. Dudarev, and M. J. Whelan, "*High-Energy Electron Diffraction and Microscopy*," Oxford University Press (2004).
- [21] B. Müller and M. Henzler, "SPA-RHEED- A novel method in reflection high-energy electron diffraction with extremely high angular and energy resolution," *Rev. Sci. Instrum.* **66**, 5232-5235 (1995).
- [22] W. Braun, L. Däweritz, and K. H. Ploog, "Surface morphology dependence of plasmon inelastic scattering in RHEED," *Surf. Sci.* **399**, 234-238 (1998).
- [23] Y. Horio and T. Hara, "Energy-filtered reflection high-energy electron diffraction apparatus combined with energy-loss measurement system," *Jpn. J. Appl. Phys.* **41**, L736-L737 (2002).
- [24] G. J. H. M. Rijnders, G. Koster, D. H. A. Blank, and H. Rogalla, "In situ monitoring during pulsed laser deposition of complex oxides using reflection high energy electron diffraction under high oxygen pressure," *Appl. Phys. Lett.* **70**, 1888-1890 (1997).

- [25] R. R. Lunt, J. B. Benziger, and S. R. Forrest, "Real-time monitoring of organic vapor-phase deposition of molecular thin films using high-pressure reflection high-energy electron diffraction," *Appl. Phys. Lett.* **90**, 181932 (1-3) (2007).
- [26] H. Nörenberg, L. Däweritz, P. Schützendübe, and K. Ploog, "Surface evolution on vicinal GaAs(001) surfaces in the transition range from two-dimensional to step-flow growth," *J. Appl. Phys.* **81**, 2611-2620 (1997).
- [27] M. Ichikawa and K. Hayakawa, "Micro-probe reflection high-energy electron diffraction technique. II. Observation of aluminum epitaxial growth on a polycrystal-silicon surface by vacuum evaporation," *Jpn. J. Appl. Phys.* **21**, 154-163 (1982).
- [28] M. Hata, A. Watanabe and T. Isu, "Surface diffusion length observed by in situ scanning microprobe reflection high-energy electron diffraction," *J. Cryst. Growth* **111**, 83-87 (1991).
- [29] J. W. Herman and H. E. Elsayed-Ali "Time-resolved study of surface disordering of Pb(110)," *Phys. Rev. Lett.* **68**, 2952-2955 (1992).
- [30] J. W. Herman, H. E. Elsayed-Ali, and E. A. Murphy "Time-resolved structural study of Pb(100)," *Phys. Rev. Lett.* **71**, 400-403 (1993).
- [31] E. Bauer, "*Reflection electron diffraction (RED)*," in "Techniques for the direct observation of structure and imperfections," ed. R. F. Bunshah, *Techniques of metals research Vol. II, Part 2*, p. 501, Interscience, New York (1969).
- [32] J. E. Mahan, K. M. Geib, G. Y. Robinson, and R. G. Long, "A review of the geometrical fundamentals of reflection high-energy electron diffraction with application to silicon surfaces," *J. Vac. Sci. Technol. A* **8**, 3692- 3700 (1990).

- [33] W. Mönch, “*Semiconductor Surfaces and Interfaces*,” Springer-Verlag, Berlin (1993).
- [34] M. A. Herman and H. Sitter, “*Molecular Beam Epitaxy: Fundamentals and Current Status*,” Springer-Verlag, Berlin (1996).
- [35] S. A. Chalmers, A. C. Gossard, P.M. Petroff, J. M. Gaines, and H. Kroemer, “A reflection high-energy electron diffraction study of (100) GaAs vicinal surfaces,” *J. Vac. Sci. Technol. B* **7**, 1357-1362 (1989).
- [36] F. Hottier, J. B. Theeten, A. Masson, and J. L. Domange, “Comparative LEED and RHEED examination of stepped surfaces; Application to Cu(111) and GaAs(100) vicinal surfaces,” *Surf. Sci.* **65**, 563-577 (1977).
- [37] D. Saloner, J. A. Martin, M. C. Tringides, D. E. Savage, C. E. Aumann, and M. G. Lagally, “Determination of terrace size and edge roughness in vicinal Si{100} surfaces by surface-sensitive diffraction,” *J. Appl. Phys.* **61**, 2884-2893 (1987).
- [38] J. Zhu, K. Brunner, and G. Abstreiter, “Step characterization on vicinal Si surfaces by reflection high-energy electron diffraction at arbitrary azimuths,” *App. Surf. Sci.* **137**, 191-196 (1999).
- [39] J. M. Van Hove, P. Pukite, P. I. Cohen, and C. S. Lent, “RHEED streaks and instrument response,” *J. Vac. Sci. Technol. A* **1**, 609-613 (1983).
- [40] Z. H. Zhang, B. Lin, X. L. Zeng, and H. E. Elsayed-Ali, “Surface morphology of laser-superheated Pb(111) and Pb(100),” *Phys. Rev. B* **57**, 9262-9269 (1998).
- [41] Z. H. Zhang and H. E. Elsayed-Ali, “Temperature dependence of step density on vicinal Pb(111),” *Phys. Rev. B* **57**, 15561-15566 (1998).

- [42] M. A. Hafez and H. E. Elsayed-Ali, "Atomic hydrogen cleaning of InP(100): Electron yield and surface morphology of negative electron affinity activated surfaces," *J. Appl. Phys.* **91**, 1256-1264 (2002).
- [43] P. R. Pukite, J. M. Van Hove, and P. I. Cohen, "Extrinsic effects in reflection high-energy electron diffraction patterns from MBE GaAs," *J. Vac. Sci. Technol. B* **2**, 243-248 (1984).
- [44] C. S. Lent and P. I. Cohen, "Quantitative analysis of streaks in reflection high-energy electron diffraction: GaAs and AlAs deposited on GaAs(001)," *Phys. Rev. B* **33**, 8329-8335 (1986).
- [45] H. Toyoshima, T. Shitara, J. Zhang, J. H. Neave, and B. A. Joyce, "A systematic RHEED study of regular and random steps on GaAs(001) surfaces," *Surf. Sci.* **264**, 10-22 (1992).
- [46] L. Daweritz and K. Ploog, "Contribution of reflection high-energy electron diffraction to nanometre tailoring of surfaces and interfaces by molecular beam epitaxy" *Semicond. Sci. Technol.* **9**, 123-136 (1994).
- [47] J. J. Harris, B. A. Joyce, and P. J. Dobson, "Oscillations in the surface structure of Sn-doped GaAs during growth by MBE," *Surf. Sci.* **103**, L90-L96 (1981).
- [48] J. R. Arthur, "Molecular beam epitaxy," *Surf. Sci.* **500**, 189-217 (2002).
- [49] G. L. Price, "The growth of semiconductor thin films studied by RHEED," *Aust. J. Phys.* **43**, 583-600 (1990).
- [50] J. H. Neave, P. J. Dobson, B. A. Joyce, and J. Zhang, "Reflection high-energy electron diffraction oscillations from vicinal surfaces – A new approach to surface diffusion measurements," *Appl. Phys. Lett.* **47**, 100-102 (1985).

- [51] M. A. Hafez and H. E. Elsayed-Ali, "Formation of In(2×1) and In islands on Si(100)-(2×1) by femtosecond pulsed laser deposition," *J. Appl. Phys.* **101**, 113515 (1-10) (2007).
- [52] M. A. Hafez H. E. Elsayed-Ali, "Activation energy of surface diffusion and terrace width dynamics during the growth of In(4×3) on Si(100)-(2×1) by femtosecond pulsed laser deposition," *J. Appl. Phys.* **103**, 093510 (1-10) (2008).
- [53] J. M. Van Hove, C. S. Lent, P. R. Pukite, and P. I. Cohen, "Damped oscillations in reflection high energy electron diffraction during GaAs MBE," *J. Vac. Sci. Technol. B* **1**, 741-746 (1983).
- [54] J. M. Van Hove, P. R. Pukite, and P. I. Cohen, "The dependence of RHEED oscillations on MBE growth parameters," *J. Vac. Sci. Technol. B* **3**, 563-567 (1985).
- [55] P. I. Cohen, P. R. Pukite, J. M. Van Hove, and C. S. Lent, "Reflection high energy electron diffraction studies of epitaxial growth on semiconductor surfaces," *J. Vac. Sci. Technol. A* **4**, 1251-1258 (1986).
- [56] F. Briones, D. Golmayo, L. Gonzalez, and J. L. DeMiguel, "Surface stoichiometry and morphology of MBE grown (001)GaAs through the analysis of RHEED oscillations," *Jpn. J. Appl. Phys.* **24**, L478-L480 (1985).
- [57] P. J. Dobson, B. A. Joyce, J. H. Neave, and J. Zhang, "Current understanding and applications of the RHEED intensity oscillation technique," *J. Cryst. Growth* **81**, 1-8 (1987).

- [58] B. A. Joyce, P. J. Dobson, J. H. Neave, and Z. Zhang, "*In two-dimensional systems: Physics and new devices*," ed. by G. Bauer, F. Kuchar, H. Heinrich, Springer Ser. Solid-State Sci., Vol. **67**, p.42, Springer, Berlin (1986).
- [59] Z. Mitura, S. L. Dudarev, and M. J. Whelan, "Phase of RHEED oscillations," Phys. Rev. B **57**, 6309-6312 (1998).
- [60] W. Braun, L. Däweritz, and K. H. Ploog, "Origin of Electron Diffraction Oscillations during Crystal Growth," Phys. Rev. Lett. **80**, 4935-4938 (1998).
- [61] A. Nemcsics, "Explanation of the initial phase change vs. incident angle of the RHEED intensity oscillation," Thin Solid Films **412**, 60-63 (2002).
- [62] B. Shin, J. P. Leonard, J. W. McCamy, and M. J. Aziz, "On the phase shift of reflection high energy electron diffraction intensity oscillations during Ge(001) homoepitaxy by molecular beam epitaxy," J. Vac. Sci. Technol. A. **25**, 221-224 (2007).
- [63] J. Resh, K. D. Jamison, J. Strozier, A. Bensaoula, and A. Ignatiev, "Phase of reflection high-energy electron diffraction intensity oscillations during molecular-beam-epitaxy growth of GaAs(100)," Phys. Rev. B **40**, 11799-11803 (1989).
- [64] W. Braun, L. Däweritz, and K. H. Ploog, "New model for reflection high-energy electron diffraction intensity oscillations," J. Vac. Sci. Technol. B **16**, 2404-2412 (1998).
- [65] C. S. Lent and P. I. Cohen, "Diffraction from stepped surfaces: I. Reversible surfaces," Surf. Sci. **139**, 121-145 (1984).
- [66] P. R. Pukite, C. S. Lent, and P. I. Cohen, "Diffraction from stepped surfaces II. Arbitrary terrace distributions," Surf. Sci. **161**, 39-68 (1985).

- [67] G. S. Petrich, P. R. Pukite, A. M. Wowchak, G. J. Whaley, P. I. Cohen, and A. S. Arrott "On the origin of RHEED intensity oscillations" *J. Cryst. Growth* **95**, 23-27 (1989).
- [68] B. Shin and M. J. Aziz, "Modeling RHEED intensity oscillations in multilayer epitaxy: Determination of the Ehrlich-Schwoebel barrier in Ge(001) homoepitaxy," *Phys. Rev. B* **76**, 165408 (1-12) (2007).
- [69] S. Clarke and D. D. Vvendsky, "Growth mechanism for molecular-beam epitaxy of group-IV semiconductors," *Phys. Rev. B* **37**, 6559-6562 (1988).
- [70] T. Shitara, D. D. Vvendsky, M. R. Wilby, J. Zhang, J. H. Neave, and B. A. Joyce "Step-density variations and reflection high-energy electron-diffraction intensity oscillations during epitaxial growth on vicinal GaAs(001)," *Phys. Rev. B* **46**, 6815-6824 (1992).
- [71] D. M. Holmes, J. L. Sudijono, C. F. McConville, T. S. Jones, and B. A. Joyce, "Direct evidence for the step density model in the initial stages of the layer-by-layer homoepitaxial growth of GaAs(111)A," *Surf. Sci.* **370**, L173-L178 (1997).
- [72] B. G. Orr, M. D. Johnson, C. Orme, J. Sudijono, and A. W. Hunt, "The surface evolution and kinetic roughening during homoepitaxy of GaAs (001)," *Solid State Electron.* **37**, 1057-1063 (1994).
- [73] P. I. Cohen, G. S. Petrich, P. R. Pukite, G. J. Whaley, and A. S. Arrott, "Birth-death models of epitaxy I. Diffraction oscillations from low index surfaces," *Surf. Sci.* **216**, 222-248 (1989).

- [74] Z. Mitura, S. L. Dudarev, L. -M. Peng, G. Gladyszewski, and M. J. Whelan, "The small terrace size approximation in the theory of RHEED oscillations," *J. Cryst. Growth* **235**, 79-88 (2002).

CHAPTER III

ELECTRON YIELD AND SURFACE MORPHOLOGY STUDY OF HYDROGEN-CLEANED InP(100)

III.1. Introduction

Indium phosphide is a material of considerable importance in the area of developing electronic and optoelectronic devices. InP-based high electron mobility transistors are attractive for low noise, high power, and high speed devices applications [1]. Preparation of a high quality InP surface is an important step prior to epitaxial growth. Surface defects lead to thin film and interface quality degradation in the growth of heterostructures. Surface cleaning at low substrate temperatures is an essential step to eliminate the interface carrier depletion region and minimize defect-induced surface states.

InP is used for negative electron affinity (NEA) device fabrication; consequently, preparation of a clean surface is required in order to reduce the density of surface states. Surface contamination produces lower quantum efficiency (QE) photocathodes. The main contaminants observed on InP surfaces are carbon and oxygen [2]. Chemical cleaning alone does not provide a carbon-free surface [3]. Native oxides are desorbed by heating to $\sim 500\text{--}530\text{ }^{\circ}\text{C}$, a temperature much higher than the InP congruent temperature ($\sim 400\text{ }^{\circ}\text{C}$) at which the phosphor atoms desorb preferentially, leaving an indium-rich rough surface with poor electronic quality [4, 5]. Adsorbed carbon is strongly bonded to III–V surfaces and remains on the surface even after annealing under phosphine overpressure at high temperatures [6].

There is a considerable interest in developing methods of producing clean InP surfaces while avoiding phosphorus loss, which leads to the creation of electronic defects. Surface cleaning of InP and GaAs using atomic hydrogen was studied [2, 5, 7]. Atomic hydrogen cleaning is used for substrate preparation before epitaxial growth [7, 8] or activation to NEA [9]. The main advantages of this technique are the low cleaning temperature and the avoidance of degradation to the surface electronic properties, which occurs in hydrogen plasma cleaning due to the presence of energetic ions (up to ~ 100 eV) that cause surface damage. The interaction of atomic hydrogen with semiconductor surfaces has been the subject of many studies [10-12]. Atomic hydrogen cleaning of III-V semiconductors has been reported using rf discharge [7], electron cyclotron resonance discharge [13], and a thermal cracking source [2]. Thermal sources produce hydrogen radicals with kinetic energies typically less than 1 eV [14]; thus, atomic hydrogen interaction is limited to the surface top layer. Exposure to atomic hydrogen removes surface contaminants and blocks the electrical activity of dangling bonds [4]. Atomic hydrogen reacts with the stable In oxide, In_2O_3 , and lowers the cleaning temperature by producing a more volatile In oxide, In_2O [2]. Auger analysis of InP surfaces shows complete removal of carbon and oxygen after hydrogen cleaning [2]. The dissociative adsorption of NH_3 and SiH_4 on InP surfaces was studied [15, 16]. It was shown that it takes much longer irradiation time to clean the InP surface than it takes for cleaning the GaAs surface [5]. For InP, atomic hydrogen cleaning can be accomplished at a surface temperature $\sim 350\text{-}400$ °C [9]. This process is limited by the removal of hydrocarbons, which persist at high temperatures, and the relatively high temperature needed to remove indium phosphate, $\text{In}(\text{PO}_3)_3$ [5].

Reflection high-energy electron diffraction (RHEED) is a useful in situ technique to study surface morphology. Surface processes such as thin film growth, phase transformation, and changes in surface morphology can be investigated by quantitative RHEED [17]. The surface we studied was a vicinal InP(100). A vicinal surface is slightly inclined to a low index surface [18, 19]. When the electron beam is incident down the staircase, the RHEED pattern is modified by the step structure, and a splitting specular beam is obtained at the out-of-phase condition. In this case, the RHEED pattern is most sensitive to surface defects. Surface terrace width and terrace width distribution of the vicinal surface can be measured from the split peak spacing and their widths at the out-of-phase condition [17]. The split peak spacing depends on the incident electron beam angle relative to the staircase direction. RHEED was previously used to study surface cleaning of hydrogen-plasma treated GaAs and Si surfaces [20].

A surface with NEA is obtained when the vacuum level is lowered below the bulk conduction band minimum at the surface; thus, the band-gap energy became greater than the work function of the material. In this case, electrons excited to the conduction band minimum can be emitted from the surface. The escape depth in this case is not limited by the mean-free path of the hot electrons, which is on the order of 10 nm, but by the diffusion length of the electrons thermalized to the conduction band minimum, which is on the order of several μm [21]. Achieving NEA requires the combination of electron affinity lowering and downward band bending [22], and thus *p*-type doping is favored (see Fig. 3.1). Quantum efficiency and high secondary emission are obtained as a result of the surface NEA and the long escape depth of photoelectrons and internal secondaries [23]. Hydrocarbons and oxides present on the surface establish a surface energy barrier.

For GaAs, air exposed surfaces are known to contain a high density of surface states that pin the surface Fermi level at midgap [24]. Thus, cleaning is a required step in preparing NEA surfaces.

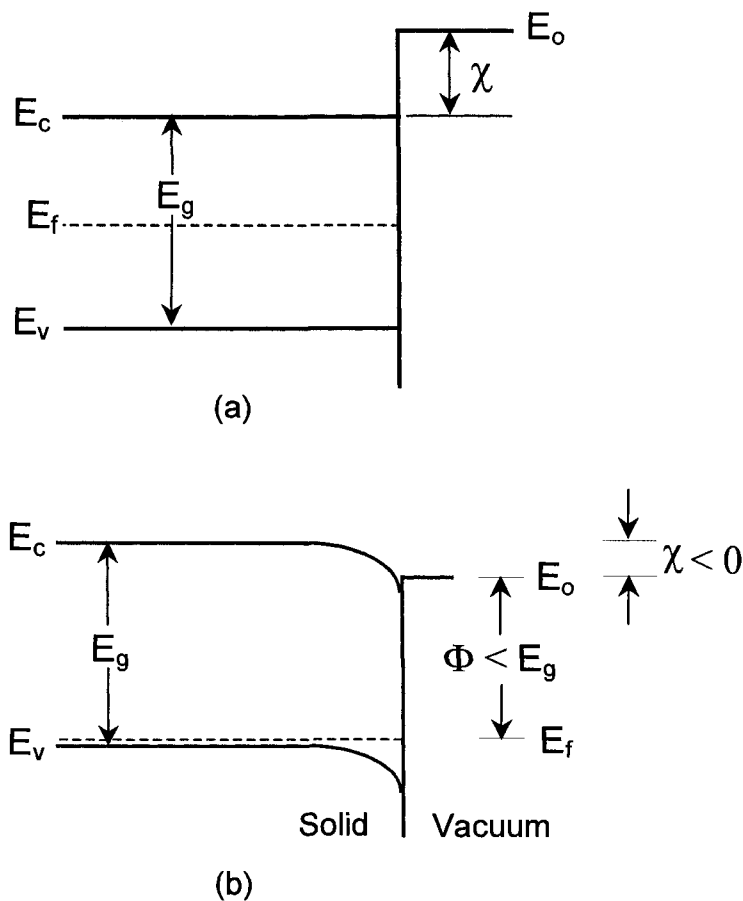


FIG. 3.1. Energy band diagrams. (a) Semiconductor band structure showing the conduction band minimum E_c , the valence band maximum E_v , the Fermi level E_f , the band-gap energy E_g , and the vacuum level E_o . The electron affinity χ is the energy required to remove an electron from lowest conduction band level and place it in vacuum. Typically, χ is 3 to 4 eV [21]. For InP, $E_g = 1.35$ eV and $\chi = 4.38$ eV. (b) Negative electron affinity achieved by band bending in a surface depletion region on a p-type semiconductor. The diagram shows conditions in relation to E_g and work function Φ . The diffusion lengths of the electrons thermalized to E_c are several orders of magnitude longer than the escape depths for conventional emitters. Emission efficiency increased as the number of electrons diffused to the NEA surface increased.

The NEA InP(100) surfaces were prepared by surface cleaning with atomic hydrogen and then activating to NEA by alternate exposure to oxygen and cesium [9]. In this chapter, the work is devoted to study the effect of atomic hydrogen cleaning on surface morphology such as surface terrace width and vacancy-adatom density. RHEED was used to monitor the development of the surface morphology with atomic hydrogen cleaning time. The secondary electron emission from the hydrogen-cleaned InP(100)-(2×4) surface was also measured. The QE and secondary yield were shown to increase with hydrogen cleaning. RHEED was previously used to study the surface morphology of hydrogen-cleaned GaAs(100) surface [25]. In the present work, RHEED is used to investigate the morphology of the InP(100) vicinal surface when heat cleaned at ~300 °C and after hydrogen cleaning at ~380 °C. Results show that removal of contaminants by atomic hydrogen and the accompanying morphology changes improve the electronic surface quality. Correlation between the measured QE and secondary electron yield with surface morphology as detected with RHEED is shown.

III.2. Experiment

The InP(100) wafers used in the present study were *p*-type Zn doped to provide a carrier density of $3 \times 10^{18} \text{ cm}^{-3}$. The wafers had an etch pit density of $< 500 \text{ cm}^{-2}$, orientation of $(100) \pm 0.1^\circ$, resistivity of 0.03 ohm-cm, and thickness of 500 μm , as determined by the manufacturer. The samples were not chemically etched, but only degreased in ethanol before loading in the ultrahigh vacuum (UHV) chamber. A schematic of the UHV chamber is shown in Fig. 3.2. The chamber was baked out after loading the sample. The experiments were carried out in a stainless-steel UHV chamber

pumped by a 220 l/s ion pump. A titanium sublimation pump was also used to reduce the base pressure. The InP wafer was mounted on a molybdenum plate on top of a resistive heater that can be heated to 600 °C. The sample was fixed with two molybdenum clamps. A thermocouple was attached to the sample holder close to the sample in order to measure its temperature. A wire was connected to the sample holder to apply a negative voltage bias to the sample for photocurrent measurement. The sample holder was connected to an *xyz* manipulator through a ceramic rod that electrically insulated the sample from the chamber walls, which was used as the anode for the negatively biased InP substrate. The manipulator provided azimuthal rotation, in order to set the direction of the incident electron beam when acquiring the RHEED patterns. The substrate faced a processing port, containing a cesium source, a leak valve for oxygen admission, a glass window to allow the laser light to activate the InP photocathode, and a port for the hydrogen cracker source. The RHEED patterns were acquired by a charge coupled device (CCD) detector connected to a computer and a video monitor. Calibration of the scaling constants from CCD pixels to reciprocal space units was carried out. The surface of the sample was raised to the desired temperature by the resistive heater and then exposed to atomic hydrogen. The hydrogen cracker source consists of a tungsten filament inserted into an 80-mm-long boron nitride tube with 4 mm inner diameter. The temperature of the filament was maintained ~2000 °C, as measured by a pyrometer. Molecular hydrogen was introduced through a leak valve and passed in the boron nitride tube where it becomes partially dissociated and the produced atomic hydrogen was transported to the sample. The dissociation efficiency, based on the filament temperature, was estimated to be ~3% [26].

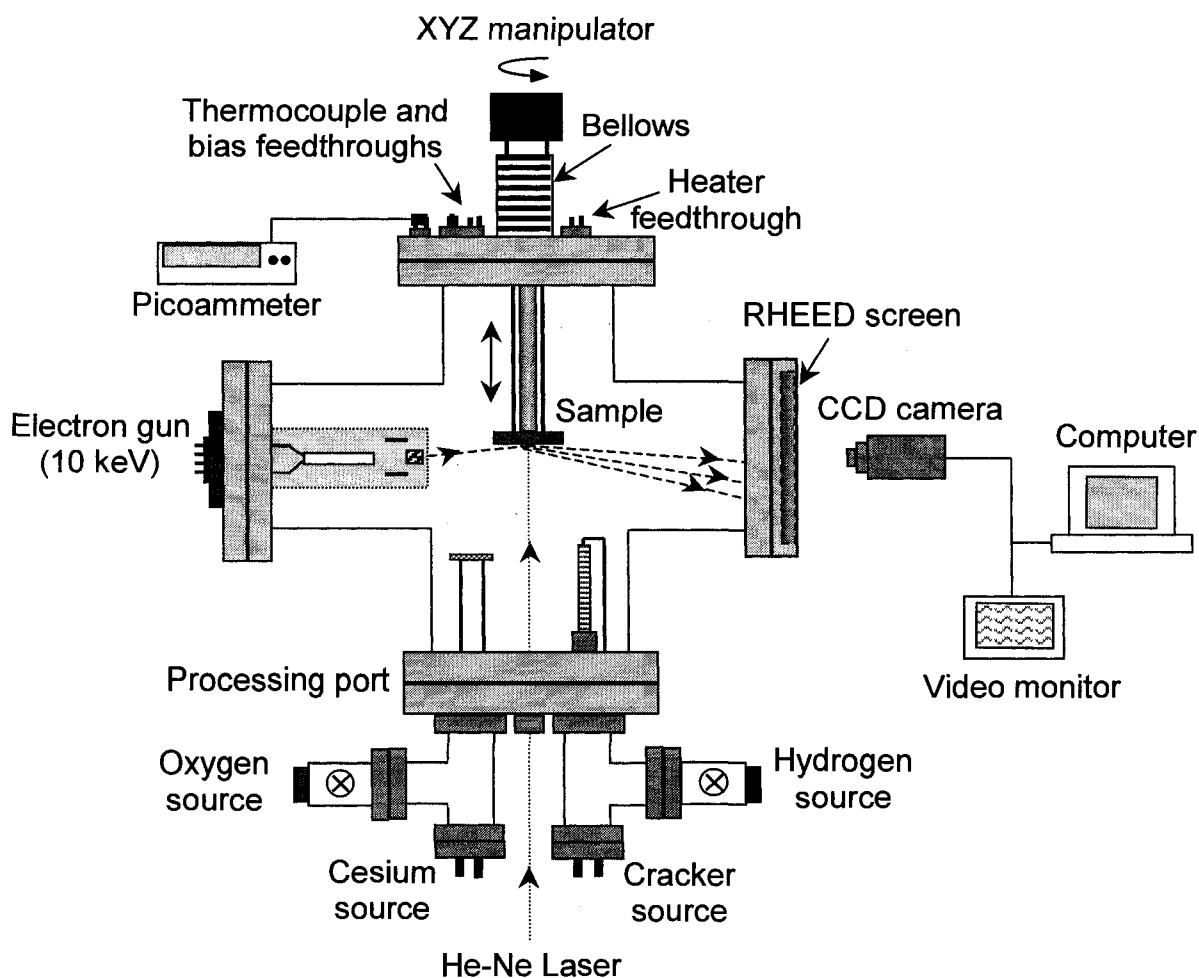


FIG. 3.2. Experimental set up for preparation and study of NEA photocathode. The sample is electrically insulated from the chamber. The UHV system consists of an ion pump (220 l/s), titanium sublimation pump, turbomolecular pump (60 l/s), and mechanical pump. An electro-pneumatic valve was used to separate the chamber from the turbomolecular and mechanical pumps. During hydrogen cleaning, the chamber is filled to $1-5 \times 10^{-6}$ Torr hydrogen as measured using the ion pump controller. For photocurrent measurement, an accelerating voltage of negative bias is applied to the sample and a He-Ne laser beam, $\lambda = 632$ nm, is used as a light source. The operating current to heat the cesium source depends on the cesium deposition rate and the distance between the sample and the source. The activation procedure is performed by applying cesium and oxygen in an alternative way. When cesiation is started, the photocurrent increases from zero to maximum value and then goes down. When the photocurrent is dropped to $\sim 90\%$ of its maximum value, the cesium current is dropped, which effectively terminates cesiation, and the oxygen leak valve is opened. This step increases the pressure and reduces the photocurrent. When the photocurrent reaches $\sim 10\%$ of its maximum value, the oxygen valve is closed and the cesium is evaporated again. This procedure is repeated until the photocurrent measurements reach the highest value.

III.3. RHEED calculations

III.3.1. Real and reciprocal lattices

The real lattice of crystalline surface constitutes a periodic net, which is obtained with repetition of a unit mesh. InP has a zincblende lattice, face centered cubic. The lattice parameter is $a = 5.86 \text{ \AA}$. Reflection RHEED patterns give a two dimensional structure in the reciprocal space. Calculation of reciprocal lattice parameters is used to determine the incident azimuth directions and the crystal structure. Figure 3.3 shows the real lattice of a zincblende structure with orientation of (100).

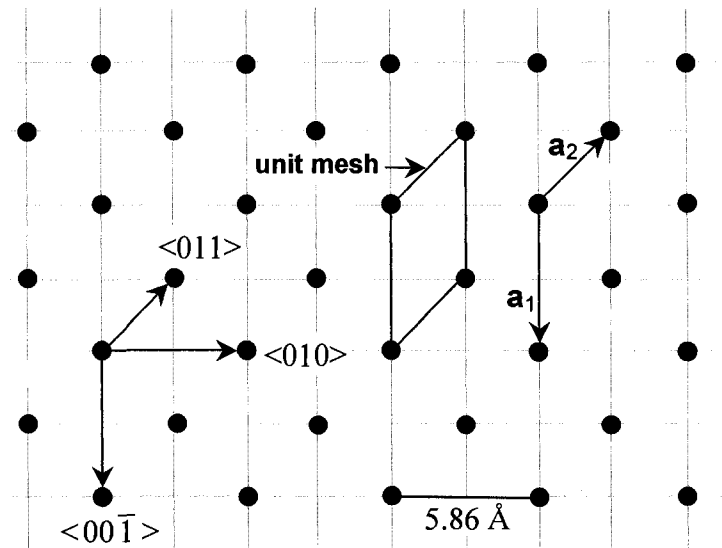


FIG. 3.3. Real lattice of InP(100) surface.

The reciprocal lattice basis vectors are obtained from:

$$a_1^* = 2\pi \frac{a_2 \times \hat{n}}{A} \quad (3.1)$$

$$a_2^* = 2\pi \frac{\hat{n} \times a_1}{A} \quad (3.2)$$

with $A = a_1 \cdot (a_2 \times \hat{n})$

where \mathbf{n} is a unit vector normal to the surface, $\mathbf{n} = \langle 100 \rangle$, and A is the area of the crystalline unit mesh. The real lattice in Fig. 3.3 has vectors \mathbf{a}_1 and \mathbf{a}_2 of

$$\mathbf{a}_1 = 5.86 \langle 00\bar{1} \rangle,$$

$$\mathbf{a}_2 = 2.93 \langle 011 \rangle,$$

The area of the unit mesh is obtained from

$$A = \mathbf{a}_1 \cdot (\mathbf{a}_2 \times \hat{\mathbf{n}}) = (5.86)(2.93) \begin{bmatrix} 0 & 0 & -1 \\ 0 & 1 & 1 \\ 1 & 0 & 0 \end{bmatrix} = 17.16 \text{ \AA}^2. \quad (3.3)$$

Then, the reciprocal lattice parameters are obtained using the above equations to be:

$$\mathbf{a}_1^* = 2\pi \frac{\mathbf{a}_2 \times \hat{\mathbf{n}}}{A} = \frac{2\pi}{17.16} [2.93 \langle 011 \rangle \times \langle 100 \rangle] = 1.07 \langle 01\bar{1} \rangle$$

$$\mathbf{a}_2^* = 2\pi \frac{\hat{\mathbf{n}} \times \mathbf{a}_1}{A} = \frac{2\pi}{17.16} [5.86 \langle 100 \rangle \times \langle 00\bar{1} \rangle] = 2.14 \langle 010 \rangle.$$

The reciprocal lattice of InP(100) with the basis vectors is shown in Figure 3.4.

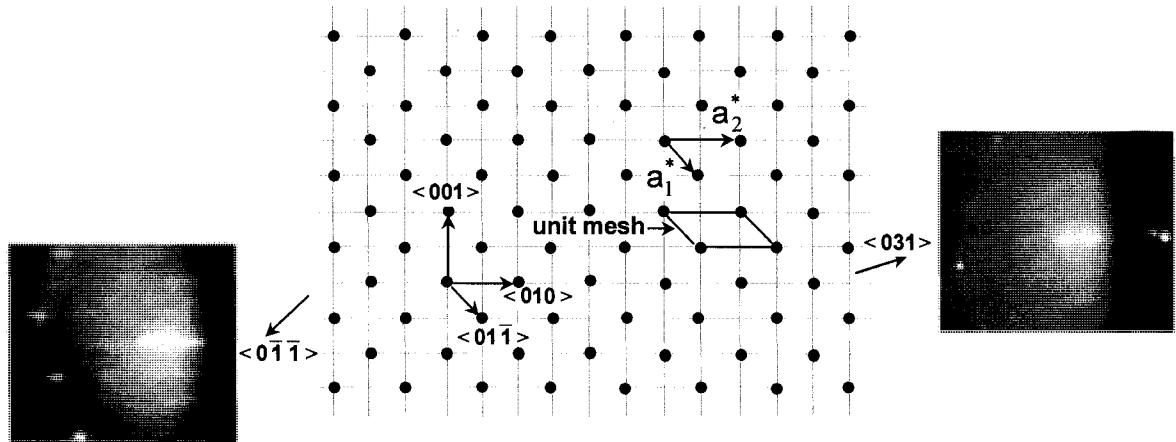


FIG. 3.4. Reciprocal lattice of InP(100) surface and unit mesh corresponding to the real lattice in the Fig. 3.3(a). RHEED patterns taken for a cleaned-surface are shown.

III.3.2. Terrace width and misorientation angle

The InP(100) surface is misoriented toward the low index planes and therefore it is required to measure the terrace width and misorientation angle. The measurements in this InP work are performed using a geometrical method and corresponding equations for cleaned surfaces as follows. Observation of the RHEED specular beam splitting is achieved by directing the primary electron beam down the staircase, perpendicular on the terrace edges. The specular beam showed splitting at the out-of-phase angle around a central part, which located within the zeroth Laue ring. The splitting beams at the out-of-phase condition defined by

$$2d\sin\theta_i = (n+1/2)\lambda, \quad (3.4)$$

where d is the monolayer step height, θ_i is the incident angle corresponding to the out-of-phase condition, n is an integer, and λ is the electron wavelength.

RHEED measurements are prepared to avoid bulk scattering, such as Kikuchi lines that lead to intersect with the specular beam and cause splitting effects. For verifying the out-of-phase condition, a scan around the splitting beams is performed by changing the e-beam incident angle. Then, the splitting beams do not shifted during the scan; only the peak intensity is changed.

The terrace width L can be measured at the out-of-phase condition using

$$\frac{2\pi}{L} = (d\theta)k \sin\theta_i, \quad (3.5)$$

where k is the Ewald sphere radius ($k = 2\pi/\lambda$) and $d\theta$ is the splitting angle.

Figure 3.5 shows geometrical electron diffraction in case of out-of-phase condition and a corresponding RHEED pattern of specular beam splitting form vicinal InP(100) surface.

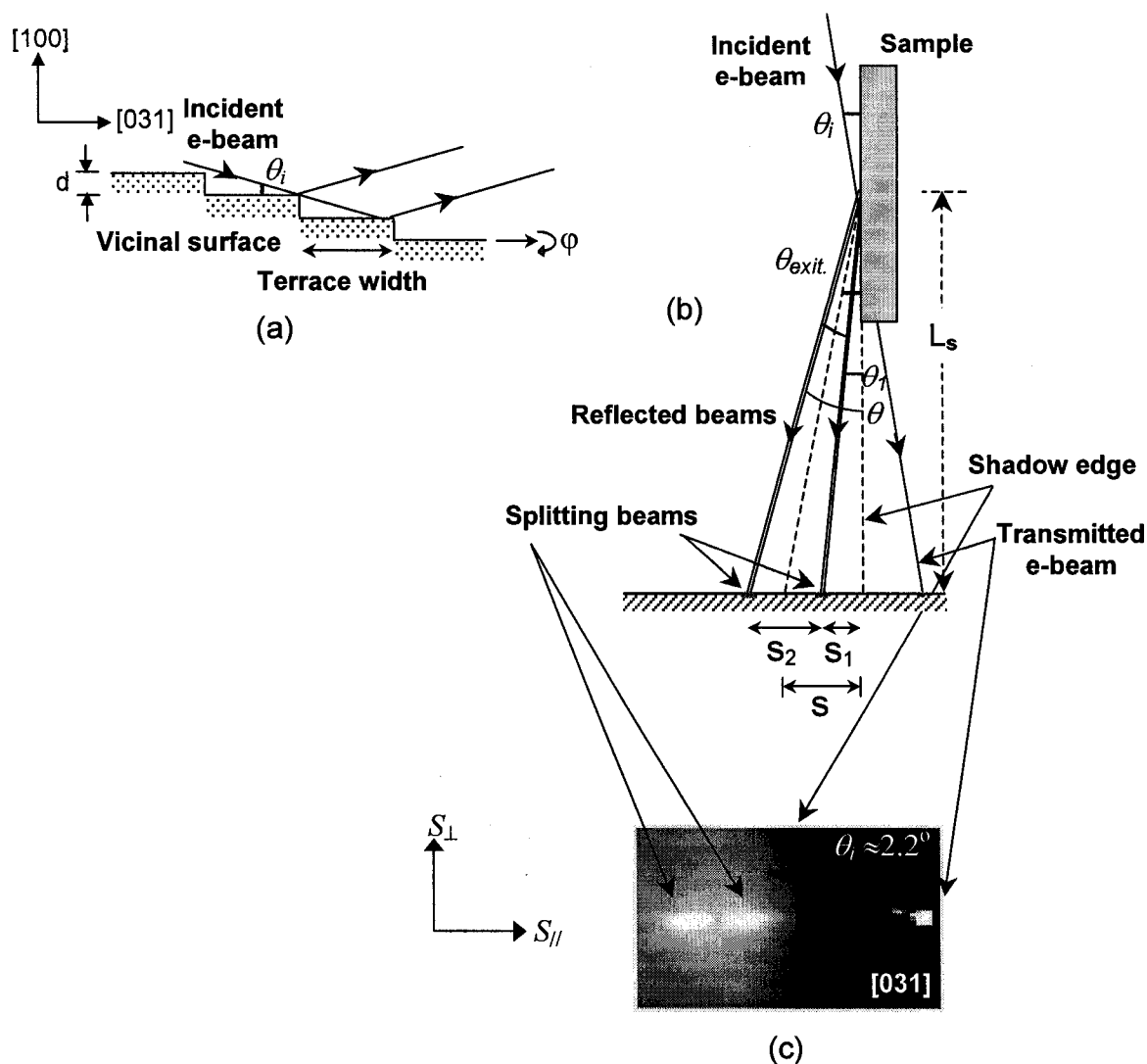


FIG. 3.5. RHEED from InP(100) vicinal surface. (a) Schematic diagram of vicinal surface. The splitting of specular beam can be observed at different azimuth angles ϕ . (b) Illustration of a geometrical method used to determine the angle of incidence and splitting of the electron diffraction in case of the out-of-phase condition. S_{\parallel} and S_{\perp} are the components of the momentum transfer parallel and perpendicular to the incident electron beam, respectively. (c) Corresponding RHEED pattern of InP(100) for incident electron beam down the staircase along the [031] azimuth.

The $\theta_{inc.}$ is determined from the geometry of the reflected RHEED spots using the relation

$$\theta_i = \theta_{exit.} = \tan^{-1} \left(\frac{S}{L_s} \right) \quad (3.6)$$

where S is the distance between the transmitted electron beam and the mid point between the splitting beams, L_s is the RHEED screen to the sample distance, and θ_{exit} is an exit angle of specular beam.

The distances S , S_1 , and S_2 are measured from the RHEED pattern in pixels and then converted to cm using a calibration along the splitting direction, parallel to the momentum transfer $S_{//}$. The instrumental response is measured at the in-phase condition from the FWHM along the specular beam. Then the corresponding angles θ and θ_l of the reflected RHEED beams are determined.

$$\theta = \tan^{-1} \left(\frac{S_1 + S_2 - Instr. response}{L_s} \right) \quad (3.7)$$

By substituting θ and θ_l , the splitting angle is obtained from:

$$(d\theta) = \theta - \theta_l \quad (\text{in radians}) \quad (3.8)$$

By substituting for $d\theta$ and θ_{exit} from equations (3) and (5) in (1) to get the terrace width L in Å

$$L = \frac{2\pi}{(d\theta) k \sin \theta_i} \quad (3.9)$$

Experimental errors due to uncertainty in the electron energy and in determining the splitting peaks are calculated and added to L . The corresponding misorientation angle θ_m for the vicinal InP(100) is obtained by knowing the terrace step height d and L .

III.4. Results and discussion

III.4.1. Quantum efficiency and secondary electron emission

The preparation of a NEA InP(100) surface was initiated by cleaning in UHV. The chamber was baked for ~48 h to attain a base pressure of $\sim 1 \times 10^{-10}$ Torr, while the InP sample was kept at ~ 350 °C during baking to reduce surface contamination. RHEED was used to monitor the effect of heat and atomic hydrogen cleaning on the InP(100) surface. The incident electron energy was 9 keV. Activation to NEA was performed, while the sample was at room temperature. The standard method of activation to NEA by alternate deposition of cesium and oxygen according to the *yo-yo* procedure was followed [27]. Before surface cleaning, the RHEED pattern showed a halo indicative of a surface covered with hydrocarbons and native oxides.

The sample cleaning was performed in several 3-h cycles. The QE and the secondary electron emission (SEE) were measured after cooling the sample to room temperature (RT) and activating the surface to NEA. The SEE was measured by directing the primary RHEED gun electron beam onto the surface at an angle of $\sim 3.5^\circ$. The resulting SEE current was measured before and after activation, and the ratio between the two currents is given as the SEE ratio ($I_{\text{activated}} / I_{\text{nonactivated}}$). A negative bias of ~ 100 V was applied to the sample when measuring electron emission. During cleaning, the hydrogen pressure inside the chamber was $\sim 4 \times 10^{-6}$ Torr, and the cracker source was operated at ~ 2000 °C.

In the first cycle, the sample temperature was raised gradually under vacuum at a rate of 4-7 °C/min to ~ 370 °C and held at that temperature for 3 h. The sample was then cooled to RT and activated to NEA. A QE of $\sim 0.2\%$ was obtained in response to 632.8

nm light. Some diffraction features of the RHEED pattern could be seen. Figure 3.6 shows the RHEED pattern obtained after heat cleaning at ~ 370 °C. No photoemission can be measured when the same activation procedure is performed on a surface that has not been heat cleaned. In another sample, heat cleaning at ~ 300 °C followed by activation to NEA resulted in a QE of $\sim 0.1\%$.



FIG. 3.6. RHEED patterns of InP(100) surface after heat cleaning at 370 °C showing a strong background due to contaminants.

In the following cycles, the temperature of the sample was raised to the desired value, also at a rate of 4-7 °C/min, and then the surface was exposed to atomic hydrogen for 3 h in each cycle. Figure 3.7 shows the measured QE and SEE ratio obtained at RT for a NEA InP(100) surface after a sequence of surface cleaning. The data points in Fig. 3.7 were obtained successively on the same sample that was first subjected to a 3 h heat cleaning indicated in Fig. 3.7 as cycle 1. Cycles 2-19 were all hydrogen cleaning 3-h cycles at the indicated sample temperature.

In the second cleaning cycle, the sample temperature was raised to ~ 350 °C and then exposed to atomic hydrogen. After activation to NEA, a QE of 1.6% was obtained and the measured SEE ratio was ~ 2.3 . The RHEED patterns obtained before activation to

NEA showed streaks with large background, indicating the presence of surface contaminants. These contaminants result in a surface interfacial barrier reducing the QE. After activation, the RHEED streak intensity decreased with cesium deposition because cesium adsorbs on the surface in a fashion that lacks long-range order. Atomic hydrogen exposure was effective in removing cesium and surface contaminants improving the surface electronic quality.

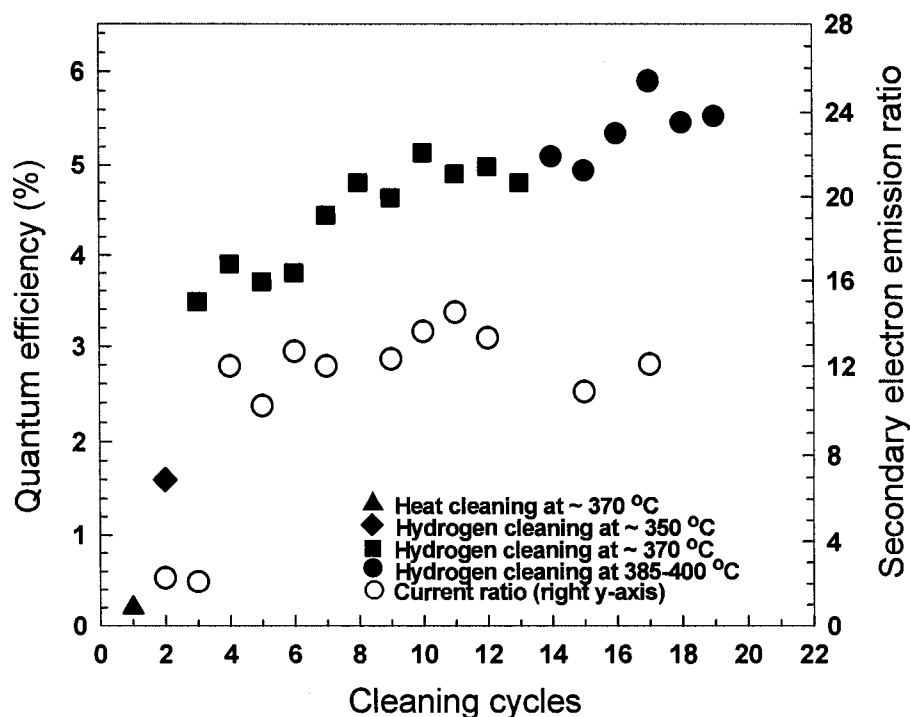


FIG. 3.7. The quantum efficiency and secondary electron emission ratios were measured for a (2×4)-reconstructed InP surface. At each cleaning cycle, the InP sample was cleaned for three hours and the measurements were taken at room temperature.

In cycles 3-13, we further exposed the sample to atomic hydrogen while its temperature was kept at ~370 °C. After the third hydrogen cleaning cycle, a QE of 3.9% was produced, and the SEE ratio increased to ~12. In addition, a clear streaky RHEED

pattern was observed with low background intensity. Figure 3.8(a) is an example of a RHEED pattern obtained after a few hydrogen cleaning cycles at $\sim 370^\circ\text{C}$ with the electron beam incident along the [031] direction. The RHEED pattern showed noticeable improvement after the surface temperature was raised to 370°C and was exposed to atomic hydrogen. However, only gradual changes in the pattern were observed with increased hydrogen cleaning time at $\sim 370^\circ\text{C}$ (cleaning cycles 3-13 in Fig. 3.7). The improvement in QE and SEE ratio is expected to be due to the removal of oxides and carbon atoms during InP surface cleaning. When the azimuthal direction of the sample was changed relative to the primary electron beam, there was no significant change in the resultant secondary emission current. After cleaning cycle 10, the QE increased to $\sim 5\%$. An $I_{\text{activated}}$ of $\sim 113\ \mu\text{A}$ was measured after activating the sample to NEA, and a SEE ratio of ~ 13 was obtained. An increase in the hydrogen cleaning time improved electron yield to a saturation level, which depended on the surface cleaning temperature and on other conditions such as the sample used, its processing history, and the vacuum condition.

In cycles 14-19, the sample was heated to $385\text{--}400^\circ\text{C}$ and then exposed to atomic hydrogen. At cleaning cycle 17, the QE increased to $\sim 6\%$ in response to $632.8\ \text{nm}$ light. There was no further increase, however, in the SEE ratio after hydrogen cleaning at $385\text{--}400^\circ\text{C}$, as shown in Fig. 2. We have previously observed QE as high as $\sim 8.5\%$ on an InP(100) NEA surface [9]. The maximum achieved quantum efficiency is highly sensitive to sample preparation and the vacuum condition. In the present work, we focused on the surface morphology of InP(100) with atomic hydrogen cleaning rather than optimizing the QE. Also, changes in the surface morphology were monitored by electron diffraction for a relatively long atomic hydrogen cleaning time.

A high-quality InP(100) surface can be obtained with atomic hydrogen cleaning. Figure 3.8(b) is a RHEED pattern obtained after hydrogen cleaning at 385-400 °C, showing the quarter-order streaks of the clean phosphorus-stabilized (2×4)-reconstructed surface. The electron beam was incident along the $[0\bar{1}\bar{1}]$ direction. The presence of well-defined diffraction spots falling on semicircles indicates that the oxides on the surface were removed with little surface damage. In addition, Kikuchi lines can be seen from the RHEED pattern, which indicates the high quality of the crystal below the top layers.

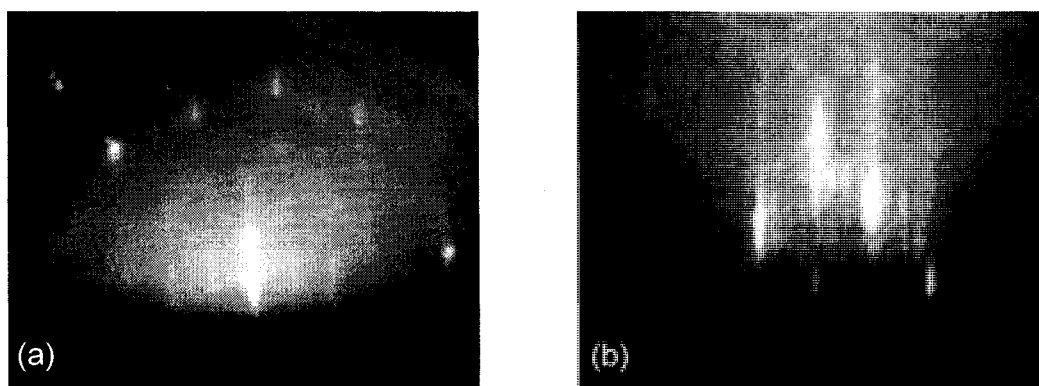


FIG. 3.8. RHEED patterns of InP(100) surface after atomic hydrogen cleaning. (a) After hydrogen cleaning at ~ 370 °C, the RHEED streaks are visible along with a strong background. The electron beam was incident along the $[031]$ direction. (b) After hydrogen cleaning at 385-400 °C, a clear (2×4)-reconstructed surface is obtained. The electron beam was incident along the $[0\bar{1}\bar{1}]$ direction.

Surface and bulk properties affect the SEE ratio and QE. In Fig. 3.9, two sets of data are shown for the SEE ratio. Each of these sets was acquired at different surface preparation conditions resulting in different QE when exposed to 632.8 nm. The secondary electron yield from cesium covered InP(100) surface was observed to depend on the surface quality as well as the primary electron energy. The SEE ratio increased

with the incident electron energy, although some saturation was observed at the higher incident electron energies (>6 keV). A higher SEE ratio was obtained for the surface that produced higher QE. This SEE ratio was obtained for a 3.5-9.5 keV electron beam incident on the InP(100) surface at an angle of $\sim 3.5^\circ$. The grazing angle of incidence was used because it can be obtained with the RHEED gun. Secondary electron emission from NEA activated semiconductor surfaces such as Si and GaAs was measured before [23], [28], and [29]. Results on a thin epitaxially grown *p*-doped GaAs(100) surface show a SEE of 400 for primary electron energy of 20 keV incident normal to the surface [28]. The electron escape depth was estimated to be 2 nm and a surface escape probability of 0.14. The grazing angle of the primary electrons in our experiment reduces their range by $\sin \theta_i$, where θ_i is the primary electron angle of incidence. Thus, in our geometry the range of the primary electron is ~ 0.06 of that for normal incidence, which we expect to be the reason for the low SEE observed in our case.

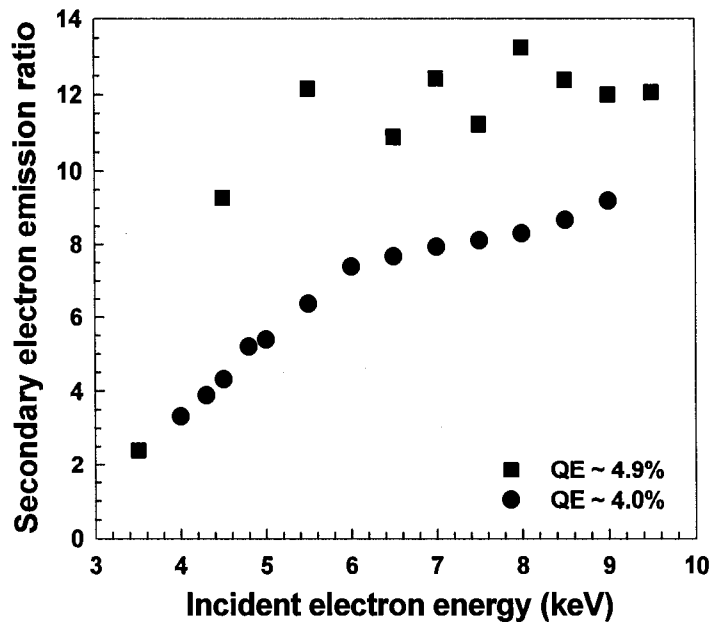


FIG. 3.9. After activating the surface with cesium and oxygen, the secondary electron emission increased with the incident electron energy. The secondary-electron yield is higher for a surface that produces higher quantum efficiency.

After activating the InP surface to NEA, the secondary electrons were observed to decrease with time, as shown in Fig. 3.10. The secondary emission decreased to ~65% of its maximum value after ~20 min, which was at a faster rate than we observe for QE decay [9]. This could be due to accelerated desorption of cesium from the InP surface due to electron stimulated desorption by the high-energy primary electrons. In our case, cesium was deposited alternately with oxygen until the highest QE was achieved, at which point the SEE ratio was also observed to reach its maximum. As the optimum cesiation degrades by desorption, for example, the number of secondary electrons able to escape from the surface is reduced. We also note that the life of the photocathode has a strong dependence on the vacuum level and processing history of the sample.

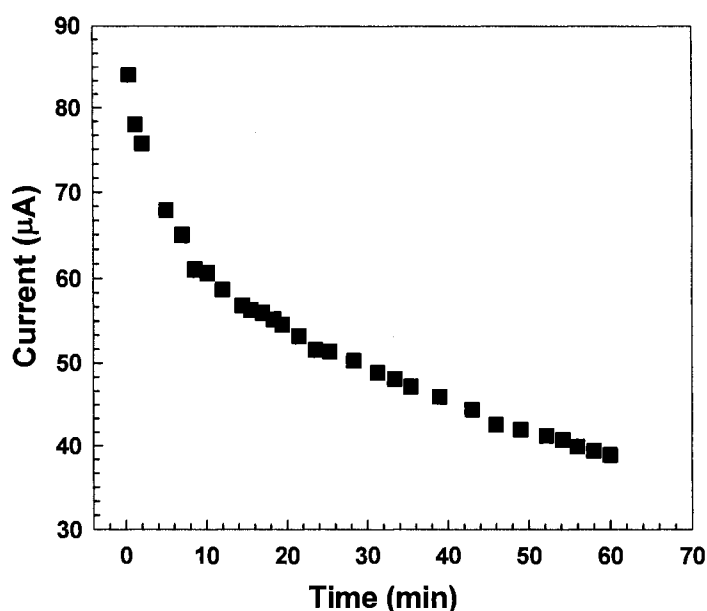


FIG. 3.10. The decrease of secondary electron emission with time after InP(100) surface activation to negative electron affinity. The measurement was taken after atomic hydrogen cleaning at ~370 °C.

After six cleaning cycles at 385-400 °C, the RHEED pattern features were observed to depend on the position of the incident electron beam on the sample. When the electron beam was incident along the [031] direction near the center of the sample, a spotty RHEED pattern appeared. Directing the 632.8 nm light to this location produced a QE of ~1.8%. Close to the sample edge, the RHEED pattern showed a streaky surface. At this location, a QE of ~2.3% was obtained. Those RHEED features can be seen in Figs. 3.11(a) and 3.11(b).

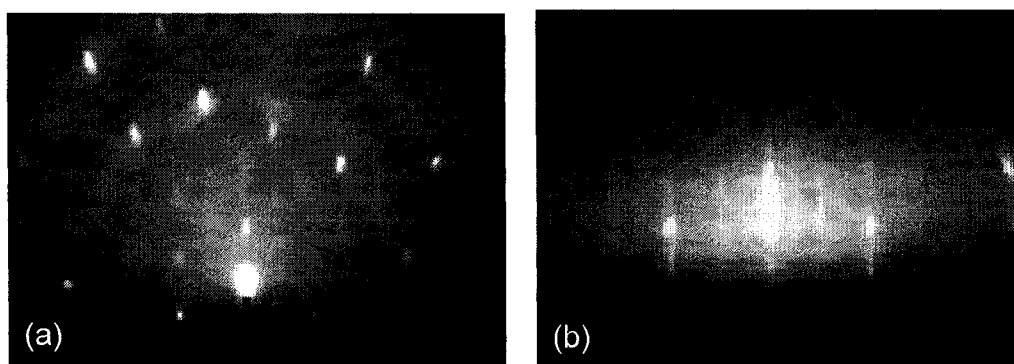


FIG. 3.11. After several hydrogen cleanings at ~385-400 °C, spotty and streaky RHEED patterns were observed at different locations as shown in (a) and (b), respectively. The electron beam was incident along the [031] direction.

As seen from the diffraction patterns, the surface structure became nonuniform over the surface area. Thus, the InP surface decomposed to form phosphorus vapor, leaving indium droplets at certain locations of the InP surface. This was also evident from the increase in the vacuum chamber pressure. Since there was some temperature variation on the surface, we expect that this variation caused the nonuniform decomposition of the InP surface. When phosphorus is desorbed from the InP surface leaving vacant sites,

surface defects are created; therefore, a rough surface is produced with poor electronic properties and low QE. With additional cleaning cycles, transmission RHEED patterns were observed all over the sample area. In addition, the base pressure of the chamber, which was $\sim 1 \times 10^{-10}$ Torr, increased to the low 10^{-9} Torr range. Prolonged heating at 385-400 °C during hydrogen cleaning resulted in desorption of phosphorus, leaving an indium-rich surface.

Hydrogen cleaning in all the above reported measurements was performed at temperatures of ~ 370 °C or higher. Atomic hydrogen cleaning at lower temperatures is less effective [9]. For InP and GaAs, some sample heating to a temperature below the congruent temperature, at which P or As desorb preferentially leaving a damaged surface, is needed to prepare a clean reconstructed surface with high QE [9, 25]. The higher the sample temperature up to the observation of surface damage, the higher the QE after activation to NEA. Repetitive hydrogen cleaning treatment cycles were used in order to show the time progression of the cleaning process. For actual device fabrication, only one hydrogen cleaning period at a temperature close, but less than, the congruent temperature is required. We have observed previously that this cleaning method generally gives the highest QE [9]. Improvement in the hydrogen cracker efficiency and atomic hydrogen delivery to the surface can significantly reduce the preparation time.

III.4.2. RHEED study of surface morphology

We next discuss a quantitative RHEED study of surface morphology of heat-cleaned and hydrogen-cleaned InP(100) surfaces. The morphology studies were conducted on a new sample cut from the same wafer. After each surface cleaning, the

RHEED images were evaluated at RT. The sample was then activated and the QE measured. When the InP sample was heat cleaned at $\sim 300^\circ\text{C}$ for 3 h and then cooled to RT, low intensity diffraction streaks with large background could be seen at different azimuthal directions. Figure 3.12 shows the angular distribution of the (00) specular beam intensity with the electron beam incident along the $[031]$ azimuth. The RHEED intensity profiles show a modulated intensity distribution that depends on the electron beam angle of incidence θ_i . At the Bragg (in-phase) condition the perpendicular momentum transfer ($q_\perp = 2k \sin\theta_i$) is an even number of the inverse monolayer step height ($q_\perp = 2n\pi/d$), where k is $2\pi/\lambda$. At the in-phase condition, the scattered electrons interfere constructively. Examples of that are shown in Fig. 3.10 at $\theta_i = 1.9^\circ$ and 3.1° . The out-of-phase condition is obtained when $q_\perp = (2n+1)\pi/d$. At this condition, electrons scattered from different surface layers interfere destructively (an example is shown in Fig. 12 at $\theta_i = 2.2^\circ$). The RHEED pattern in Fig. 3.12 shows a sharp specular spot at the in-phase condition and a broadened split peak at the out-of-phase condition, which is indicative of regular steps from a vicinal surface [17]. For angles between that satisfying the in-phase or out-of-phase conditions, the intensity of the two peaks in the split specular beam are unequal. An example of that is shown in Fig. 3.12 at $\theta_i = 2.0^\circ$. Observation of the split specular beam depended on the azimuthal direction of the incident electron beam. When the incident electron beam was directed along the $[0\bar{1}\bar{3}]$ direction, a split peak was also observed in the specular beam. The measured RHEED rocking curve for the specular beam at the $[0\bar{1}\bar{3}]$ azimuth obtained at RT is shown in Fig. 3.13. An out-of phase condition is achieved at an electron angle of incidence $\theta_i \sim 2.1^\circ$. At $\theta_i \sim 3.4^\circ$, the

intensity has a maximum. At this angle, the incident electron beam penetrates deeper into the InP sample and the bulk Kikuchi-like scattering effects contribute to the intensity.

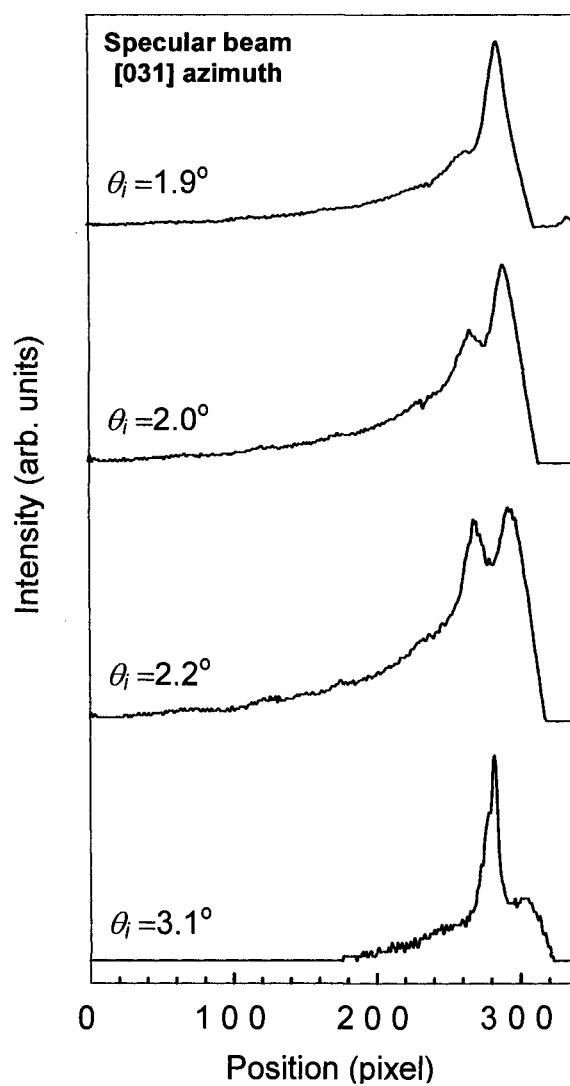


FIG 3.12. Intensity profiles along the specular RHEED spot showing the in-phase and out-of-phase conditions. The electron beam was incident along the [031] azimuth.

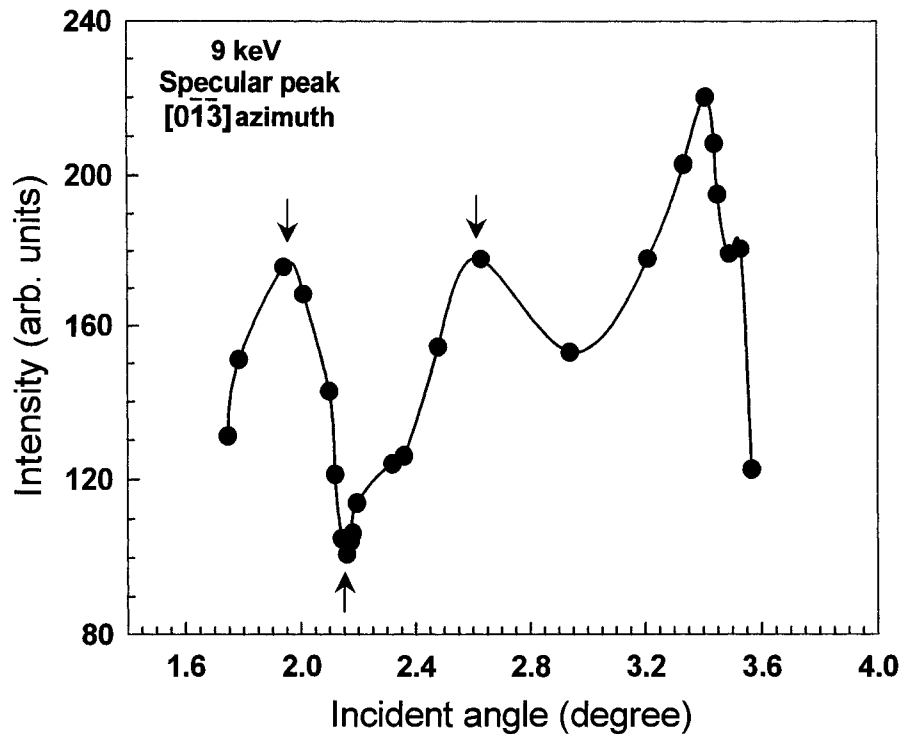


FIG. 3.13. RHEED rocking curve of the peak intensity of the specular spot for the heat-cleaned vicinal InP(100) surface at $\sim 300^\circ\text{C}$. The intensity profile was obtained close to room temperature in the $[0\bar{1}\bar{3}]$ azimuth. The intensity peaked at in-phase angles while it reach minimum at out-of-phase angle as indicated by the arrows.

The terrace width and the split peak profiles of the studied InP(100) surface after heat cleaning at $\sim 300^\circ\text{C}$ were investigated. For terrace width measurement, the electron beam was incident along the $[031]$ direction at which the split specular beam was clearest compared to other azimuthal directions. All RHEED measurements were obtained at RT. The average terrace width for a vicinal surface is determined by the amount of surface misorientation from a low-index plane [30]. The split peak spacing is given by $2\pi/L$, where L is the average separation of terraces. The angle $d\theta$ between the specular split peaks was about 14 mrad. Taking into account the instrumental response of 0.89 ± 0.06

\AA^{-1} , the average terrace width of the heat-cleaned InP(100) vicinal surface was obtained to be $301 \pm 96 \text{ \AA}$. For a single-layer step height ($d = 1.468 \text{ \AA}$), the misorientation angle is approximately 0.3° . The instrumental response was obtained from the FWHM along the specular beam at the in-phase condition. The FWHM was measured after subtracting the background, due to inelastic scattering. The intensity profile of the split peaks for the heat-cleaned surface at $\sim 300^\circ\text{C}$ shows high background and is broadened along and across the (00) beam, when observed at the out-of-phase condition. After the first activation to NEA, the heat-cleaned surface produced a QE of $\sim 0.1\%$.

Next, the InP sample was exposed to atomic hydrogen for 3-h cleaning cycles, while the sample was kept at $\sim 380^\circ\text{C}$. A clear RHEED pattern at the out-of-phase condition was obtained after cooling the sample to RT. At the out-of-phase condition, the splitting angle $d\theta$ was 20.6 mrad . At the in-phase condition, the instrumental response was $0.66 \pm 0.052 \text{ \AA}^{-1}$. After one 3-h cycle of hydrogen cleaning, the average terrace width of the InP surface was obtained to be $299 \pm 42 \text{ \AA}$, and the background of the RHEED pattern decreased, indicating reduction in surface contaminants. Moreover, the broadening along the split specular peak at the out-of-phase condition was less than before hydrogen cleaning. The QE of the activated surface increased from $\sim 0.1\%$ to 1.4% after the first hydrogen cleaning cycle, which was performed at 380°C .

The out-of-phase diffraction was used to evaluate the development of surface morphology with hydrogen cleaning. Following each hydrogen cleaning cycle at $\sim 380^\circ\text{C}$, the average terrace width was measured after allowing the sample to cool to RT. Figure 3.14 shows the RHEED intensity profiles along the (00) specular beam at the out-of-phase condition after different cleaning cycles. The inset of the Fig. 3.14 is a RHEED

image of the split peak, where S_{\parallel} and S_{\perp} are the components of the momentum transfer parallel and perpendicular to the electron beam, respectively. The incident electron beam was along the [031] azimuth.

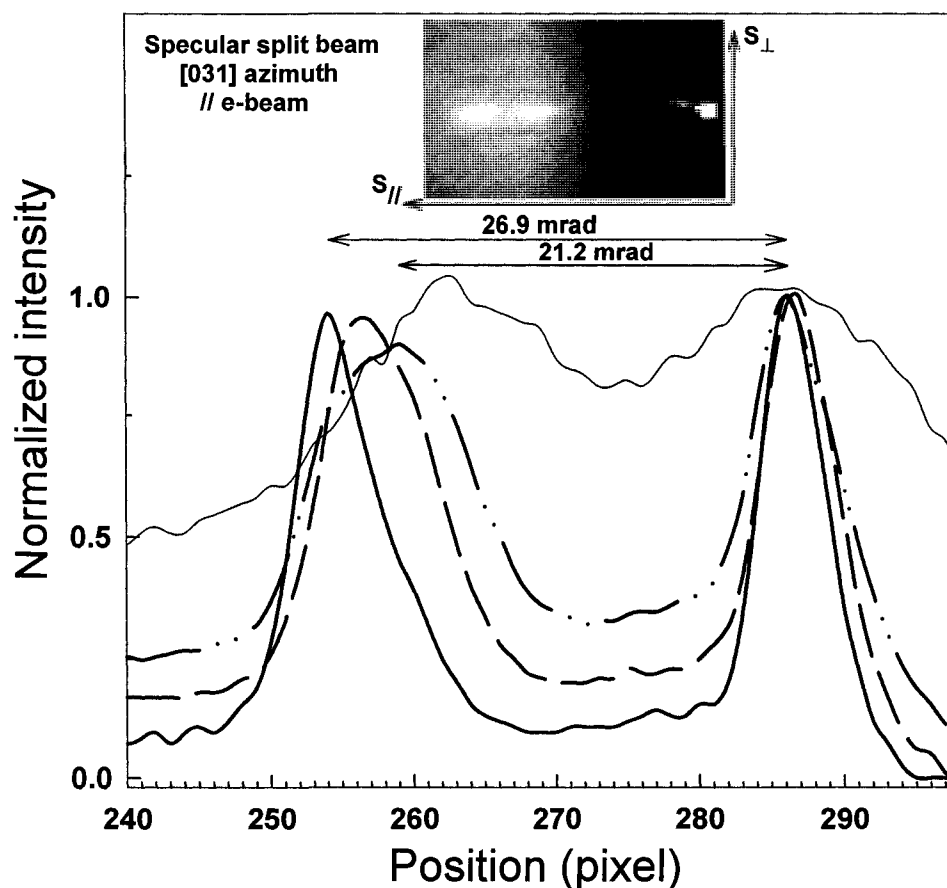


FIG. 3.14. The RHEED intensity profiles of the split specular beam taken in the out-of-phase condition were obtained after heat cleaning at ~ 300 °C (—) and atomic hydrogen cleaning at ~ 380 °C; (— · —), (— — —), and (— · — · —) denote the second, fourth, and sixth cleaning cycles. The split peak spacing increases with hydrogen cleaning, indicating the decrease in the average terrace width. The inset is the RHEED pattern at the out-of-phase condition after hydrogen cleaning.

The split peak spacing was observed to increase with cleaning cycles, indicating that the average terrace width of the InP surface was reduced. After the second hydrogen cleaning cycle, an average terrace width of 291 ± 67 Å was obtained. With additional

hydrogen cleaning cycles, further decrease in the average terrace width was observed reaching 229 ± 20 Å after hydrogen treatment at ~ 380 °C (cycles 1-6), as shown in Fig. 3.15(a). For each point, the RHEED intensity profiles were taken four to five times, and the average value was recorded. The errors indicate the accuracy of determining the split peak spacing. After hydrogen cleaning cycle 6 at ~ 380 °C, the average terrace width was reduced by $\sim 20\%$, compared to the heat-cleaned surface at ~ 300 °C. Preferential etching at terrace edges and movement of the surface atoms could have resulted in the reduced average terrace width.

When the incident electron beam is scattered from terrace edges, the diffracted specular beam width contains information on the density of kinks and meanders at the step edge. Unequal terrace widths or terrace roughness will affect the terrace periodicity and lead to broadening of the split peaks [30]. Line scans along the specular beam of the RHEED pattern were obtained at the out-of-phase condition. Figure 3.15(b) shows the FWHM in mrad along the split peak in the out-of-phase condition, after subtracting the background, as it developed with cleaning cycles. The broadening decreased from ~ 25 to ~ 8 mrad with hydrogen cleaning. In addition, line scans were taken across the specular beam as shown in Fig. 16(a). The broadening of the peak profile across the specular beam decreased with atomic hydrogen cycles compared with the heat-cleaned InP(100). The FWHM across the specular beam profile was obtained after subtracting the background and was observed to decrease from ~ 7 to ~ 4 mrad, as shown in Fig. 16(b). The widths of the split peak decreased with hydrogen cleaning cycles, indicating a decreased kink density at the step edges.

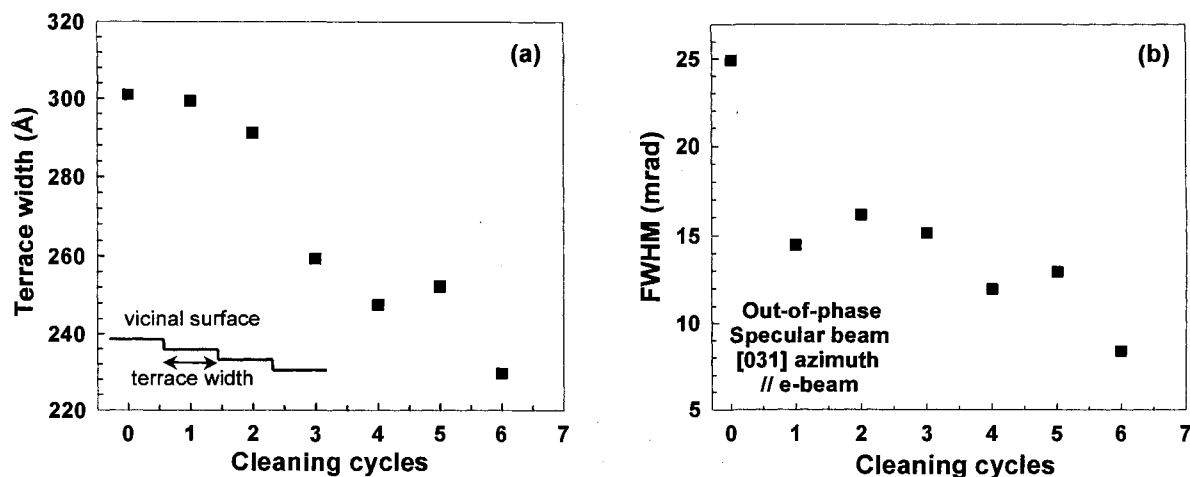


FIG. 3.15. (a) The average terrace width decreases with atomic hydrogen cleaning from 301 ± 42 Å after heat cleaning to 229 ± 20 Å after the sixth hydrogen cleaning cycle. Cycle 0 is heat cleaned at ~ 300 °C; 1-6 are hydrogen cleaned at ~ 380 °C. The inset gives a sketch of the terrace width of a vicinal surface. (b) The measured FWHM along the specular beam ($S_{//}$ direction).

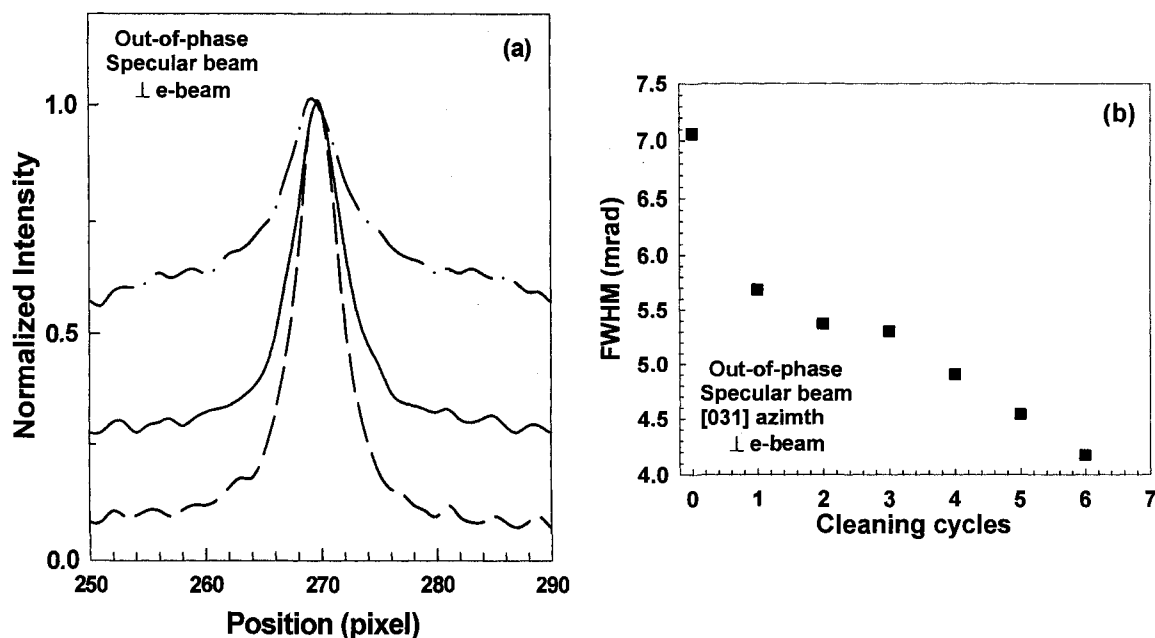


FIG. 3.16. (a) Line scans across the specular beam at the out of phase condition; $(-\cdot-)$, $(—)$, and $(---)$ denote the profiles after heat cleaning, second and sixth hydrogen cleaning cycles. (b) The measured FWHM across the specular beam (S_{\perp} direction).

The observed change in surface morphology from cycle 1 to 6 was accompanied by an increase in QE from 1.4% to ~3.9%. Since the thermal cracker source produces atomic hydrogen with kinetic energy <1 eV, no physical sputtering of surface atoms can occur; any changes in surface morphology are due to chemical etching and surface atom diffusion. Chemical etching can preferentially occur at step edges. Atomic hydrogen removed the surface contaminants, reducing the surface interfacial barrier for electron emission, thus improving the QE. Changes in the surface average terrace width do not show correlation with the measured QE. However, the RHEED intensity-to-background ratio shows good correlation with the QE of the hydrogen-cleaned InP surface as described next.

The out-of-phase RHEED intensity of the specular beam was measured before activation to NEA, and this measurement was correlated to the quantum efficiency of the hydrogen-cleaned InP sample. In the out-of-phase condition, the RHEED pattern intensity is most sensitive to surface defects. Maximum intensity of the out-of-phase specular beam corresponds to a smooth clean surface, while lower intensities correspond to rougher or contaminated surfaces [31]. In the out-of-phase condition, the ratio $R = (I_p - I_b)/I_b$, where I_p and I_b are the RHEED peak and background intensities, respectively, is inversely related to surface defect density, either roughness or contaminants [32]. For a clean surface, the ratio R is a measure of adatom-vacancy density on the surface terraces. Figure 3.17 shows the RHEED intensity R and QE after several 3-h cleaning cycles. After hydrogen cleaning, the sample was cooled to RT, the RHEED pattern was acquired, and the QE measured after activation to NEA. The RHEED intensity was obtained several times at RT and the average values were reported. When the sample was heat-cleaned at

~ 300 °C, a RHEED intensity ratio $R \sim 0.3$ was obtained. This surface produced a QE $\sim 0.1\%$ in response to 632.8 nm light. This indicates that the heat-cleaned InP surface is covered with contaminants expected to be hydrocarbons and native oxides. The background intensity was taken at a location between the (00) and the (01) streaks.

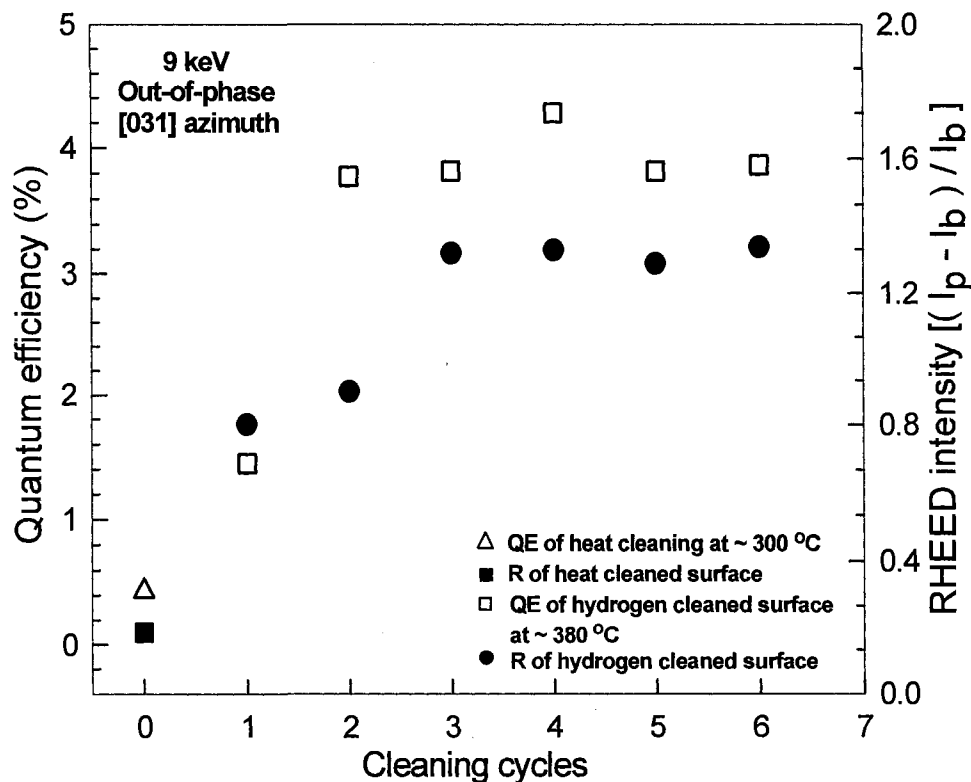


FIG 3.17. Hydrogen cleaning increases the ratio $R = (I_p - I_b) / I_b$, where I_p and I_b are the RHEED peak and background intensities, respectively, measured at the out-of-phase condition. After activation to NEA, the QE correlates with the ratio R measured before activation.

The RHEED intensity ratio R and the QE were measured for the hydrogen-cleaned surface, where hydrogen cleaning was performed at ~ 380 °C. After the first hydrogen cleaning cycle, we obtained a RHEED intensity R of ~ 0.6 , and a QE $\sim 3.5\%$ when activated to NEA. When more hydrogen cleaning cycles were performed, the

background intensity of the RHEED pattern at the out-of-phase condition decreased. The RHEED intensity R at the out-of-phase condition is a good indicator of the obtained QE after activation to NEA. The maximum specular RHEED intensity obtained for this hydrogen-cleaned surface is $R \sim 1.3$. When activated to NEA, this particular surface produced a QE of 4.3% in response to 632.8 nm laser radiation. The obtained QE is highly sensitive to the vacuum conditions and the surface preparation history.

The picture that emerges about the morphology of atomic hydrogen cleaned InP surface is a complicated one. Quantitative RHEED by itself as a surface probe gives information on average surface characteristics, such as the average terrace width and adatom-vacancy density of a clean surface. At steps, the atoms generally have lower coordination than at other surface sites and are quite reactive [19]. This suggests that atomic hydrogen etching occurs preferentially at terrace edges, which causes the observed decrease of the average terrace width accompanied with an increase in terrace width fluctuation. This could be a result of a combination of thermal and chemical effects of hydrogen interaction with the surface. Thermal diffusion of atoms on the surface can also cause changes in the terrace edge morphology due to atoms diffusing and reaching sites on the terrace edge. Hydrogen ion beam smoothening of Ge(001) was previously observed and the mechanism was proposed to be both physical and chemical and could be enhanced thermally [31]. Because of the low kinetic energy of atomic hydrogen in our case, physical sputtering effects are negligible. The RHEED peak-to-background ratio R is a good measure of adatom vacancy concentration on the surface terraces for a clean surface. The increase in the value of R that we observe with cleaning time is due to removal of contaminants at the earlier cleaning cycles. After the surface becomes

atomically clean, the ratio R becomes sensitive only to surface morphology. We observed a relatively small reduction in the average terrace width after the first hydrogen cleaning cycle along with a narrowing of the distribution of the terrace widths. While the RHEED information does not indicate the origin of that reduction, previous atomic force microscopy work on hydrogen plasma processing of GaAs(001) showed that removal of surface oxides at temperatures above 600 K led to the development of a Ga-rich surface with facet formation [33]. The relatively small reduction observed in the terrace width might be related to surface facet formation, although this occurs without apparent surface electronic quality reduction because the QE increased after the first and second hydrogen cleaning cycles at $\sim 380^\circ\text{C}$ and then reached a saturation level with further cleaning (Fig. 11). Thus, the reduction in the average terrace width observed in Fig. 3.15(a) is not accompanied by noticeable electronic surface quality degradation.

III.5. Conclusion

The effect of atomic hydrogen cleaning on the morphology of the InP(100) surface was investigated and this was followed by surface activation to NEA. Atomic hydrogen cleaning produced a clean, phosphorus-stabilized (2×4) -reconstructed InP surface. InP(100) hydrogen cleaned at $385\text{--}400^\circ\text{C}$ gave a QE of $\sim 6\%$ after activation to NEA. The decrease in surface disorder, as determined by the RHEED background-to-peak intensity ratio $R = (I_p - I_b)/I_b$, correlated with the increased QE. A higher R surface produced higher QE. Secondary electron emission from the hydrogen-cleaned surface followed the same trends as the QE. With increased hydrogen cleaning time at $385\text{--}400^\circ\text{C}$, surface defects due to phosphorus desorption were observed along with a reduction in

QE. Thus, quantitative RHEED can be used to optimize semiconductor surface preparation prior to activation to NEA. While RHEED offers a view of surface morphology development with hydrogen cleaning and is suitable for surface probing during preparation, studies using other surface techniques are needed to resolve the nature of the microscopic reactions of atomic hydrogen with the surface and its effect on the surface electronic quality.

III.6. References

- [1] D. C. Streit, "Advance Progress of Twelfth International Conference On Indium Phosphide and Related Materials," May 14-18, IEEE, Williamsburg, VA, p. 11. (2000).
- [2] Y. Chun, T. Sugaya, Y. Okada, and M. Kawabe, "Low Temperature Surface Cleaning of InP by Irradiation of Atomic Hydrogen," *Jpn. J. Appl. Phys.* **32**, Part 2, L287-L289 (1993).
- [3] F. Ciccacci, S. De Rossi, and D. M. Campbell, "Low energy Mott polarimetry of electrons from negative electron affinity photocathodes," *Rev. Sci. Instrum.* **66**, 4161-4165 (1995).
- [4] E. Petit, F. Houzay, and J. Moison, "Interaction of atomic hydrogen with native oxides on InP(100)," *Surf. Sci.* **269/270**, 902-908 (1992).
- [5] T. Kikawa, I. Ochiai, and S. Takatani, "Atomic hydrogen cleaning of GaAs and InP surfaces studied by photoemission spectroscopy," *Surf. Sci.* **316**, 238-246 (1994).
- [6] D. Gallet, G. Hollinger, C. Santinelli, and L. Goldstein, "In situ characterization of InP surfaces after low-energy hydrogen ion cleaning," *J. Vac. Sci. Technol. B* **10**, 1267-1272 (1992).
- [7] C. M. Rouleau and R. M. Park, "GaAs substrate cleaning for epitaxy using a remotely generated atomic hydrogen beam," *J. Appl. Phys.* **73**, 4610-4613 (1993).
- [8] Z. Yu, S. L. Buczkowski, N. C. Giles, and T. H. Myers, "Defect reduction in ZnSe grown by molecular beam epitaxy on GaAs substrates cleaned using atomic hydrogen," *Appl. Phys. Lett.* **69**, 82-84 (1996).

- [9] K. A. Elamrawi, M. A. Hafez, and H. E. Elsayed-Ali, "Atomic hydrogen cleaning of InP(100) for preparation of a negative electron affinity photocathode," *J. Appl. Phys.* **84**, 4568-4572 (1998).
- [10] W. Widdra, S. I. Yi, R. Maboudian, G. A. D. Briggs, and W. H. Weinberg, "Adsorption, abstraction, and pairing of atomic hydrogen on Si(100)-(2×1)," *Phys. Rev. Lett.* **74**, 2074-2077 (1995).
- [11] E. Pehlke and P. Kratzer, "Density-functional study of hydrogen chemisorption on vicinal Si(001) surfaces," *Phys. Rev. B* **59**, 2790-2800 (1999).
- [12] C. Su, C.-S. Tsai, C.-E. Lin, K.-H. Chen, J.-K. Wang, and J.-C. Lin, "Interaction of atomic hydrogen with a Ge(111) surface: Low-energy electron diffraction and surface Raman studies," *Surf. Sci.* **445**, 139-150 (2000).
- [13] N. Kondo, Y. Nanishi, and M. Fujimoto, "Surface cleaning of AlGaAs substrates by hydrogen electron cyclotron resonance (ECR) plasma," *Jpn. J. Appl. Phys.* **31**, Part 2, L913-L915 (1992).
- [14] G. R. Bell, N. S. Kaijaks, R. J. Dixon, and C. F. McConville, "Atomic hydrogen cleaning of polar III-V semiconductor surfaces," *Surf. Sci.* **401**, 125-137 (1998).
- [15] J. M. Moison, Y. I. Nissim, and C. Licoppe, "Stabilization and removal of the native oxides at the surface of (100)InP by low-pressure exposure to NH₃," *J. Appl. Phys.* **66**, 3824-3830 (1989).
- [16] C. Licoppe, J. M. Moison, Y. I. Nissim, J. L. Regolini, and D. Bensahel, "Surface reactions of silane with oxidized InP and their application to the improvement of chemical vapor deposition grown, InP-based metal-insulator-semiconductor devices," *Appl. Phys. Lett.* **53**, 1291-1293 (1988).

- [17] M. G. Lagally, D. E. Savage, and M. C. Tringides, "*Reflection high-energy electron diffraction and reflection imaging of surfaces*," edited by P. K. Larson and P. J. Dobson, Vol. 188, p. 139, Plenum Press, New York (1988).
- [18] P. R. Pukite, J. M. Von Hove, and P. I. Cohen, "Sensitive reflection high-energy electron diffraction measurement of the local misorientation of vicinal GaAs surfaces," *Appl. Phys. Lett.* **44**, 456-458 (1984).
- [19] C. S. Lent and P. I. Cohen, "Diffraction from stepped surfaces: I. Reversible surfaces," *Surf. Sci.* **139**, 121-154 (1984).
- [20] I. Suemune, Y. Kunitsugu, Y. Kan, and M. Yamanishi, "Incidence angle effect of a hydrogen plasma beam for the cleaning of semiconductor surfaces," *Appl. Phys. Lett.* **55**, 760-762 (1989).
- [21] R. U. Martinelli and D. G. Fisher, "The application of semiconductors with negative electron affinity surfaces to electron emission devices," *Proc. IEEE* **62**, 1339-1360 (1974).
- [22] C. I. Wu and A. Kahn, "Electronic states and effective negative electron affinity at cesiated *p*-GaN surfaces," *J. Appl. Phys.* **86**, 3209-3212 (1999).
- [23] R. U. Martinelli, "Reflection and transmission secondary emission from silicon," *Appl. Phys. Lett.* **17**, 313-314 (1970).
- [24] W. Mönch, "Chemisorption-induced defects at interfaces on compound semiconductors," *Surf. Sci.* **132**, 92-121 (1983).
- [25] K. A. Elamrawi, M. A. Hafez, and H. E. Elsayed-Ali, "Atomic hydrogen-cleaned GaAs(100) negative electron affinity photocathode: Surface studies with

- reflection high-energy electron diffraction and quantum efficiency," J. Vac. Sci. Technol. A **18**, 951-955 (2000).
- [26] G. W. Wicks, E. R. Rueckwald, and M. W. Koch, "Analysis of cracking efficiency of an atomic hydrogen source, and its effect on desorption of $\text{Al}_x\text{Ga}_{1-x}\text{As}$ native oxides," J. Vac. Sci. Technol. B **14**, 2184-2186 (1996).
 - [27] F. Ciccacci and G. Chiaia, "Comparative study of the preparation of negative electron affinity GaAs photocathodes with O_2 and with NF_3 ," J. Vac. Sci. Technol. A **9**, 2991-2995 (1991).
 - [28] W. A. Gutierrez, H. D. Pommerrenig, and S. L. Holt, "Secondary electron emission from GaAs," Appl. Phys. Lett. **21**, 249-250 (1972).
 - [29] R. U. Martinelli, M. L. Schultz, and H. F. Gossenberger, "Reflection and transmission secondary emission from GaAs," J. Appl. Phys. **43**, 4803-4804 (1972).
 - [30] S. A. Chalmers, A. C. Gossard, P. M. Petroff, J. M. Gaines, and H. Kroemer, "A reflection high-energy electron diffraction study of (100) GaAs vicinal surfaces," J. Vac. Sci. Technol. B **7**, 1357-1362 (1989).
 - [31] K. M. Horn, J. Y. Tsao, E. Chason, D. K. Brice, and S. T. Picraux, "Hydrogen ion beam smoothening of Ge(001)," J. Appl. Phys. **69**, 243-249 (1991).
 - [32] Z. H. Zhang, B. Lin, X. L. Zeng, and H. E. Elsayed-Ali, "Surface morphology of laser-superheated Pb(111) and Pb(100)," Phys. Rev. B **57**, 9262-9269 (1998).
 - [33] S. W. Robey, "Development of surface morphology during H_2 plasma processing of GaAs(001)," American Vacuum Society Symposium, Baltimore, MD, November 2-6, p. 133. (1998).

CHAPTER IV

GROWTH OF INDIUM ON Si(100)-(2×1) BY FEMTOSECOND PULSED LASER DEPOSITION

IV.1. Introduction

Growth of group-III metals on Si surfaces has been the subject of many theoretical and experimental studies due to its fundamental and technological interests. Many studies have focused on structure determination and behavior of group-III induced reconstructions on Si surfaces [1-5]. It has been observed that group-III metals grown on Si form self assembled nanowires and nanoclusters with potential applications in devices [6-8]. Moreover, understanding the growth of group-III metals is important in metallization applications and in the growth of III-V and III-IV semiconductors on Si [9, 10]. The study of the initial growth modes of group-III metals on Si surfaces and the subsequent film morphology development is important for further developments in electronic and optoelectronic devices.

Indium was previously grown on Si(100)-(2×1) using molecular beam epitaxy (MBE) and conventional evaporation [11-15]. In these studies, the growth was observed by low-energy electron diffraction (LEED), scanning tunneling microscopy (STM), reflection high-energy electron diffraction (RHEED), time-of-flight impact collision ion scattering spectroscopy (ICISS), and Auger electron spectroscopy (AES). Indium was found to grow on clean Si(100) surfaces through the Stranski-Krastanov (SK) mechanism in which the initially deposited In nucleates and grows two dimensionally (2D) up to a coverage of between two and three monolayers (ML), depending upon the substrate

temperature (T_s), after which three-dimensional (3D) islands were formed. Growth of In on Si(100)-(2×1) surfaces induces different surface reconstructions depending on the In coverage and T_s . Results showed that the In(2×2) was the main structure observed in the initial growth of In on Si(100)-(2×1) below 150 °C. STM studies showed that Al, Ga, and In initially form long one-dimensional ad-dimers on the Si(100)-(2×1) surface [3, 5]. This growth mode continued until the (2×2) structure was completed at 0.5 ML (monolayers) [1 ML = 6.8×10^{14} atoms/cm² for unreconstructed Si(100) surface] [2, 16, 17]. Other submonolayer phases of Al and In deposited on a wide terrace single domain Si(100)-(2×1) were also observed using LEED [4]. For surfaces annealed at ~100 °C following deposition at room temperature (RT), sequences of (2×3) and (2×5) LEED patterns at ~0.3 and ~0.4 ML, respectively, were observed before forming the In(2×2) reconstruction [4]. It has been found by STM that a strained In(2×1) structure grew as flat 2D islands above a coverage of 1 ML on the initial In(2×2) layer [18]. The further deposition of In led to the formation of 3D islands at coverage above ~3 ML in order to accommodate the strain in the film resulting from the ~15% lattice mismatch between In and Si [11]. Thin film deposition conditions were previously observed to affect the strain relaxation during film growth [19, 20]. Therefore, the morphology of the grown film depends on the growth conditions, as well as on the substrate orientation and lattice mismatch [21-25].

Compared with surface microscopy techniques, surface electron diffraction, such as RHEED, probes a large area (e.g., 1 mm²). Thus, diffraction provides information on the structure and morphology averaged over the probed area and can provide quantitative information on average values, which can be used to study growth kinetics [26]. During deposition, RHEED provides real time information on nucleation and monolayer

formation. For example, the growth transition from layer-by-layer to step flow mode on vicinal surfaces has been used to estimate diffusion parameters from RHEED observations [27, 28]. The recovery of the RHEED intensity after interruption of MBE growth has been used to study the film growth kinetics [29-35].

Growth of In on Si(100)-(2×1) at high temperatures results in the formation of well ordered In(4×3) superlattice [1, 11, 36, 37]. For In coverage of ~0.15 ML, the In(4×3) surface grown on Si(100)-(2×1) at 500 °C was identified to be composed of nearly identical-size nanoclusters randomly distributed. The In(4×3) surface became ordered arrays at ~0.5 ML In coverage [38]. The structural and electronic properties of these nanoclusters show that they have potential for future nanoscale and electronic device applications [39-42].

The In(4×3) surface phase was studied by AES, RHEED, LEED, STM, ICISS, and x-ray diffraction [1, 11, 36, 37, 43-47]. The In(4×3) structural model has been a subject of debate. Theoretical and experimental studies using first principle total energy calculations, STM image simulations, and photoelectron holography were performed to solve the structural model of the In(4×3) on Si(100) [48-50]. Their results favored the x-ray diffraction analysis by Bunk et al. [46], in which the (4×3) unit cell comprises a stable pyramid-like Si₇In₆ cluster. Results showed that the initial structure is a mix of In(4×3) and Si(2×1) until the surface becomes fully In(4×3) at a coverage of 0.5 ML. Using STM, Baski et al. [1] suggested that the growth of the In(4×3) at 0.5 ML In is accompanied by displacement of the underlying Si surface atoms. Knall et al. [11, 37] grew In on nominally flat Si(100)-(2×1) surfaces by molecular beam epitaxy (MBE) and observed the In(4×3) phase by RHEED and LEED for $T_s = 150-600$ °C. For In coverages > 2 ML,

the (4×3) surface was decorated with three-dimensional (3D) islands or replaced by a disordered phase. This transition between the (4×3) + 3D islands morphology to a disordered 2D layer + 3D islands occurred as T_s was raised above ~ 450 °C. Scanning electron microscopy (SEM) showed hemispherical-shaped islands grown on the $\text{In}(4\times 3)$ surface at 15 ML of In. Changes in surface morphology induced by adsorption of In on $\text{Si}(100)-(2\times 1)$ surfaces were studied by STM and low energy electron microscopy (LEEM) [51, 52]. The (4×3) structure was found to transform to a (4×1) structure when the $\text{Si}(100)\text{-In}(4\times 3)$ surface was exposed to atomic hydrogen at 300 °C and at room temperature [53, 54]. In addition, the film morphology was changed from 2D layers to In clusters.

Compared with MBE and conventional evaporation sources, pulsed laser deposition (PLD) technique produces highly energetic species with high instantaneous deposition rates [55]. The energetic species in PLD increases the deposits' surface diffusion and promotes epitaxy. The high nucleation density of deposits in PLD improves 2D growth, and this property has led to growth of high quality metallic thin films [56, 57]. An imposed 2D growth mode due to the pulsed nature of PLD followed by a relaxation time has been demonstrated [58]. RHEED intensity modulation by each deposition laser pulse was used to estimate the surface diffusion parameters [59]. The effects of deposition of In on Si at RT by PLD on the initial layers growth and the film morphology need to be studied. While most published studies focused on the determination of surface phases induced by submonolayer of In on Si, the kinetic parameters and morphology changes during growth of $\text{In}(4\times 3)$ need further study. Growth of In on $\text{Si}(100)$ by femtosecond pulsed laser deposition (fsPLD) at high

temperatures can be used to investigate the effect of PLD characteristics on the growth mode and kinetics of In(4×3) formation.

In this chapter, the study of In growth on vicinal Si(100)-(2×1) surface by fsPLD is presented in two sections, namely IV.5.1 and IV.5.2. In section IV.5.1, fsPLD is used to grow In on vicinal Si(100)-(2×1) below In melting point (156.6 °C), mainly at RT. Real-time RHEED is used to observe the in-plane lattice spacing and the growth morphology by monitoring the profiles of the diffracted spots. The initial growth structure and the In island morphology were studied and related to the growth kinetics by fsPLD. The diffusion parameters of deposited In on surface terraces were investigated by quantitative RHEED. The intensity and full width at half maximum (FWHM) of the RHEED specular beam were measured during In growth. The grown film morphology was examined by ex situ atomic force microscopy (AFM) and STM.

In section IV.5.2, study of In growth on a Si(100)-(2×1) surface was performed in the temperature range of 350-420 °C. RHEED was used to probe the growth dynamics of In(4×3) on Si(100)-(2×1). The film morphology was examined ex situ with AFM and STM. The activation energy and diffusion frequency for the formation of In(4×3) were estimated from the RHEED intensity relaxation at In coverage of ~0.5 ML. The terrace width dynamics was studied at different deposition conditions to investigate the associated surface processes during the growth of In(4×3). The variation in the average terrace width with In coverage and its effect on the growth mode and morphology were examined.

IV.2. Thin film nucleation and growth

Growth of thin films from the gas phase is essentially a non-equilibrium phenomenon governed by a competition between kinetics and thermodynamics [60]. Understanding the initial stages of film growth and the nucleation mechanisms can give the capability to control the deposition and, thus, the properties of the grown films. Structural defects at surfaces might play a predominant role in many surface processes such as adsorption, surface diffusion, chemical reaction, and thin film growth [61]. Most surface defects can be illustrated schematically in terms of the terrace-step-kink (TSK) model, Fig.4.1. The TSK model can be applied to crystal growth, surface diffusion, and roughening [61, 62]. The relative number of defects such as vacancies, step kinks, and adatoms depend on their formation energies and on the temperature. Defects such as ledges, kinks, dislocations, and point defects modify the binding energy of an adatom to the surface and hence modify nucleation.

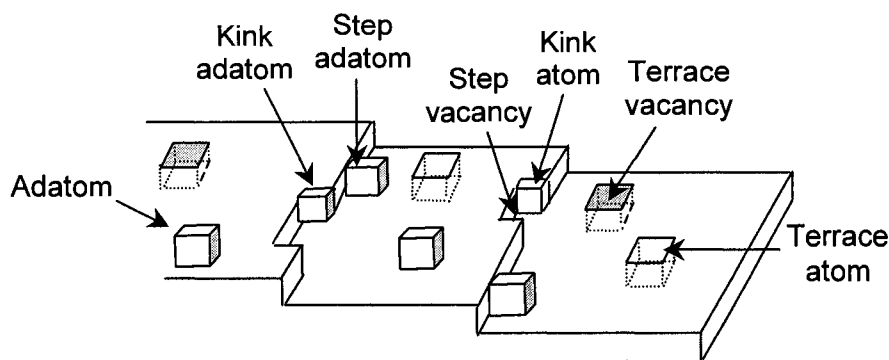


FIG. 4.1. TSK model showing atomic sites and defects on a surface of a simple cubic crystal. Each atom in the lattice is represented by a cube and has a certain number of nearest neighbors (its coordination numbers). The TSK model is based upon the idea that the energy of an atom on the surface is determined by its bonding to the neighboring atoms and that transition involves the counting of broken and formed bonds [61].

There are three primary modes of film growth on substrates; 3D islands growth (Volmer-Weber), 2D layer-by-layer growth (Frank-Van der Merwe), and a mixture of 2D and 3D growth (Stranski-Krastanov). The occurrence of different growth modes is qualitatively attributed to the surface or interface energy [62]. In addition, surface diffusion energy is a key element in determining the growth mode [63]. It gives rise to nucleation of islands on substrate terraces or step flow growth at elevated temperatures [64]. The transition temperature at which the growth changes from layer-by-layer to step flow depends on the surface diffusion as well as the terrace width and the deposition rate.

Surface processes responsible for nucleation and growth of thin films on a substrate depend on several factors such as deposition rate, roughness and crystalline properties of the substrate, and temperature. The film growth is affected by the supersaturation $S = p/p_e$ and thermodynamic driving force $\Delta\mu = (k_B T \ln S)$, where k_B is the Boltzmann's constant, T is the absolute temperature of the vapor source, p is the vapor pressure, p_e is the equilibrium vapor pressure [62]. $\Delta\mu$ is zero in equilibrium, is positive during condensation, and negative during sublimation or evaporation. The deposition rate or flux R is related, using kinetic theory, to p as $R = p/(2\pi m k_B T)^{1/2}$, where m is the atomic mass. Monte Carlo calculations of 0.25 ML deposition on terraces under different supersaturations, at the same temperature, shows that when growth does occur, it proceeds through nucleation and growth stages, with monolayer thick islands (pits) having to be nucleated before growth can proceed [65]. Atoms arriving from the vapor at a rate R can adsorb on the surface, becoming adatoms. The adsorption residence time τ_{ad} is determined by the adsorption energy, E_{ad} , and is given by

$$1/\tau_{ad} = \nu_{ad} \exp(-E_{ad}/k_B T), \quad (4.1)$$

where ν_{ad} specifies a pre-exponential factor as an atomic vibration frequency. During the residence time, adatoms diffuse over the surface with diffusion energy E_d and diffusion coefficient D . It is expected that $E_d < E_{ad}$. If desorption process will take place, E_{ad} will denote as a desorption energy and τ_{ad} is the adatom lifetime before desorption. Adatoms diffusion is derived from considering a random walk in 2D, and the 2D diffusion coefficient is given by

$$D = D_0 \exp(-E_d/k_B T), \quad (4.2)$$

where $D_0 = [\nu_0 (a_d)^2/4]$ is the diffusion coefficient constant corresponding to the pre-exponential and a_d is the jump distance of the order of the surface repeat distance. The number of substrate sites visited by an adatom in time τ_{ad} is $D\tau_{ad}/N_0$, where N_0 is the areal density of such sites, of the same order as $(a_d)^{-2}$. In the case of thin film growth on vicinal surfaces and using a simple model for surface diffusion based on the Einstein relation, assuming no anisotropy, then [27]

$$\ell = (2D\tau_{ad})^{1/2} \quad (4.3)$$

where ℓ is the mean displacement distance of the adatom from the arrival site before capture (or desorption).

Both experiment and theory show evidence that surface diffusion can occur by different atomistic mechanisms such as hopping, atomic exchange, tunneling, and vacancy mechanism [61]. Surfaces of different crystallographic orientation have different atomic structures, which cause orientation anisotropy of surface diffusion. Other kinds of diffusion anisotropy occurred when the diffusion coefficient depends on the direction at the surface, directional anisotropy. In their diffusion over the surface, the adatoms might become captured by existing clusters or at defect sites such as steps, Fig.4.2(a) and (b). In

another process, the adatoms might combine with one another. Depending on the size of the binding energy between these atoms, and on their areal density, they will form small clusters, which may then grow to form large clusters of atoms on the surface, in the form of 2D or 3D islands, Fig.4.2(a). This binding energy and the energy of the critical cluster are important to understanding of nucleation and growth processes on surfaces. Nucleation of clusters and atom attachment to islands depends on the coverage and deposits activation energy.

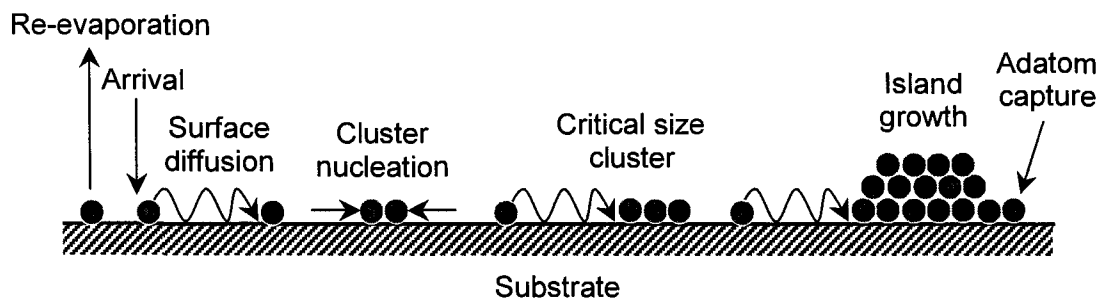


FIG. 4.2(a). Surface processes involved in 3D nucleation and film growth. The incoming flux of film species first thermally accommodated with the substrate. The adatoms then diffuse on the surface to interact with adatoms or re-evaporate. Surface diffusion leads to nucleation of clusters, such as metastable and critical size clusters, and continue to grow in size and became islands and film growth.

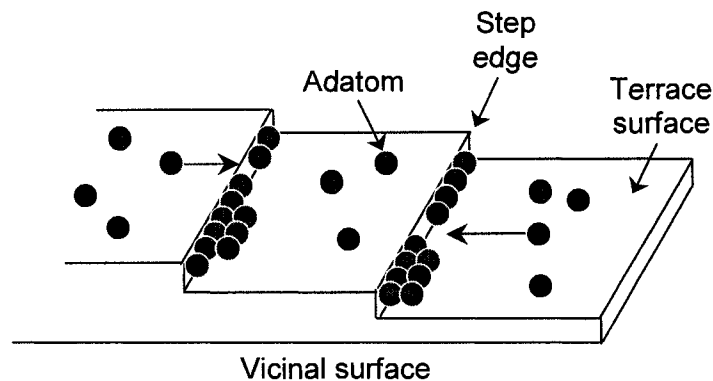


FIG. 4.2(b). Growth on vicinal surface. Surface steps can act as a sink for deposits where the adatoms are incorporated under the step flow growth mode. Adatom can move on the terrace through a horizontal jump or move from terrace to lower level through a vertical jump.

IV.3. Femtosecond pulsed laser deposition

PLD is used for growing a wide variety of thin films and nanoscale particles [55, 66]. Study of laser ablation and thin film deposition processes in the PLD are important for the sake of understanding the physics behind them and achieving high quality thin films. PLD has been shown to provide a high nucleation density of deposits and improve 2D growth [56]. PLD produces highly energetic species with high instantaneous deposition rates, which have the potential to assist in crystalline phase formation in thin films [55, 66]. These characteristic features of PLD can alter the thin film properties. A theoretical study of growth for Ag/Ag(111) indicated that increasing the incident atom energy from 0.1 to 10 eV changed the growth from 3D to layer-by-layer growth, through enhanced diffusion of surface atoms from unstable positions to stable positions [67]. In a molecular dynamics simulation, an incident energetic Si atomic beam on Si(100) and Si(111) surfaces induced local surface heating and formed a crystalline film, at less than half the absolute temperature required for thermal adatoms [68].

Compared to longer laser pulses, fs laser significantly alters the processes associated with the ablation [69]. The fs laser pulse duration is shorter than the electron phonon coupling, the conventional thermal deposition is significantly limited, and the ablation can be considered as direct solid-vapor (or solid-plasma) transition [56]. In addition, the limited heating of the surrounding lattices of the target is useful for controlled material removal. The fs laser is characterized by the high radiation intensity that has the ability to create high-density plasmas [55]. The use of fs lasers has been proposed as a possible solution to overcome the occurrence of droplets often observed in classical nanosecond PLD due to thermal effects at the target surface [70, 71]. Therefore,

using a fsPLD, the formation of particulates can be minimized or eliminated and thus improves the grown thin film quality.

For metals, the optical absorption depth is smaller than the thermal diffusion length in contrast to ceramic materials [56]. The thermal diffusion length L_{th} is given by $L_{th} = (\kappa \tau_L)^{1/2}$, where κ is the thermal diffusion constant, and τ_L is the pulse length. The energy from the laser pulse will be first transferred into the absorption layer, and then thermally transported to the level of thermal diffusion length, which is proportional to $(\tau_L)^{1/2}$. The high thermal conductivity of metals results in a large energy loss by heat diffusion into the bulk during the laser pulse. This leads to dissipate thermal energy outside the laser spot and resulting in modification of the material structure. Using fs laser pulses, heat diffusion into the material is negligible and the energy loss during the laser pulse is minimized. Consequently, the rapid energy accumulates in limited optical volume and the ablation take place. Therefore, fs laser has a higher efficiency of ablation than nanosecond laser pulses. The ablation threshold fluence for solid In decreases by a factor of 40 from 100 mJ/cm² to 2.5 mJ/cm² when a 0.5 picosecond pulse is used instead of a 15 nanosecond laser pulse [72]. Another distinctive feature of the ultra short interaction mode is that the energy transfer time from the electrons to ions by Coulomb collisions is significantly longer (picoseconds) than the laser pulse duration (~100 fs). Therefore, the conventional hydrodynamics motion does not occur during the fs interaction time [73].

IV.4. Experiment

The thin films deposition was performed in an ultrahigh-vacuum (UHV) PLD system, Fig. 4.3. The UHV is achieved using mechanical (Varian-rotary van type), turbomolecular (Varian-70 l/s), and ion (Perkin-Elmer TNB-X system-220 l/s) vacuum pumps. Bakeout of the PLD vacuum chamber was carried out in the range of 200-250 °C to desorb of water molecules from internal surfaces. Degassing the filaments of the internal vacuum components is performed during the bakeout. Residual gas analyzer (RGA) (Model: RGA 200-Stanford research systems) is a mass spectrometer that is connected directly to the vacuum system to monitor the gases inside the vacuum chamber. The base pressure during deposition was in the low 10^{-9} Torr range.

The femtosecond laser system (spectra-physics) consists of four main units; diode-pumped continuous laser, mode-locked Ti:sapphire laser oscillator, multikilohertz intra-cavity doubled Nd:YLF laser, and multikilohertz pulsed Ti:sapphire amplifier. The amplified Ti:sapphire laser, (pulse width ~130 fs FWHM) operating at a wavelength of 800 nm and a repetition rate in the range of 1-50 Hz, was used to ablate the In target. The laser was incident on a 99.99% pure In target at $\sim 45^\circ$, and focused on the In target using a convex lens with a 30-cm focal length. The target was rotated at a speed of ~ 2 revolutions per minute in order to minimize particulate formation. The target-to-substrate distance was fixed at ~ 5 cm. RHEED was used to observe the surface structure of the substrate and the film growth during deposition. The RHEED electron gun was operated at electron energy of 8.6 keV. A charge-coupled device (CCD) camera was used to image the diffraction patterns. Real time evaluation of the intensity and FWHM of the RHEED beams were performed and correlated with the deposition conditions. RHEED analyses

along and across the diffracted beams were obtained in the reciprocal space and then converted to length scales after taking into account the instrumental response. The uncertainties in the electron energy and the RHEED camera length were determined by measuring the in-plane lattice parameter of the Si(100) surface. The surface morphology of the In films was imaged and characterized ex situ with a non-contact AFM and STM.

The $\sim 5 \times 10$ mm Si substrates were cut from a low-resistivity Si(100) wafer (p-type, boron-doped, 500- μm thick, 0.01-0.03 ohm-cm resistivity). The Si surfaces were misoriented from the low-index (100) plane by 1.0° towards the $\langle 110 \rangle \pm 0.5^\circ$. The Si(100)-(2 \times 1) surface was prepared by chemical etching just prior to being loaded into the UHV chamber. This was followed by in situ heat cleaning to 600 $^\circ\text{C}$ for several hours using direct current, then flash heating at ~ 1100 $^\circ\text{C}$ to remove native oxides and carbon. A manual rotatable shutter was used between the target and the substrate to minimize heat transfer to the In target. Just prior to In deposition, the Si(100)-(2 \times 1) was raised in temperature to ~ 1000 $^\circ\text{C}$ for ~ 2 minutes by direct-current heating. During flash heating of the substrate the chamber pressure was in the low 10^{-8} Torr. The heating was then terminated and the substrate cooled down to the growth temperature. RHEED patterns acquired after annealing were characteristic of clean reconstructed Si(100)-(2 \times 1).

Calibration of the deposition rate per laser pulse was accomplished using the phenomenon of RHEED intensity oscillations, which provides a highly accurate method of obtaining film thickness. RHEED oscillations were observed at substrate temperatures near the melting point of In. Thus, we performed several depositions at this condition to observe RHEED oscillations. The deposition rate was estimated to be ~ 0.05 ML/pulse. This was confirmed by a post deposition estimate of film thickness using a profilometer.

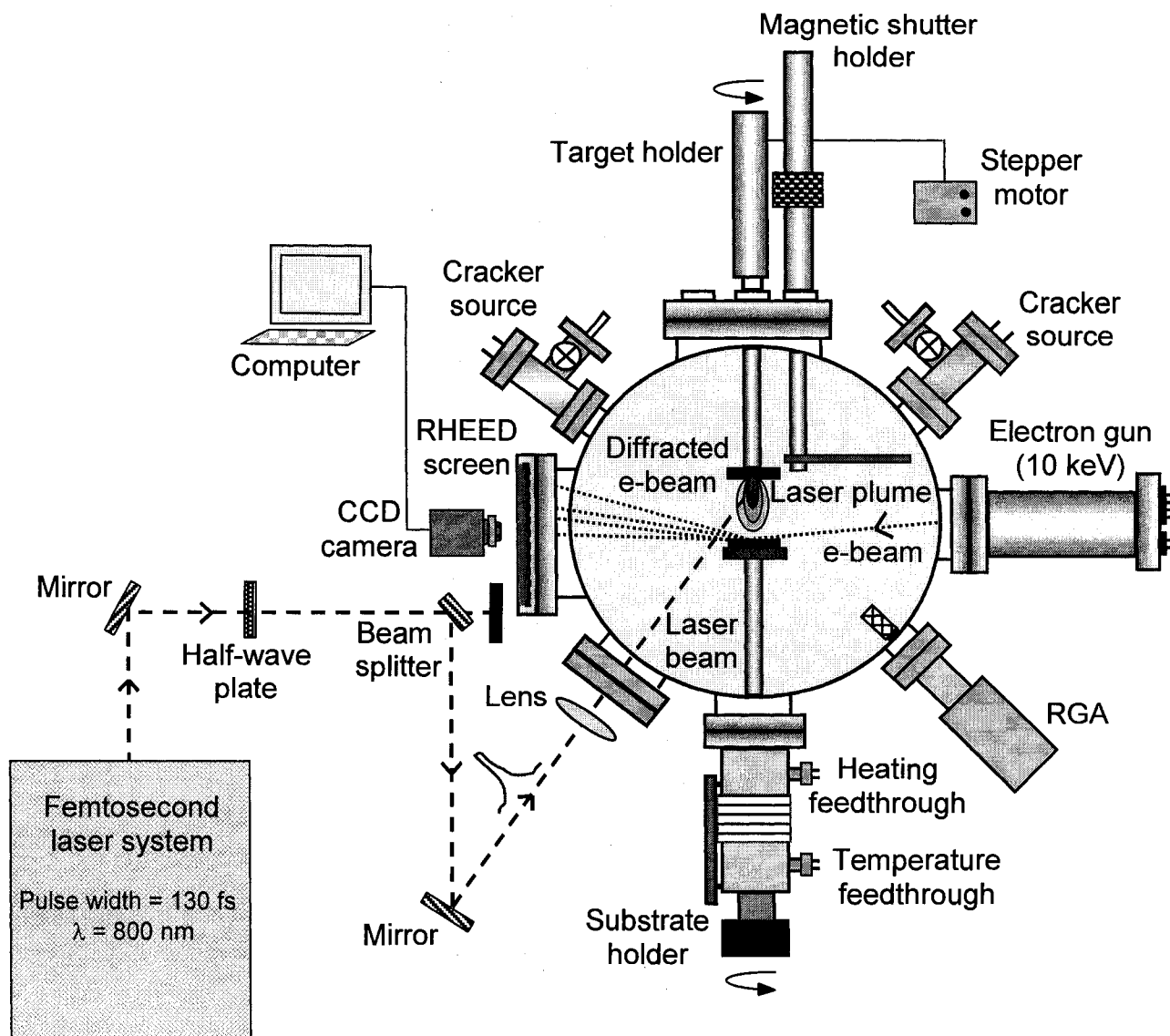


FIG. 4.3. Schematic diagram of the PLD experimental set up and components arrangement.

IV.5. Results and discussion

IV.5.1. Growth of In on Si(100)-(2×1) at room temperature

IV.5.1.1. Growth mode and morphology

IV.5.1.1.1. General observations by RHEED

Just prior to In deposition, the Si(100)-(2×1) was raised in temperature to ~1000 °C for ~2 min by direct-current heating. The heating was then terminated and the substrate cooled down to RT. The RHEED pattern acquired after this annealing showed clean reconstructed Si(100)-(2×1) with less RHEED background, indicating a smooth well-ordered surface, as shown in Fig. 4.4(a). The pulsed laser deposition of In was then begun with the Si substrate kept at RT. The laser was operated at a 2 Hz repetition rate and a fluence of 0.5 J/cm² on the In target. When the RHEED electron beam directed down the staircase of the vicinal Si surface, along the [011] azimuth, the (2×1) structure was observed to preserve for ~100 s of deposition. Figure 4.4(a) shows the RHEED patterns of the In film taken during the first 20 s (corresponds to ~2 ML). No other RHEED structure, such as the (2×2), has been observed in the fsPLD of In on Si(100)-(2×1). It was observed that In formed different RHEED structure on Si(100)-(1×1) surface during substrate heating, Fig. 4.4(b). This In film caused by convection heating of the Si substrate. Next, by using a laser repetition rate of 1 Hz and a laser energy density of 0.3 J/cm², the same behavior of initially maintaining the (2×1) RHEED structure during In growth for ~330 s was observed in the [011] azimuthal direction. This indicates that In deposits initially form in a 2D In(2×1) structure. By directing the electron beam along the [013] azimuthal direction, no additional reflection or transmission RHEED

features were observed. Figures 4.4(c) shows RHEED patterns before and after 400 s of In deposition (the laser was operated at 1 Hz and 0.5 J/cm^2), respectively. With continued In deposition, the integral and half-order RHEED streaks, intensities continuously decreased until the RHEED pattern became faint. These observations suggest that In growth on Si(100)-(2×1) by fsPLD follows the SK mode. This result is consistent with the previously reported MBE growth of In on Si(100)-(2×1) by the SK mode, where transmission diffraction spots were not observed in the RHEED patterns [11]. When In grew on Si following the Volmer-Weber (VW) growth mode, a transmission RHEED pattern was observed at low coverage [11, 15].

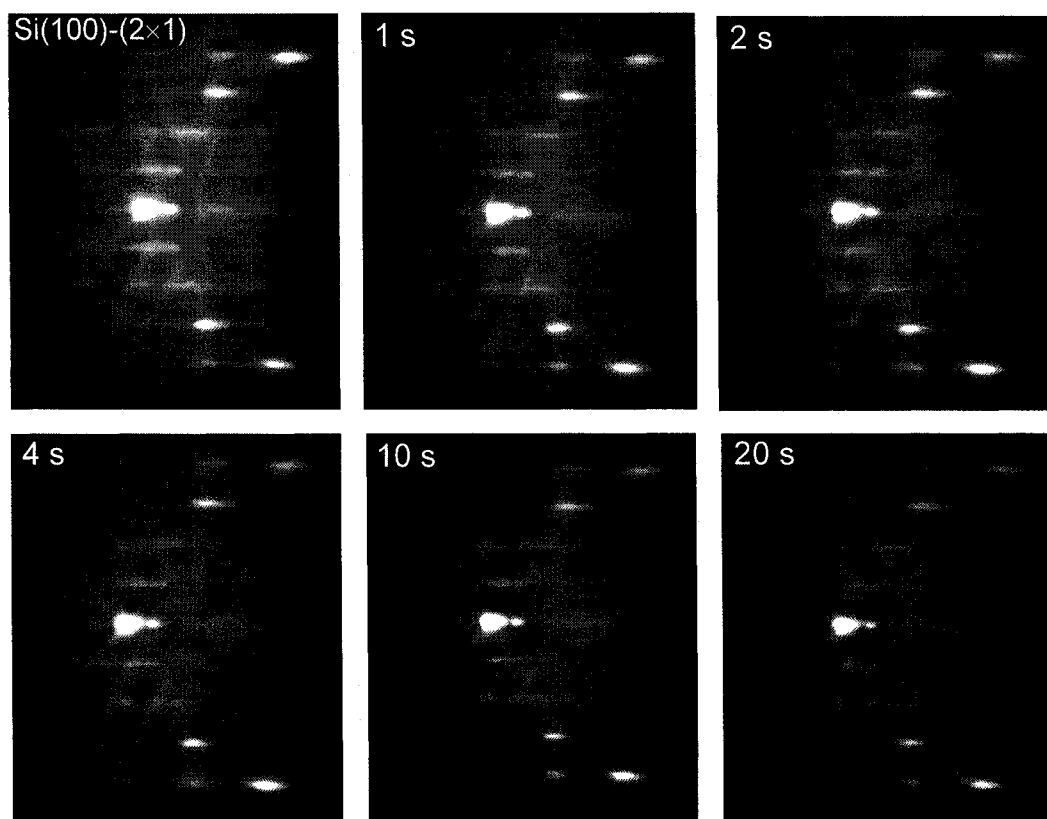


FIG 4.4(a). RHEED patterns of the Si(100)-(2×1) substrate surface and In film after deposition by fsPLD at different deposition time taken in the [011] azimuth down the Si vicinal surface. Deposition conditions were 2-Hz laser repetition rate and 0.5 J/cm^2 laser energy density.

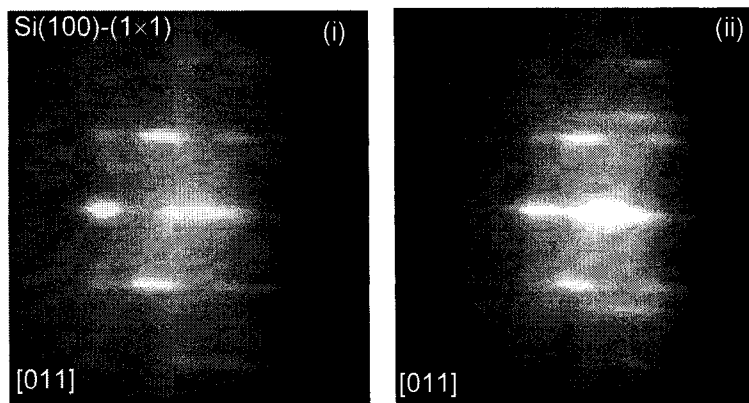


FIG. 4.4(b). (i) and (ii) are RHEED patterns of the Si substrate and In film, respectively, which formed by convection heating during heat cleaning of the Si substrate. During heating the Si, the shutter between the target and the substrate was opened. The additional RHEED streaks indicate the structure of the In film.

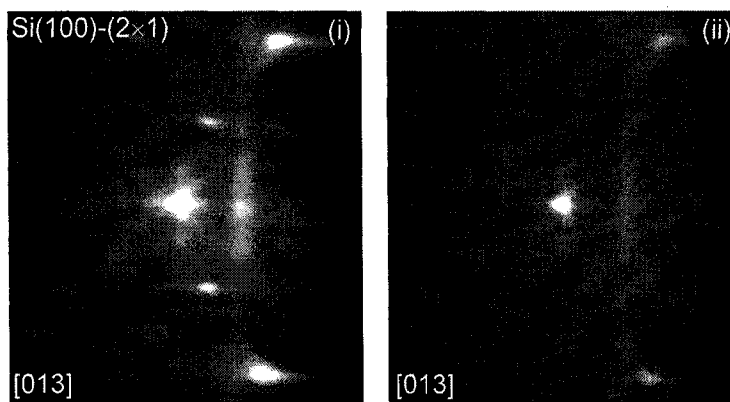


FIG. 4.4(c). (i) and (ii) are RHEED patterns of the Si(100)-(2x1) substrate surface before and after deposition time of 400 s of In by fsPLD, respectively. Deposition conditions were 1-Hz laser repetition rate and 0.3 J/cm^2 laser energy density.

IV.5.1.1.2. Film in-plane lattice spacing

We have used in situ RHEED to investigate the change in the film-lattice parameter during In growth on Si(100)-(2×1) by fsPLD. The surface-lattice constant, and hence the surface strain, is inversely proportional to the separation of the RHEED streaks. The strain relaxation during the growth was determined from in-plane lattice spacing as a function of time. The in-plane lattice spacing, measured from the separation of the first-order RHEED peaks, was monitored over time by the RHEED patterns taken in the [011] azimuthal direction of the Si surface. The intensity profiles of the $(\bar{1}0)$ and (10) peaks were fitted to Gaussian line shapes to obtain peak spacing with high precision. Then, the film strain was calculated according to the ratio $(a_{\text{In}} - a_{\text{Si}})/a_{\text{Si}}$, where a_{In} and a_{Si} are the measured lattice constants of the In film and the Si(100) surface, respectively.

Figure 4.5(a) shows the strain relaxation of the In film during the first 70 s. From our calculations, we obtain the in-plane lattice parameter of the Si surface $a_{\text{Si}} = 3.73 \text{ \AA}$, which is close to the known value, where the surface lattice parameter of Si(100) is 3.84 \AA . This calculation of the a_{Si} from RHEED is in agreement with the expected experimental errors, which come from uncertainty in the electron energy and the RHEED camera length. After a deposition time of 2 s, the in-plane lattice parameter decreased immediately by $\sim 2\%$. After this sudden in-plane lattice parameter decrease of the In film, the in-plane lattice parameter changed around a measured mean value of 3.65 \AA during the first 7 ML. The structure of the In bulk is face-centered tetragonal, and the lattice constant of the In(100) surface is 3.24 \AA . This indicates the formation of a 2D strained In(2×1) layer in the early stages of deposition. This strained layer was formed due to the lattice mismatch between the Si substrate and In and the difference in their crystal

structure. As shown in Fig. 4.5(b), the corresponding RHEED intensity of the specular beam as well as the higher-order $(\bar{1}0)$ and $(\frac{3}{2}0)$ beams decreased immediately after starting the In growth. The formation of the wetting In(2×1) layer of the surface was linked with the initial drop of the intensity. The intensities then decreased slowly, indicating development of some surface roughness due to growth of 2D In islands. The intensities were measured at the Bragg condition and the electron beam was incident along the [011] direction.

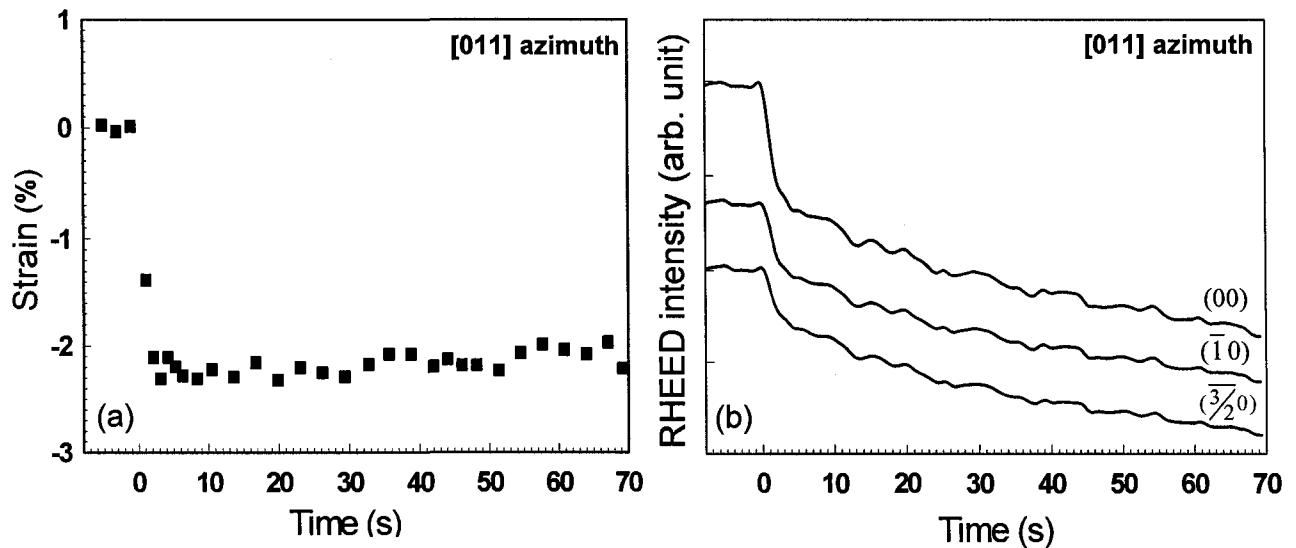


FIG 4.5. (a) The behavior of the strain during the deposition of In on Si(100)-(2×1) surface at RT in the first 70 s of the deposition time. The in-plane lattice parameter is calculated from the spacing between the $(\bar{1}0)$ and (10) diffraction RHEED streaks ([011] azimuth). At the beginning of the indium deposition, instant relaxation of ~2 % after 2 sec occurred. (b) RHEED intensities of the (00), $(\bar{1}0)$, and $(\frac{3}{2}0)$ beams taken in the [011] azimuth direction. Deposition conditions were 2-Hz laser repetition rate and 0.5 J/cm² laser energy density.

In the SK growth mode, for the initial wetting layer, the film in-plane lattice spacing changes during the growth toward its lattice constant. For the In/Si(100) system, Ryu et al. investigated the growth of In on a clean Si(100) surface at RT by STM and reported the formation of a 2D strained In layer with lattice spacing of roughly 4 Å [15]. Using STM, Kubo et al. observed a (2×1) periodicity of the In strained layer associated with a lattice spacing of 3.89 Å [18]. In our results, In adatoms formed a strained 2D layer that exhibited the (2×1) RHEED structure similar to Si(100)-(2×1), but with a different lattice parameter (3.65 Å). We have grown three samples of In thin film on Si(100)-(2×1) at RT, with each sample showing the same strain behavior, while the (2×1) structure remained. We did not observe other RHEED structures (such as 2×2) during the In growth. It was suggested previously that the In(2×1) strained layer plays an important role as the intermediate structure between 2D growth to 3D growth [18]. This In(2×1) layer affects the film-strain relaxation and therefore, the In islands' morphology. For instance, the size of the 2D islands, which nucleate on the top of the In(2×1) layer, could be increased before the growth mode changes to the 3D islands.

IV.5.1.1.3. FWHM of the RHEED specular beam

The FWHM of the specular beam is inversely proportional to the average surface coherence [74]. We monitored the width of the specular beam to observe the morphological changes in the In/Si(100) system. Figure 4.6 shows the deposition-time dependence of both full width at half maximum measured parallel to the electron beam ($\text{FWHM}_{//}$) and that perpendicular to the electron beam (FWHM_{\perp}) taken along and across the RHEED specular beam in the [011] azimuthal direction, respectively.

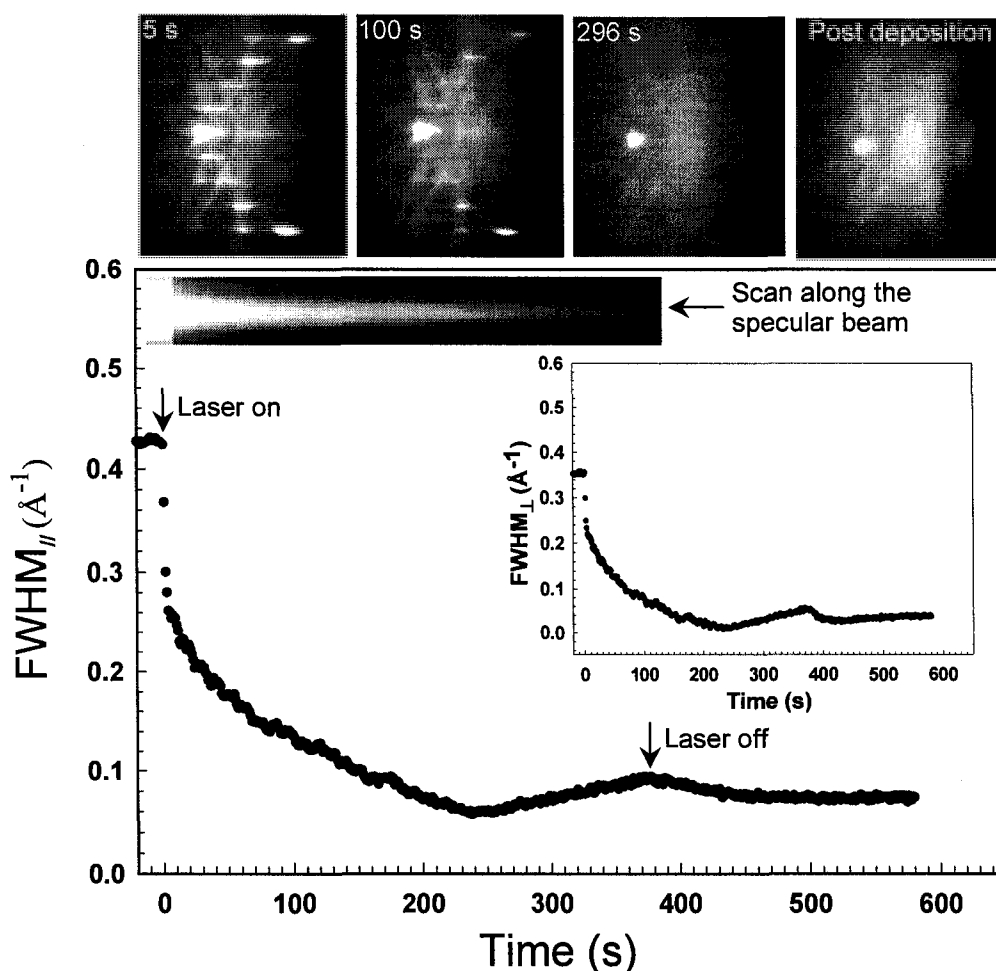


FIG. 4.6. The FWHM_{\parallel} taken along the (00) specular beam. The electron beam was incident in the [011] azimuth down the staircase of the vicinal Si surface. Deposition conditions were 2-Hz laser repetition rate and 0.5 J/cm^2 laser energy density. As deposition started, the FWHM_{\parallel} decreased for the first 240 s, indicating an increase of In islands size. The top inset figure shows the line track of the (00) beam width during the film growth. The FWHM_{\perp} across the (00) shows the same behavior as FWHM_{\parallel} , as seen in the inset figure. After a deposition time of 240 s, the FWHM_{\parallel} started to increase, indicating an increase of surface roughness. RHEED patterns taken in the [011] azimuth at time sequences of 5 s, 100 s, 296 s, and after terminating the deposition, are shown on top.

RHEED patterns taken during and after terminating the deposition are shown on the top. The deposition time of In on the Si substrate was 380 s. The FWHM was measured at the Bragg diffraction condition. As soon as the deposition started, the $\text{FWHM}_{//}$ dropped suddenly and began to decay at a slower rate with further deposition. After 70 s of deposition, the $\text{FWHM}_{//}$ was reduced to $\sim 22\%$ of its original value before deposition. The FWHM was calculated in the reciprocal lattice space by taking into account the instrumental responses of $0.24 \pm 0.014 \text{ \AA}^{-1}$ and $0.30 \pm 0.015 \text{ \AA}^{-1}$ parallel to and across the electron beam, respectively. After 230 s of deposition (film thickness of ~ 23 ML), the $\text{FWHM}_{//}$ decreased from an initial value of 0.42 \AA^{-1} to 0.06 \AA^{-1} , while the FWHM_{\perp} decreased from 0.35 \AA^{-1} to 0.01 \AA^{-1} . This indicates an increased average crystalline size and low edge roughness as In adatoms diffused to the islands' edges. However, above ~ 23 ML coverage, the FWHM started to increase while the specular beam intensity continued to decrease throughout the entire deposition time. Broadening of the FWHM and intensity loss of the (00) diffracted beam indicate a rougher surface as growth proceeded. The RHEED patterns of the In film (Fig. 4.6) show a decrease in the integral and fractional order intensities with deposition time, while the remaining (2 \times 1) structure changed to faint (1 \times 1) structure with a high RHEED background. The specular beam spot remained visible up to the termination of the deposition.

IV.5.1.1.4. Morphology of In film on Si(100)

An In film was grown on a Si(100)-(2 \times 1) substrate by fsPLD via interval deposition (deposition for a given amount of time followed by an interval of no deposition) to assist in increasing the 2D island density. A RHEED pattern of the 38 ML

In film obtained after a deposition time of 380 s is shown in Fig. 4.6. The RHEED pattern shows faint rings on a high background, indicating random in-plane crystallographic orientation. Figure 4.7(a) shows energy dispersive x-ray (EDX) spectrum performed to a sample prepared by fsPLD indicating an In peak of the thin film on Si substrate. Next, the morphology of the grown In film was examined ex situ using AFM. Figure 4.7(b-e) shows AFM images of the grown In film on the Si(100)-(2×1) substrate at RT that corresponds to the post-deposition RHEED pattern. The AFM images show 3D In islands, which are found at different surface locations. The examined location shows the growth of high-density In islands. Figure 4.7(c) is a magnified AFM image of Fig. 4.7(b), showing that the islands have an approximately similar hexagonal shape.

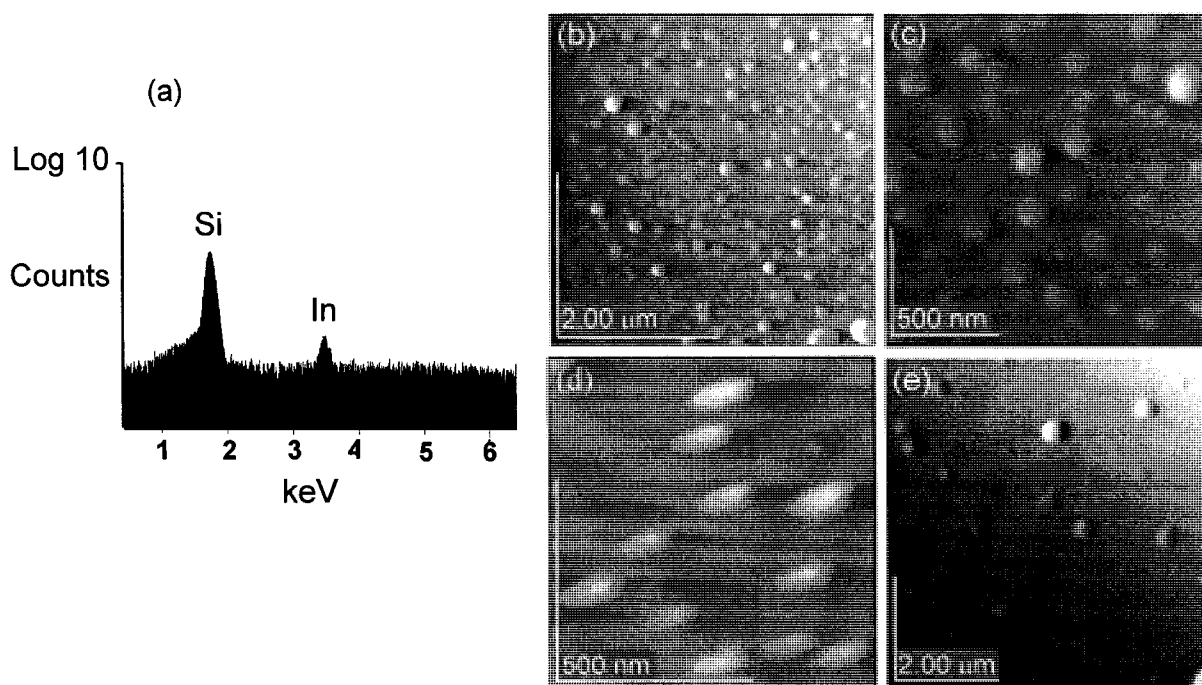


FIG. 4.7. (a) EDX spectrum showing peak of the resultant In film deposited by fsPLD on Si. AFM images of the grown In film on Si(100)-(2×1) substrate after deposition at RT by the fsPLD (corresponding to the post deposition RHEED pattern in Fig. 4.6): (b) AFM image of size 4 μm × 4 μm showing In islands located close to the middle of the sample; (c) magnified AFM image with size of 1.5 μm × 1.5 μm showing the indium islands have approximately similar hexagonal shapes; (d) elongated In islands found at different sample locations exhibiting preferential growth orientation; and (e) hemispherical islands were found close to the sample edges.

The formed In islands took a variety of shapes. Figure 4.7(c) is an example of elongated islands that grew at different locations on the sample surface. As seen in the AFM image, the elongated islands exhibit preferential growth orientation with respect to the Si substrate and the elongated islands' density is found to be less than the hexagonal ones. This type of island was previously shown to grow along the $[011]$ and $[01\bar{1}]$ directions on the Si(100)-(2 \times 1) surface [11]. As seen in the AFM image, the elongated 3D islands grew on a flat surface. This indicates that, as observed from the RHEED analysis, the morphology of the In film evolved from the flat film of the 2D layer up to the nucleation of the 3D islands. The hexagonal and elongated islands were distributed in the middle of the sample, where the PLD plume had its maximum flux.

By examining the In film morphology close to the sample edges, hemispherical island shapes were seen by the AFM, as shown in Fig. 4.7(d). These islands have a size in the range of 30-50 nm and an average height of 7 nm. Previously, it was found that spherical and hemispherical In islands were formed on hydrogen-terminated and contaminated Si(100)-(2 \times 1) surfaces, respectively [11, 15]. In this case, surface contamination acted as preferential nucleation sites and modified the growth mode from the SK mode to the VW mode. Kanal et al. [11] observed a transmission RHEED pattern from a contaminated Si(100)-(2 \times 1) surface with oxygen and carbon at In coverage ≥ 2 ML. The impurities served to block the $[011]$ and $[01\bar{1}]$ channels, thus inhibiting the formation of the oriented islands' growth. We do not believe potential surface contamination played a significant role in our growth morphology over most of the surface area. The Si(100)-(2 \times 1) substrate was a freshly prepared surface giving strong reconstruction features that are characteristic of a clean surface. The background pressure

in our chamber was maintained at low 10^{-9} Torr. It is known that the hydrogen-terminated Si(100) surface does not form any reconstruction phase such as $\text{In}(2\times 1)$ [15]. We also did not observe any transmission RHEED features during the In deposition on the Si(100)- (2×1) surface, which excludes the VW growth mode previously observed for a contaminated surface. We note that the observed hemispherical islands were localized to areas near the sample edges, which might be due to the presence of surface contaminants near the edges. For most of the surface area, these hemispherical islands were not detected. Also, because low fs laser energy density (0.5 J/cm^2) was used in PLD, no particulates were observed on the surface.

The morphology of the grown 3D islands and the corresponding height profiles were observed by the AFM, as shown in Fig. 4.8. An area histogram of hexagonal islands is displayed in Fig. 4.8(a), indicating an average island area of $17\times 10^3 \text{ nm}^2$. The island height profile in Fig. 4.8(a) shows a flat top plane with a diameter of $\sim 70 \text{ nm}$ and inclined surface planes, indicating the formation of faceted surfaces. The island profile perpendicular to the surface shows a height of $\sim 5 \text{ nm}$ and a diameter of $\sim 220 \text{ nm}$. From the line scans taken over different In hexagonal islands, the lateral size is found to be larger than the height by about ten times. The 3D image of the elongated In islands and a line profile taken over an island are shown in Fig. 4.8(b). The line profile shows a height of $\sim 4.5 \text{ nm}$. Lines scans along and across the island indicate an average length and width of 200 and 60 nm, respectively. These elongated islands were grown on the initial $\text{In}(2\times 1)$ layer with a highly oriented direction [Fig. 4.8(b)]. The hemispherical islands are smaller in size than the other In island types [Fig. 4.8(c)]. The line scan shows quite a uniform distribution with an average radius of 50 nm and a height of 6 nm.

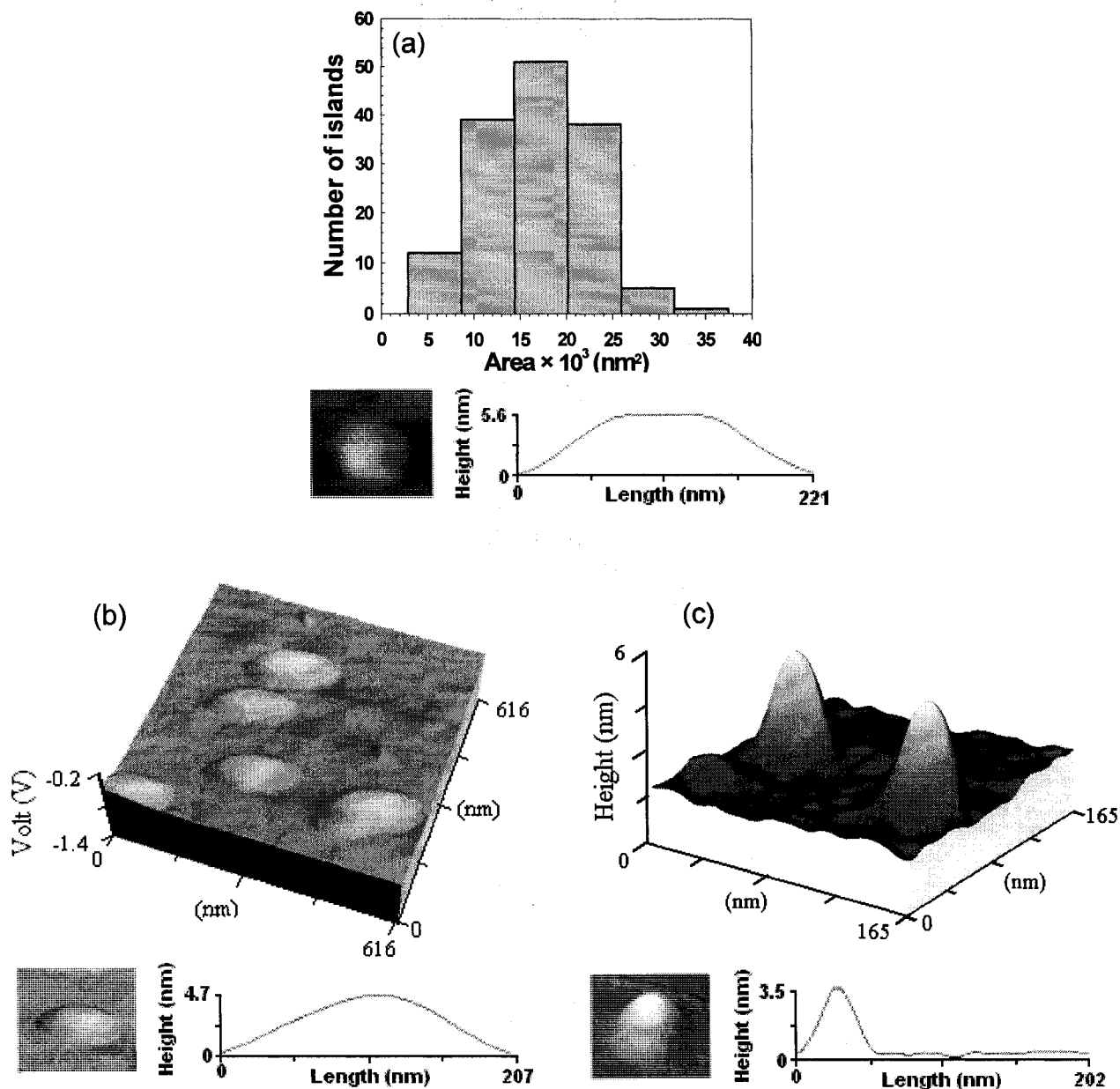


FIG. 4.8. In islands' shape and height profiles measured by the AFM: (a) An area histogram of hexagonal islands is shown. A line scan taken over an island shows a flat top plane with diameter of ~ 70 nm and inclined planes at the sidewalls, indicating formation of faceted In islands. The island has a height of ~ 5 nm and width of ~ 220 nm; (b) Three-dimensional image of the elongated islands. A line scan along an elongated island shows a height and length of ~ 4.5 nm and ~ 200 nm, respectively. The island has a width of ~ 60 nm. The lateral sizes of the hexagonal and elongated islands are larger with respect to their heights. (c) Three-dimensional image of the hemispherical islands. The corresponding line profile over a hemispherical island shows a radius of ~ 50 nm and height of ~ 6 nm. The root-mean-square surface roughness along the line profile is 0.9 nm.

Although the $\text{In}(2\times 1)$ was observed previously by RHEED in MBE growth, [11] we did not observe the $\text{In}(2\times 2)$ reconstruction during In deposition by fsPLD. While Zhu et al. [75] reported that the $\text{In}(2\times 2)$ and $\text{In}(2\times 1)$ reconstructions coexist at coverages between 0.5 and 1.0 ML, Ryu et al. [15] did not observe $\text{In}(2\times 1)$ reconstruction using STM. In general, thin film structure and morphology depend on the deposition conditions such as deposition rate, coverage, and substrate temperature. Femtosecond PLD is known to result in the formation of energetic plume species, [76] which is expected to favor the growth of $\text{In}(2\times 1)$ over the $\text{In}(2\times 2)$ structure. This is supported by the work of Northrup et al., [77] who have used the first-principle total-energy calculations to show that the $\text{In}(2\times 1)$ dimer structure would occur if the In chemical potential is larger than that of the bulk. STM study of In on Si(100) showed that a strained $\text{In}(2\times 1)$ layer of ~ 1.4 ML grew preferentially at the terrace edges [18].

The formation of the $\text{In}(2\times 1)$ structure for the first monolayer in fsPLD results in the growth of In island morphologies that differ from that formed in MBE and thermal deposition [11, 15]: faceted hexagonal In islands and elongated ones were observed in the case of fsPLD. These islands had a width larger than their height, indicating that the growth of In islands parallel to the surface was dominant in the first ~ 23 ML of In coverage, as seen in Fig. 4.6. Since the 2D initial layer $\text{In}(2\times 1)$ has a dimer structure similar to the Si(100)-(2 \times 1) surface, which takes the $[011]$ or $[01\bar{1}]$ direction, In adatoms grow along these directions, rather than across them, showing preferential orientation. As the 3D In islands grew by the SK mode, different island morphologies gave rise to the diffuse RHEED scattering observed as the high background in the RHEED pattern.

IV.5.1.2. Growth kinetics of the initial In(2×1) layer and the In islands

IV.5.1.2.1. RHEED intensity recovery and growth kinetics

RHEED intensity recovery was used to investigate growth kinetics of deposition of In on Si(100)-(2×1). The In films were prepared on the Si(100)-(2×1) at RT by fsPLD, while the RHEED specular beam intensity was measured at the Bragg condition as a function of In deposition thickness. The growth was performed using interval deposition, i.e., deposition by a number of laser pulses with a given amount of In, followed by an interval of no deposition, with this sequence then repeated. The laser was operated at a 2 Hz repetition rate and an energy density of 0.5 J/cm² on the In target. During the deposition of the initial ~1.5 ML, the (2×1) structure was preserved, as observed from the RHEED patterns. The RHEED electron beam was incident along the [011] azimuth down the vicinal Si surface. At other azimuthal directions, such as [013] and $[0\bar{1}\bar{1}]$, the RHEED patterns showed no change in the predeposition Si(100)-(2×1) pattern, although there was an observed change of the in-plane lattice spacing, as will be discussed later. Figure 4.9 shows specular beam intensities taken from a series of sequential In depositions on top of the initial 1.5 ML that had the In(2×1) structure. Recovery of the RHEED specular intensity is monitored after growth termination by turning off the laser upon deposition of a known In thickness. After terminating the deposition at ~0.5 ML of In (total In coverage ~2 ML), the specular beam intensity increased to a value close to its predeposition intensity, as shown in Fig. 4.9(a). This indicates that the deposited In diffused on surface terraces and grew epitaxially, thus resulting in increased long-range order to a value close to that prior to deposition. After deposition of the next 1 ML, giving a total coverage of ~3 ML of In, the recovery of the RHEED specular intensity

became slower, as shown in Fig. 4.9(b). The RHEED intensity recovery is dependent on the smoothness of the surface before deposition, the deposited In diffusion energy, and the amount of the deposited In. Deposition of ~ 4 ML of In on a substrate already covered by 5 ML In led to a continuous decrease in the specular intensity with only weak RHEED intensity recovery after deposition, as shown in Fig. 4.9(c). This indicates an increase of surface roughness due to island nucleation on the surface. The RHEED intensity recovery after growth termination is observed up to an In coverage of ~ 7 ML and was accompanied by maintaining the $\text{In}(2\times 1)$ structure.

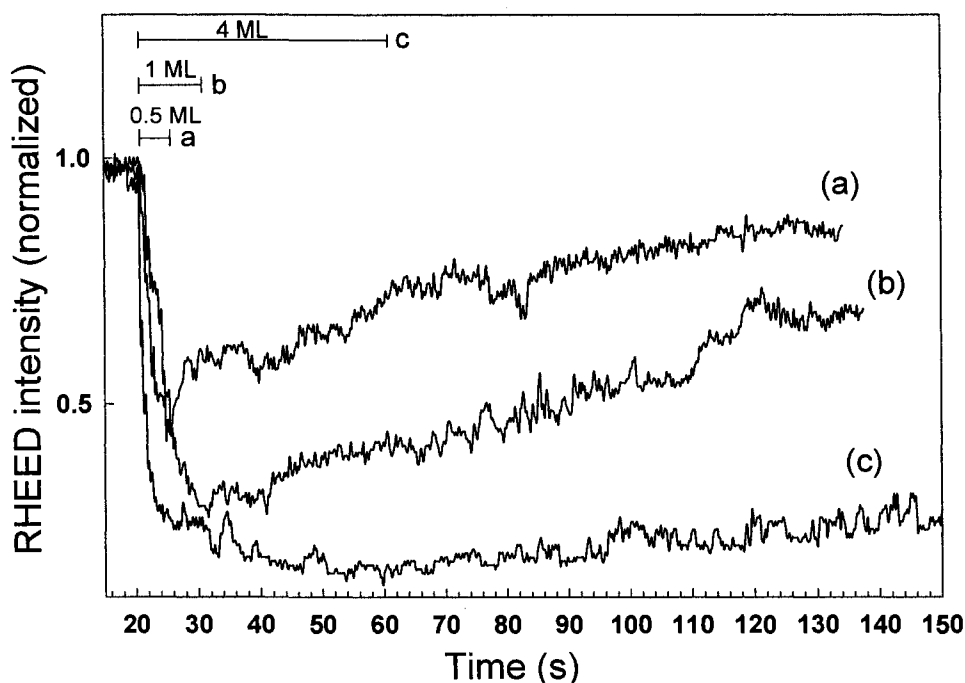


FIG. 4.9. Specular beam RHEED intensity after deposition of: (a) ~ 0.5 ML on an initial ~ 1.5 ML $\text{In}(2\times 1)$, (b) an additional ~ 1 ML giving a total coverage of ~ 3 ML, and (c) ~ 4 ML on an initial ~ 5 ML of In. The deposition was performed with the laser operated at 2-Hz laser repetition rate and 0.5 J/cm^2 laser energy density. The RHEED electron beam was incident along the $[011]$ azimuth down the vicinal Si surface. The initial 2D layer formed in the $\text{In}(2\times 1)$ structure.

Deposition of In on Si(100)-(2×1) at substrate temperatures near but below the In bulk melting point showed recovery of the RHEED specular beam intensity after growth termination. Figure 4.10 shows the RHEED intensity of the (20) diffracted beam for a substrate temperature of ~145 °C. The laser was operated at 1 Hz repetition rate with an energy density of 0.5 J/cm² on the In target. The growth was performed on ~2.7 ML of In that was initially prepared on Si(100)-(2×1). When the growth was started, a reduction in the RHEED intensity was observed. After growth termination, the RHEED intensity recovered its original value within a certain time. The recovery of the RHEED beam intensity after growth termination is known to be characteristic of step flow growth [27, 78]. In a previous STM study of In on Si(100) at RT, it was found that a flat 2D In(2×1) island of ~1.4 ML, on the initial In(2×2) layer, grew preferentially at the surface terrace edges [18]. In the step flow growth mode, the deposited material attaches to the step terrace edges and the surface recovers the original surface order, along with the RHEED intensity. Step flow growth in PLD was previously observed and showed relaxation of RHEED intensity after each laser pulse [79, 80]. For a substrate temperature of ~145 °C, relaxation of the RHEED intensity was observed after each laser pulse during fsPLD of In, as shown in the inset of Fig. 4.10. To capture this relaxation of the RHEED intensity, the CCD camera was operated at a fast frame rate. The intensity of the $(\bar{2}0)$ diffracted beam showed similar relaxation behavior during the fsPLD of In but out of phase to the (20) diffracted beam. This RHEED relaxation indicates that surface smoothing occurred between deposition pulses. The recovery and relaxation of the RHEED intensity, as shown in Fig. 4.10, are attributed to step flow growth of the 2D In(2×1) layer.

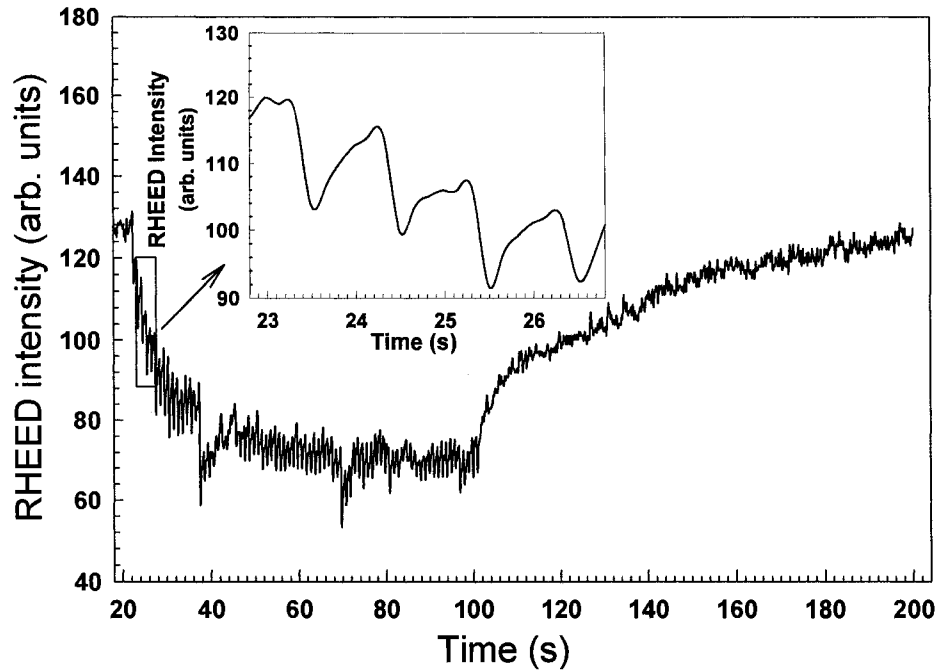


FIG. 4.10. RHEED intensity of the (20) diffraction beam as a function of In deposition time on Si(100)-(2×1) at a substrate temperature of ~145 °C. The laser was operated at 1 Hz repetition rate with an energy density of 0.5 J/cm² on the In target. Relaxation of the RHEED intensity was observed during In deposition after each laser pulse as seen in the inset figure, which displays the RHEED intensity for laser pulse numbers 2 to 5 from starting the deposition.

The characteristic diffusion parameters of deposited In on the In(2×1) wetting layers can be measured from the recovery time profile of the RHEED specular beam intensity. The diffusion length ℓ is related to the diffusion coefficient D by $\ell = (2D\tau)^{1/2}$, where τ is the average diffusion time on the surface terraces, which depends on the density of nucleation sites and the diffusion velocity [27]. Figure 4.11(a) shows the RHEED recovery of the specular beam intensity of Fig. 4.9(a) after growth termination.

The RHEED intensity exhibited a rapid, then slow recovery, indicating that the growth kinetics varied during the entire surface recovery. Lewis et al. and Joyce et al. have shown that surface recovery after growth termination occurs in two stages, a fast and a slow process [32, 81]. The RHEED intensity in Fig. 4.11(a) is well represented by a sum of two exponentials in the form of $I(t) = A_0 + A_1 (1 - \exp(-t/\tau_1)) + A_2 (1 - \exp(-t/\tau_2))$, where A_0 , A_1 , and A_2 are constants, while τ_1 and τ_2 represent the time constants that correspond to the fast and slow processes of recovery. From a curve fit to the RHEED intensity, the time constants for recovery are obtained such that $\tau_1 = 2 \pm 0.4$ s, while $\tau_2 = 80 \pm 5$ s.

For film growth by step flow mode, one can use the intensities of the specular beam or higher-order diffraction beams in RHEED to monitor the diffusion process [82]. Figure 4.11(b) shows a curve fit to the intensity recovery of the (20) beam in Fig. 4.10 after growth termination. In this case, the time constants τ_1 and τ_2 are found to be 1.9 ± 0.3 and 53 ± 2 s, respectively. The inset of Fig. 4.11(b) shows RHEED intensity behavior between the second and third deposition laser pulses from starting the deposition. The RHEED intensity dropped and then increased before the next pulse. Each laser pulse ablates the In target, creating $\sim 3.4 \times 10^{13}$ atoms/cm² of In to the surface. In this case, the RHEED intensity decreased because of the increased random distribution of incoming In deposits on the surface. The deposited In was reorganized by diffusion on the surface, increasing the RHEED intensity until the arrival of the next In flux. During In deposition, the surface smoothness changed with each laser pulse in a periodic fashion, which can be viewed as a kind of interrupted growth. The relaxation time depends on the substrate temperature, surface condition, deposited material, and the repetition rate of the laser pulse [83].

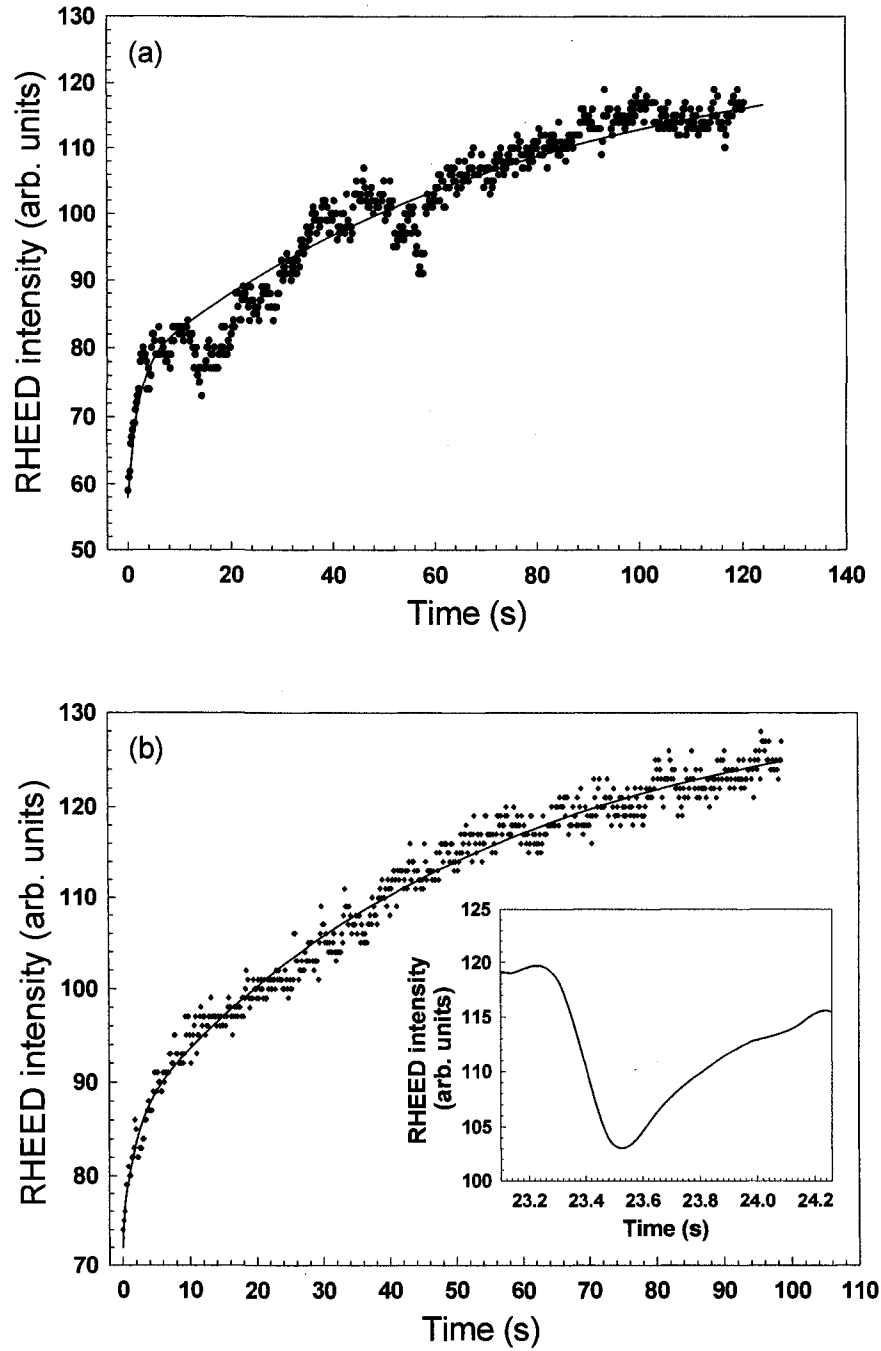


FIG. 4.11. (a) Recovery of the RHEED specular beam intensity after deposition of In at RT and coverage of ~ 2 ML. (b) Recovery of the RHEED (20) beam intensity after deposition of In at a substrate temperature of ~ 145 °C performed on initially ~ 2.7 ML of In. The RHEED intensity shows an initial fast increase and then a slow recovery, characterized by two exponential recovery times τ_1 and τ_2 , respectively. The x-axis start with 0 in (a) and (b) for curves fit. The inset in (b) shows a decrease and then a relaxation of the RHEED intensity after and before the second and third deposition laser pulses, respectively.

Upon growth termination, the surface order recovered to its original state as before deposition. The RHEED intensity showed fast and slow recoveries after growth termination with each recovery rate characterized by its diffusion coefficient. For films grown by step flow, diffusion to the terrace step edges with a time constant τ depends on the surface terrace width. Therefore, knowing the surface terrace width, one can determine the surface diffusion coefficient D .

The average terrace width of the vicinal Si(100)-(2×1) surface is expected to be affected by the chemical etching and heat cleaning. Thus, the average terrace width of the Si(100)-(2×1) substrate was measured before In deposition. This was accomplished by directing the RHEED electron beam down the staircase of the vicinal Si surface, along the [011] azimuth. The specular beam showed splitting peaks at the out-of-phase condition defined by $2d\sin\theta_{inc} = (n+1/2)\lambda$, where d is the monolayer step height, θ_{inc} is the incident angle corresponding to the out-of-phase condition, n is an integer, and λ is the electron wavelength. The out-of-phase diffraction condition was used to study clean vicinal surface structures [84, 85]. Figure 4.12 shows the RHEED pattern of the vicinal Si(100)-(2×1), showing splitting of the specular beam in the $S_{//}$ direction, where $S_{//}$ and S_{\perp} are the components of the momentum transfer parallel and perpendicular to the electron beam, respectively. The out-of-phase angle of incidence θ_{inc} was ~ 65 mrad. The average terrace width was determined from the split peak spacing $L = 2\pi/(d\theta) k \sin\theta_{inc}$, where $k = 47.78 \text{ \AA}^{-1}$ is the Ewald sphere radius and $d\theta = 32.7$ mrad is the splitting angle. Taking into account the RHEED instrumental response of $0.20 \pm 0.02 \text{ \AA}^{-1}$, the average terrace width of the Si(100)-(2×1) surface was obtained to be $L = 61 \pm 10 \text{ \AA}$. The instrumental response was obtained from the FWHM along the specular beam at the Bragg diffraction

condition. The corresponding misorientation angle for the vicinal Si(100)-(2×1) substrate with a step height of 1.36 Å is approximately 1.3°, which is consistent with the $1.0 \pm 0.5^\circ$ miscut angle specified by the manufacturer.

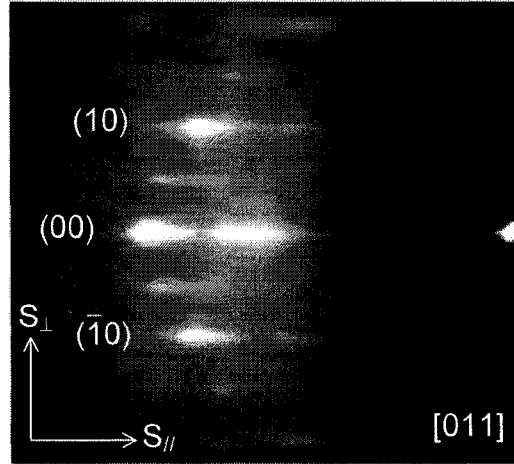


FIG. 4.12. RHEED pattern of the Si(100)-(2×1) vicinal surface taken at the out-of-phase condition corresponding to $\theta_{inc.}$ of ~ 65 mrad. The primary electron energy of 8.6 keV was incident down the staircase of the vicinal surface along the [011] azimuth. $S_{//}$ and S_{\perp} are the components of the momentum transfer parallel and perpendicular to the electron beam, respectively. The specular beam is split in the $S_{//}$ direction into two peaks around a central part, which is located within the RHEED zeroth Laue zone.

The surface diffusion coefficient D of the fast and slow recovery processes of deposited In over the In(2×1) wetting layer grown by fsPLD was determined. In the case of film growth by the step flow mode, the diffusion length ℓ is limited by the terrace width and thus is equal to L . By knowing the diffusion parameters τ and ℓ , D can be determined. From the RHEED intensity recovery of Fig. 4.11(a), the In diffusion coefficient at RT is found to be $D_1 = 9 \pm 1.6 \times 10^{-14} \text{ cm}^2/\text{s}$ for the initial fast recovery and $D_2 = 2 \pm 0.4 \times 10^{-15} \text{ cm}^2/\text{s}$ for the slow recovery. The In diffusion coefficient of the RHEED

intensity recovery, Fig. 4.11(b), for the deposition conditions at substrate temperature of $\sim 145^\circ\text{C}$ is $D_1 = 9 \pm 1.5 \times 10^{-14} \text{ cm}^2/\text{s}$ for the initial fast recovery and $D_2 = 3 \pm 0.6 \times 10^{-15} \text{ cm}^2/\text{s}$ for the slow recovery. The experimental errors in calculating D arise from the instrumental response and uncertainty in determining the split peak spacing.

The surface processes that lead to the recovery of the RHEED intensity depend on the growth mode and the deposition parameters. In MBE growth of GaAs, the initial recovery was attributed to surface reconstruction changes and the slow process of rearrangement of 2D islands [81]. Neave et al. have explained the initial recovery in the growth of GaAs(001)-(2 \times 4) by Ga-As bond dissociation at step edges [29]. Indium incorporation during the growth of Si(100) has shown a strong surface segregation leading to formation of an abrupt interface with Si [11, 86]. Deposition by MBE is characterized by a steady-state, thermal atom flux, while in PLD, pulsed plumes of energetic species are obtained. Indium atoms landing on the Si substrate with a high deposition rate lead to the formation of small In clusters. The drop of the specular RHEED intensity after each fsPLD pulse, shown in the inset of Fig. 4.10, indicates the reduction of surface order after the plume arrives on the surface. At the terrace step edges, atoms have lower coordination, making them more reactive. Because of their high reactivity, surface step edges provide preferred sites for film growth. Metal islands and clusters were observed to decorate the steps of the substrates [18, 87, 88]. The growth of the 2D In(2 \times 1) layer occurred by surface diffusion to the step edges, which was responsible for the observed RHEED intensity recovery. In a proposed model for growth of superconducting thin films by PLD, the RHEED intensity recovery was attributed to the diffusion of material units, with D in the order of $10^{-12} \text{ cm}^2/\text{s}$, rather than to the

diffusion of adatoms [89]. In our case, the initial fast RHEED recovery is expected to be due to surface diffusion of In clusters, with D in the order of 10^{-14} cm²/s. These In clusters diffused toward terrace edges, in a step flow growth mode, thereby causing an increase in the RHEED intensity. Previous experimental observation of fast diffusion of clusters and a study of 2D island diffusion on surfaces were reported [90-92]. Diffusion of adatom and vacancy islands of Ag on Ag(100) was found to occur by different diffusion mechanisms [93, 94]. The slower process following the initial fast decay in the RHEED intensity was attributed to recovery of long-range order of the terrace step edges.

IV.5.1.2.2. Island growth and morphology

Next, the development of In film morphology on Si(100)-(2×1) in fsPLD is discussed. Figure 4.13 shows the RHEED specular beam intensity of In on Si(100)-(2×1) grown at RT using a laser pulse repetition rate of 2 Hz and a laser energy density of 0.5 J/cm². The electron beam was incident with θ_{inc} of ~68 mrad along the [011] azimuth. RHEED patterns of the Si(100)-(2×1) substrate and the grown In film are shown in the inset of Fig. 4.13. The RHEED intensity of the specular beam as well as higher-order diffracted beams decreased after starting the In growth. Formation of the In(2×1) wetting layer on the Si surface is associated with the initial drop of the intensity. The RHEED specular intensity then decreased slowly, indicating development of surface roughness due to growth of In islands in the SK mode. This result is consistent with the previously reported MBE growth of In on Si(100)-(2×1), where transmission diffraction spots were not observed in the RHEED patterns because of the combination of the low coverage area and small density of islands [11]. Postdeposition RHEED pattern of ~38 ML of In on

Si(100)-(2×1), shown in the inset of Fig. 4.13, has wide faint rings on a high background, indicating random in-plane crystallographic orientation of the grown 3D islands.

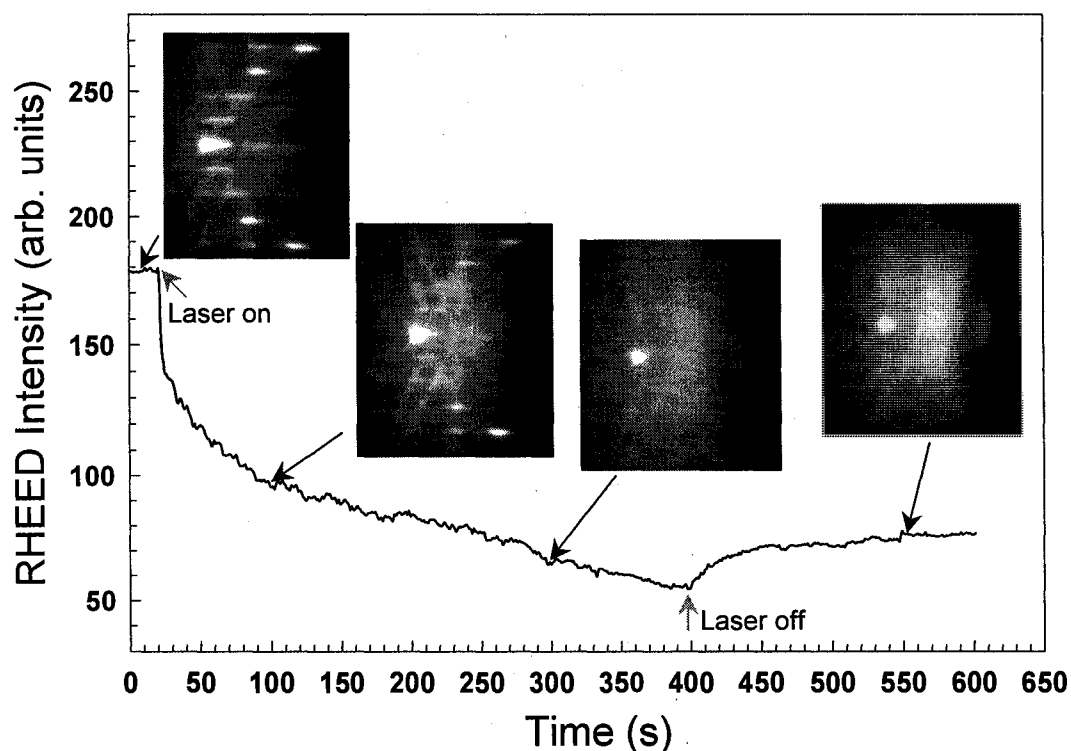


FIG. 4.13. RHEED intensity of the specular beam was monitored with deposition time. The electron beam was incident with $\theta_{inc.}$ of ~ 68 mrad along the [011] substrate azimuth. The deposition conditions were 2 Hz laser repetition rate and 0.5 J/cm^2 laser energy density. RHEED patterns taken in the [011] azimuth of the Si(100)-(2×1) substrate and of the grown In film at 100 s, 296 s, and post-deposition are shown in the inset. The In(2×1) structure was preserved during the initial growth. The final film shows wide faint rings on a high background, indicating random in-plane crystallographic orientation.

The peak profile of the RHEED intensity is analyzed during the growth of the In thin film by measuring the FWHM across the specular beam (S_{\perp} direction). The FWHM is measured close to the in-phase diffraction condition down the vicinal Si surface during deposition. As the islands grow on the surface, their size distribution can be determined

from the intensity profile. The size distribution is extracted from a Gaussian profile fit to the RHEED specular spot. An example of this curve fit is shown in Fig. 4.14(a) for film coverages of ~ 7 and ~ 14 ML, giving FWHMs of 0.39 and 0.35 \AA^{-1} , respectively. The width of the specular beam profile in Fig. 4.14(a) is a convolution of instrumental broadening and broadening in the reciprocal lattice rods of the grown In domains on the surface. The instrumental response was determined from the FWHM of the main electron beam on the RHEED screen and is found to be $0.30 \pm 0.015 \text{ \AA}^{-1}$ in the S_{\perp} direction. Taking into account the instrumental response, Fig. 4.14(b) shows the change in the FWHM of the specular beam intensity profile with deposition time corresponding to film coverage between ~ 0.3 and ~ 14 ML (left y axis). The FWHM decreased from ~ 0.22 to 0.04 \AA^{-1} , which indicates an increase in the average surface coherence [74]. Figure 4.14(b) (right y axis) shows the specular spot intensity-to-background ratio $I_{\text{spec}}/I_{\text{back}}$ during film deposition, where I_{spec} and I_{back} are the specular peak and RHEED background intensities, respectively. The background intensity I_{back} is measured at a location between the specular and (10) diffracted beams. Its value is dependent on step edge density and roughness of the grown film. The ratio $I_{\text{spec}}/I_{\text{back}}$ increased initially during growth of the 2D wetting layer, indicating an improvement of the surface quality. Then, it started to decrease with In thickness after ~ 7 ML. The film coverage at which the transition from 2D growth to 3D growth occurs depends on the difference between the In and Si crystal structures as well as on the structure of the initial $\text{In}(2 \times 1)$ layer. During the transition growth stage, small In islands grew on the surface before completion of the underlying layers. As growth proceeds, the size of the islands increased, leading to shadowing of the incident electron beam, which yields low specular beam intensity.

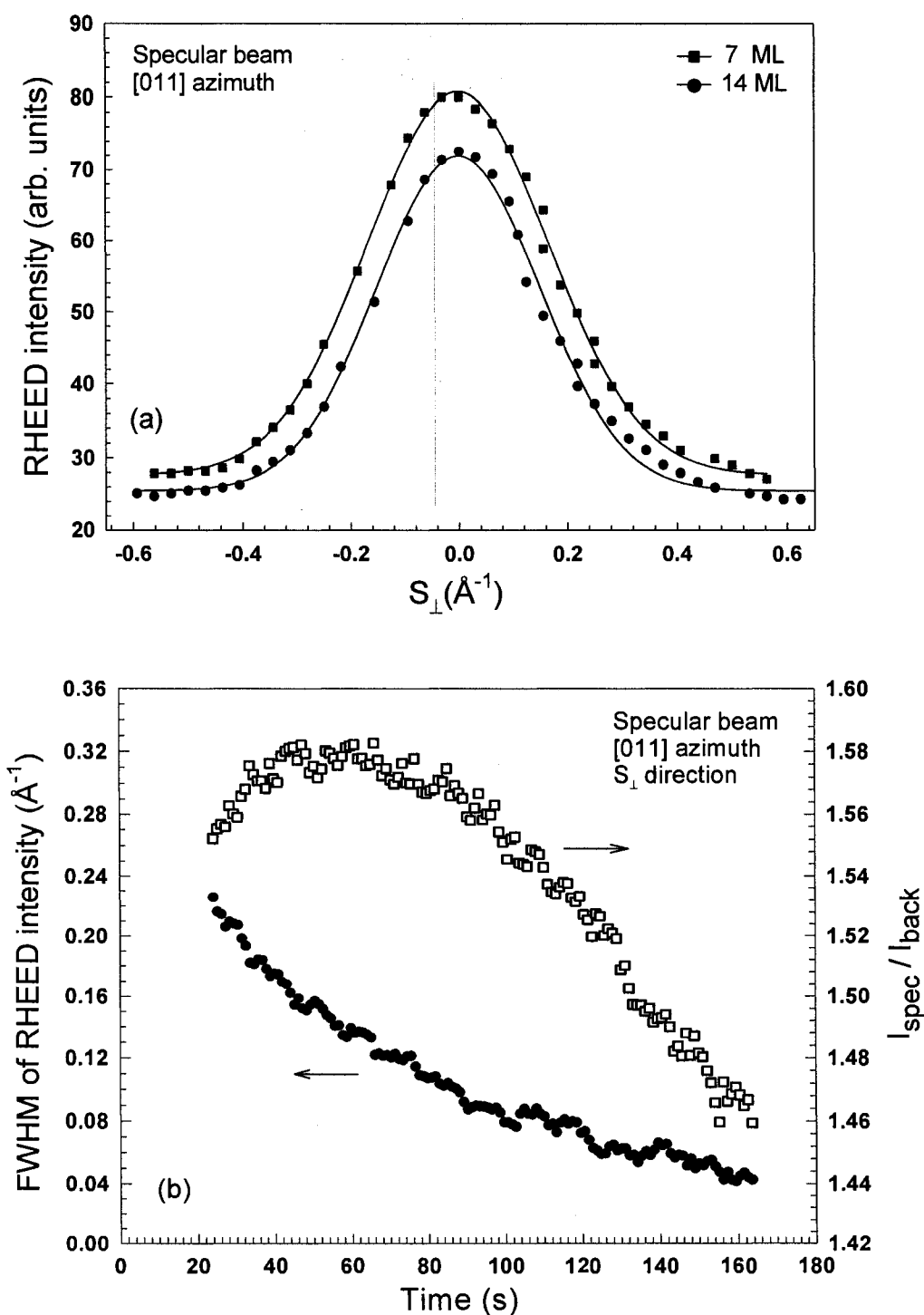


FIG. 4.14. (a) RHEED intensity profiles of the specular beam at film coverage of ~ 7 and ~ 14 ML versus the momentum transfer S_{\perp} parallel to the substrate surface. (b) FWHM of specular RHEED intensity profile as a function of the deposition time taking into account an instrumental response of $0.30 \pm 0.015 \text{ \AA}^{-1}$ in the S_{\perp} direction. The FWHM decreased from $\sim 0.22 \text{ \AA}^{-1}$ to 0.04 \AA^{-1} . The spot intensity-to-background ratio of $I_{\text{spec}}/I_{\text{back}}$ (open squares) during film deposition is shown, where I_{spec} and I_{back} are the specular peak and RHEED background intensities, respectively.

Next, the morphology of the grown In film was examined *ex situ* using AFM. Figures 4.15(a)-4.15(d) show AFM images of the grown crystalline In islands on the Si(100)-(2×1) substrate at RT, which correspond to the postdeposition RHEED pattern in Fig. 4.13. The In islands took a variety of elongated, circular, and triangular shapes. These 3D islands grew on a smooth 2D In surface as seen in the AFM images. This is consistent with the RHEED observation of SK growth. The elongated and triangular islands show preferential growth orientations toward the $[011]$ and $[01\bar{1}]$ azimuths of the Si(100)-(2×1) surface. These orientations were confirmed by taking AFM images of a Si(100) surface, without deposition of In, and the AFM tip was scanned over the same direction similar to that examined for samples after In deposition. The directions $[011]$ and $[01\bar{1}]$ were determined by observing the orientation of terrace edges of the vicinal surface. These growth directions are affected by the 2D In layer on the Si vicinal surface, where the (2×1) domains are known to be rotated by 90° alternately parallel and normal to the terrace step edges [61]. Hexagonal-shaped faceted In islands were observed, Fig. 4.15(d).

Three-dimensional AFM images of the elongated In islands show polyhedral shapes, for which an example is shown in Fig. 4.16(a). Line profiles taken along and across the polyhedral island imaged in Fig. 4.16(a) show a major axis of ~215 nm along the $[011]$ direction and a width of ~100 nm, as shown in Figs. 4.16(b) and 4.16(c). The top plane of the island in Fig. 4.16(b) is inclined to the substrate surface by an angle of $\theta = 3 \pm 0.6^\circ$, while the front plane made an angle $\theta = 15 \pm 0.8^\circ$ with the substrate surface. The sidewall planes in Fig. 4.16(c) made an angle $\theta = 25 \pm 3.3^\circ$ with the substrate surface. Some of the grown elongated islands did not show a faceted polyhedral structure. Figure

4.17(a) is a 3D image of a circular island, which shows that its perimeter has a higher edge forming a ring around an inner flat central part, which is parallel to the Si(100) surface. On top of the island, some growth features are observed. Figure 4.17(b) is a line profile taken across the island in Fig. 4.17(a), showing that the rounded edge has a height of ~ 60 nm while the flat top plane has a height of ~ 52 nm. Figure 4.18(a) is a 3D STM image of another In circular island, showing complex ring structure with nanoscale roughness on the ring and top surface of the island. Figure 4.18(b) is a 3D STM image taken in the region between the large circular islands, showing small In islands of different sizes. The elongated-polyhedral and circular islands were found with a low number density but had mostly large size and regular well-defined step edges.

The AFM and STM observation shows that the height-to-diameter aspect ratios of the circular islands are small. For islands with a mean diameter of 220 nm, the heights measured from the rounded edges are around 6% of the diameter. For islands of a diameter in the range of 490-690 nm, the average height is 11% of the diameter. The circular islands show central flat top planes, which covered $\sim 40\%$ of the total island surface area. In a previous study of growth of In on GaAs(001) by MBE, In islands with flat top surfaces were observed after using Sb as a surfactant [95]. For elongated islands, the height-to-length aspect ratios are relatively small. The measured heights were in the range of 2%-7% of the elongated axes length. The small height-to-length aspect ratios of In islands and the decrease of the FWHM of the specular RHEED beam with In coverage, shown in Fig. 4.14(b), suggest that In nucleation took place at the edges of the islands more than on their top surface.

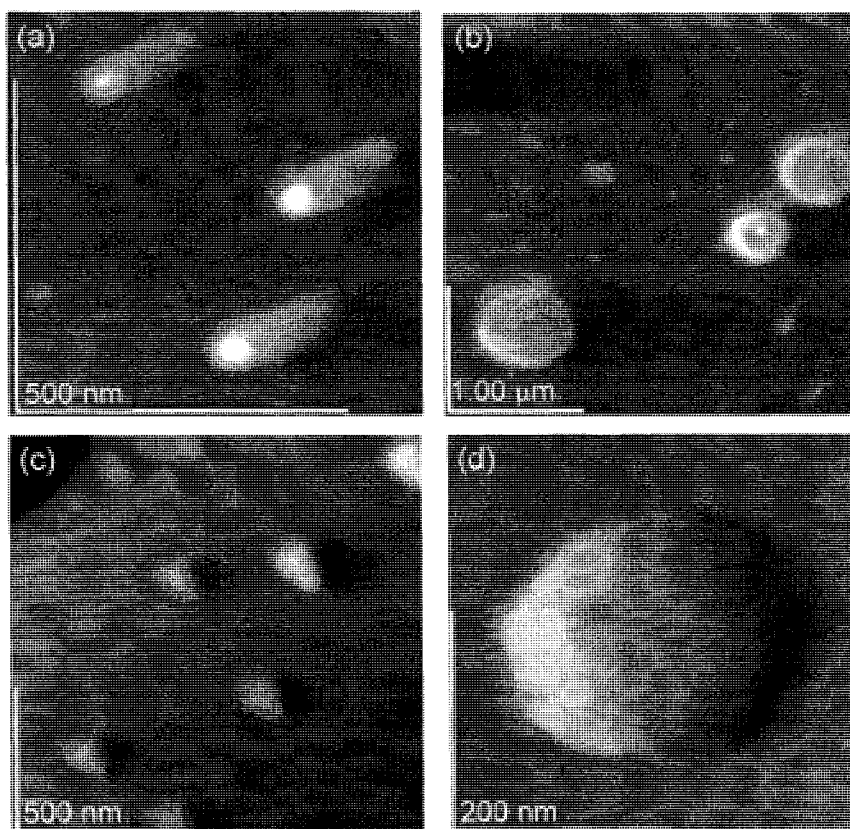


FIG. 4.15. (a)-(d) AFM images taken after deposition of In on Si(100)-(2×1) substrate at RT by fsPLD (corresponding to the post-deposition RHEED pattern in Fig. 4.13). The 3D islands in (b)-(d) show elongated, circular, and triangular shapes, respectively. The elongated and triangular islands are highly oriented towards $[011]$ and $[01\bar{1}]$ azimuths of the Si(100)-(2×1) surface. (d) Hexagonal-shaped In island.

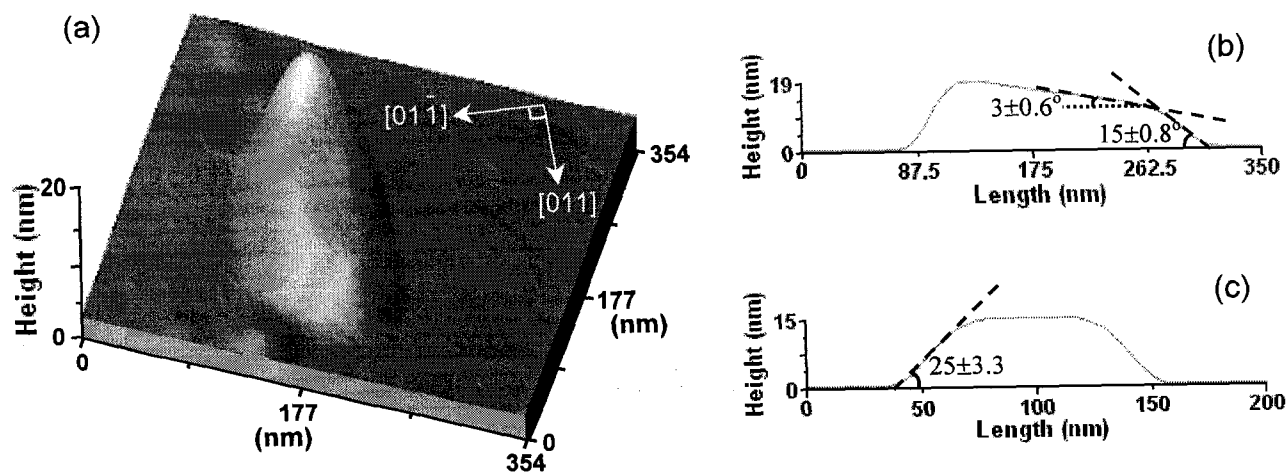


FIG. 4.16. (a) 3D AFM image of an elongated In island oriented toward the [011] substrate azimuth. (b) and (c) are line profiles taken along and across the elongated island in (a), respectively.

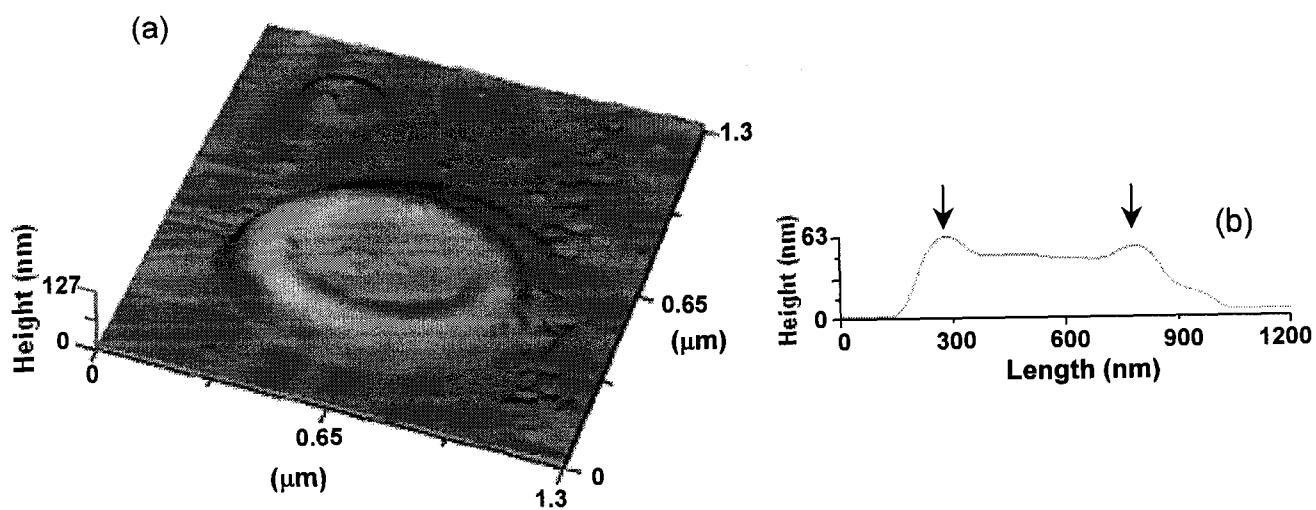


FIG. 4.17. (a) 3D AFM image of a circular In island. (b) Line profile across center of the island in (a) showing a higher edge surrounding a flat central part as indicated by arrows.

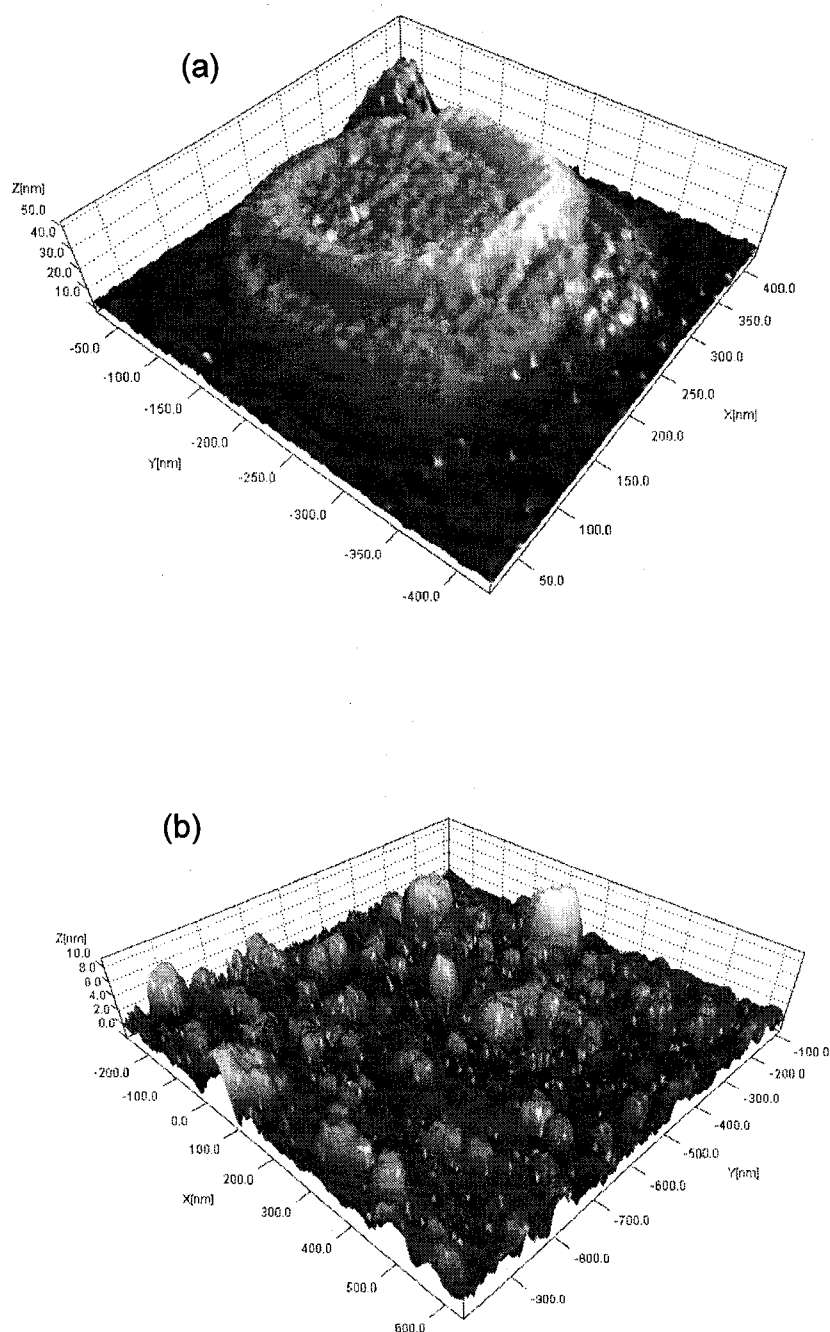


FIG. 4.18. STM 3D scans of an In circular island (a) and small In clusters (b).

IV.5.1.2.3. fsPLD effects

At the initial stages of In growth on the Si(100)-(2×1) at RT by fsPLD, the (2×1) RHEED pattern was preserved but was accompanied by a sudden drop in the RHEED intensity of the specular beam as well as the higher-order diffracted beams. Moreover, a decrease in the in-plane lattice spacing of the grown film occurred. Development of another RHEED pattern such as (2×2) during the In deposition by fsPLD has not been observed. Using STM, Zhu et al. [75] reported that In(2×2) and In(2×1) reconstructions coexist at coverages between 0.5 and 1.0 ML, while in a STM observation Ryu et al. [15] did not observe In(2×1) reconstruction. In MBE growth of In/Si(100)-(2×1), the In(2×2) structure was observed by RHEED and LEED [11]. In general, thin film structure and morphology depend on the deposition conditions, such as the incident atom energy, deposition rate, and coverage. The In(2×1) structure has not been previously reported as an initial layer in the deposition of In on Si(100)-(2×1).

Femtosecond PLD is known to result in the formation of a plume containing energetic species [76]. The high energy of atoms and ions in the ablated In plume affects the In film growth in two ways. The first is due to the impact of the incident energetic In species with the Si substrate, leading to displacement in substrate surface lattice sites and possible removal of the Si(100)-(2×1) reconstruction. The second effect is due to the large deposited In diffusion rate because of its high kinetic energy and local surface lattice heating due to inelastic energy transfer from different In plume species. Northrup et al. [77] used first-principles total-energy calculations to show that the In(2×1) dimer structure occurs rather than In(2×2) only when the In adsorbate chemical potential is larger than that of the In bulk under nonequilibrium conditions. The In(2×1) structure

considered has a 1 ML of In dimers and is obtained by replacing the Si dimers on Si(100)-(2×1) with In dimers. Accordingly, the In(2×1) structure would not occur under equilibrium conditions. However, the high kinetic energy of In atoms and ions in fsPLD could allow for nonequilibrium conditions to occur. In addition, the incident energetic In species in fsPLD can affect island morphology, which depends on the surface diffusion of the deposited In.

The (2×1) reconstruction induced by group-III atoms on the Si(100) surface cannot be explained by the dimer-on-dimer model [96]. Therefore, in the In/Si(100) system, the underlayer Si(100)-(2×1) reconstruction is most likely removed and the top surface layer becomes bulklike terminated: Si(100)-(1×1) structure with two dangling bonds per Si atom. Figure 4.19 shows a proposed model structure for the grown In(2×1) on the Si(100) surface based on RHEED observations. The deposited In atoms occupy the dangling bonds of the Si surface. To achieve the threefold coordination configuration, each In atom bonds to one In atom from the first layer and two Si atoms from the second layer in order to reduce the number of unsaturated bonds at the surface. Therefore, a coverage of 1 ML of In is needed to saturate all the dangling bonds of the underlying Si(100)-(1×1) surface, whereas in the case of the In(2×2) structure, a coverage of 0.5 ML saturates the dimerized Si(100)-(2×1) surface. We used the RHEED patterns of the In film to estimate the in-plane lattice parameter a . This parameter is measured from the separation of the first-order RHEED peaks, fitted to Gaussian line shapes, which are taken in the [011] azimuthal direction of the Si surface. The in-plane lattice parameter is found to be $a = 3.65 \pm 0.1$ Å, while the surface lattice parameters of In(100) and Si(100) are 3.24 Å and 3.84 Å, respectively. This indicates that the first In monolayers formed a

strained 2D layer, creating a (2×1) RHEED structure similar to $\text{Si}(100)\text{--}(2\times 1)$ but with a different lattice parameter a .

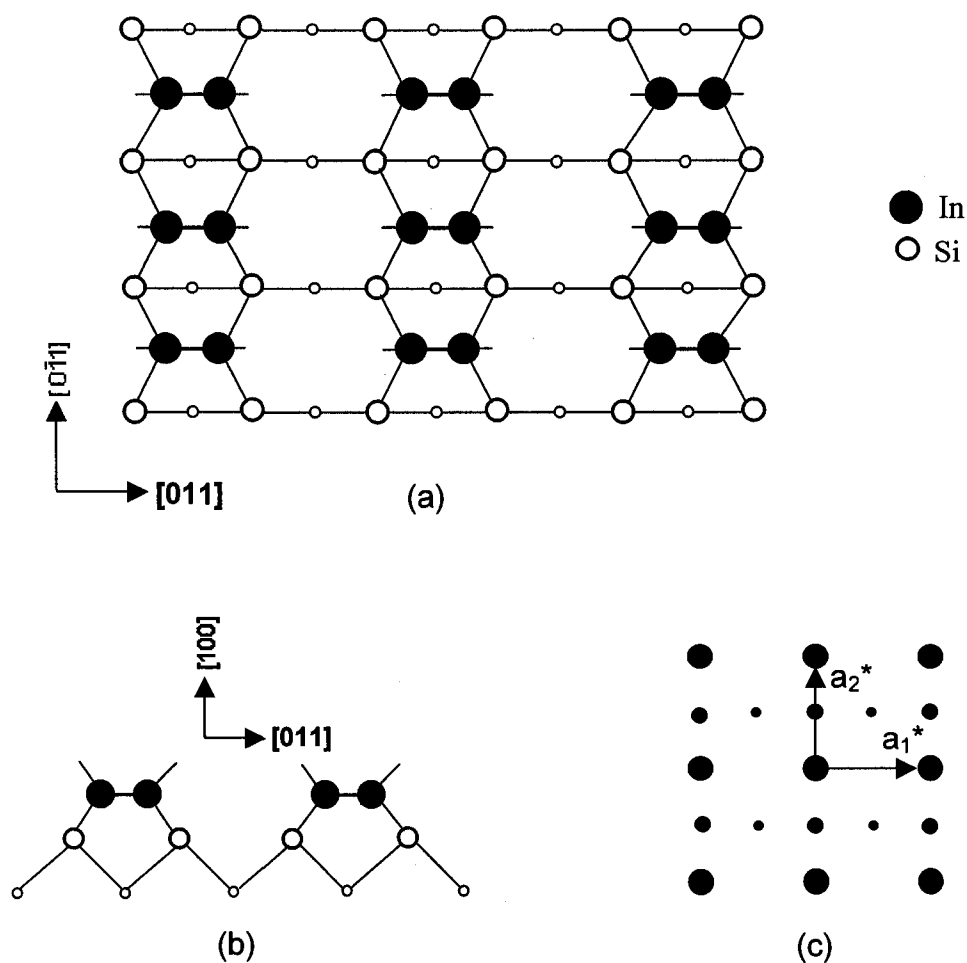


FIG. 4.19. Structure model proposed for the $\text{In}(2\times 1)$ grown on the $\text{Si}(100)$ surface by fsPLD. (a) Top view showing In first layer on Si terminated surface with In dimer along $[011]$ direction. (b) Side view of the $\text{In}(2\times 1)$ model showing top dimers bonded to the Si atoms in the second layer. (c) The reciprocal lattice with its coordinates determined in term of the measured in-plane lattice parameter $a = 3.65 \pm 0.36 \text{ \AA}$, where a^* and b^* are reciprocal lattice axes.

Further In growth by fsPLD on the initial strained In(2×1) layer showed formation of different island morphologies. The 3D island morphology is affected by kinetics and the structure of the In(2×1) layer. In PLD, the expanding plume containing different species has a wide range of energy [66]. When the In deposits were influenced by the dimer structure of the initial In(2×1) layer, elongated-polyhedral islands developed, which exhibit preferential growth orientation with respect to the Si substrate. This type of island was observed in MBE growth of In on Si(100)-(2×1) surface and was referred to as anisotropic growth due to the anisotropic strain in the (2×1) structure [11]. When the In deposits have enough diffusion energy to overcome the anisotropic strain in the underlying In(2×1) first layers, the deposits move across as well as along the dimer rows and the growth results in the formation of different island morphologies, such as the circular and triangular shapes. Quantitative analysis of the FWHM of the RHEED specular beam, parallel to the substrate surface, indicated an increase of the long-range order of the In islands with deposition time. The grown In island shapes and their lateral size-to-height ratios indicated that growth of islands spreads laterally, more than vertically, due to preferential diffusion of In to the islands' edges. This can be seen in the elongation and flattened top surface of the grown polyhedral and circular In islands, respectively.

IV.5.2. Growth of In on Si(100)-(2×1) at high temperature

IV.5.2.1. Growth of In(4×3) on Si(100)

The growth of In on the vicinal Si(100)-(2×1) surface was performed at different deposition conditions. Figure 4.20(a) and 4.20(b) show RHEED patterns of clean Si(100)-(2×1) surface before deposition taken along the $[011]$ and $[0\bar{1}\bar{1}]$ azimuths, down and up the staircase, respectively. Short streaks in the RHEED Laue semicircles and Kikuchi lines were visible. For In growth at T_s in the range of 350-420 °C, the RHEED pattern began to change from that characteristic of the initial Si(100)-(2×1) reconstruction to that of the In(4×3) reconstruction at coverage of ~0.5 ML of In. Figures 4.20(c) and 4.20(d) show RHEED patterns of the In(4×3) superstructure on Si(100)-(2×1) in the $[011]$ and $[0\bar{1}\bar{1}]$ azimuths, respectively. The laser was operated at a 2 Hz repetition rate with an energy density of 0.50 J/cm². The In(4×3) RHEED patterns show streaky integral and fractional orders with sharp spots indicating smooth and high quality epitaxial In film. It was noticed that the Si(100)-(2×1) RHEED pattern improved when In was deposited on Si at lower than 500 °C and then desorbed by heating the Si surface at ~1000 °C. After In desorption and cooling the substrate, the diffracted spots became more pronounced at the higher Laue zones with less background on the RHEED screen. This was observed to considerably enhance the appearance of the In(4×3) structure with subsequent In deposition. This is consistent with a previous study which reported that In can be evaporated on a hot Si surface in UHV to eliminate native oxide without in-diffusion of In and introduction of surface defects into Si during the desorption process [97].

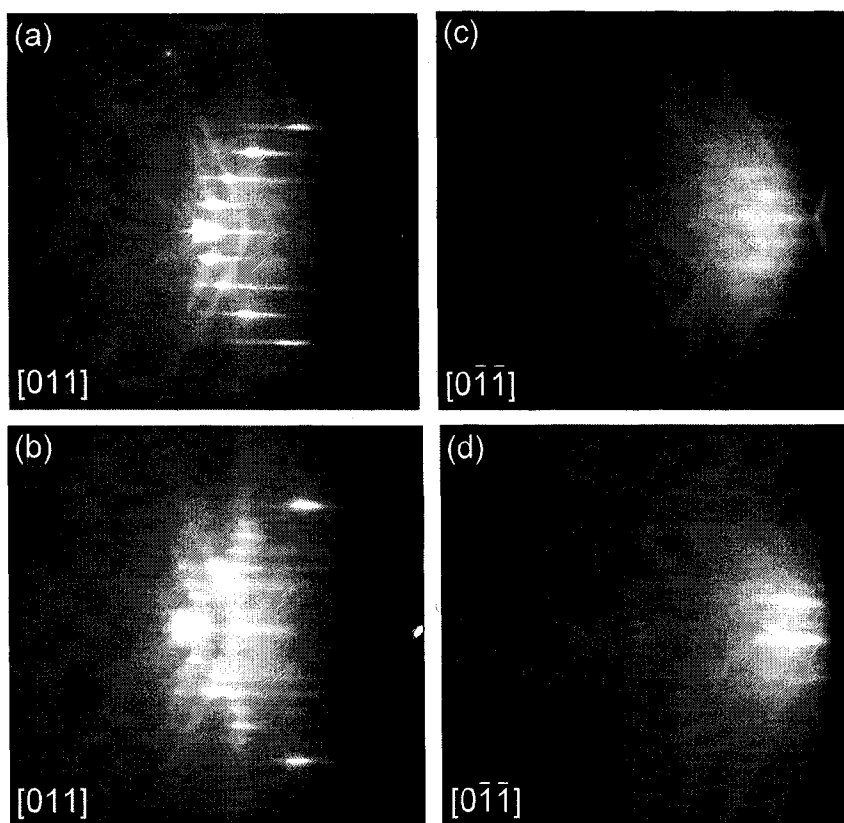


FIG. 4.20. (a) and (b) RHEED patterns of Si(100)-(2 \times 1) surface before In deposition taken along the [011] and $[0\bar{1}\bar{1}]$ azimuths, respectively. (c) and (d) RHEED patterns of In(4 \times 3) grown on Si(100)-(2 \times 1) by fsPLD taken along the [011] and $[0\bar{1}\bar{1}]$ azimuths, respectively. The laser was operated at 2 Hz repetition rate with an energy density of 0.50 J/cm² on the In target.

Figure 4.21 shows the RHEED intensity of the specular beam during growth of In at $T_s = 400$ °C. The laser was operated at 50 Hz repetition rate and an energy density of 0.07 J/cm². At these deposition conditions, the In(4 \times 3) was still observable for ~ 50 s after starting the deposition. With increasing In coverage, a continuous increase in the RHEED

background intensity was observed and the (4×3) RHEED pattern was replaced by a streaky (1×1) pattern. Knall et al. [37] reported that at temperatures less than 450 °C, only a continuous decrease of the diffraction spots and weak In(4×3) RHEED and LEED patterns were still visible at 1000 ML of In, the highest coverage used in their experiment, indicating 3D growth on top of the In(4×3) layer. In our case, the high RHEED background indicated the growth of In islands on the surface. As growth proceeded, shadowing of the incident electron beam by the islands decreased reflections from the In(4×3) underlayer and caused a reduction in the specular beam intensity. For laser energy densities on the In target in the range of 0.07-0.50 J/cm², the transition from Si(100)-(2×1) to In(4×3) reconstruction followed by a transformation to the (1×1) pattern with increasing In coverage. We did not observe bulk transmission diffraction features in RHEED throughout the entire deposition conditions. The morphology of the grown In films was examined ex situ using AFM. Figure 4.22(a) shows an AFM image of an In film grown on Si(100)-(2×1) at 386 °C at coverage of ~38 ML of In. At this coverage, the In(4×3) RHEED pattern was still observable but had a higher background as the In coverage was increased. The laser was operated at 2 Hz repetition rate and the energy density on the In target was 0.50 J/cm². The AFM image shows In islands of almost identical size grown on the surface. Figure 4.22(b) shows a line scan taken over an In island with a rounded shape characterized by a height of ~1 nm and width of ~25 nm. Figure 4.22(c) is a 3D STM image of the film morphology, showing In islands of comparable shape and size distributed over the surface. In a previous MBE growth of In on Si(100)-(2×1), SEM images showed hemispherical In islands of an average diameter of 300 nm with a minimum separation of 500 nm between islands at a film coverage of

15 ML [11]. The streaky (1×1) RHEED pattern, as shown in Fig. 2 at 100 s, and the AFM profile indicate growth of In 2D rounded islands on top of the In(4×3) surface. The rounded shape of the islands show that the In deposits have isotropic growth on the In(4×3) surface compared with the In(2×1) surface structure that forms on Si(100)-(2×1) at room temperature, where anisotropic growth leads to formation of elongated In islands [11, 98].

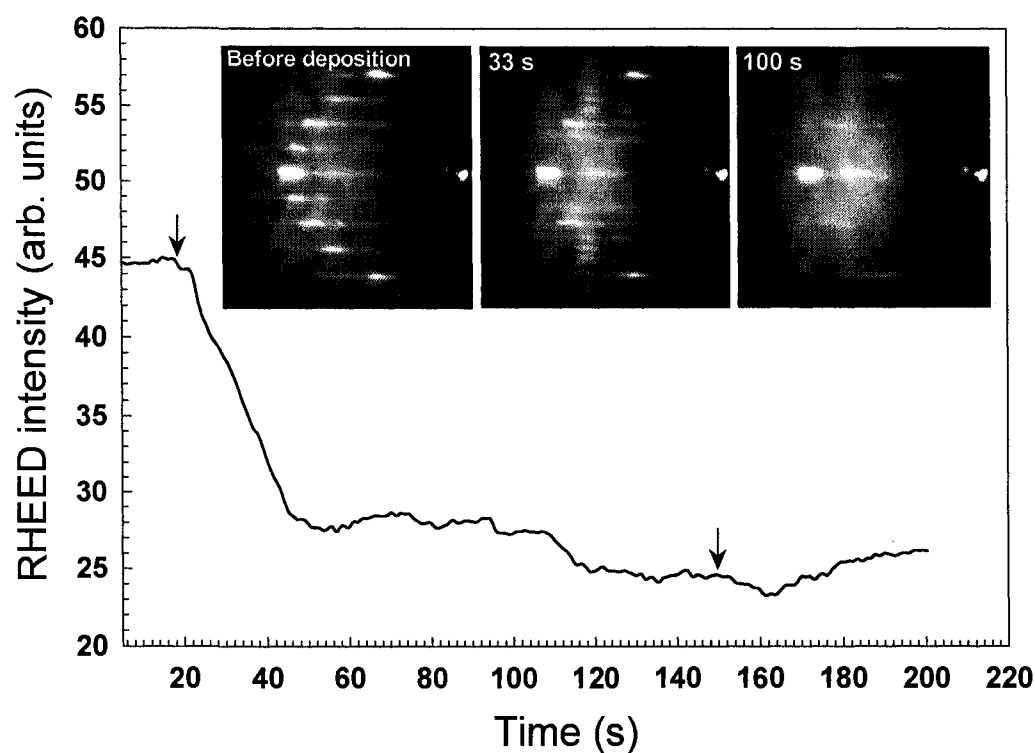


FIG. 4.21. RHEED intensity of the specular beam during growth of In at a substrate temperature of 400 °C. The laser was operated at 50 Hz repetition rate and 0.07 J/cm² laser energy density on the In target. The surface structure changed successively from (2×1) to (4×3) to (1×1) after ~1500 laser shots as shown in the inset RHEED patterns. The RHEED patterns are taken in the [011] azimuth before and during In deposition for 33 s and 100 s. The arrows indicate the time at which the ablating laser was turned on and off.

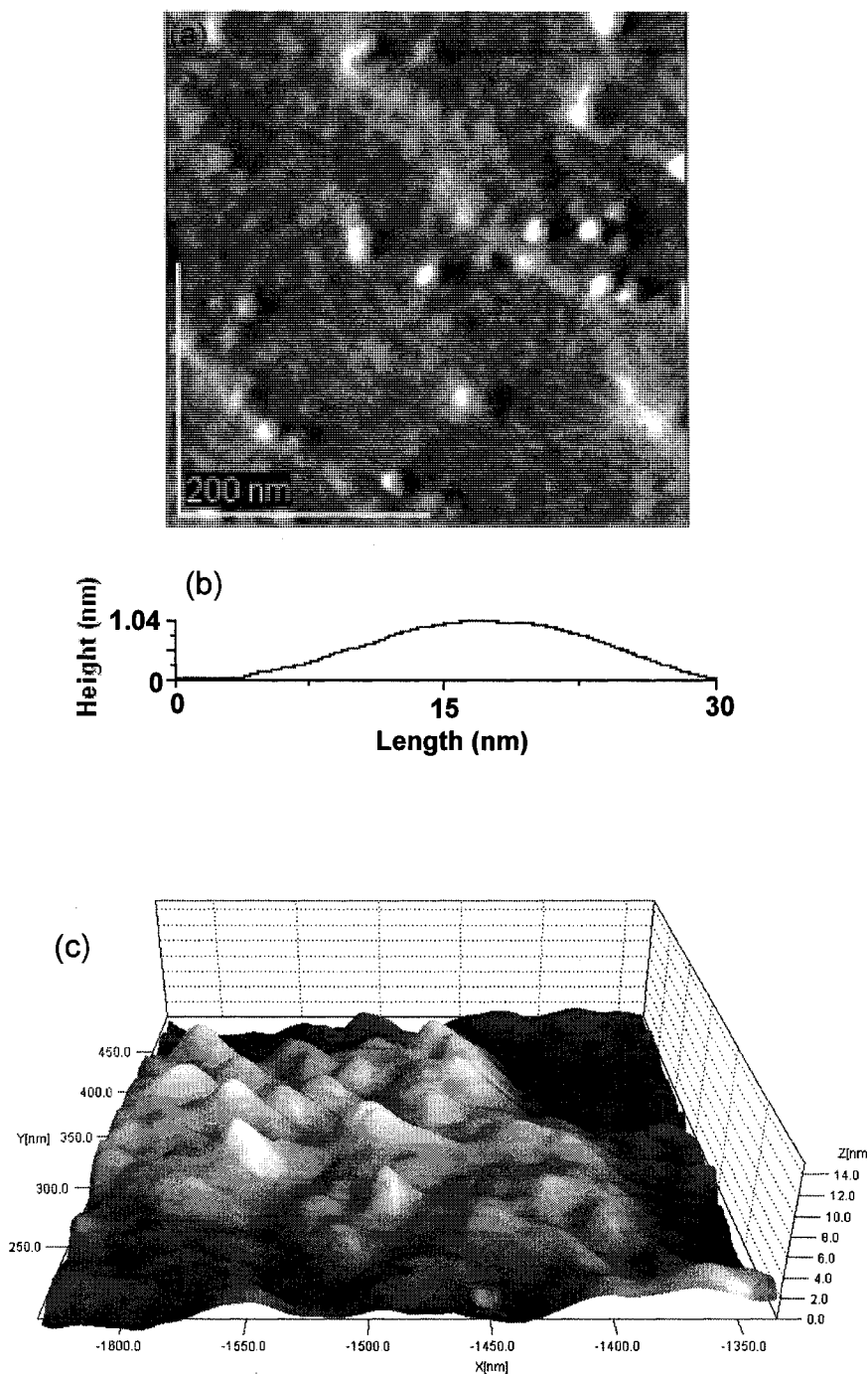


FIG 4.22. (a) AFM image of the grown In film on Si(100)-(2 \times 1) at 386 °C for an In coverage of \sim 38 ML. The laser was operated at 2 Hz repetition rate and the laser energy density was 0.50 J/cm² on the In target. (b) Line profile of an In island shows a rounded shape with height of \sim 1 nm and width of \sim 25 nm. (c) 3D STM image of the In film morphology showing grown islands.

Next, the RHEED intensity was monitored to determine the growth mode and kinetic parameters associated with the formation of the initial $\text{In}(4\times 3)$ structure in the fsPLD of In on $\text{Si}(100)-(2\times 1)$. Figure 4.23 shows the specular beam RHEED intensity during growth of $\text{In}(4\times 3)$ on $\text{Si}(100)-(2\times 1)$ at $T_s = 390^\circ\text{C}$. The laser was operated at 2 Hz repetition rate with an energy density of 0.50 J/cm^2 on the In target. In the first $\sim 1\text{ ML}$, the RHEED intensity relaxes between the deposition laser-pulses. After terminating In deposition, recovery of the RHEED intensity to its initial value was observed. The inset in Fig. 4 shows similar behavior of the RHEED intensity for In film deposited at $T_s = 400^\circ\text{C}$ and 0.37 J/cm^2 ablating laser energy density.

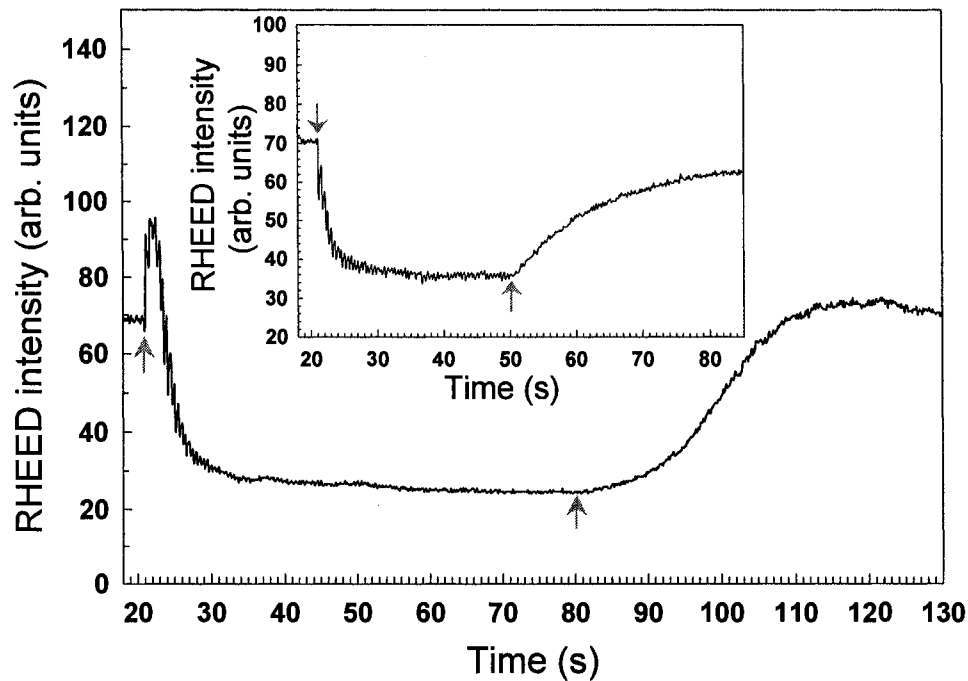


FIG. 4.23. RHEED intensity of the specular beam during growth of In on $\text{Si}(100)-(2\times 1)$ by fsPLD. The In film was grown at a substrate temperature of 390°C using 2 Hz laser repetition rate and an energy density of 0.50 J/cm^2 on the In target. Specular beam intensity is shown in the inset for In film grown at 400°C using 2 Hz laser repetition rate and an energy density of 0.37 J/cm^2 on the In target. Recovery of the RHEED intensity occurred after termination of the deposition. The arrows indicate the time at which the ablating laser was turned on and off.

IV.5.2.2. RHEED intensity relaxation and activation energy

Deposition of In on Si(100)-(2×1) was performed at T_s in the range of 386-405 °C, and the growth was monitored by RHEED. For In coverage of ~6 ML, the RHEED intensities showed full recovery after growth termination similar to Fig. 4.23. Figure 4.24 (a) shows the RHEED specular peak intensity during growth of the first ~2 ML of In at different T_s . These films were grown with a total coverage of ~6 ML. The laser was operated at a 2 Hz repetition rate with an energy density of 0.50 J/cm² on the In target. The primary electron beam was incident along the [011] azimuth, down the staircase of the vicinal Si surface. At $T_s = 386$ °C, the RHEED specular beam intensity decreased and reached a steady value after deposition of ~1 ML. Whereas, for $T_s = 390$ °C and 400 °C, the specular beam intensity increased initially, reaching a peak value, then decreased with deposition time. The increase in the specular beam intensity was higher at $T_s = 400$ °C than at 390 °C. At $T_s = 405$ °C, the specular beam intensity increased to a peak value in the first ~0.5 ML, reaching almost a flat peak that decreased slowly with further deposition. RHEED intensity relaxations were observed in the early stages of the growth of In(4×3) up to the first ~2 ML. The relaxations of the RHEED intensity indicate that surface smoothing took place between pulses during the In growth. The In(4×3) RHEED pattern showed sharp spots lying on the RHEED zeroth Laue semicircle similar to Fig. 4.20(c). The smoothing of the growth is attributed to the energetic effect of the incident In deposits on the substrate surface. Fig. 4.24 (b) shows a magnified RHEED intensity of the specular beam for the sixth to the eleventh laser-pulses during In deposition at $T_s = 390$ °C.

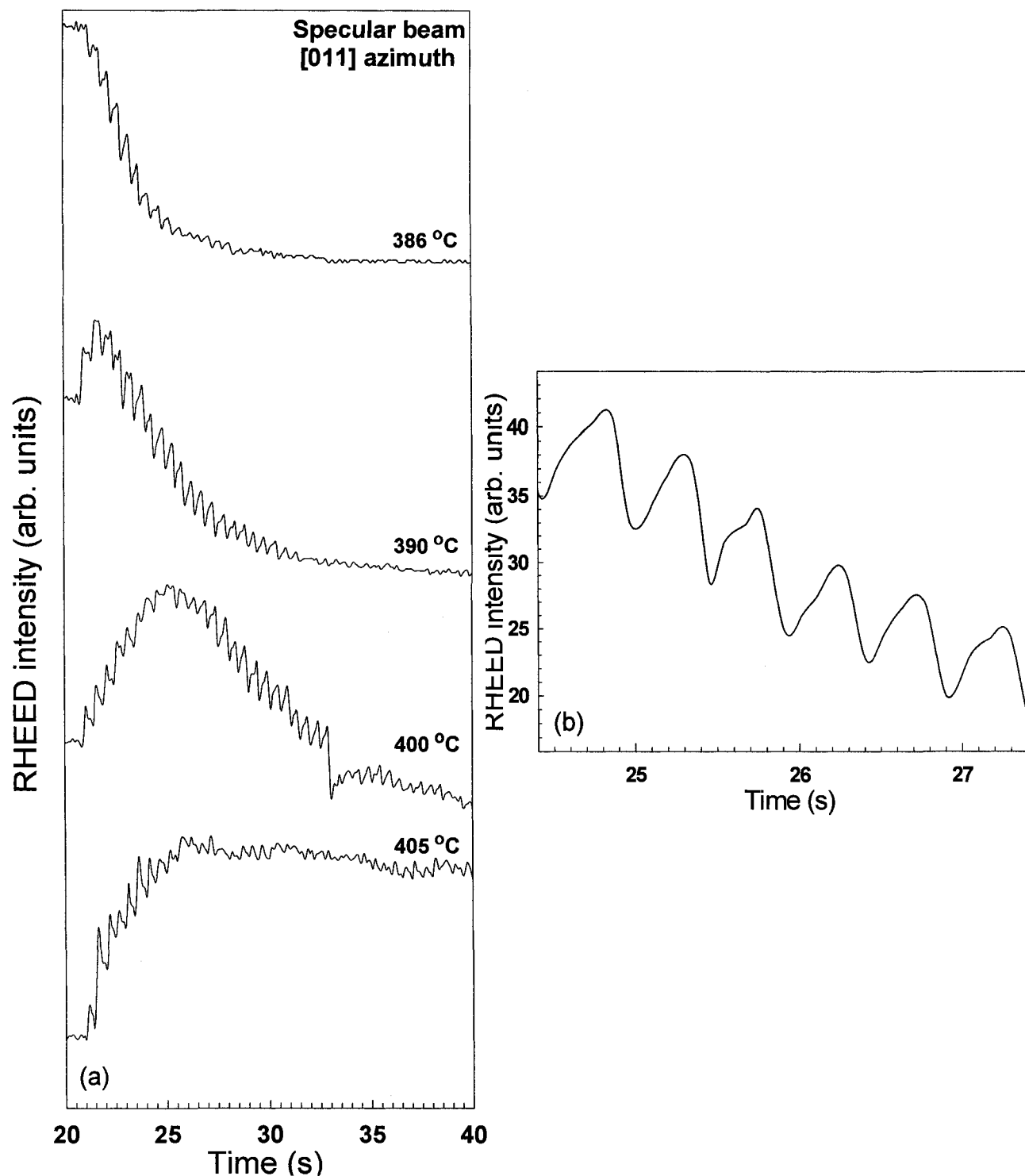


FIG. 4.24. (a) RHEED intensity of the specular beam was monitored during growth of In within the first ~ 2 ML at different substrate temperatures. The laser was operated at a 2 Hz repetition rate with an energy density of 0.50 J/cm^2 on the In target. The primary electron beam was incident along the [011] azimuth down the staircase of the vicinal Si surface. (b) A magnified time scale of RHEED intensity relaxation observed after laser pulses during fsPLD of In on Si(100) at T_s of 390 °C from the sixth to the eleventh laser pulse.

The RHEED intensity oscillates with a period corresponding to the laser pulse repetition rate of 2 Hz. Each laser pulse ablating the In target deposits $\sim 3.4 \times 10^{13}$ atom/cm² of In on the surface. This causes the specularly reflected RHEED intensity to decrease instantaneously because of the increased random distribution of the incoming In deposits on the surface. Then, the deposited In atoms and the formed clusters rearrange on the surface, leading to increased RHEED specular intensity until the arrival of the next In flux. During fsPLD of In on Si, the surface smoothness changed with each laser pulse in a periodic fashion, which can be viewed as a kind of interrupted growth. In contrast, due to the continuous nature of MBE, this feature does not appear. The RHEED intensity relaxations between laser pulses during growth of In was observed to decay after deposition of the first ~ 2 ML of In.

The surface morphology prior to the deposition influenced the growth mode. For the vicinal Si(100)-(2 \times 1) surface, the nucleation sites, such as vacancies and kinks, are located at terrace step edges at which atoms have lower coordination, making them more reactive. RHEED investigation showed that the In surface segregation strength is reduced on vicinal substrates due to the effect of surface steps [99]. It has been shown that no RHEED intensity relaxation takes place after each laser-pulse when the growth mode is 2D layer-by-layer, while RHEED intensity relaxation is observed when the growth mode is step flow [80]. Step flow growth in PLD was previously observed and showed relaxation of RHEED intensity after each laser pulse [80, 100]. The RHEED specular beam intensity development in Fig. 4.23 and 4.24 is indicative of step flow growth. No RHEED oscillations characteristic of layer-by-layer growth were observed. Moreover, the recovery of the specular spot intensity after growth termination observed in Fig. 4.23

rules out increased surface roughness associated with columnar growth. The amount of In deposited in a single pulse, 0.05 ML/pulse, was much smaller than what was needed to grow a single monolayer. Depending on surface diffusion energy, the deposits diffused on the surface reaching terrace step edges.

The RHEED intensity relaxation depends on the growth temperature, as shown in Fig. 4.25. The time dependence of the normalized RHEED intensity for different T_s is shown in the inset of Fig. 4.25. The RHEED relaxation intensities were taken after the eighth laser-pulse, In coverage of ~ 0.5 ML, for each deposition temperature. The relaxations have a rise that is well described by a single exponential in the form $I(t) = A(1 - \exp(-t/\tau))$, where A is a constant and τ represents a time constant for intensity rise. From the curve fits to the RHEED intensity, the time constant τ was found to decrease from 0.10 s to 0.03 s for T_s of 386 and 405 °C, respectively. The characteristic time constant τ of the RHEED intensity relaxation following a laser-pulse is related to the activation energy of surface diffusion by $1/\tau = \nu_0 \exp(-E_d/k_B T_s)$, where ν_0 is the diffusion frequency constant, E_d is the activation energy, and k_B is Boltzmann's constant. The time constant τ has Arrhenius temperature dependence as shown in Fig. 4.25. The data is plotted in a logarithm τ versus $1/T_s$ scale. A least-square fit is used to yield E_d and ν_0 . The activation energy E_d of the surface diffusion for In(4×3) on Si(100)-(2×1) by fsPLD was 1.4 ± 0.2 eV. The diffusion frequency ν_0 measured from the plot is $1.0 \pm 0.1 \times 10^{11} \text{ s}^{-1}$. The vertical and horizontal error bars in the Arrhenius plot represent statistical error and systematic uncertainty in the temperature measurements.

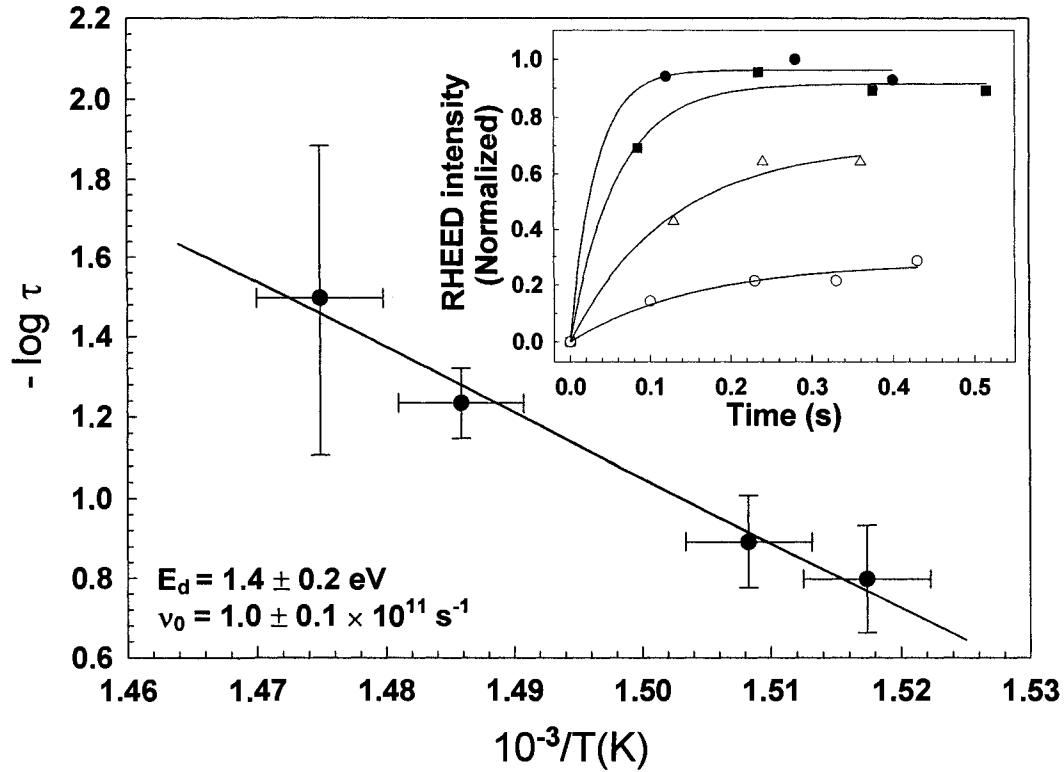


FIG. 4.25. The RHEED intensity relaxation measured at different growth temperatures. The inset shows time dependence of the normalized RHEED intensity taken after the eighth laser deposition pulse, coverage of ~ 0.5 ML of In. The solid lines are exponential fit. The time constant τ has Arrhenius temperature dependence. The activation energy E_d and the diffusion frequency constant ν_0 of the surface diffusion are determined.

In general, the thin film growth mechanism depends on the deposition conditions such as the deposition rate, the incident atom energy and the surface condition. The activation energy depends on these various parameters. In the growth of superconducting thin films by PLD, an activation energy of 0.7 ± 0.1 eV for diffusion of material units have been estimated from the RHEED intensity oscillations [59, 89]. Growth of homoepitaxial SrTiO_3 thin films by PLD at high temperatures (900-1380 °C) showed RHEED intensity modulation at the laser pulse repetition rate. Activation energies of the surface diffusion

of 3.8 ± 0.3 and 3.3 ± 0.2 eV were estimated from the slow surface recovery after growth termination [100]. Such large activation energies were associated with detaching unit cells from kink sites at the edge of small islands [100]. In a MBE study of In on GaAs, activation energy for migration of In adatoms, at a temperature of 450-530 °C, was reported to be 1.6 eV [101]. The activation energy of surface diffusion for the growth of In(4×3) on Si(100)-(2×1) has not been previously reported. Both the energy of the ejected material from the In target and the substrate temperature influence the In(4×3) film growth process. The substrate temperature can affect the mobility of deposits on the surface. According to a Monte Carlo simulation of PLD, the incident particles' kinetic energies can play a similar role in film growth as the increase in substrate temperature [102]. The influence of the former on the activation energy is complex due to the interaction between the incident particles and the surface atoms [102]. Femtosecond PLD is known to result in the formation of a plume containing energetic species [76]. Growth of In on Si(100)-(2×1) by fsPLD at room temperature showed formation of the initial In(2×1) layer, instead of In(2×2) layer as in MBE growth. The In(2×1) is formed by removing the reconstruction of Si(100)-(2×1) surface because of the energetic effect of the In species. This process affects the development of the film morphology [98]. Surface diffusion to the terrace step edges is influenced by the high kinetic energy of In deposits and the local surface lattice heating. The inelastic energy transfer from different In plume species to the surface causes surface lattice heating enhancing surface diffusion.

The diffusion parameters during growth of the In(4×3) layers depend on the type of the diffusing species. The diffusion frequency ν_0 of the adatoms over a surface is known to be in the range 10^{13} s^{-1} (the vibrational frequency) [89]. During growth of

In(4×3) by fsPLD, the diffusion frequency constant determined from the Arrhenius plot $\nu_0 = 1.0 \pm 0.1 \times 10^{11} \text{ s}^{-1}$ is two orders of magnitude lower than that for adatoms. This indicates that the rate limiting process is due to surface diffusion of clusters rather than of adatoms. The kinetics of In growth can be explained by the energetic and pulsed nature of PLD. The plume species that are mainly In atoms reach the surface and initially occupy disordered sites. The high instantaneous deposition rate results in high nucleation density on the surface. Subsequently, the In atoms form small clusters that diffuse on the surface before they reach the terrace step edges. The diffusion frequency constant ν_0 , obtained from RHEED intensity relaxation, is that of cluster diffusion. Previous experimental observation of fast diffusion of clusters and 2D island diffusion on surfaces were reported [90-92]. In a proposed model of heteroepitaxy growth by PLD, a diffusion frequency constant of 10^7 s^{-1} was obtained and referred to as diffusion of material units rather than adatoms [89]. For In(4×3) growth on vicinal Si(100)-(2×1) by fsPLD, formation of small In clusters occurred during the high supersaturation period of a deposition pulse followed by surface diffusion of the small clusters to surface step edges with $E_d = 1.4 \pm 0.2 \text{ eV}$.

IV.5.2.3. Terrace width growth dynamics

The use of a vicinal Si(100)-(2×1) surface as a substrate enables the study of the influence of terrace step edges on In growth by PLD. Real-time RHEED patterns were acquired in the out-of-phase diffraction condition in order to measure the average terrace width during the growth of In on Si. In the out-of-phase condition, incident electrons scattered from different surface layers interfere destructively. This results in a splitting of the specular RHEED beam for a vicinal surface when the electron beam direction has a

component down the staircase. The diffracted beam profiles are sensitive to terrace periodicity and step edges disorder. Kinematical approaches were previously utilized for quantitative analysis of RHEED during thin film growth on vicinal surfaces [103, 104]. The average terrace width of the clean vicinal Si(100)-(2×1) surface was measured prior to In deposition as discussed in section IV.5.1.2.1. The splitting of the specular beam was observed by the RHEED pattern along the [011] azimuth in $S_{//}$ direction, as shown in Fig. 4.12. The average terrace width of the Si(100)-(2×1) surface was obtained to be $L = 61 \pm 10 \text{ \AA}$. The average terrace width depends on the misorientation angle from the low-index (100) plane. For a cleaned vicinal Si(100) surface tilted 4° towards [011], STM showed terraces 40-45 \AA in widths [45]. No inner potential correction is needed since the interference condition in RHEED depends only on the extra external path length; a refraction correction at the top or bottom of a step would be identical and thus cancels [103]. Dynamic interaction due to surface wave resonance does not change the splitting or streak asymmetry [105].

The temporal evolution of the terrace width during growth of In(4×3) was measured by directing the RHEED electron beam down the staircase, along the [011] azimuth of the Si surface, and line scans were taken over the splitting peaks with a frame rate of 7-8 frame/s. The split peak spacing was measured during In growth at different growth temperatures and laser energy densities. Figure 4.26 shows the average terrace width L during growth of In at T_s of 358 °C. The laser was operated at 2 Hz repetition rate with an energy density of 0.50 J/cm² on the In target. L decreased from $61 \pm 10 \text{ \AA}$ to $53 \pm 8 \text{ \AA}$ during growth of the first ~11 ML of In. The width of the split peaks, which is related to defects, decreased slightly with deposition time. The inset of Fig. 4.26 shows RHEED

intensity profiles taken across one of the split peaks, in S_{\perp} direction, before and during the deposition at ~ 1 ML and ~ 7.6 ML. The corresponding FWHM extracted from a Lorentzian fit to the intensity profiles were 0.24 \AA^{-1} , 0.21 \AA^{-1} , and 0.20 \AA^{-1} , respectively. Growth of $\text{In}(4\times 3)$ by two different laser ablation energy densities of 0.25 J/cm^2 and 0.50 J/cm^2 at T_s of 400°C showed decrease of the average terrace width to $49\pm 7 \text{ \AA}$ and $52\pm 8 \text{ \AA}$, respectively, as shown in Fig. 4.27. The decrease in the average terrace width during growth of In indicates alternation of the terrace edge morphology.

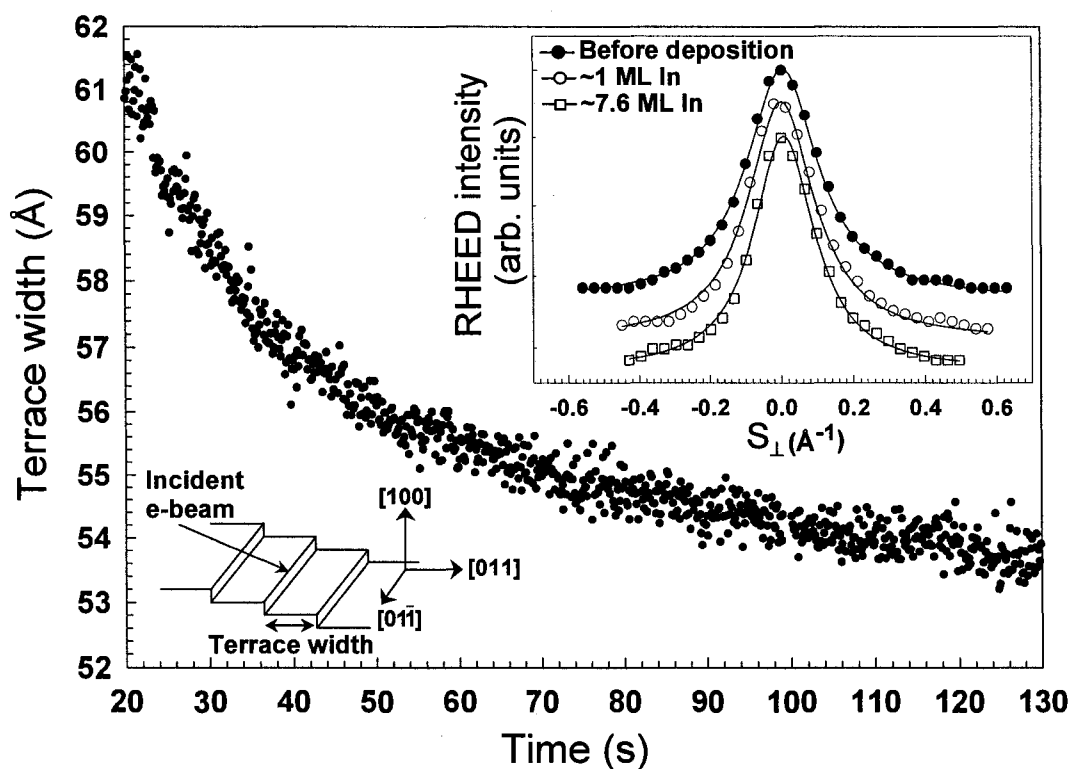


FIG. 4.26. The average terrace width L during growth of In at T_s of 358°C on the vicinal $\text{Si}(100)-(2\times 1)$ surface. The laser was operated at a 2 Hz repetition rate and an energy density of 0.50 J/cm^2 on the In target. The primary electron energy of 8.6 keV was incident down the staircase along the $[011]$ azimuth of the Si surface. L was decreasing during growth of the first $\sim 11 \text{ ML}$ of In . RHEED intensity profiles taken across one of the split peaks, in S_{\perp} direction, before and during the deposition at $\sim 1 \text{ ML}$ and $\sim 7.6 \text{ ML}$ are shown in the inset. The FWHM is measured from a Lorentzian fit to the intensity profiles. A schematic diagram of a vicinal surface is shown in the inset.

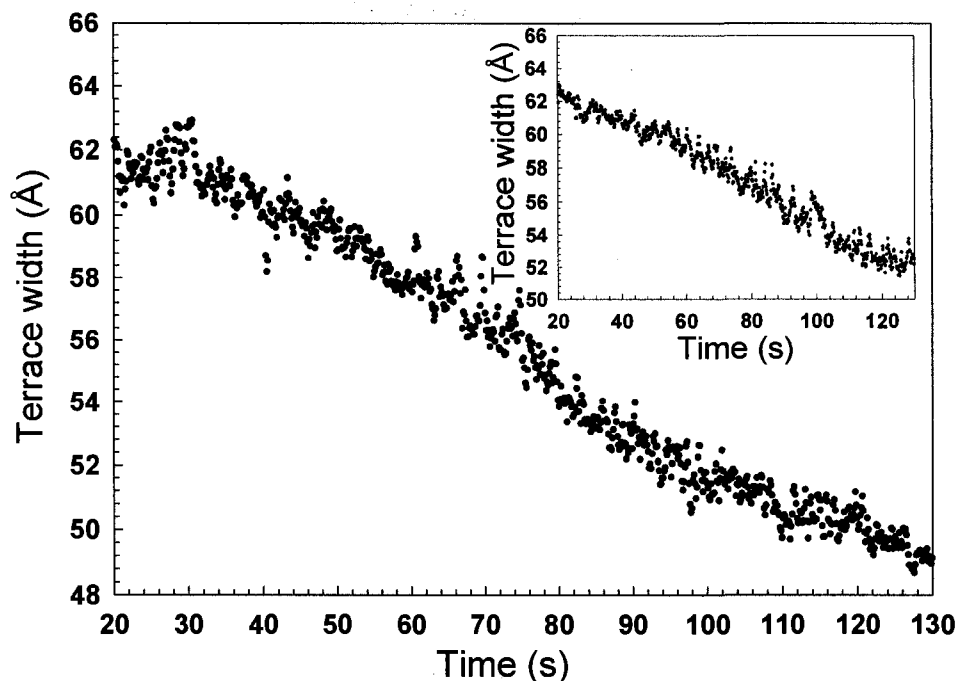


FIG. 4.27. The average terrace width L during fsPLD of In by two different laser energy densities of 0.25 J/cm^2 and 0.50 J/cm^2 (inset) for ablation of In target. The laser was operated at 2 Hz repetition rate and the growth temperature T_s was 400°C . The 8.6 keV electron beam was incident down the staircase along the $[011]$ azimuth of the Si surface.

The variation of the average terrace width during In growth on the vicinal Si(100)-(2×1) depends on the deposition conditions. STM study showed step rearrangement on vicinal Si(100) induced by In adsorption and annealing [51]. At an annealing temperature of 500°C , STM showed an increase of terrace width from 40 Å to $\geq 200 \text{ Å}$, which occurred by step bunching. The original step direction of $[0\bar{1}1]$ changed to a preferred low-index $[010]$ and $[001]$ directions, and the terraces widened to $\sim 400 \text{ Å}$ after annealing at 510°C [51]. Using reflection electron microscopy, step bunching on a Si(001) vicinal surface during Au deposition resulted in an increase of the terrace width

with deposition time [106]. Step bunching occurs when the steps on the vicinal surface become unstable and come together to form strips of high and low step density. This results in changing the terrace width distribution. If the RHEED electron beam is incident along the miscut direction, step bunching causes a decrease of the splitting angle $d\theta$. We observed an increase of $d\theta$ during In growth, indicating a decrease in the split peak spacing L . Previous studies have shown that the average terrace width of vicinal surfaces decreased with deposition time or temperature [85, 107, 108]. Moreover, roughening or meandering at the step edges increases disorder at terraces edges, which, for a stepped surface, causes fluctuation in the terrace width [109]. If the degree of disorder were high, the electrons would effectively traverse more up and down steps along its path. This causes the diffracted beam to broaden, and the staircase could be lined up in other low-index directions, leading to a decrease or disappearance of the split peak spacing from the miscut direction of the vicinal Si surface [109]. In the present study, the split peak spacing, measured for the [011] azimuth, remained at its maximum with further In deposition.

The change in the terrace width distribution during In growth suggests that collective surface processes occurred. The sticking probability of In on Si(100) become appreciably less than unity as the temperature is increased above 550 °C where In desorption becomes considerable [11, 86]. In our study, a strong (4×3) pattern was observed at substrate temperatures of 350-420 °C. Li et al. [51] showed that the In(4×3) on the Si(100) terraces did not desorb at temperatures below 500 °C. This was consistent with the desorption kinetics studies of Knall et al. [37], who determined that the binding energy of In on top of the (4×3) surface is lower than that of In in the (4×3) surface, 2.45

eV versus 2.85 eV respectively, implying that it is more difficult to desorb In from a (4×3) surface than from In on top of it. The detachment of In atoms from step edges is more likely than direct desorption from the step edges because the former process generally has a smaller activation energy [110].

In the reciprocal lattice of a vicinal surface, the split peak results from the intersection of the Ewald sphere with the lattice rods of the terrace edges. Changes in the terrace edge morphology can be qualitatively observed by the RHEED diffraction pattern. Surface atoms at step edges have lower coordination than atoms at terraces, making them less stable, particularly at high temperatures. The observed decrease of the average terrace width could be attributed to the detachment of In atoms from step edges followed by diffusion on the terrace surface. The In atoms can then form clusters and/or desorb from the surface. Previous work by dark-field LEEM showed that rearrangement of the Si(001) surface occurred through etching of the Si surface by In at temperatures greater than 650 °C.¹⁹ This suggests that etching by energetic In deposits occurs preferentially at terrace edges of the Si surface, which could be the cause of the observed decrease of the average terrace width at the beginning of the deposition.

Figure 4.28 shows the time evolution of the average terrace width L during In growth at T_s of 405 °C for a total coverage of ~38 ML. The RHEED pattern of In(4×3) taken after deposition of ~38 ML is shown in the inset of Fig. 4.28. The splitting of the specular beam indicates that the In film forms a staircase in the [011] azimuth of the Si surface due to growth by step flow. The deposition was started at time 20 s. The laser was operated at 2 Hz repetition rate with an energy density of 0.50 J/cm² on the In target. The terrace width L decreased from 61±10 Å to an equilibrium value of 45±7 Å after

deposition of ~ 23 ML of In. From the start of the deposition until the deposition time was ~ 230 s, which is the range at which the terrace width was decreasing, the $\text{In}(4\times 3)$ film grew by step flow. At 230 s, corresponding to coverage of ~ 23 ML, the terrace width reached a steady value.

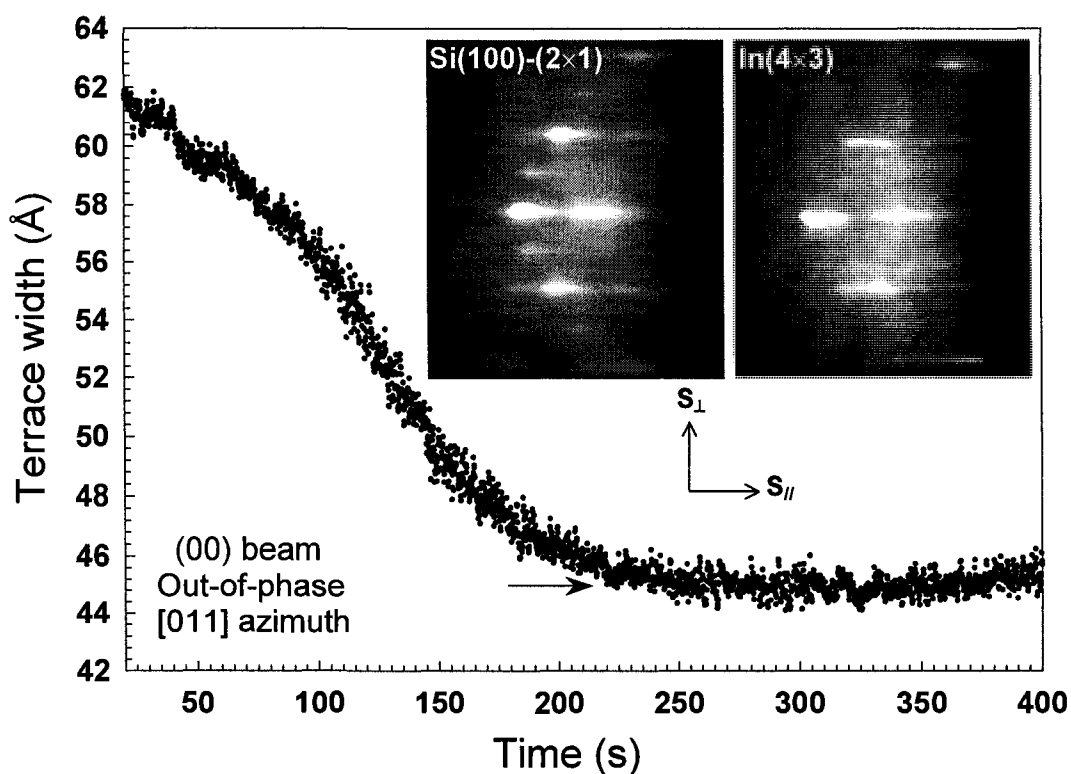


FIG. 4.28. The average terrace width L during growth of In by fsPLD at T_s of 405 °C on the vicinal $\text{Si}(100)\text{--}(2\times 1)$ surface. The laser was operated at a 2 Hz repetition rate and an energy density of 0.50 J/cm² on the In target. The 8.6 keV electron beam was incident down the staircase along the [011] azimuth of the Si surface. L decreased until an equilibrium reached after deposition of ~ 23 ML of In. The arrow indicates the equilibrium L . The $\text{In}(4\times 3)$ RHEED pattern remained observable during the deposition. In the inset, RHEED patterns of $\text{Si}(100)\text{--}(2\times 1)$ before deposition and $\text{In}(4\times 3)$ for In coverage of ~ 38 ML are shown. The splitting of the specular beam was along the [011] azimuth of the vicinal $\text{Si}(100)$ surface and parallel to the RHEED shadow edge.

Because of surface processes such as detachment of In atoms from step edges, competition between growth by step flow and growth on surface terraces arises as the film coverage was increased. Also, with the increase in coverage, the concentration of In on surface terraces increased and the growth of the In film could be a mixture of In islands formation and step flow growth over part of the surface. When the equilibrium terrace width was reached, the possibility of growth of In islands increased. At high film coverage more than 38 ML, the density and size of islands increased on surface terrace, which gave rise to a (1×1) RHEED pattern and the disappearance of the (4×3) RHEED pattern.

IV.6. Conclusion

The growth dynamics, structure, and morphology of In on vicinal Si(100)-(2×1) surface by fsPLD were studied using in situ RHEED and ex situ AFM or STM. The growth of In on Si(100)-(2×1) vicinal surface by fsPLD is followed the SK mode. At RT, the initial 2D layer was formed in the In(2×1) structure and the in-plane lattice spacing was changed during the growth toward a strained layer of 3.65 Å. On the 2D In(2×1) layer, surface order recovery was observed during deposition and after growth termination. The periodic change in surface smoothness led to the observed RHEED intensity relaxation between the laser depositing pulses. The recovery and relaxation of the RHEED intensity are attributed to the step flow mode of the 2D growth stage. The surface diffusion coefficient of deposited In was measured by quantitative RHEED. The FWHM of the RHEED specular beam decreased during the deposition, indicative of

well-ordered growth and an increase of the island size. As growth proceeds, 3D islands developed into polyhedral-elongated, circular, hexagonal and triangular shapes. The occurrence of these 3D In island morphology indicates that the growth was caused to undergo the influence of the structure of the 2D In(2×1) layer and In diffusion. The results suggest that fsPLD of In removed the reconstruction of the Si(100)-(2×1) surface in the early growth and formed the initial In(2×1) layer.

In the temperature range of 350-410 °C, In layers formed in the In(4×3) structure. Unlike thermal evaporation, the energetic and pulsed nature of PLD led to the creation of mobile In clusters enhancing the 2D growth. The growth of the In(4×3) layers occurred by the step flow mode. The growth stages of the In(4×3) layer, probed by RHEED intensity relaxation, proceeds in a two-step-process; formation of small In clusters and surface diffusion to the terrace step edges with a characteristic activation energy E_d and a diffusion rate constant v_0 . The estimation of the E_d and v_0 were determined from Arrhenius relation. During growth of the In film, reduction of the average terrace width occurred and was attributed to detachment of In atoms from terrace edges. As In coverage was increased, the terrace width reached an equilibrium length, where the possibility of growth of In islands increased. Observation of the RHEED pattern transition from (4×3) to (1×1) was associated with growth of In islands on the terrace surfaces. AFM profile indicated rounded islands with an average height of ~1 nm and width of ~25 nm.

IV.7. References

- [1] A. A. Baski, J. Nogami, and C. F. Quate, "Indium-induced reconstructions of the Si(100) surface," *Phys. Rev. B* **43**, 9316-9319 (1991).
- [2] J. Nogami, A. A. Baski, and C. F. Quate, "Aluminum on the Si(100) surface: Growth of the first monolayer," *Phys. Rev. B* **44**, 1415-1418 (1991).
- [3] H. Itoh, J. Itoh, A. Schmid, and T. Ichinokawa, "Structures of low-coverage phases of Al on the Si(100) surface observed by scanning tunneling microscopy," *Phys. Rev. B* **48**, 14663-14666 (1993).
- [4] H. W. Yeom, T. Abukawa, M. Nakamura, S. Suzuki, S. Sato, K. Sakamoto, T. Sakamoto, and S. Kono, "Initial stage growth of In and Al on a single-domain Si(001) 2×1 surface," *Surf. Sci.* **341**, 328-334 (1995).
- [5] N. Takeuchi, "Adsorption of group III and group V metals on Si(001): One-dimensional versus two-dimensional growth," *Phys. Rev. B* **63**, 035311 (1-5) (2001).
- [6] D. J.-L. Li, X.-L. Liang, J.-F. Jia, X. Liu, J.-Z. Wang, E.-G. Wang, and Q.-K. Xue, "Spontaneous formation of ordered indium nanowire array on Si(001)," *Appl. Phys. Lett.* **79**, 2826-2828 (2001).
- [7] J.-Z. Wang, J.-F. Jia, X. Liu, W.-D. Chen, and Q.-K. Xue, "Ordered Ga wires formed on Si(100)- $2 \times n$: Scanning tunneling microscopy study," *Phys. Rev. B* **65**, 235303 (1-5) (2002).
- [8] J.-L. Li, J.-F. Jia, X.-J. Liang, X. Liu, J.-Z. Wang, Q.-K. Xue, Z.-Q. Li, J. S. Tse, Z. Zhang, and S. B. Zhang "Spontaneous assembly of perfectly ordered identical-size nanocluster arrays," *Phys. Rev. Lett.* **88**, 066101 (1-4) (2002).

- [9] P. C. Sharma, K. W. Alt, D. Y. Yeh, and K. L. Wang, "Temperature-dependent morphology of three-dimensional InAs islands grown on silicon," *Appl. Phys. Lett.* **75**, 1273-1275 (1999).
- [10] B. H. Koo, T. Hanada, H. Makino, J. H. Chang, and T. Yao, "RHEED investigation of the formation process of InAs quantum dots on (1 0 0) InAlAs/InP for application to photonic devices in the 1.55 μm range," *J. Cryst. Growth* **229**, 142-146 (2001).
- [11] J. Knall, J.-E. Sundgren, G. V. Hansson, and J. E. Greene, "Indium overlayers on clean Si(100)-(2 \times 1): Surface structure, nucleation, and growth," *Surf. Sci.* **166**, 512-538 (1986).
- [12] M. M. R. Evans, J. C. Glueckstein, and J. Nogami, "Indium on Si(001): Growth beyond the first atomic layer," *Surf. Sci.* **406**, 246-253 (1998).
- [13] J.-T. Ryu, K. Kui, K. Noda, M. Katayama, and K. Oura, "The effect of hydrogen termination on In growth on Si(100) surface," *Surf. Sci.* **401**, L425-L431 (1998).
- [14] M. M. R. Evans and J. Nogami, "Indium and gallium on Si(001): A closer look at the parallel dimer structure," *Phys. Rev. B* **59**, 7644-7648 (1999).
- [15] J. T. Ryu, O. Kubo, H. Tani, T. Harada, M. Katayama, and K. Oura, "The growth of indium thin films on clean and hydrogen-terminated Si(100) surfaces," *Surf. Sci.* **433-435**, 575-580 (1999).
- [16] A. A. Baski, J. Nogami, and C. F. Quate, "Gallium growth and reconstruction on the Si(100) surface," *J. Vac. Sci. Technol. A* **8**, 245-248 (1990).
- [17] A. A. Baski, J. Nogami, and C. F. Quate, "Evolution of the Si(100)-2 \times 2-In reconstruction," *J. Vac. Sci. Technol. A* **9**, 1946-1950 (1991).

- [18] O. Kubo, J. T. Ryu, H. Tani, T. Harada, M. Katayama, and K. Oura, "Direct observation of strained layer formation at the initial stage of In thin film growth on Si(100)," *Jpn. J. Appl. Phys., Part 1* **38**, 3849-3852 (1999).
- [19] T. Chen, X. M. Li, and S. Zhang, "Enhanced strain relaxation induced by epitaxial layer growth mode of MgO thin films," *Solid State Commun.* **131**, 523-526 (2004).
- [20] L. S.-J. Peng, X. X. Xi, B. H. Moeckly, and S. P. Alpay, "Strain relaxation during in situ growth of SrTiO₃ thin films," *Appl. Phys. Lett.* **83**, 4592-4594 (2003).
- [21] F. Qian, R. K. Singh, S. K. Dutta, and P. P. Pronko, "Laser deposition of diamondlike carbon films at high intensities," *Appl. Phys. Lett.* **67**, 3120-3122 (1995).
- [22] B. V. Rao, M. Atoji, D. M. Li, T. Okamoto, T. Tambo, and C. Tatsuyama, "In(4×3) reconstruction mediated heteroepitaxial growth of InSb on Si(001) substrate," *Jpn. J. Appl. Phys., Part 1* **37**, L1297-L1300 (1998).
- [23] P. C. Sharma, K. W. Alt, D. Y. Yeh, and K. L. Wang, "Temperature-dependent morphology of three-dimensional InAs islands grown on silicon," *Appl. Phys. Lett.* **75**, 1273-1275 (1999).
- [24] J. Y. Park and R. J. Phaneuf, "Polarity dependence in pulsed scanning tunneling microscopy fabrication and modification of metal nanodots on silicon," *J. Appl. Phys.* **92**, 2139-2143 (2002).
- [25] Y. Temko, T. Suzuki, and K. Jacobi, "Shape and growth of InAs quantum dots on GaAs(113)A," *Appl. Phys. Lett.* **82**, 2142-2144 (2003).

- [26] H. Busch and M. Henzler, "Domain-growth kinetics of Ag on Ge(111)," *Phys. Rev. B* **41**, 4891-4896 (1990).
- [27] J. H. Neave, P. J. Dobson, B. A. Joyce, and J. Zhang, "Reflection high-energy electron diffraction oscillations from vicinal surfaces – A new approach to surface diffusion measurements," *Appl. Phys. Lett.* **47**, 100-102 (1985).
- [28] N. Bertru, M. Nouaoura, J. Bonnet, and L. Lassabatere, "GaSb molecular beam epitaxy growth on vicinal surfaces studied by RHEED," *J. Cryst. Growth* **160**, 1-6 (1996).
- [29] J. H. Neave, B. A. Joyce, P. J. Dobson, and N. Norton, "Dynamics of film growth of GaAs by MBE from RHEED observations," *Appl. Phys. A* **31**, 1 (1983).
- [30] H. Sakaki, M. Tanaka and J. Yoshino, "One atomic layer heterointerface fluctuations in GaAs-AlAs quantum well structures and their suppression by insertion of smoothing period in molecular beam epitaxy," *Jpn. J. Appl. Phys.* **24**, L417-L420 (1985).
- [31] A. Madhukar, T. C. Lee, M. U. Yen, P. Chen, J. Y. Kim, S. V. Ghaisas, and P. G. Newman, "Role of surface kinetics and interrupted growth during molecular beam epitaxial growth of normal and inverted GaAs/AlGaAs(100) interfaces: A reflection high-energy electron diffraction intensity dynamics study," *Appl. Phys. Lett.* **46**, 1148-1150 (1985).
- [32] B. F. Lewis, F. J. Grunthaner, A. Madhukar, T. C. Lee, and R. Fernandez, "Reflection high energy electron diffraction intensity behavior during homoepitaxial molecular beam epitaxy growth of GaAs and implications for growth kinetics and mechanisms," *J. Vac. Sci. Technol. B* **3**, 1317-1322 (1985).

- [33] S. Clarke, D. D. Vvedensky, and M. W. Ricketts, "Influence of surface morphology upon recovery kinetics during interrupted epitaxial growth," *J. Cryst. Growth* **95**, 28-31 (1989).
- [34] S. V. Ghaisas and A. Madhukar, "Surface kinetics and growth interruption in molecular-beam epitaxy of compound semiconductors: A computer simulation study," *J. Appl. Phys.* **65**, 3872-3876 (1989).
- [35] D. D. Vvedensky and S. Clarke, "Recovery kinetics during interrupted epitaxial growth," *Surf. Sci.* **225**, 373-389 (1990).
- [36] N. Kuwata, T. Asai, K. Kimura, and M. Mannami, "Superlattice structures of Si(100) surfaces deposited with In and Sn atoms," *Surf. Sci.* **143**, L393- L397 (1984).
- [37] J. Knall, S. A. Barnett, J.-E. Sundgren, and J. E. Greene, "Adsorption and desorption kinetics of In on Si(100)," *Surf. Sci.* **209**, 314-334 (1989).
- [38] V. G. Kotlyar, A. V. Zotov, A. A. Saranin, T. V. Kasyanova, M. A. Cherevik, O. V. Bekhtereva, M. Katayama, K. Oura, and V. G. Lifshits, "Magic nanoclusters of group III metals on Si(100) surface," *e-J. Surf. Sci. Nanotech.* **1**, 33-40 (2003).
- [39] V. G. Kotlyar, A. V. Zotov, A. A. Saranin, E. N. Chukurov, T. V. Kasyanova, M. A. Cherevik, I. V. Pisarenko, H. Okado, M. Katayama, K. Oura, and V. G. Lifshits, "Doping of magic nanoclusters in the submonolayer In/Si(100) system," *Phys. Rev. Lett.* **91**, 026104(1-4) (2003).
- [40] J. R. Ahn, J. H. Byun, W. H. Choi, H. W. Yeom, H. Jeong, and S. Jeong, "Nonmetallic nature of In-induced nanoclusters on Si(100)," *Phys. Rev. B* **70**, 113304(1-4) (2004).

- [41] A. A. Saranin, A. V. Zotov, V. G. Kotlyar, H. Okado, M. Katayama, and K. Oura, "Modified Si(100)4×3-In nanoclusters arrays," *Surf. Sci.* **598**, 136-143 (2005).
- [42] A. A. Saranin, A. V. Zotov, I. A. Kuyanov, M. Kishida, Y. Murata, S. Honda, M. Katayama, K. Oura, C. M. Wei, and Y. L. Wang, "Atomic dynamics of In nanoclusters on Si(100)," *Phys. Rev. B* **74**, 125304(1-4) (2006).
- [43] A. V. Zotov, A. A. Saranin, V. G. Lifshits, J.-T. Ryu, O. Kubo, H. Tani, M. Katayama, and K. Oura, "Structural model for the Si(100)4×3-In surface phase," *Phys. Rev. B* **57**, 12492-12496 (1998).
- [44] A. A. Saranin, A. V. Zotov, V. G. Lifshits, J.-T. Ryu, O. Kubo, H. Tani, T. Harada, M. Katayama, and K. Oura, "Analysis of surface structures through determination of their composition using STM: Si(100)4×3-In and Si (111)4×1-In reconstructions," *Phys. Rev. B* **60**, 14372-14381 (1999).
- [45] B. E. Steele, D. M. Cornelison, L. Li, and I. S. T. Tsong, "The structure of the Si(100)-(4×3)In surface studied by STM and ICISS," *Nucl. Instr. and Meth. in Phys. Res. B* **85**, 414-419 (1994).
- [46] O. Bunk, G. Falkenberg, L. Seehofer, J. H. Zeysing, R. L. Johnson, M. Nielsen, R. Feidenhans'l, and E. Landemark, "Structure determination of the indium induced Si(001)-(4×3) reconstruction by surface X-ray diffraction and scanning tunneling microscopy," *Appl. Surf. Sci.* **123/124**, 104-110 (1998).
- [47] O. Bunk, G. Falkenberg, J. H. Zeysing, R. L. Johnson, M. Nielsen, and R. Feidenhans'l, "Comment on "Structural model for the Si(001) 4×3-In surface phase"," *Phys. Rev. B* **60**, 13905-13906 (1999).

- [48] N. Takeuchi, "First-principles calculations of the atomic structure of the In-induced Si(001)-(4×3) reconstruction," *Phys. Rev. B* **63**, 245325(1-7) (2001).
- [49] T. M. Schmidt, J. L. P. Castineira, and R. H. Miwa, "Solving the structural model for the Si(001)-In(4×3) surface," *Appl. Phys. Lett.* **79**, 203-205 (2001).
- [50] P. J. E. Reese, T. Miller, and T.-C. Chiang, "Photoelectron holography of the In-terminated Si(001)-(4×3) surface," *Phys. Rev. B* **64**, 233307(1-4) (2001).
- [51] L. Li, Y. Wei, and I. S. T. Tsong, "Reconstruction, step-bunching and faceting of a vicinal Si(100) surface induced by indium adsorption," *Surf. Sci.* **304**, 1-11 (1994).
- [52] H. A. McKay and R. M. Feenstra, "Low energy electron microscopy of indium on Si(001) surfaces," *Surf. Sci.* **547**, 127-138 (2003).
- [53] A. V. Zotov, A. A. Saranin, K. V. Ignatovich, V. G. Lifshits, M. Katayama, and K. Oura, "Si(100)4×3-In surface phase: identification of silicon substrate atom reconstruction," *Surf. Sci.* **391**, L1188-L1193 (1997).
- [54] J. T. Ryu, T. Fuse, O. Kubo, T. Fujino, H. Tani, T. Harada, A. A. Saranin, A. V. Zotov, M. Katayama, and K. Oura, "Adsorption of atomic hydrogen on the Si(001) 4×3-In surface studied by coaxial impact collision ion scattering spectroscopy and scanning tunneling microscopy," *J. Vac. Sci. Technol. B* **17**, 983-988 (1999).
- [55] J. C. Miller and R. F. Haglund, "*Laser ablation and desorption*," *Experimental Methods in the Physical Sciences* **30**, Academic Press, Boston (1998).
- [56] J. Shen, Z. Gai, and J. Kirschner, "Growth and magnetism of metallic thin films and multilayers by pulsed-laser deposition," *Surf. Sci. Rep.* **52**, 163-218 (2004).

- [57] H. Jenniches, M. Klaua, H. Hoche, and J. Kirschner, "Comparison of pulsed laser deposition and thermal deposition: Improved layer-by-layer growth of Fe/Cu(111)," *Appl. Phys. Lett.* **69**, 3339-3341 (1996).
- [58] G. Koster, G. J. H. M. Rijnders, D. H. A. Blank, and H. Rogalla, "Imposed layer-by-layer growth by pulsed laser interval deposition," *Appl. Phys. Lett.* **74**, 3729-3731 (1999).
- [59] H. Karl and B. Stritzker, "Reflection high-energy electron diffraction oscillations modulated by laser-pulse deposited $\text{YBa}_2\text{Cu}_3\text{O}_{7-x}$," *Phys. Rev. Lett.* **69**, 2939-2942 (1992).
- [60] Z. Zhang and M. G. Lagally, "Atomistic processes in the early stages of thin-film growth," *Science* **276**, 377-383 (1997).
- [61] K. Oura, V. G. Lifshits, A. A. Saranin, A. V. Zotov, and M. Katayama, "*Surface Science, An Introduction*," Springer-Verlag, Berlin (2003).
- [62] J. A. Venables, "*Introduction to Surface and Thin Film Processes*," Cambridge University Press, Cambridge (2000).
- [63] J. R. Arthur, "Molecular beam epitaxy," *Surf. Sci.* **500**, 189-217 (2002).
- [64] H. Brune, "Microscopic view of epitaxial metal growth: nucleation and aggregation," *Surf. Sci. Reports* **31**, 121-229 (1998).
- [65] J. D. Weeks and G. H. Gilmer, "Advances in chemical physics," vol. **40**, pp. 157-227, New York, Wiley (1979).
- [66] D. B. Chrisey and G. K. Hubler, "*Pulsed laser deposition of thin films*," John Wiley and Sons, New York (1994).

- [67] C. M. Gilmore and J. A. Sprague, "Molecular-dynamics simulation of the energetic deposition of Ag thin films," *Phys. Rev. B* **44**, 8950-8957 (1991).
- [68] G. H. Gilmer and C. Roland, "Simulations of crystal growth: Effects of atomic beam energy," *Appl. Phys. Lett.* **65**, 824-826 (1994).
- [69] D. Bauerle, "*Laser Processing and Chemistry*," Second Edition, Springer, Berlin, Heidelberg (1996).
- [70] E.G. Gamaly, A.V. Rode, and B. Luther-Davies, "Ultrafast ablation with high-pulse-rate lasers. Part I: Theoretical considerations," *J. Appl. Phys.* **85**, 4213-4221 (1999).
- [71] E. G. Gamaly, A.V. Rode, V.T. Tikhonchuk, and B. Luther-Davies, "Electrostatic mechanism of ablation by femtosecond lasers," *Appl. Surf. Sci.* **197-198**, 699-704 (2002).
- [72] T. Götz and M. Stuke, "Short-pulse UV laser ablation of solid and liquid metals: indium," *Appl. Phys. A* **64**, 539-543 (1997).
- [73] E. G. Gamaly, A. V. Rode, and B. L. Davies "Ablation of solids by femtosecond lasers: Ablation mechanism and ablation thresholds for metals and dielectrics," *Physics of Plasmas* **9**, 949-957 (2002).
- [74] J. M. Van Hove, P. Pukite, P. I. Cohen, and C. S. Lent, "RHEED streaks and instrument response," *J. Vac. Sci. Technol. A* **1**, 609-613 (1983).
- [75] C. Zhu, T. Hayashi, S. Misawa, and S. Tsukahara, "Observation of initial growth of In on silicon(100) surface," *Jpn. J. Appl. Phys., Part 1* **33**, 3706-3709 (1994).

- [76] J. Perriere, E. Millon, W. Seiler, C. Boulmer-Leborgne, V. Carciun, O. Albert, J. C. Loulergue, and J. Etchepare, "Comparison between ZnO films grown by femtosecond and nanosecond laser ablation," *J. Appl. Phys.* **91**, 690-696 (2002).
- [77] J. E. Northrup, M. C. Schabel, C. J. Karlsson, and R. I. Uhrberg, "Structure of low-coverage phases of Al, Ga, and In on Si(100)," *Phys. Rev. B* **44**, 13799-13802 (1991).
- [78] T. Frey, C. C. Chi, C. C. Tsuei, T. Shaw, and F. Bozso, "Effect of atomic oxygen on the initial growth mode in thin epitaxial cuprate films," *Phys. Rev. B* **49**, 3483-3491 (1994).
- [79] M. Lippmaa, N. Nakagawa, M. Kawasaki, S. Ohashi, Y. Inaguma, M. Itoh, and H. Koinuma, "Step-flow growth of SrTiO₃ thin films with a dielectric constant exceeding 10⁴," *Appl. Phys. Lett.* **74**, 3543-3545 (1999).
- [80] J. Choi, C. B. Eom, G. Rijnders, H. Rogalla, and D. H. A. Blank, "Growth mode transition from layer by layer to step flow during the growth of heteroepitaxial SrRuO₃ on (001) SrTiO₃," *Appl. Phys. Lett.* **79**, 1447-1449 (2001).
- [81] B. A. Joyce, T. Shitara, A. Yoshinaga, D. D. Vvedensky, J. H. Neave, and J. Zhang, "Elementary processes in the MBE growth of GaAs," *Appl. Surf. Sci.* **60/61**, 200-209 (1992).
- [82] X. D. Zhu, "Determination of surface-diffusion kinetics of adatoms in epitaxy under step-flow growth conditions," *Phys. Rev. B* **57**, R9478-R9481 (1998).
- [83] D. H. A. Blank, G. J. H. M. Rijnders, G. Koster, and H. Rogalla, "In situ monitoring by reflective high energy electron diffraction during pulsed laser deposition," *Appl. Surf. Sci.* **138-139**, 17-23 (1999).

- [84] Z. H. Zhang, B. Lin, X. L. Zeng, and H. E. Elsayed-Ali, "Surface morphology of laser-superheated Pb(111) and Pb(100)," *Phys. Rev. B* **57**, 9262-9269 (1998).
- [85] M. A. Hafez and H. E. Elsayed-Ali, "Atomic hydrogen cleaning of InP(100): Electron yield and surface morphology of negative electron affinity activated surfaces," *J. Appl. Phys.* **91**, 1256-1264 (2002).
- [86] J. Knall, J.-E. Sundgren, J. E. Greene, A. Rockett, and S. A. Barnett, "Indium incorporation during the growth of (100)Si by molecular beam epitaxy: Surface segregation and reconstruction," *Appl. Phys. Lett.* **45**, 689-691 (1984).
- [87] J. A. Venables, "Kinetic studies of nucleation and growth at surfaces," *Thin Solid Films* **50**, 357-369 (1978).
- [88] G. M. Francis, L. Kuipers, J. R. A. Cleaver, and R. E. Palmer, "Diffusion controlled growth of metallic nanoclusters at selected surface sites," *J. Appl. Phys.* **79**, 2942-2947 (1996).
- [89] V. S. Achutharaman, N. Chandrasekhar, O. T. Valls, and A. M. Goldman, "Origin of RHEED intensity oscillations during the growth of (Y,Dy)Ba₂Cu₃O_{7-x} thin films," *Phys. Rev. B* **50**, 8122 (1994).
- [90] L. Bardotti, P. Jensen, A. Hoareau, M. Treilleux, and B. Cabaud, "Experimental observation of fast diffusion of large antimony clusters on graphite surfaces," *Phys. Rev. Lett.* **74**, 4694-4697 (1995).
- [91] P. Deltour, J.-L. Barrat, and P. Jensen, "Fast diffusion of a Lennard-Jones cluster on a crystalline surface," *Phys. Rev. Lett.* **78**, 4597-4600 (1997).

- [92] A. Bogicevic, S. Liu, J. Jacobsen, B. Lundqvist, and H. Metiu, "Island migration caused by the motion of the atoms at the border: Size and temperature dependence of the diffusion coefficient," *Phys. Rev. B* **57**, R9459-R9462 (1998).
- [93] J.-M. Wen, S.-L. Chang, J. W. Burnett, J. W. Evans, and P. A. Thiel, "Diffusion of large two-dimensional Ag clusters on Ag(100)," *Phys. Rev. Lett.* **73**, 2591-2594 (1994).
- [94] J.-M. Wen, J. W. Evans, M. C. Bartelt, J. W. Burnett, and P. A. Thiel, "Coarsening mechanisms in a metal film: From cluster diffusion to vacancy ripening," *Phys. Rev. Lett.* **76**, 652-655 (1996).
- [95] S. Schintke, U. Resch-Esser, N. Esser, A. Krost, W. Richter, and B. O. Fimland, "Surfactant-mediated growth of indium on GaAs(001)," *Surf. Sci.* **377-379**, 953-957 (1997).
- [96] W. Monch, "*Semiconductor surfaces and interfaces*," Springer-Verlag, Berlin, (1993).
- [97] H. T. Yang and W. S. Berry, "Interaction of indium on Si surface in Si molecular beam epitaxy (MBE)," *J. Vac. Sci. Technol. B* **2**, 206-208 (1984).
- [98] M. A. Hafez and H. E. Elsayed-Ali, "Formation of In-(2×1) and In islands on Si(100)-(2×1) by femtosecond pulsed laser deposition," *J. Appl. Phys.* **101**, 113515 (1-10) (2007).
- [99] S. Martini, A. A. Quivy, T. E. Lamas, and E. C. F. da Silva, "Real-time RHEED investigation of indium segregation in InGaAs layers grown on vicinal GaAs(001) substrates," *Phys. Rev. B* **72**, 153304(1-4) (2005).

- [100] M. Lippmaa, N. Nakagawa, M. Kawasaki, S. Ohashi, and H. Koinuma, "Growth mode mapping of SrTiO₃ epitaxy," *Appl. Phys. Lett.* **76**, 2439-2441 (2000).
- [101] K. Shiramine, T. Itoh, and S. Muto, "Critical cluster size of InAs quantum dots formed by Stranski-Krastanow mode," *J. Vac. Sci. Technol. B* **22**, 642-646 (2004).
- [102] D. M. Zhang, L. Guan, Z. H. Li, G. J. Pan, H. Z. Sun, X. Y. Tan, and L. Li, "Influence of kinetic energy and substrate temperature on thin film growth in pulsed laser deposition," *Surf. Coat. Technol.* **200**, 4027-4031 (2006).
- [103] C. S. Lent and P. I. Cohen, "Quantitative analysis of streaks in reflection high-energy electron diffraction: GaAs and AlAs deposited on GaAs(001)," *Phys. Rev. B* **33**, 8329-8335 (1986).
- [104] L. Daweritz and K. Ploog, "Contribution of reflection high-energy electron diffraction to nanometre tailoring of surfaces and interfaces by molecular beam epitaxy," *Semicond. Sci. Technol.* **9**, 123-136 (1994).
- [105] P. R. Pukite, J. M. Van Hove, and P. I. Cohen, "Extrinsic effects in reflection high-energy electron diffraction patterns from MBE GaAs," *J. Vac. Sci. Technol. B* **2**, 243-248 (1984).
- [106] H. Minoda and K. Yagi, "Dynamics of Au-adsorption-induced step bunching on a Si(001) vicinal surface studied by reflection electron microscopy," *Phys. Rev. B* **60**, 715-2719 (1999).
- [107] K. Fang, T.-M. Lu, and G.-C. Wang, "Roughening and faceting in a Pb thin film growing on the Pb(110) surface," *Phys. Rev. B* **49**, 8331-8339 (1994).

- [108] U. Hessinger, M. Leskovaar, and M. A. Olmstead, "Role of step and terrace nucleation in heteroepitaxial growth morphology: Growth kinetics of $\text{CaF}_2/\text{Si}(111)$," *Phys. Rev. Lett.* **75**, 2380-2383 (1995).
- [109] M. G. Lagally, D. E. Savage, and M. C. Tringides, "*Reflection high-energy electron diffraction and reflection electron imaging of surfaces*," edited by P. K. Larson, and P. J. Dobson, Vol. 188, p. 139, Plenum, New York (1988).
- [110] K.-S. Kim, Y. Takakuwa, T. Abukawa, and S. Kono, "RHEED-AES observation of In desorption on a single-domain $\text{Si}(001)-(2\times 1)$ surface," *Surf. Sci.* **410**, 99-105 (1998).

CHAPTER V

FEMTOSECOND PULSED LASER DEPOSITION OF INDIUM NITRIDE ON Si(100)

V.1. Introduction

Group III-nitrides (AlN, GaN, InN) are the subject of much attention in their fundamental physical properties and a promising system for semiconductor devices. The large interest originates from their potential use in optoelectrical applications, blue and ultraviolet light emitting diodes (LEDs), laser diodes and optical detectors, and high temperature and high power semiconductor devices [1-8]. However, InN has not received as much experimental attention as GaN because of the difficulties associated with the growth of high quality crystals [9, 10]. InN has the smallest direct band gap and the highest electron mobility among the group III-nitrides [9]. In recent years, InN has emerged as a potential material for optoelectronic devices. The use of InN and its alloys with GaN and AlN makes it possible to extend the emission of nitride-based LEDs from the UV to the near infrared region [10]. Theoretical calculation suggests that InN should have superior electron transport properties to both GaN and GaAs over a wide temperature range from 150 to 500 K. InN can have a refractive index greater than 3 [11]. The high air-InN and/or high oxide/InN contrast in refractive index is attractive for photonic band gap design.

The crystal structure of the group III-nitrides consists of a thermodynamically stable phase with hexagonal wurtzite structure (α -phase) and a metastable phase with cubic zincblende structure (β -phase). Because the α - and β - phases only differ in the

stacking order of nitrogen and metal atoms, the coexistence of hexagonal and cubic phases is possible in epitaxial layers, for example due to stacking faults [2]. The most attractive points of β -phase nitrides are their ability to grow on cubic substrates, like GaAs and Si [4]. These substrates are easy to be cleaved and have higher crystal symmetry than sapphire substrates. The most serious problems of β -phase nitrides is their poor crystalline quality obtained [4]. Both bulk and surface properties of III-nitrides can depend on polarity, on whether the surface is terminated by nitrogen or metal atoms [12, 13]. The most popular growth techniques for InN are the metalorganic vapor phase epitaxy (MOVPE) and molecular beam epitaxy (MBE) [9, 10]. The source materials generally used for the MOVBE growth of InN are trimethylindium as an In source and ammonia (NH_3) as a nitrogen source. Nitrogen (N_2) is being used as a carrier gas. The most suitable temperature region for the MOVBE growth of InN is 500-650 °C [10]. Surface morphology for InN films grown on sapphire by MOVBE showed columnar, two-dimensional (2D) growth, and pits on grain surface [14]. For MBE, a solid source of In is used and atomic reactive nitrogen is obtained by dissociation of N_2 molecules by radio-frequency plasma or electron cyclotron resonance plasma [10]. A drawback of these methods is that ions generated by the high plasma density can cause damage to the epitaxial films. Ion tapping by static electric field has been used, such as a biasable grid between the substrate and the nitrogen flux, to control the nitrogen ions and to avoid the ion damage problem [15]. The other problem induced by plasma may be contamination by species such as oxygen or carbon dioxide [10]. To minimize this, the discharge may be electrodeless and the plasma contained in a pyrolytic boron nitride discharge tube capped with a boron nitride exit plate [16]. For MBE, most samples were grown in the

temperature range from 450 °C to 550 °C [10]. The growth mode of InN on GaN(0001) by plasma-assisted MBE was investigated under the influence of a deposition flux of In and N [17]. Both 2D [layer-by-layer] and three-dimensional (3D) [Stranski-Krastanove (SK)] growth modes have been observed in spite of the lattice mismatch of ~10%. Low temperature or high atomic nitrogen flux favors SK growth, whereas high temperature and high In flux leads to 2D growth. Other growth techniques of InN, such as metalorganic MBE, sputtering, hydride vapor phase epitaxy (HVPE), pulsed laser deposition (PLD), and reactive evaporation have been attempted [3, 10].

The fundamental parameters of the grown InN films, including the band-gap, lattice constant and effective electron mass, have shown wide variations in measured values. With the crystallinity improvement, the band gap of InN was found to be 0.6-0.9 eV [18-22], much narrower than the earlier cited value of 1.9 eV. Earlier studies carried out on poor quality InN films and contaminated by oxygen showed higher band gap energy value than films of higher quality [10]. One of the main limitations to accurate measurement has been the difficulty in consistently applying standard measurement techniques developed for other III-V materials [9]. For example, the 0.7 eV band gap measured from resonant Mie scattering was thought to be metallic In clusters, assigned from x-ray diffraction (XRD) [21]. In another study, optical characterization by absorption and photoluminescence (PL) showed that the bandgap of single-crystalline and polycrystalline wurtzite InN is 0.70 ± 0.05 eV [22]. Careful indexing of wide-angle XRD scans showed that no evidence of metallic In clusters in the studied samples. Instead polycrystalline InN grains were observed [22]. Results showed that there is no one reason for the band gap variation, but a large number of factors influenced the band

gap measurements [9]. Suggestions for observations of a higher band gap have included a strong Moss-Burstein effect, oxygen inclusion, quantum size effects and stoichiometry changes [9]. The Moss-Burstein effect occurs when the carrier concentration exceeds the conduction band edge density of states and the Fermi level lies within the conduction band [9]. Electrons fill the bottom of the conduction band and the band gap measured by optical absorption is increased. At high carrier concentration, nearing 10^{21} cm^{-3} , which corresponds to an impurity level of at least 3% in InN, a band gap change can be expected as a result of alloying effects and lattice changes that result from the inclusion of impurities at such a high doping level. The stoichiometry in InN is related to the pressure of In-rich or nitrogen-rich materials. The In-rich debate originates from the suggestion that the $\sim 0.7 \text{ eV}$ feature may be the result of deep level defects [9] and/or Mie resonances [21, 23] resulting from In-related point defects or In-rich aggregates, respectively. On the nitrogen-rich side, the N: In ratios as large as 4:3 have been observed for radio frequency (RF) sputtered material [9, 24], while MBE and remote plasma enhanced chemical vapor deposition (RPECVD) grown InN have been observed to be nitrogen-rich but with lesser extents. Grown under conditions of thermal equilibrium, the possibility of nitrogen-rich InN should not occur [25]; however, RF sputtering, RPECVD and MBE are using plasma sources of nitrogen so that non-equilibrium growth regimes result [9].

It has been suggested that the high band gap may result from quantum size effects related to the polycrystalline structure [26]. Growth of InN-based nanorods by CVD showed that rod diameters of 30-50 nm material result in 1.9 eV PL, whereas nanorods of more than 50 nm diameter material were observed to have a 0.77 eV PL peak [27].

However, the undefined differences in growth temperature and the impurity concentration between the two materials were large. RPECVD growth of polycrystalline InN showed ~ 0.85 eV PL peak [28]. The properties of InN quantum dots differ from those observed for InN films [9]. Growth of InN quantum dots has been reported, but no quantum confinement effects have been identified [29]. The presence of oxygen, in particular InN-In₂O₃ alloy, was suggested as a possible explanation for the observed higher band gap [30]. Sufficient quantities of oxygen in InN may affect the band gap in two ways [9]. The first requires oxygen to form optically active centers in high densities, which modify an oxygen-free band gap by band filling, as in the Moss-Burstein effect, or by impurity banding within the forbidden band. These effects will increase or decrease the InN band gap, respectively. The second requires the formation of a semiconducting pseudo-binary alloy phase, InN_xO_y, with a band gap different from InN. Amorphous In oxynitride had previously been observed using X-ray photoelectron spectroscopy. Such a structure maintains near-stoichiometry between nitrogen and In, while the oxygen adsorbate is invisible in XRD spectra [31]. If growth temperatures are low enough, lower adatom mobility reduces surface diffusion length and promotes polycrystalline structure formation, which leads to greater post-growth oxygen incorporation [9]. Potential dopant sources may have significant effects on the InN band gap. Early experimental evidence taken from sputtered samples suggested that there is at least one donor species resonant with or extremely close to the conduction band of InN, while other, deeper donor levels at 40-50 meV and 150 meV have also been identified [32].

The growth of high quality InN films is the most difficult among the III-nitrides due to various problems [9, 10]. The first problem is the lack of suitable substrates, which

has made it difficult to grow high quality epitaxial nitride films because of the difference in the lattice constants and thermal expansion coefficients. The lattice mismatch between InN and sapphire, which is the most commonly used substrate, is about ~25%. This large lattice mismatch and thermal expansion coefficient difference can result in a high density of structural defects, such as threading dislocations in InN epitaxial films [10]. The second problem with the InN crystal growth is the low dissociation temperature of around 600 °C and 500 °C for N-polar and In-polar InN, respectively [33-35]. It has been shown that InN single crystal films are thermally stable up to 500 °C and when the temperature was raised above 550 °C, the films were degraded due to the decomposition and desorption of nitrogen [36]. The third problem is the equilibrium vapor pressure of nitrogen over the InN, which is several orders higher than for AlN and GaN [37]. Therefore, the growth temperature of InN is a critical parameter that controls the film quality.

For device applications, it is desirable to grow InN on a conducting substrate, instead of an insulating one such as sapphire [10]. Growth of InN on Si(100) is less studied compared to InN on sapphire. InN on Si(100) was grown using different techniques such as laser-assisted CVD, electron cyclotron resonance-assisted MBE, halide CVD under atmospheric pressure, ion beam assisted filtered cathodic vacuum arc, and ion implantation [38-42]. Si has a good thermal stability under nitride growth conditions, and its surfaces can be prepared with a smooth finish [43]. In addition, it is particularly interesting as a substrate for quantum dots applications because of its electrical conductivity and transparency in the near infrared. It has been shown that growth of InN on Si(111) substrate by MOVPE was unsuccessful because of the

formation of an amorphous SiN_x layer at $\sim 500^\circ\text{C}$ [44]. Later, an intermediate layer ($\sim 0.5\ \mu\text{m}$) of GaAs on Si(111) was used to avoid the surface nitridation, and a single crystal InN film was obtained [45]. Growth of 200-880 nm thick InN films on 10 nm thick InN buffer layers on Si(001) and Si(111) substrates, by electron cyclotron resonance-assisted MBE, showed strong band edge PL emission at room temperature [46].

PLD was recently used to grow III-nitrides films mainly on sapphire substrates. Atomic nitrogen beam and glow discharge plasma were used to assist the PLD of elemental metal targets [47, 48]. XRD pattern showed that the InN films consisted of predominant zincblend structure along with hexagonal wurtzite structure [48]. Results showed that it is possible to grow InN at a low substrate temperature and without substrate nitridation. Laser ablation of InN solid target on sapphire in high vacuum and in few mTorr of nitrogen atmosphere showed that the films have preferred crystalline orientation and the surfaces have In droplets [49]. Previous studies showed crystalline InN formation and reduction in the interface energy indicating that the PLD technique, assisted by RF atomic nitrogen source, is capable of growth of high-quality InN films on sapphire [50]. PLD of InN films on $(\text{Mn,Zn})\text{Fe}_2\text{O}_4$ (111) and MgAl_2O_4 (111) substrates showed that suppression of the interfacial reactions between the InN films and the substrate is important to obtain high quality InN films [51]. PLD of InN on the *c*-cut sapphire substrates using DC plasma showed single phase, polycrystalline films with wurtzite structure [52]. The surface morphology of the films, as seen by atomic force microscopy, showed densely packed nanocrystalline grains of InN.

Growth temperature influences the crystallinity, surface morphology, and electrical properties of the grown InN film. Because of the low InN dissociation

temperature and the high equilibrium nitrogen vapor pressure over the InN film, the preparation of InN film requires a low growth temperature. PLD is a suitable technique for low temperature epitaxial growth of thin films, since the laser-ablated species from a target material in PLD possess high kinetic energies [53, 54]. The energetic species in PLD increases the surface diffusion and promotes epitaxy. In addition, the laser parameters such as the laser energy density and laser pulse duration can influence the growth process and properties of the films. In the femtosecond lasers ablation, heating to the target material is limited, which results in a higher ablation efficiency than the nanosecond lasers [55, 56]. The use of femtosecond lasers has been proposed as a possible solution to overcome the occurrence of droplets often observed in nanosecond PLD due to thermal effects at the target surface [57, 58]. Therefore, using a femtosecond pulsed laser deposition (fsPLD), the formation of particulates can be minimized or eliminated thus improving the quality of thin film.

The main motivation of the present work is to grow high quality InN on Si(100) substrates for device application. A femtosecond laser is used for PLD. The previous studies of PLD growth of InN utilized nanosecond lasers [47-52]. The In buffer layer is grown by fsPLD as described previously [59]. The nitridation source is obtained using either thermal cracking source or a laser induced gas breakdown of ammonia. In this chapter, the growth and characterization of InN films on Si(100) by the fsPLD are studied by in situ reflection high-energy electron diffraction (RHEED) and ex situ atomic force microscopy (AFM), secondary electron microscopy (SEM), and XRD.

V.2. Crystal structure

The hexagonal wurtzite structure is formed by two interpenetrating hexagonal closed-packed structures, Fig. 5.1(a). The hexagonal close-packed structure is produced by creating a triangular lattice of lattice constant a in two dimensions. Then a copy of this lattice is stacked vertically over the first one, in such a way that the particles of the second lattice are over the centers of triangles of the first one. Each atom in the lattice forms a tetragonal set of bonds. The N atom is positioned at the center of mass of the tetragonal structure, Fig. 5.1(b).

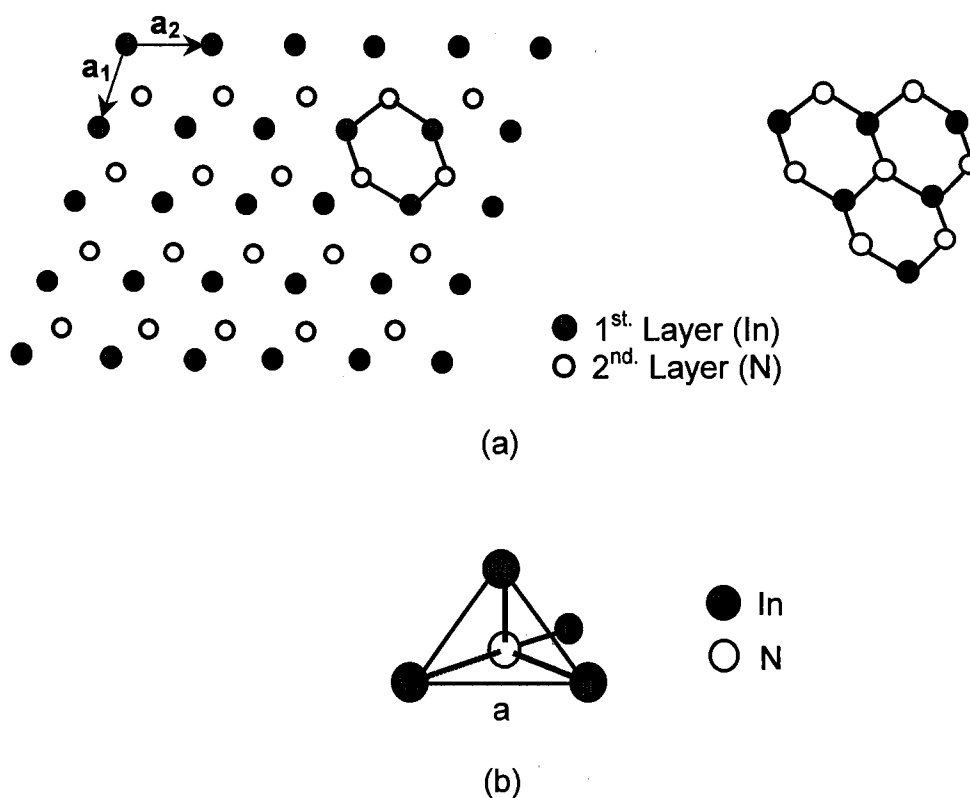


FIG. 5.1. (a) The hexagonal wurtzite structure. The parameter $a_1 = a_2 = a$ is the lattice constant. (b) Tetragonal bonding of In and N. The N atom sits down the center of a triangle of In atoms and above an In atom of the next layer.

The wurtzite unit cell of InN is described by edge length $a = 3.54 \text{ \AA}$, height $c = 5.70 \text{ \AA}$ and an internal parameter $u = (3/8) c$ [1, 3, 10], Fig. 5.2(a).

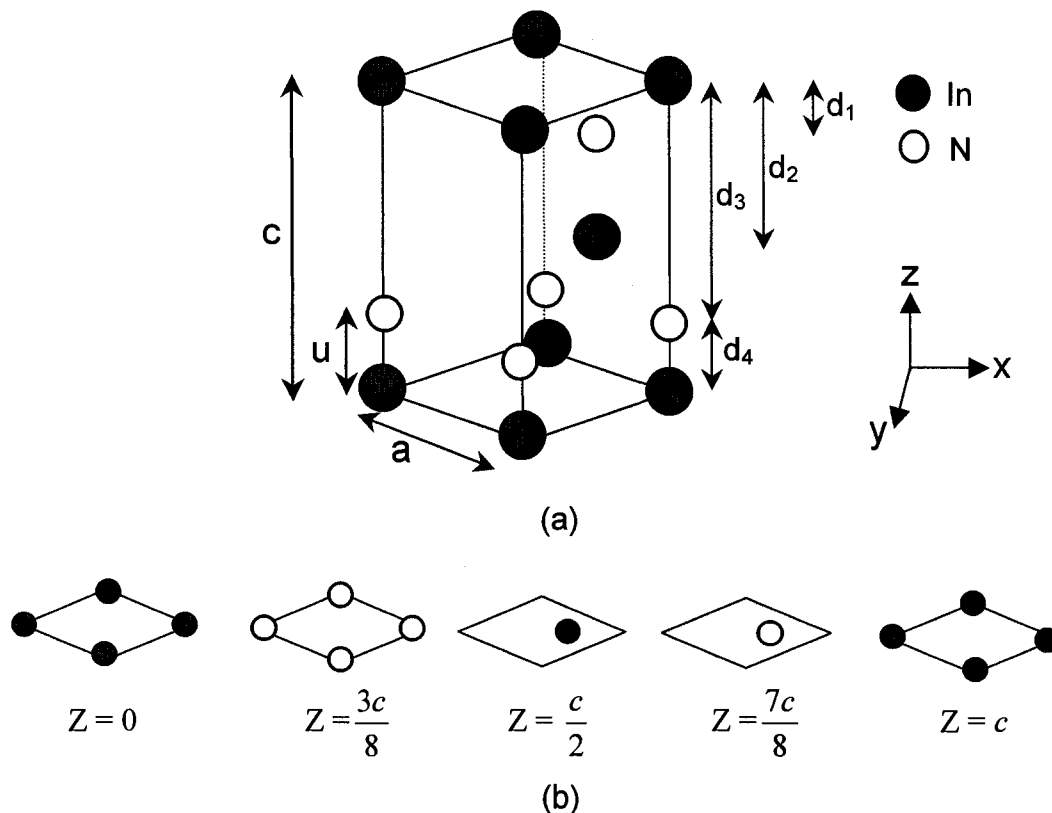


FIG. 5.2. (a) The hexagonal unit cell of InN. a and c are the lattice constants. (b) The layer sequences in terms of the lattice constant c .

The distance between the layers of the unit cell are $d_1 = (1/8) c$, $d_2 = (1/2) c$, $d_3 = (5/8) c$, and $d_4 = (3/8) c$, Fig. 5.2(b). The wurtzite structure of InN is a hexagonal lattice with a basis of 4 atoms per hexagonal unit cell. The positions of the 4 atoms are b_1 , b_2 , b_3 and b_4 and given by:

$$b_1 = (0, 0, 0)$$

$$b_2 = (1/2) a X - (\sqrt{3}/2) a Y + (1/2) c Z \equiv (1/2 a, -\sqrt{3}/2 a, 1/2 c)$$

$$b_3 = u Z \equiv (0, 0, uc)$$

$$b_4 = (1/2) a X - (3/2) a Y + (1/2 + u) Z \equiv (1/2 a, -3/2 a, c/2 + uc)$$

V.3. Experiment

The InN films growth were conducted in an ultrahigh-vacuum (UHV) PLD system with a base pressure of 1×10^{-9} Torr. High purity ammonia gas was introduced into the PLD chamber through a leak UHV valve. The nitridation source was obtained using two techniques; a thermal cracking source and laser induced gas breakdown. A residual gas analyzer (RGA) is connected to the UHV system to monitor the nitrogen partial pressure. RGA was installed away from the target and substrate holders to protect its filament from plume. A thermal cracker source was used to dissociate the ammonia gas. It consists of a tungsten filament inserted into an 80 mm long boron nitride tube with 4 mm inner diameter along with ceramic tubes. The filament source is placed ~ 15 cm from the substrate sample.

The Si substrates were cut from a low-resistivity Si(100) wafer (p-type, boron-doped, 500- μm thick, 0.01-0.03 ohm-cm resistivity). The Si surfaces were misoriented from the low-index (100) plane by 1.0° towards the $\langle 110 \rangle \pm 0.5^\circ$. The Si(100)-(2 \times 1) surface was prepared by chemical etching just prior to being loaded into the UHV chamber. This was followed by in situ heat cleaning to 600 $^\circ\text{C}$ for several hours using direct current, then flash heating at ~ 1100 $^\circ\text{C}$ to remove native oxides and carbon. During flash heating of the substrate the chamber pressure was in the low 10^{-8} Torr. The heating was then terminated and the substrate cooled down to the growth temperature.

Amplified Ti:sapphire laser, (pulse width ~ 130 fs at the full width at half maximum) operating at a wavelength of 800 nm was used. Laser ablation of the In target was carried out with a laser repetition rate in the range of 2-10 Hz and laser energy density in the range of 0.5-0.9 J/cm². The laser was incident on a 99.99% pure In target at

$\sim 45^\circ$, and focused on the In target using a convex lens with a 30-cm focal length. The target was rotated at a speed of 2 revolutions per minute during the deposition to obtain uniform ablation and to avoid pitting of the target surface, thus minimize particulate formation. The target-to-substrate distance was fixed at ~ 5 cm. While the In plume arrives at the substrate, the atomic nitrogen flux was transported to the substrate in a downward geometry in the case of the thermal cracking source, Fig. 5.3.

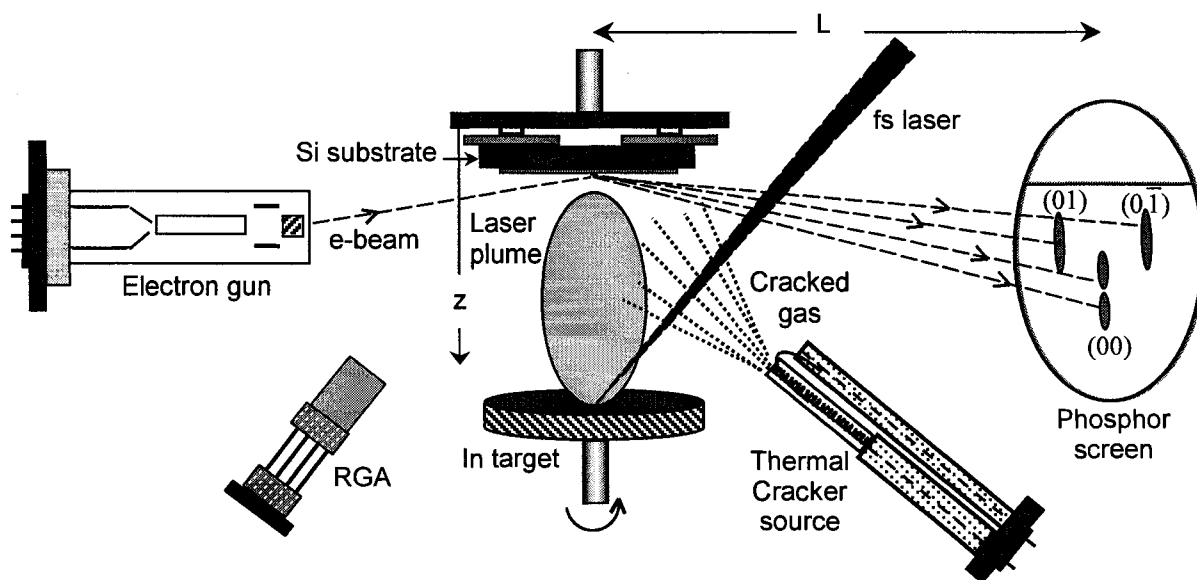


FIG. 5.3. Schematic diagram of the geometry of PLD and the in situ components.

Laser induced gas breakdown was performed using laser repetition rate of 1000 Hz in an ammonia background of ~ 2 Torr while ablation of In target was carried out by a laser repetition rate in the range of 2-10 Hz using an optical shutter. RHEED was used to observe the surface structure of the substrate and the film growth during deposition. The RHEED electron gun was operated at an electron energy of 8.6 keV. A charge-coupled device camera was used to image the diffraction patterns. The surface morphology of the In films was characterized ex situ with AFM, SEM, and XRD.

V.4. Results and discussion

InN films were grown via a three step-growth processes. In the first step, a few monolayers of In were deposited on the Si(100) surface by fsPLD at a substrate temperature below the In melting point (156.6 °C). In the second step, a buffer layer of InN was grown at low substrate temperature (~250 °C). Then, growth of the final InN film was performed below the InN thermal dissociation temperature (550 °C). Thermal cracking of ammonia was done for pressure in the low 10^{-6} Torr. The cracker products and partial pressures of ammonia were monitored by the RGA. Figure 5.4(a) and (b) show the RGA spectra of ammonia before and after thermal cracking. Atomic nitrogen resulted from the dissociation of ammonia molecules.

PLD of In with thermal cracking of the ammonia gas were carried out to grow InN on Si(100). Buffer layers of In were deposited by PLD on the Si(100) surface before growth of the InN film. The film growth was monitored by in situ RHEED, which provides information on the crystal quality of the films during growth. For InN films grown on Si(100)-(1×1) at room temperature, the RHEED pattern showed rings on a high background, Fig. 5.5. The RHEED intensities of the rings were not uniform indicative of fiber-like texture of a polycrystalline film [60]. It has been suggested that the cracking products of ammonia might influence the growth and delay or prevent a transition from 2D to 3D growth [61]. It has been reported that atomic hydrogen breaks the In-Si bonds, leaving a hydrogen terminated Si surface [62-64]. It is therefore possible that atomic hydrogen produced in the cracking process of ammonia resulted in hydrogen terminated Si(100)-(1×1) surface. In this case, the hydrogen terminated surface could prevent the growth of InN and the resulting film is randomly oriented 2D In islands.

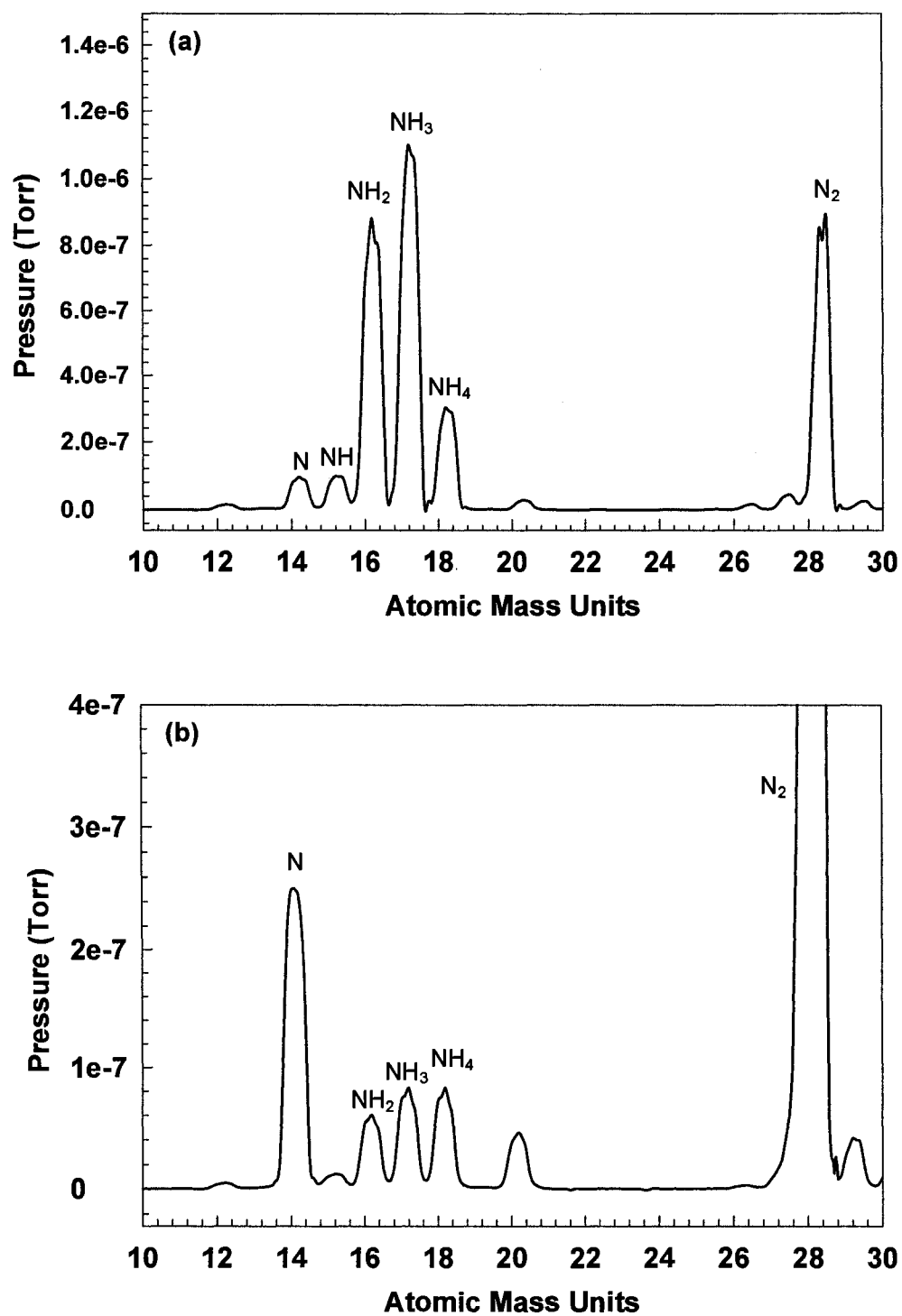


FIG. 5.4. RGA spectra before and after thermal cracking of ammonia in (a) and (b), respectively. Atomic nitrogen resulted after dissociation of the ammonia molecules.

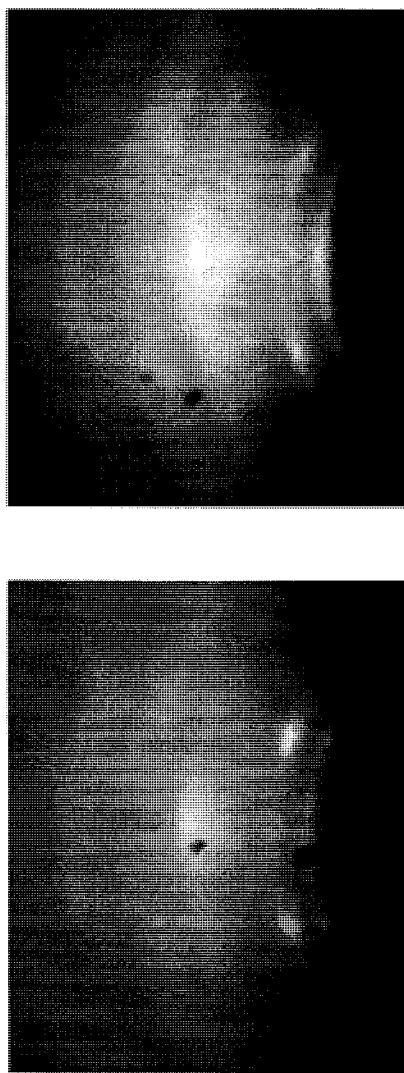


FIG. 5.5. RHEED patterns of InN films grown on Si(100)-(1×1) substrates at room temperature. The growth was carried out by fsPLD of In target during thermal cracking of ammonia at pressure of $\sim 5 \times 10^{-6}$ Torr. Buffer layer of In was deposited on the substrate surface before growth of the InN film. The RHEED patterns were taken for two samples prepared at the same deposition conditions.

On the other hand, when In was deposited on Si(100)-(2×1) surface in a thermally cracked ammonia environment (pressure of $\sim 5 \times 10^{-6}$ Torr), a transmission RHEED pattern was observed indicating that the growth mode of InN was 3D. The initial deposition of In at coverage of ~ 6 monolayers (ML) and at temperature of ~ 70 °C shows streaky In(2×1) RHEED pattern indicating 2D growth, Fig. 5.6(a). After deposition of the InN buffer layers at a substrate temperature of ~ 250 °C, the (2×1) RHEED pattern disappeared and the diffused background increased. This corresponds to the stage where transition from 2D to 3D growth occurred and the long-range order was limited to very small dimensions. Deposition of the final InN at substrate temperature of ~ 350 °C showed epitaxial growth as verified from the in situ RHEED, Fig. 5.6(d).

Next, a solid InN target was used to deposit InN on the Si(100)-(2×1) surface and to determine the film growth using the in situ RHEED. The target was prepared by pressing InN powder into a pellet. Deposition of initial layers of In at coverage of ~ 6 ML was made on the substrate surface. Then, growth of InN on Si(100)-(2×1) surface was carried out at substrate temperature of ~ 100 °C at a background pressure of $\sim 2 \times 10^{-8}$ Torr. The RHEED patterns taken for the grown InN film at $[011]$, $[0\bar{1}1]$, and $[01\bar{1}]$ azimuths of the Si(100) surface showed diffraction spots, which indicate epitaxial growth, Fig. 5.7. In addition, the RHEED patterns had noticeable diffuse background and no obvious Kikuchi lines, compared with the RHEED pattern of the initial grown In(2×1) layer. These RHEED features are attributed to the diffracted electrons from grown InN islands over the substrate surface.

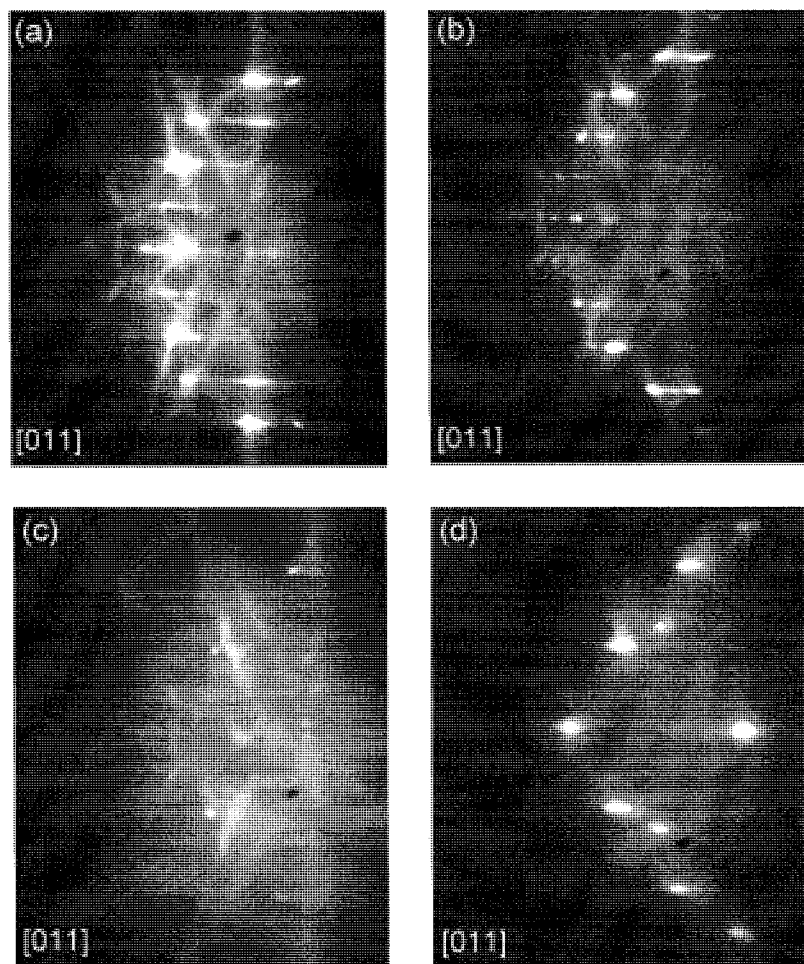


FIG. 5.6. (a) Reflection RHEED pattern of Si(100)-(2 \times 1) surface before deposition. (b) RHEED pattern after deposition of In for \sim 6 ML on Si(100)-(2 \times 1) at substrate temperature of \sim 70 °C. (c) RHEED pattern after deposition of InN buffer layer at temperature of \sim 250 °C. (d) Transmission RHEED pattern after growth of the final InN film at temperature of \sim 350 °C. Thermal cracking of ammonia occurred at pressure of $\sim 5 \times 10^{-6}$ Torr.

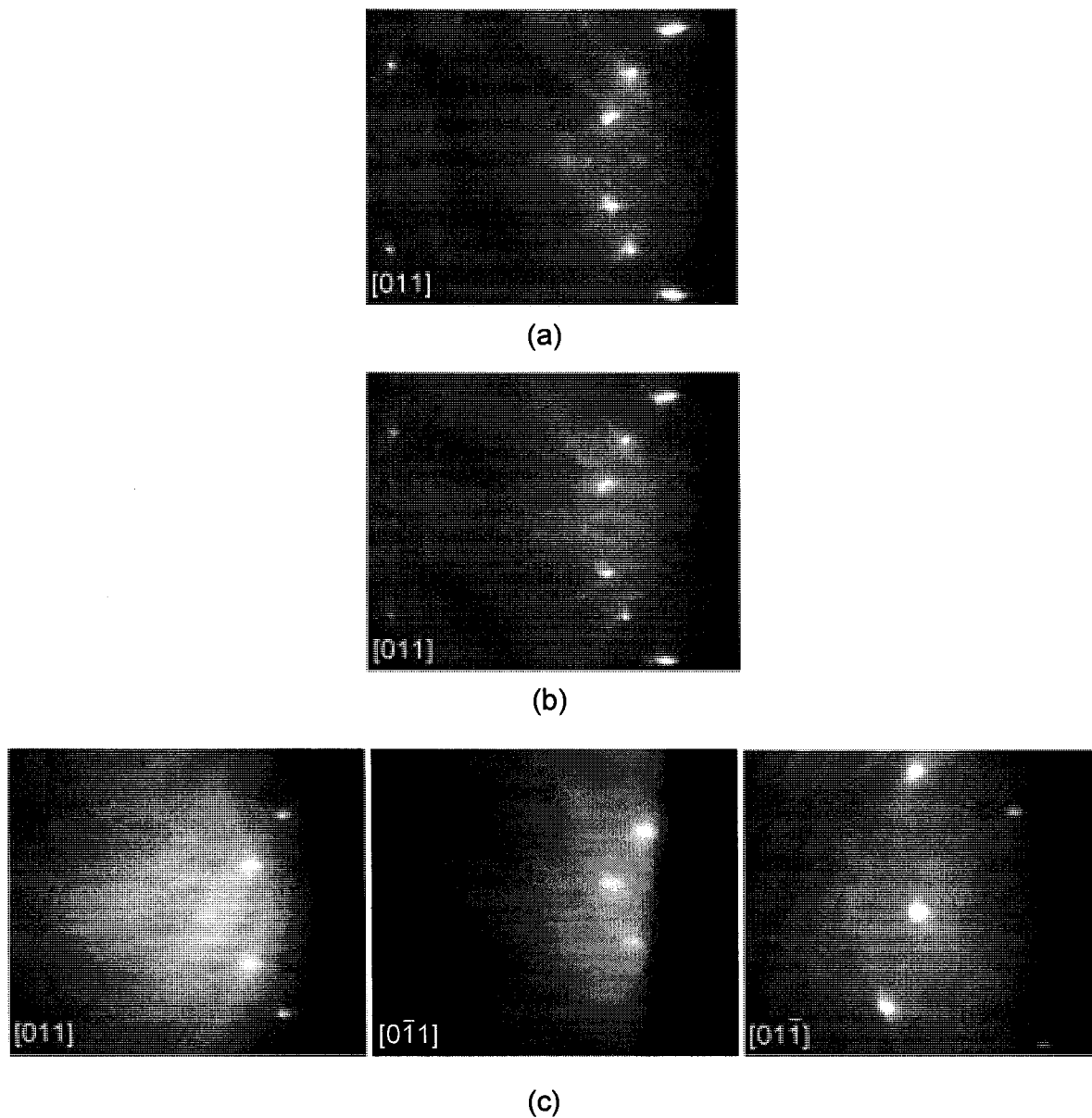


FIG. 5.7. (a) Reflection RHEED pattern of Si(100)-(2x1) surface before deposition. (b) RHEED pattern shows In(2x1) structure after deposition of ~6 ML In. (c) RHEED patterns after growth of InN at temperature of ~100 °C at pressure of $\sim 2 \times 10^{-8}$ Torr taken at [011], [01̄1], and [01̄1̄] azimuths of the Si(100) surface. The deposition of InN film on Si(100)-(2x1) surface was performed using a solid InN target made from powder sample.

PLD of In with laser induced breakdown of ammonia gas was performed to grow InN on Si(100) substrate. Laser induced gas breakdown is used in conjunction with PLD to break ammonia molecules and generate reactive nitrogen for InN formation. A schematic diagram of the PLD of In target and laser induced breakdown of ammonia in the UHV system is shown in Fig. 5.8. The ammonia gas was introduced into the chamber and maintained at pressure in the range of ~2 Torr during the deposition. A beam splitter was used to split the laser beam, one for the PLD and the second for the gas breakdown. Optical mirrors were used to control the direction and focusing position for the gas breakdown. The gas breakdown was accomplished by focusing the laser beam in front of the substrate surface. For the laser beam diameter of 4 mm, the focal spot size after focusing was $1.68 \times 10^{-4} \text{ cm}^2$. The intense laser pulse generates a microplasma at a temperature sufficient to dissociate the ammonia molecules. Then, the ammonia plasma plume expands towards the substrate surface.

Next, growth of InN on Si(100) substrate was performed at a temperature of ~350 °C. Before deposition, RHEED pattern showed Si(100)-(1×1) with high background. Just prior to In deposition, the Si(100) was raised in temperature to ~1000 °C for ~2 minutes by direct-current heating and then cooled down to the growth temperature. Then, the fsPLD of In was begun to form buffer layers on top of the Si(100) surface. Following, the fsPLD of In was stopped and the ammonia gas inserted to the chamber. The laser induced gas breakdown started in the front of the substrate surface at a temperature of ~250 °C. Then, the growth of the InN film was performed by fsPLD of In and laser breakdown of ammonia. During deposition of InN, the RHEED beams intensities were observed to continuously decrease while RHEED transmission features started to appear. RHEED

patterns were taken for the grown InN film at $[011]$, $[001]$, $[0\bar{1}0]$, and $[031]$ azimuths showed diffraction spots, which indicate epitaxial growth of InN, Fig. 5.9. In addition to the transmission spots, a streaky RHEED pattern was observed when the incident electron beam was scanned over the grown film at $[001]$ and $[0\bar{1}0]$ azimuths of the Si(100) surface, Fig. 5.10. This was indicative of a reflection of the incident electron beam from a 2D underlayer.

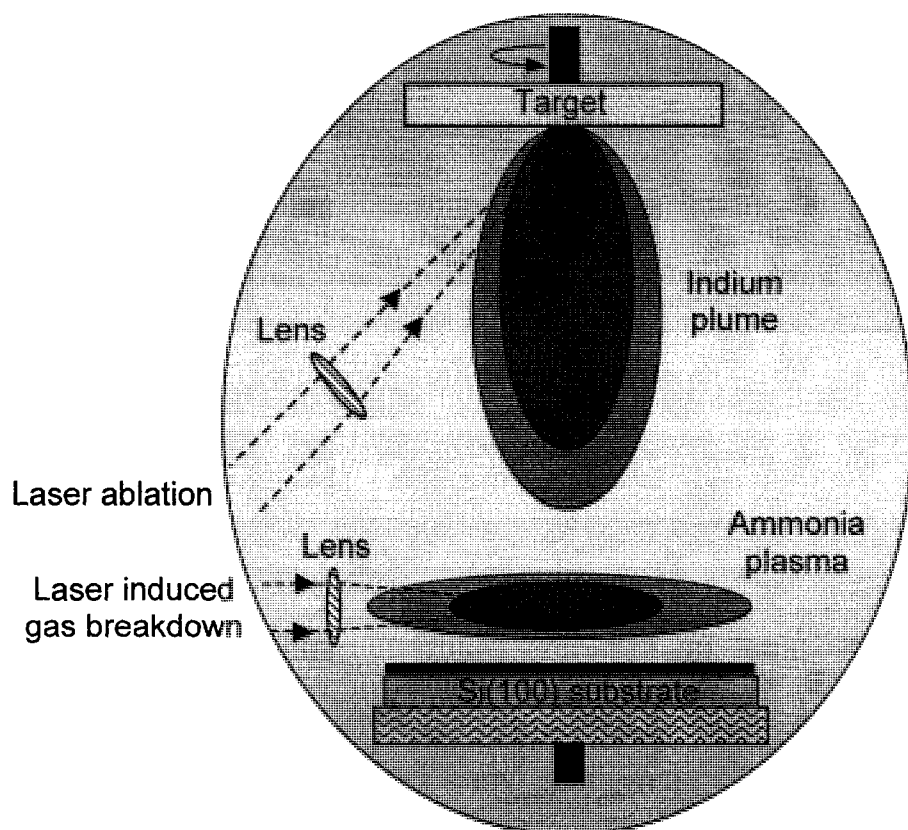


FIG. 5.8. Schematic diagram of the laser induced ammonia breakdown to assist PLD process for growth of InN film on the Si(100) substrate. Laser ablation and laser breakdown create high-density plasmas, which propagate towards the substrate surface where the energetic deposits took place.

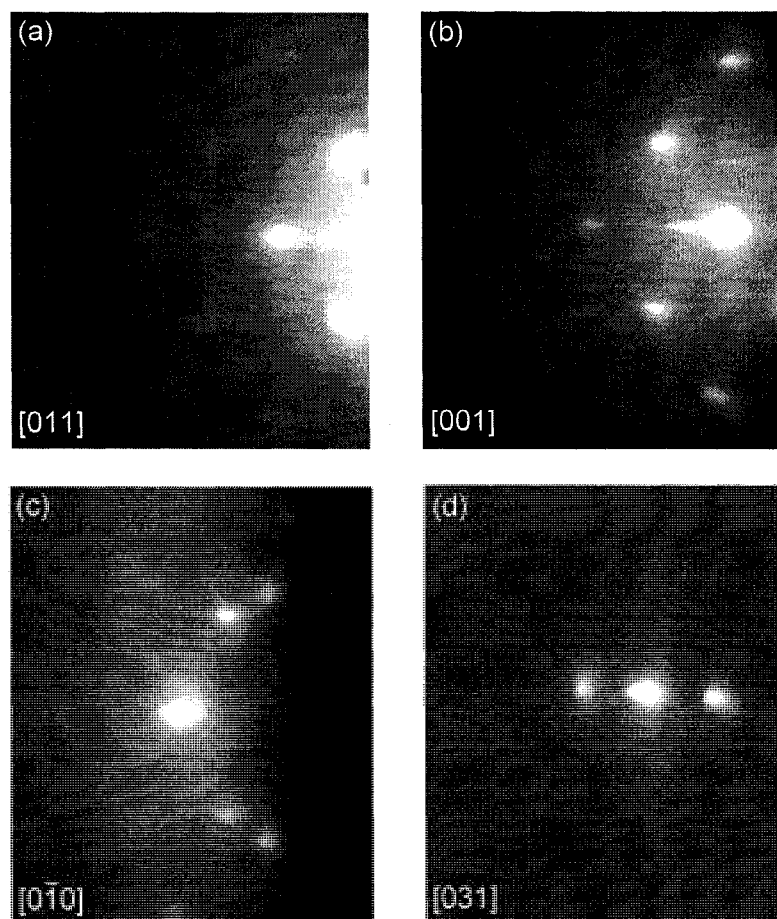


FIG. 5.9. RHEED patterns of the grown InN film on Si(100) substrate at a temperature of $\sim 350^\circ\text{C}$ and pressure of ~ 2 Torr ammonia. Initially, buffer layers of In was grown on top of the Si(100). Then, laser induced ammonia breakdown performed at a substrate temperature of $\sim 250^\circ\text{C}$ without fsPLD of In before the final film InN took place. RHEED patterns were taken at [011], [001], [010], and [031] azimuths of the Si(100) surface are shown in (a), (b), (c), and (d), respectively.

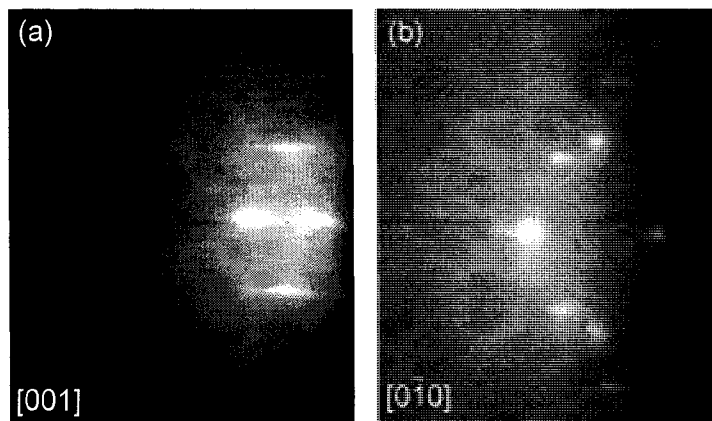


FIG. 5.10. Streaky RHEED patterns observed at [001] and [010] azimuths of the Si(100) surface are shown in (a) and (b), respectively. Transmission and short streaks diffraction beams are overlapped in (b).

The growth mode of the InN on the Si(100)-(2×1) showed that the film morphology developed from 2D to 3D growth, as concluded from the RHEED observations. The Si(100)-(2×1) substrate was a freshly prepared surface giving strong reconstruction features that are characteristic of a clean surface. Transmission RHEED features were not observed during deposition of the buffer In layer or the initial InN growth on the Si(100)-(2×1) surface, which excludes the Volmer-Weber growth mode. The RHEED patterns varied with growth time from streaky to spotty patterns implying that InN growth on Si(100)-(2×1) by fsPLD follows the SK mode. After growth of the 2D wetting layer, the subsequent growth involves strain relaxation and 3D islands formation. The morphology of InN films grown on the Si(100)-(2×1) at ~350 °C, as seen by AFM and SEM, showed elongated and rounded islands distributed on the surface, Fig. 5.11.

The in situ RHEED was used to determine the change in the in-plane lattice parameter during film growth on Si(100)-(2×1) by fsPLD. The surface lattice constant, and hence the surface strain, is inversely proportional to the distance between RHEED streaks. Figure 5.12(a) and (b) shows RHEED pattern along the $[0\bar{1}0]$ azimuth of Si(00) surface and intensity profiles of overlapping In and InN diffraction beams. The in-plane lattice parameter of the InN was measured from the RHEED intensity profiles of the first-order peaks. RHEED analyses along and across the diffracted beams were obtained in the reciprocal space and then converted to length scales. The uncertainty of the incident electron beam energy and the camera length of the RHEED were determined by measuring the in-plane lattice parameter of the Si(100) surface. The lattice spacing of the initial strained 2D In layer measured to be 3.65 ± 0.5 Å. The strain in the InN film grown

on Si(100) was reduced as growth transition occurred from the In to the InN lattice. The in-plane lattice parameter of InN was measured to be $3.50 \pm 0.4 \text{ \AA}$, which corresponds to the relaxed InN lattice constant [26, 65].

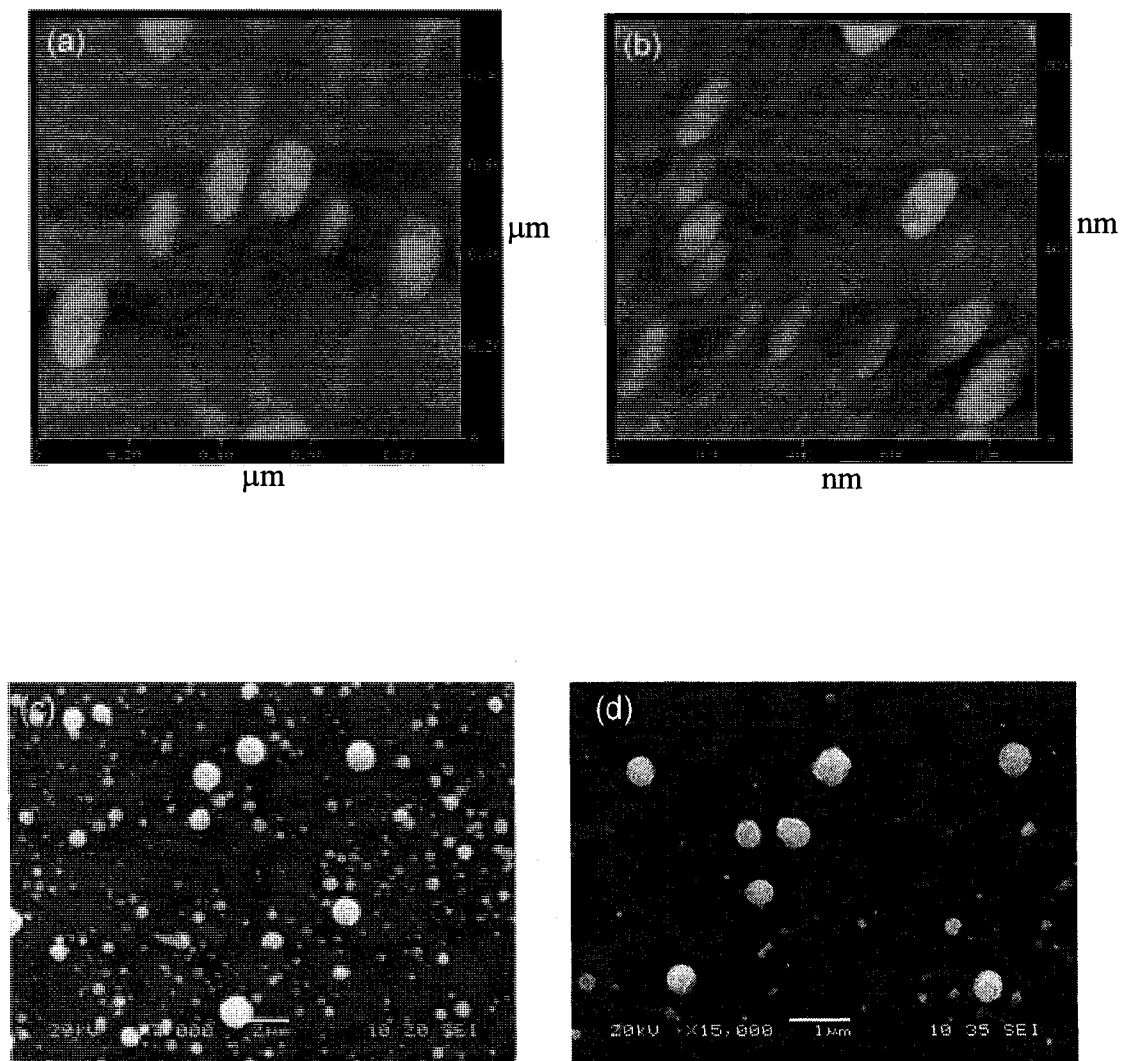


FIG. 5.11. (a) and (b) are AFM images taken at different surface locations of the grown InN film on Si(100) at $\sim 350 \text{ }^{\circ}\text{C}$ by the fsPLD. (c) and (d) are SEM images taken at different surface locations of the grown film.

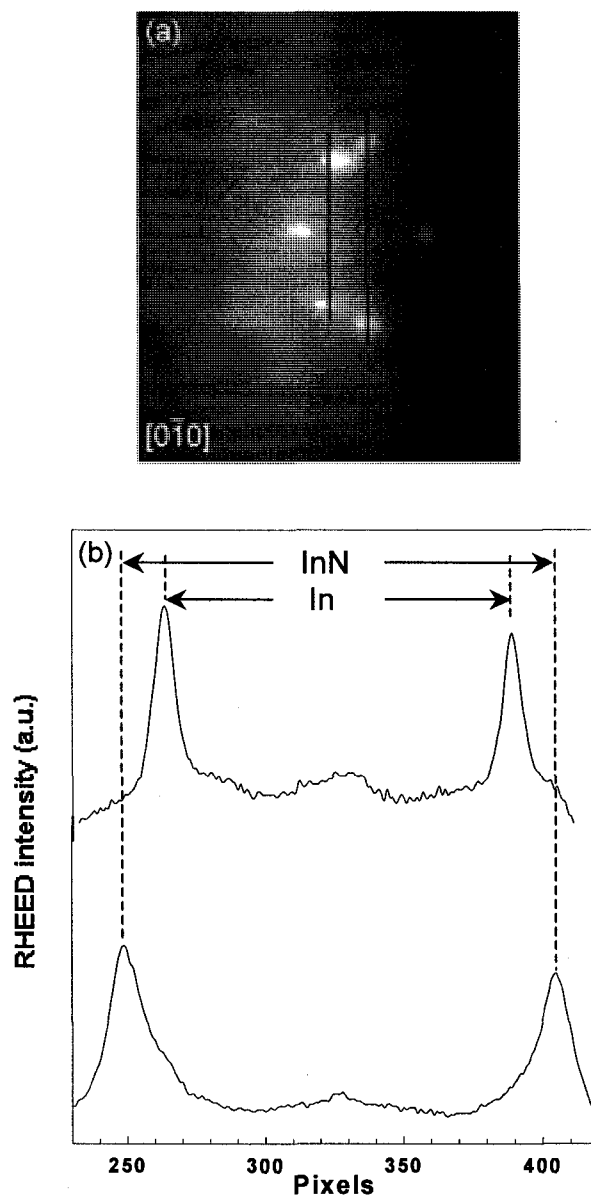


FIG. 5.12. (a) RHEED pattern along the $[0\bar{1}0]$ azimuth of the Si(100) surface. (b) RHEED intensity profiles of the first-order peaks of the In and InN. The bright diffraction beams correspond to the 2D In initial layer and the faint beams corresponds to the InN lattice. The distance between the neighboring streaks is inversely proportional to the in-plane lattice parameter.

Figure 5.13 shows the XRD reflections of InN film deposited on the Si(100) substrate. Two peaks were observed at 2θ of $\sim 33.1^\circ$ and $\sim 62.6^\circ$, which are corresponding to InN($10\bar{1}1$) and InN($11\bar{1}2$), respectively. The pronounced peak intensity located at 2θ of $\sim 69.5^\circ$ corresponds to the Si(400) reflection from the Si(100) substrate. The sample was aligned by searching for the maximum diffraction intensity of the Si(400). The results indicate that the InN film prepared by the fsPLD has a wurtzite crystal structure. Previous growth of InN films on sapphire(0001) and GaAs(111) by microwave-excited MOVPE showed preferred orientation mainly at (0002) and (0004) planes with wurtzite structure [66, 67]. The crystallinity and morphology of the thin films are related to the deposition process and the orientation of the substrate surface. The laser plumes of the PLD and gas breakdown contain energetic species [68]. The resultant nitrogen ion energy in the laser gas breakdown affects the structural properties of the grown InN film on the Si(100) substrate. Previous XRD and Raman spectroscopy study showed that when nitrogen ion energy increases from 50 to 100 eV, the intensity of the (0002) InN peak increased dramatically [41]. However, any further increase beyond 100 eV led to a drastic decrease in the (0002) peak intensity along with increase of the ($10\bar{1}1$) peak intensity. In our case, the preferred orientations and the peak intensities at ($10\bar{1}1$) and ($11\bar{1}2$) are indicative of the kinetic effect of the incident deposits on the substrate surface. The angular position of the diffraction peak is related to the lattice constant. Based on determination of the angular position θ of the diffraction InN($10\bar{1}1$) peak, the interplanar spacing for is 2.69 Å [69]. This results in a lattice constant of 3.53 Å, which is very close to the RHEED measurement.

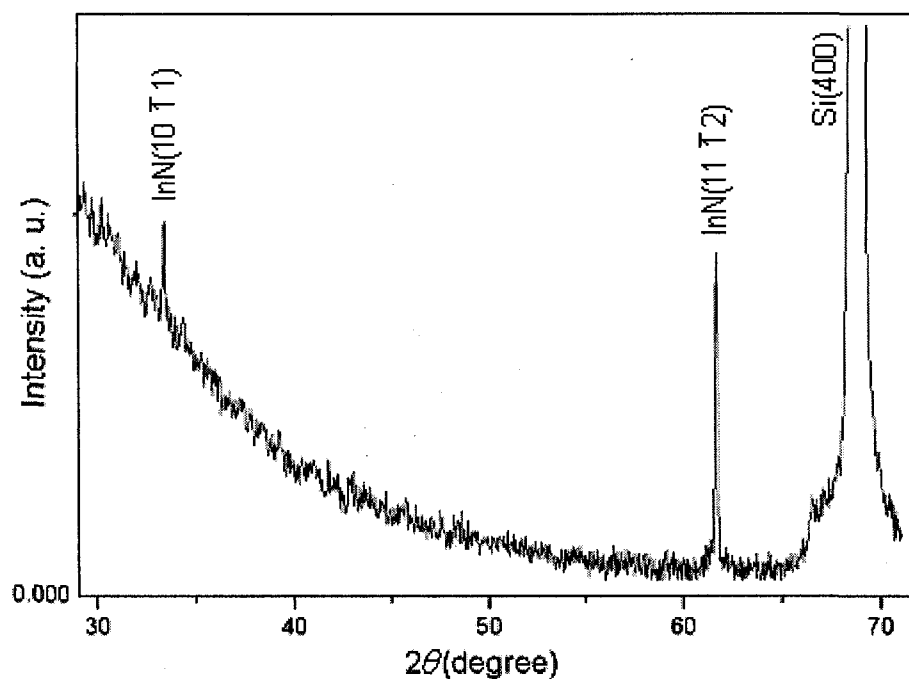


FIG. 5.13. XRD profile of the epitaxial InN film grown on Si(100) at temperature of ~ 350 °C. Buffer layers of In was deposited before growth of InN. Two peaks from InN($10\bar{1}1$) and InN($11\bar{1}2$) InN are observed. The peak (400) is reflection from the Si substrate.

RHEED and XRD analysis provided information about the film growth and morphology at different deposition conditions. Throughout the entire InN growth steps, introducing of an intermediate In layer on the Si(100) substrate by fsPLD has several advantages. It reduces the lattice mismatch between the InN film and the Si(100) substrate. In addition, deposit of initial In on Si(100) surface prevents the formation of the amorphous silicon nitride layer, which could occur when the Si(00) surface was exposed to reactive nitrogen sources [43]. The amorphous silicon nitride phase hinders

the growth of heteroepitaxial InN on Si and causes poor quality films [44]. Growth of In on Si(100)-(2×1) by fsPLD at room temperature showed formation of the initial In(2×1) layer, which has a higher surface energy than the In(2×2) structure grown by MBE [70, 71]. RHEED observations indicate that the In(2×1) has similar surface structure as the Si(100)-(2×1) but with different in-plane lattice constant. Moreover, the presence of In(2×1) at the film/substrate interface minimizes surface defects caused by the hydrogen atoms, which influence the crystallinity and morphology in the growth InN. Therefore, growth of InN on the buffer In(2×1) layer is expected to assist in improving the film quality. Nitridation was performed using thermal cracking and laser induced breakdown of ammonia. Samples prepared by the thermal cracker did not show XRD reflections of InN. This indicates a shortage in InN formation due to deficiency of atomic nitrogen in the case of the thermal cracker source. However, laser induced gas breakdown resulted in a high-density ammonia plasma enhancing the nitride production and accordingly the InN. The advantage of using the resultant plasma is that it can effectively produce reactions to form the InN at low substrate temperature. Moreover, the energetic species in fsPLD, in terms of the ablated In plume and atomic nitrogen from laser breakdown ammonia, promote the epitaxial growth of InN. It affects the film-preferred orientation as discussed in the XRD measurement. The high kinetic energy of deposited species, hence the surface diffusion, influence the film morphology. RHEED images from the initial In and InN buffer layers by fsPLD showed reflection patterns indicating smooth 2D surface for the growth of InN films.

V.5. Conclusion

The fsPLD was used to grow nitride films of InN on Si(100) substrates. The films were grown by three step-growth process with different nitridation procedures. Samples prepared by the thermal cracker source (at pressure of $\sim 5 \times 10^{-6}$ Torr) indicate deficiency of atomic nitrogen. Deposition of initial monolayers of In on Si(100) surfaces by fsPLD promote the epitaxial growth of InN and improve the film quality. The initial In buffer layer has a dual advantage such that it prevents formation of the amorphous silicon nitride and reduces the effects of hydrogen, a product of ammonia dissociation. Laser induced gas breakdown is an efficient source of nitridation process, which influenced the crystallinity and morphology of the InN films. RHEED and XRD analysis show high quality InN films grown at a substrate temperature of ~ 350 °C. RHEED observation showed that InN grew on the Si(100)-(2 \times 1) surface by the SK growth mode. The in-plane lattice parameter was reduced as growth transition occurred from the In to the InN lattice. The XRD profile shows that the InN film has a wurtzite structure.

V.6. References

- [1] S. Strite and H. Morkoc, "GaN, AlN, and InN: A review," *J. Vac. Sci. Technol. B* **10**, 1237-1266 (1992).
- [2] O. Ambacher, "Growth and applications of group III-nitrides," *J. Phys. D: Appl. Phys.* **31**, 2653-2710 (1998).
- [3] S. C. Jain, M. Willander, J. Narayan, and R. Van Overstraeten, "III-nitrides: Growth, characterization, and properties," *J. Appl. Phys.* **87**, 965-1006 (2000).
- [4] S. Yoshida, "Growth of cubic III-nitride semiconductors for electronics and optoelectronics application," *Physica E* **7**, 907-914 (2000).
- [5] I. Akasaki, "Progress in crystal growth of nitride semiconductors," *J. Cryst. Growth* **221**, 231-239 (2000).
- [6] T. D. Moustakas, E. Iliopoulos, A. V. Sampath, H. M. Ng, D. Doppalapudi, M. Misra, D. Korakakis, and R. Singh, "Growth and device applications of III-nitrides by MBE," *J. Cryst. Growth* **227-228**, 13-20 (2001).
- [7] I. Akasaki, "Nitride semiconductors – Impact on the future world," *J. Cryst. Growth* **237-239**, 905-911 (2002).
- [8] B. Monemar, P. P. Paskov, T. Paskova, J. P. Bergman, G. Pozina, W. M. Chen, P. N. Hai, I. A. Buyanova, H. Amano, and I. Akasaki, "Optical characterization of III-nitrides," *Materials Sci. Eng. B* **93**, 112-122 (2002).
- [9] K. S. A. Butcher and T. L. Tansley, "InN, latest development and a review of the band-gap controversy," *Superlattices and Microstructures* **38**, 1-37 (2005).

- [10] A. G. Bhuiyan, A. Hashimoto, and A. Yamamoto, "Indium nitride (InN): A review on growth, characterization, and properties," J. Appl. Phys. **94**, 2779-2808 (2003).
- [11] M. Leroux and B. Gil, "*Bandedge and optical functions of InN*," in J. H. Edgar, S. Strite, I. Akasaki, H. Amano, C. Wetzel (Eds.), Gallium Nitride and Related Semiconductors, Publ. INSPEC, London, p. 117 (1999).
- [12] C. J. Sun, P. Kung, A. Saxler, H. Ohsato, E. Bigan, and M. Razeghi, and D. K. Gaskill, "Thermal stability of GaN thin films grown on (0001) Al_2O_3 , (01 $\bar{1}2$) Al_2O_3 and (0001)_{Si} 6H-SiC substrates," J. Appl. Phys. **76**, 236-241 (1994).
- [13] T. Sasaki and S. Zembutsu "Substrate-orientation dependence of GaN single-crystal films grown by metalorganic vapor-phase epitaxy," J. Appl. Phys. **61**, 2533-2540 (1987).
- [14] A. Yamamoto, Y. Murakami, K. Koide, M. Adachi, and A. Hashimoto "Growth temperature dependences of MOVPE InN on sapphire substrates," Phys. Status Solidi B **228**, 5-8 (2001).
- [15] A. Botchkarev, A. Salvador, B. Sverdlov, J. Myoung, and H. Morkoc, "Properties of GaN films grown under Ga and N rich conditions with plasma enhanced molecular beam epitaxy," J. Appl. Phys. **77**, 4455-4458 (1995).
- [16] W. E. Hoke, P. J. Lemonias, and D. G. Weir, "Evaluation of a new plasma source for molecular beam epitaxial growth of InN and GaN films," J. Cryst. Growth **111**, 1024-1028 (1991).

- [17] Y. F. Ng, Y. G. Cao, M. H. Xie, X. L. Wang, and S. Y. Tong, "Growth mode and strain evolution during InN growth on GaN(0001) by molecular-beam epitaxy," *Appl. Phys. Lett.* **81**, 3960-3962 (2002).
- [18] J. Wu, W. Walukiewicz, K. M. Yu, J. W. Ager III, E. E. Haller, H. Lu, W. J. Schaff, Y. Saito, and Y. Nanishi, "Unusual properties of the fundamental band gap of InN," *Appl. Phys. Lett.* **80**, 3967-3969 (2002).
- [19] T. Matsuoka, H. Okamoto, M. Nakao, H. Harima, and E. Kurimoto, "Optical bandgap energy of wurtzite InN," *Appl. Phys. Lett.* **81**, 1246-1248 (2002).
- [20] M. Higashiwaki and T. Matsui, "Estimation of band-gap energy of intrinsic InN from photoluminescence properties of undoped and Si-doped InN films grown by plasma-assisted molecular-beam epitaxy," *J. Cryst. Growth* **269**, 162-166 (2004).
- [21] T. V. Shubina, S. V. Ivanov, V. N. Jmerik, D. D. Solnyshkov, V. A. Vekshin, P. S. Kop'ev, A. Vasson, J. Leymarie, A. Kavokin, H. Amano, K. Shimono, A. Kasic, and B. Monemar, "Mie resonances, infrared emission, and the band gap of InN," *Phys. Rev. Lett.* **92**, 117407 (1-4) (2004).
- [22] K. M. Yu, Z. Liliental-Weber, W. Walukiewicz, W. Shan, J. W. Ager III, S. X. Li, R. E. Jones, E. E. Haller, H. Lu, and W. J. Schaff, "On the crystalline structure, stoichiometry and band gap of InN thin films," *Appl. Phys. Lett.* **86**, 071910-071912 (2005).
- [23] S. V. Ivanov, T. V. Shubina, V. N. Jmerik, V. A. Vekshin, P. S. Kop'ev, and B. Monemar, "Plasma-assisted MBE growth and characterization of InN on sapphire," *J. Cryst. Growth* **269**, 1-9 (2004).

- [24] K. S. A. Butcher, M. Wintrebert-Fouquet, P. P.-T. Chen, T.L. Tansley, H. Dou, S. K. Shrestha, H. Timmers, M. Kuball, K. E. Prince, and J. E. Bradby, "Nitrogen-rich indium nitride," *J. Appl. Phys.* **95**, 6124-6128 (2004).
- [25] C. Stampfl, C. G. Van De Walle, D. Voggel, P. Krugger, and J. Pollman, "Native defects and impurities in InN: First-principles studies using the local-density approximation and self-interaction and relaxation-corrected pseudopotentials," *Phys. Rev. B* **61**, R7846-R7849 (2000).
- [26] V. Yu. Davydov, A. A. Klochikhin, R. P. Seisyan, V. V. Emtsev, S. V. Ivanov, F. Bechstedt, J. Furthmüller, H. Harima, A. V. Mudryi, J. Aderhold, O. Semchinova, and J. Graul, "Absorption and emission of hexagonal InN. Evidence of narrow fundamental band gap," *Phys. Status Solidi. B* **229**, R1-R3 (2002).
- [27] Z. H. Lan, W. M. Wang, C. L. Sun, S. C. Shi, C. W. Hsu, T. T. Chen, K. H. Chen, C. C. Chen, Y. F. Chen, and L. C. Chen, "Growth mechanism, structure and IR photoluminescence studies of indium nitride nanorods," *J. Cryst. Growth* **269**, 87-94 (2004).
- [28] M. Kuball, J.W. Pomeroy, M. Wintrebert-Fouquet, K.S.A. Butcher, Hai Lu, W.J. Schaff, "A Raman spectroscopy study of InN," *J. Cryst. Growth* **269**, 59-65 (2004).
- [29] O. Briot, B. Maleyre, and S. Ruffenach, "Indium nitride quantum dots grown by metalorganic vapor phase epitaxy," *Appl. Phys. Lett.* **83**, 2919-2921 (2003).
- [30] V. Yu. Davydov, A. A. Klochikhin, V. V. Emtsev, D. A. Kurdyukov, S. V. Ivanov, V. A. Vekshin, F. Bechstedt, J. Furthmüller, J. Aderhold, J. Graul, A. V.

- Mudryi, H. Harima, A. Hashimoto, A. Yamamoto, and E. E. Haller, "Band gap of hexagonal InN and InGaN alloys," *Phys. Status Solidi. B* **234**, 787-795 (2002).
- [31] C.P. Foley and J. Lyngdal, "Analysis of indium nitride surface oxidation," *J. Vac. Sci. Technol. A* **5**, 1708-1712 (1987).
- [32] T. L. Tansley and R. J. Egan, "Point-defect energies in the nitrides of aluminum, gallium, and indium," *Phys. Rev. B* **45**, 10942-10950 (1992).
- [33] Y. Nanishi, Y. Saito and T. Yamaguchi, "RF-molecular beam epitaxy growth and properties of InN and related alloys," *Jpn. J. Appl. Phys.* **42**, 2549-2559 (2003).
- [34] K. Xu and A. Yoshikawa, "Effects of film polarities on InN growth by molecular-beam epitaxy," *Appl. Phys. Lett.* **83**, 251-253 (2003).
- [35] E. Dimakis, E. Lliopoulos, K. Tsagaraki, Th. Kehagias, Ph. Komninou, and A. Georgakilas, "Heteroepitaxial growth of In-face InN on GaN (0001) by plasma-assisted molecular-beam epitaxy," *J. Appl. Phys.* **97**, 113520 (1-10) (2005).
- [36] Q. Guo, O. Kato, and A. Yoshida, "Thermal stability of indium nitride single crystal films," *J. Appl. Phys.* **73**, 7969-7971 (1993).
- [37] C. B. Vartuli, S. J. Pearton, C. R. Abernathy, J. D. MacKenzie, and E. S. Lambers, and J. C. Zolper, "High temperature surface degradation of III-V nitrides," *J. Vac. Sci. Technol. B* **14**, 3523-3531 (1996).
- [38] Y. Bu, L. Ma, and M. C. Lin, "Laser-assisted chemical vapor deposition of InN on Si(100)," *J. Vac. Sci. Technol. A* **11**, 2931-2937 (1993).
- [39] T. Yodo, H. Yona, H. Ando, D. Nosei, and Y. Harada, "Strong band edge luminescence from InN films grown on Si substrates by electron cyclotron

- resonance-assisted molecular beam epitaxy,” *Appl. Phys. Lett.* **80**, 968-970 (2002).
- [40] N. Takahashi, A. Niwa, and T. Nakamura “Investigations of morphology, purity and crystal defects of the InN pillar crystals prepared by means of halide chemical vapor deposition under atmospheric pressure,” *J. Phys. Chem. Solids* **65**, 1259-1263 (2004).
- [41] X. H. Ji and S. P. Lau, “Polycrystalline InN thin films prepared by ion-beam-assisted filtered cathodic vacuum arc technique,” *J. Cryst. Growth* **282**, 271-278 (2005).
- [42] Y. Huang, C. Liu, Y. Lai, C. Wang, Y. Lai, and C. Wang, Y. Lai, and H. Chung “Structural and optical properties of cubic-InN quantum dots prepared by ion implantation in Si(100) substrate,” *Appl. Phys. Lett.* **91**, 091921-091923 (2007).
- [43] L. Liu and J. Edgar, “Substrates for gallium nitride epitaxy,” *Mater. Sci. Eng. R* **37**, 61-127 (2002).
- [44] A. Yamamoto, M. Tsujino, M. Ohkubo, and A. Hashimoto, “Nitridation effects of substrate surface on the metalorganic chemical vapor deposition growth of InN on Si and α -Al₂O₃ substrates,” *J. Cryst. Growth* **137**, 415-420 (1994).
- [45] A. Yamamoto, Y. Yamauchi, M. Ohkubo, A. Hashimoto, and T. Saitoh, “Heteroepitaxial growth of InN on Si(111) using a GaAs intermediate layer,” *Solid-State Electronics* **41**, 149-154 (1997).
- [46] T. Yodo, H. Yona, H. Ando, D. Nosei, and Y. Harada, “Strong band edge luminescence from InN films grown on Si substrates by electron cyclotron

- resonance-assisted molecular beam epitaxy,” Appl. Phys. Lett. **80**, 968-970 (2002).
- [47] F. E. Fernandez, E. Rodrigez, M. Pumarol, T. Guzman, W. Jia, and A. Martinez “Nitride thin films grown by pulsed laser deposition assisted by atomic nitrogen beam,” Thin Solid Films **377-378**, 781-787 (2000).
- [48] P. Bhattacharya, T. K. Sharma, S. Singh, A. Ingale, and I. M. Kukreja, “Observation of zincblende phase in InN thin films grown on sapphire by nitrogen plasma-assisted pulsed laser deposition,” J. Cryst. Growth **236**, 5-9 (2002).
- [49] D. Feiler, R. S. Williams, A. A. Talin, H. Yoon, and M. S. Goorsky, “Pulsed laser deposition of epitaxial AlN, GaN, and InN thin films on sapphire(0001),” J. Cryst. Growth **171**, 12-20 (2002).
- [50] J. Ohta, H. Fujioka, T. Honke, and M. Oshima, “Epitaxial growth of InN on c-plane sapphire by pulsed laser deposition with r.f. nitrogen radical source,” Thin Solid Films **457**, 109-113 (2004).
- [51] K. Mitamura, J. Ohta, H. Fujioka, and M. Oshima “Growth of InN films on spinel substrates by pulsed laser deposition,” Phys. Status Solidi. (RRL) **1**, 211-213 (2007).
- [52] K.P. Adhi, S. Harchirkar, S. M. Jejurikar, P.M. Koinkar, M.A. More, D.S. Joag, and L.M. Kukreja, “Pulsed laser deposited nanostructured InN thin films as field emitters,” Solid State Communications **142**, 110-113 (2007).
- [53] D. B. Chrisey and G. K. Hubler, “*Pulsed laser deposition of thin films*,” John Wiley and Sons, New York (1994).

- [54] J. C. Miller and R. F. Haglund, "*Laser ablation and desorption*," Experimental Methods in the Physical Sciences **30**, Academic Press, Boston (1998).
- [55] D. Bauerle, "*Laser processing and chemistry*," Second Edition, Springer, Berlin, Heidelberg (1996).
- [56] J. Shen, Z. Gai, and J. Kirschner, "Growth and magnetism of metallic thin films and multilayers by pulsed-laser deposition," Surf. Sci. Rep. **52**, 163-218 (2004).
- [57] E.G. Gamaly, A.V. Rode, and B. Luther-Davies, "Ultrafast ablation with high-pulse-rate lasers. Part I: Theoretical considerations," J. Appl. Phys. **85**, 4213-4221 (1999).
- [58] E. G. Gamaly, A.V. Rode, V.T. Tikhonchuk, and B. Luther-Davies, "Electrostatic mechanism of ablation by femtosecond lasers," Appl. Surf. Sci. **197-198**, 699-704 (2002).
- [59] M. A. Hafez and H. E. Elsayed-Ali, "Indium growth on Si(100)-(2×1) by femtosecond pulsed laser deposition," J. Vac. Sci. Technol. A **23**, 1681-1686 (2005).
- [60] S. Andrieu and P. Frechard, "What information can be obtained by RHEED applied on polycrystalline films," Surf. Sci. **360**, 289-296 (1996).
- [61] C. Norenberg, M. G. Martin, R. A. Oliver, M. R. Castell, and G. A. D. Briggs, "Heteroepitaxial growth of InN islands studied by STM and AFM," J. Phys. D: Appl. Phys. **35**, 615-619 (2002).
- [62] F. Owman and P. Martensson, "STM study of hydrogen exposure of the Si(111) $\sqrt{3} \times \sqrt{3}$ -In surface," Surf. Sci. **359**, 122 (1996).

- [63] J.-T. Ryu, K. Kui, K. Noda, M. Katayama, and K. Oura, "The effect of hydrogen termination on In growth on Si(100) surface," *Surf. Sci.* **401**, L425-L431 (1998).
- [64] F. P. Leisenberger, H. Ofner, M. G. Ramsey, and F. P. Netzer, "The growth of indium on the H-terminated Si(111)1×1 surface," *Surf. Sci.* **383**, 25 (1997).
- [65] I. J. Lee, J. W. Kim, Y.-H. Hwang and H.-K. Kim "Synchrotron x-ray scattering study of lattice relaxation in InN epitaxial layers on sapphire(0001) during dc sputter growth," *J. Appl. Phys.* **92**, 5814-5818 (2002).
- [66] Q. Guo, H. Ogawa, H. Yamano, and A. Yoshida, "Growth of InN films on GaAs(111) and GaP(111) substrates by microwave-excited metalorganic vapor phase epitaxy," *Appl. Phys. Lett.* **66**, 715-717 (1995).
- [67] H.-J. Kwon, Y.-H. Lee, O. Miki, H. Yamano, and A. Yoshida, "Raman spectra of indium nitride thin films grown by microwave-excited metalorganic vapor phase epitaxy on (0001) sapphire substrates," *Appl. Phys. Lett.* **69**, 937-939 (1996).
- [68] J. Perriere, E. Millon, W. Seiler, C. Boulmer-Leborgne, V. Carciun, O. Albert, J. C. Loulergue, and J. Etchepare, "Comparison between ZnO films grown by femtosecond and nanosecond laser ablation," *J. Appl. Phys.* **91**, 690-696 (2002).
- [69] M. F. Wu, S. Q. Zhou, A. Vantomme, Y. Huang, H. Wang, and H. Yang, "High-precision determination of lattice constants and structural characterization of InN thin films," *J. Vac. Sci. Technol. A* **24**, 275-279 (2006).
- [70] M. A. Hafez and H. E. Elsayed-Ali, "Formation of In(2×1) and In islands on Si(100)-(2×1) by femtosecond pulsed laser deposition," *J. Appl. Phys.* **101**, 113515 (1-10) (2007).

- [71] J. E. Northrup, M. C. Schabel, C. J. Karlsson, and R. I. Uhrberg, "Structure of low-coverage phases of Al, Ga, and In on Si(100)," *Phys. Rev. B* **44**, 13799-13802 (1991).

CHAPTER VI

SUMMARY

The effect of atomic hydrogen cleaning on the morphology of the InP(100) surface was investigated using in situ RHEED, and this was followed by surface activation to NEA. Atomic hydrogen cleaning produced a clean, phosphorus-stabilized (2×4)-reconstructed InP surface. Hydrogen cleaning of InP(100) performed at temperatures of ~370 °C and 385-400 °C showed improvement of the QE, which reached ~6% after activation to NEA. A secondary electron emission from a hydrogen-cleaned surface was measured. The QE and secondary yield were shown to increase with hydrogen cleaning time. As the optimum cesiation degraded by desorption, the number of secondary electrons able to escape from the surface was reduced. With increased hydrogen cleaning time at 385-400 °C, surface defects due to phosphorus desorption were observed along with a reduction in QE. Results show that removal of surface contaminants by atomic hydrogen, which improves the electronic surface quality, was associated with morphology changes. The RHEED specular beam split peak spacing, which is characteristic of a vicinal surface, was analyzed. Quantitative RHEED, as a surface probe, gave information on average surface characteristics of terrace width and adatom vacancy density of the hydrogen-cleaned InP surface. RHEED observation showed reduction in the average terrace width with hydrogen exposure time and was not accompanied by noticeable electronic surface quality degradation. This suggests that atomic hydrogen etching occurs preferentially at terrace edges, which causes the observed decrease of the average terrace width with an increase in terrace width

fluctuation. This could be a result of a combination of thermal and chemical effects of hydrogen interaction with the surface. Besides, thermal diffusion of atoms on the surface can cause changes in the terrace edge morphology due to atoms diffusing to sites on the terrace edge. The decrease in surface disorder, as determined by the RHEED intensity-to-background ratio R , correlated with the increased QE. A higher R surface produced higher QE. Thus, quantitative RHEED can be used to optimize semiconductor surface preparation prior to activation to NEA. While RHEED offers a view of surface morphology development with hydrogen cleaning and is suitable for surface probing during preparation, studies using other surface techniques are needed to resolve the nature of the microscopic reactions of atomic hydrogen with the surface and its effects on the surface electronic quality.

The growth dynamics, structure, and morphology of In on vicinal Si(100)-(2×1) surface by fsPLD were studied using in situ RHEED and ex situ AFM and STM real image techniques. It was found that In grew on Si(100) by the Stranski-Krastanov mode. At room temperature, the initial growth formed in the In(2×1) structure. During the growth of the first monolayers, the in-plane lattice parameter changed to be 3.65 ± 0.1 Å, which indicated formation of strained 2D layers. During In growth, development of another RHEED pattern such as (2×2), as in MBE growth, was not observed. Relaxation and recovery of the RHEED intensity was observed during the deposition and after growth termination, respectively. Each laser pulse ablating the In target created random distribution of deposits on the substrate surface, which instantaneously decreased the specular RHEED intensity. Then, the In deposits rearranged by diffusion on the surface, leading to the increased RHEED intensity until the next In flux. This periodic change in

surface smoothness led to the observed RHEED intensity relaxation between the laser depositing pulses. RHEED observation showed that surface recovery after growth termination occurs in two stages, a fast and a slow process. The recovery and relaxation of the RHEED intensity are attributed to the step flow mode of the 2D growth stage. The surface diffusion coefficient of deposited In on the initial 2D In(2×1) layer was estimated from the fast recovery by quantitative RHEED to be on the order of 10^{-14} cm²/s. This indicated that the initial fast RHEED recovery was attributed to surface diffusion of In small clusters. As growth proceeds, 3D islands grew on the 2D In(2×1) layers. The FWHM of the RHEED specular peak decreased during In film growth, indicative of well-ordered growth and an increase of the island size. The ex situ AFM analysis showed that the 3D islands developed into elongated-polyhedral, circular, and triangular shapes. The occurrence of these different morphologies of In islands indicated that the growth was caused to undergo the influence of the structure of the 2D In(2×1) layer and the growth kinetics of the fsPLD. For example, when the In deposits were influenced by the dimer structure of the initial In(2×1) layer, elongated islands developed, which showed preferential growth orientation with respect to the Si substrate. When the In deposits have enough surface diffusion energy to overcome the anisotropic strain in the underlying In(2×1) first layers, the deposits move across as well as along the surface, and the growth results in different island shapes, such as the circular islands. The islands lateral size-to-height ratios indicated that the growth of islands spreads laterally more than vertically on the surface. The results suggest that fsPLD of In removed the reconstruction of the Si(100)-(2×1) surface in the early growth and result in the initial In(2×1) structure. Next, growth of In on Si(100)-(2×1) at temperature of 350-420 °C was studied and showed

formation of $\text{In}(4\times 3)$ structure. Unlike thermal evaporation, the energetic and pulsed nature of PLD led to the creation of mobile In deposits, enhancing the 2D growth. RHEED intensity relaxation was observed during the growth of $\text{In}(4\times 3)$ layers by the step flow. The activation energy of surface diffusion for growth of $\text{In}(4\times 3)$ on $\text{Si}(100)-(2\times 1)$ by fsPLD, determined from Arrhenius relation, was 1.4 ± 0.2 eV. The diffusion frequency was measured to be $1.0\pm 0.1\times 10^{11} \text{ s}^{-1}$, which indicates that the rate limiting process was due to surface diffusion of cluster rather than of adatoms. The growth stages of the $\text{In}(4\times 3)$ layer, probed by RHEED intensity relaxation, proceeds in a two-step-process, formation of small In clusters and surface diffusion to the terrace step edges with a characteristic activation energy and a diffusion rate constant. The terrace width dynamics during growth of the $\text{In}(4\times 3)$ phase and the related surface processes were studied. Gradual reduction in the terrace width occurred and was attributed to detachment of In atoms from terrace edges. At a substrate temperature of 405°C , the average terrace width decreased from $61\pm 10 \text{ \AA}$, corresponding to the vicinal $\text{Si}(100)$ surface, to an equilibrium value of $45\pm 7 \text{ \AA}$ after deposition of ~ 23 ML. As In coverage was increased, the terrace width reached an equilibrium length, where the possibility of growth of In islands on terrace surface increased. As growth proceeded, RHEED pattern transition from (4×3) to (1×1) was observed. AFM profile indicated a rounded islands with average height of ~ 1 nm and width of ~ 25 nm. The rounded shape of the islands show that the In deposits have isotropic growth on the $\text{In}(4\times 3)$ surface compared with the $\text{In}(2\times 1)$ surface structure that forms on $\text{Si}(100)-(2\times 1)$ at room temperature, where anisotropic growth leads to formation of elongated In islands.

Finally, the fsPLD was used to grow nitride films of InN on Si(100) substrates. The motivation of this study was to grow high quality InN on Si(100) substrates for device application. The InN material has shown previously a band gap controversy due to the difficulty of synthesizing high quality films, especially in the sense of crystal growth. In the present work, the results of fsPLD growth of In on Si(100) surface was employed by growing buffer layers of In prior to growth of InN on Si. The nitridation source was obtained using two different procedures, thermal cracking and laser induced gas breakdown of ammonia. The growth and characterization of InN films were studied by in situ RHEED and ex situ AFM, SEM, and XRD. RHEED observation showed that InN grew on Si(100)-(2×1) surface by the SK growth mode. XRD profile shows that the InN film has a wurtzite structure. The initial In(2×1) layer and nitridation source have influenced the crystallinity and morphology of the InN films.

APPENDIX A

PULSED LASER DEPOSITION SYSTEM

The PLD system and components used in this work are shown in Fig. A.1. The chamber is a stainless steel cylinder mounted on an ion pumped stand of 220 L/s with a base of 16" O.D. conflate flange to obtain ultrahigh vacuum (UHV). It consists of vacuum gauges and pumps, feedthroughs, viewports, flanges, and valves. The base pressure is in the range of low 10^{-9} to mid 10^{-10} Torr. The RHEED system, thermal cracker sources, and residual gas analyzer (RGA) are installed in geometry around the substrate and target holders.

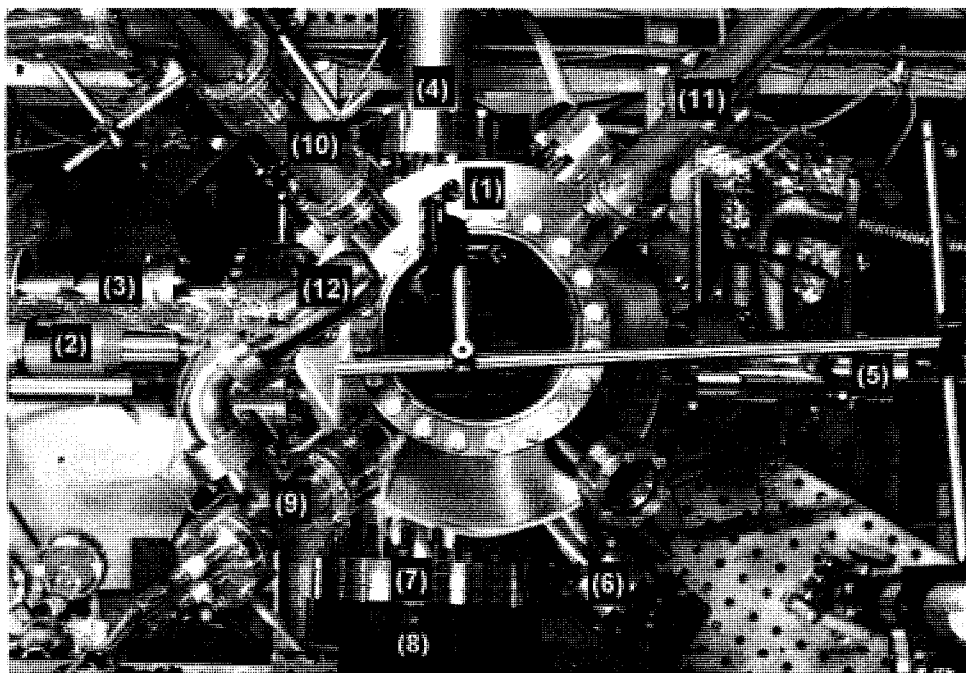


FIG. A.1. Top view of the PLD system showing components arrangement: (1) chamber; (2) target holder; (3) shutter holder; (4) RHEED gun; (5) substrate holder; (6) laser window; (7) phosphor RHEED screen; (8) CCD camera; (9) and (10) thermal cracker sources; (11) RGA; and (12) UHV high precision leak valve.

A.1. Opening the PLD system

Before starting pumping up the system check the following:

- Disconnect wires and thermocouples connections from the substrate manipulator.
- Verify that the RHEED electron gun source is turned off.
- Turn on the pressure gauges (ionization and convector) to monitor the pressure.

Next, prepare the following steps:

- 1- Make sure that the manual vent valve of the turbo pump is closed.
- 2- Turn on the mechanical pump and then turn on the turbo pump.
- 3- Wait for the mechanical and turbo pumps to run for 20 min.
- 4- Turn off the ion pump and then close its gate valve to keep the parts inside the ion pump under vacuum.
- 5- The pressure in the chamber will increase to high 10^{-8} or to low 10^{-7} Torr range (due to system degassing).
- 6- Open slowly the right angle UHV valve, which connect the turbo to the chamber.
- 7- Wait 10 min for the system pumping by the turbo and the mechanical pumps.
- 8- Turn off the turbo then the mechanical pump and watch for the pressure.
- 9- Fill out the chamber with dry nitrogen to atmospheric pressure using a regulating vacuum valve. The dry nitrogen maintains the chamber's interior from the water vapor or moisture. The alternative way is to open the turbo vent valve gradually (in case of manual ventilation).
- 10- The chamber should not be left open for long period of time. To install a new target or substrate, take out the target or the substrate manipulator carefully and avoid scratching the knife-edge of the conflate flanges or losing holder's

components. Cover the opened ports of the chamber. Always use a new copper gasket and clean the vacuum components with methanol or acetone before installing inside the vacuum chamber.

A.2. The target and substrate holders

A.2.1. The target holder

- The target holder is mounted on 1.33" O.D. CF of the 8" O.D. CF processing flange, Fig. A.2. The base of the holder is stainless steel of 2.5" in diameter and connected to a rotation driver dc controller.
- Polish and clean the new target's surface, such as In, before installation in the chamber. Fix the target on the holder using an UHV adhesive material such as Torr Seal.
- For low melting point targets, such as In, it is necessary to use a rotatable shutter to minimize heat transfer by radiation during heating the substrate. The 8" processing port has a magnetic holder mounted on 1.33" O.D. flange; therefore the shutter can be rotated to shield the target. Caution is required during rotating the shutter so as not to hit vacuum components such as the substrate holder, filaments, and wire connections.
- Before turning on the laser beam, the shutter should be away from the laser beam path. In addition, it should be away from the electron beam path in case of using the RHEED electron gun.
- Make sure that the target's surface is at laser focusing. The mirrors before the focusing lens are used to scan the laser beam over the target's surface.

- Turn on the target rotation before starting laser ablation.
- To remove a target from the base holder, use a heat gun to heat the target-holder interface till the “Torr Seal” is completely loose and the target is detached.

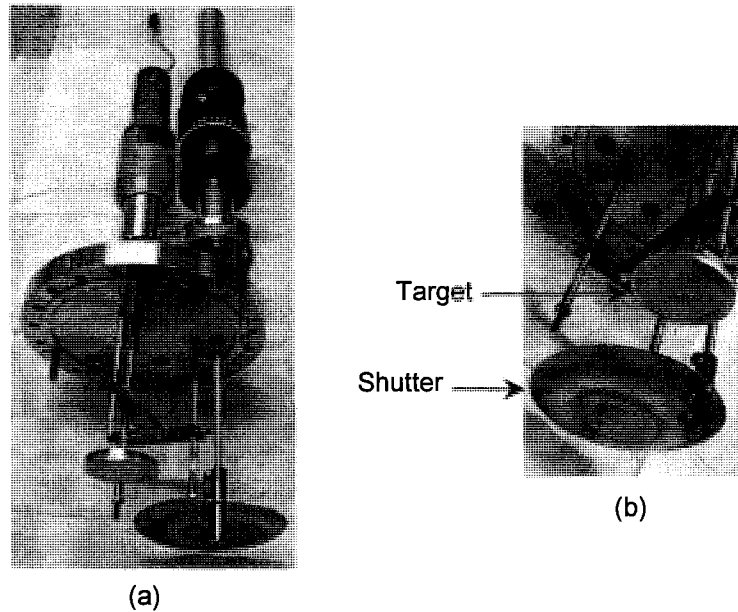


FIG. A.2. The target manipulator showing the target and the shutter holders on the 8" O.D. CF flange in (a) and magnified image in (b).

A.2.2. The substrate holder

- The substrate holder has a 4.5" O.D. CF flange, Fig. A.3.
- A thermocouple wire, k-type, is used to measure the substrate temperature. The temperature is measured by a thermometer connected to feedthrough terminals located on a 1.33" O.D. CF. The terminals are k-type, and therefore k-type thermocouples should be used to avoid junction contacts between different types.

- Substrate heating, such as Si, is performed in regular steps to avoid a sudden increase for the pressure of the chamber. Always monitor the pressure and substrate temperature.
- Avoid hitting the substrate holder by the RHEED electron beam in case of using a heating resistive stage.
- The substrate holder can move in a linear motion and azimuthally during the PLD experiments.
- During heat cleaning to high temperatures, move the substrate holder backward to reduce heating effects on the target material.

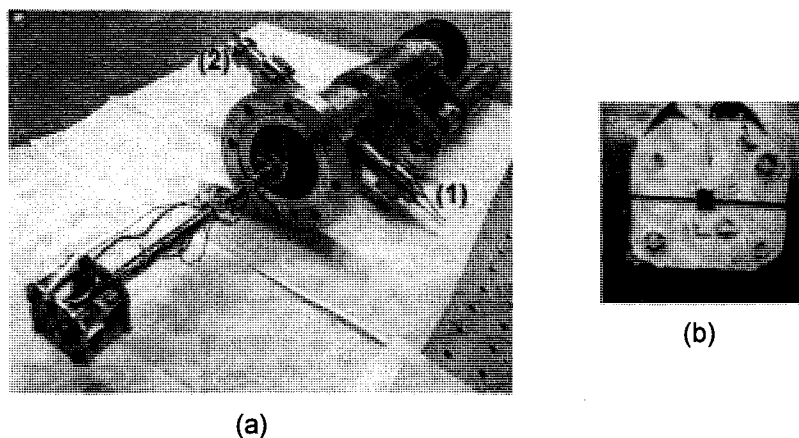


FIG. A.3. (a) Substrate manipulator on the 4.5" O.D. CF flange: (1) power terminals and (2) thermocouple terminals. (b) Sample holder.

A.3. Substrate heating stages

There are two different heating substrate holders. The first holder is a direct-current heating stage, which is used for high heating temperatures (>1000 °C). The second holder is an indirect heating stage using a high resistive material (max. 600 °C).

A. 3.1. Direct heating holder

The direct heating holder, Fig. A.4, is used to heat cleaning Si samples.

- The clips and the plates of the stage are made of molybdenum (Mo).
- When installing the holder, make sure that the plates are aligned.
- The clips, plates, and screws are required to be cleaned regularly in acetone and methanol ultrasonic baths to remove deposited thin films and ensure that the substrate mounts with good contact on the stage.
- Securely mount the substrate on the holder by the clips and connect the thermocouple. Check the resistance of the sample using an ohmmeter.
- For substrate heating, such as Si, use a regulator dc power supply, typically in the range of 10-20 A and 15-20 V.

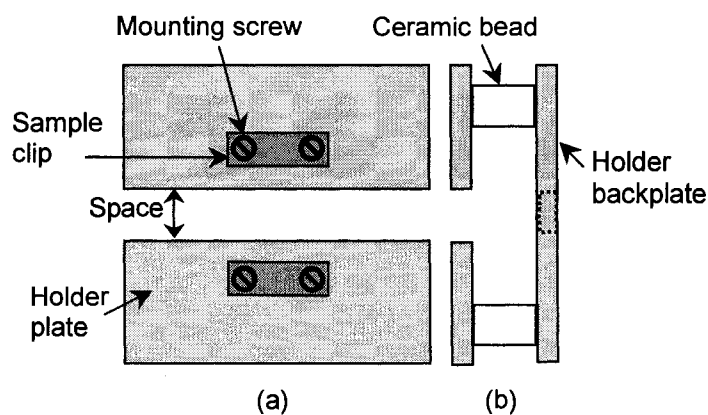


FIG. A.4. Schematic diagram of the direct heating stage: (a) front view and (b) side view.

A. 3.2. Resistive heater holder

The resistive heater holder, Fig. A.5, is an UHV stage used to heat substrate by conduction and radiation [1]. A dc power supply is used to operate and control the substrate temperature. The heating characteristics are more dependent on the properties of

the substrate material (specific heat capacity, emissivity, conductivity, mass, and size) than the heater. The heating must therefore be controlled within the power and current limitations given by the manufacturer [1]:

- Sample size: 14 mm x 14 mm maximum
- Heater element and its insulation are made of Tungsten wire and Alumina.
- Power: 90 W max. 80 W continuous. Current: 3 A max. 2.75 A continuous
- Thermocouples options: K-type (Ni-Cr / Ni-Al) Green/White

The heating element is tungsten wire, insulated by alumina. The sample plate and the clips are made from Mo. Three Mo radiation screens minimize heat loss to the support structure. The heater is electrically and thermally isolated by means of four sapphire balls and two alumina bushes. The substrate should be placed securely in position on the Mo sample plate of the heater and retained by the Mo clips or by other suitable means (such as spot-welding tantalum strips over the edge of the sample).

A. 3.2.1. Thermocouples:

There are several points when using thermocouples to record the sample temperature

- Thermocouple hot junctions must be carefully mounted and monitored. A loss of contact pressure between the hot junction and measurements point will cause the measured temperature to change. The hot junction should be securely welded or screwed in position. The sample clips will lose some resilience at higher temperatures and are unsuitable for holding junctions above 600 °C for long periods.
- Thermocouples can drift out of calibration because of chemical and physical changes in the material, due to contact with non-inert materials, trace elements in

the wire, mechanical stress or electromagnetic fields. Thermocouples can be periodically calibrated against a known thermocouple.

- The thermocouple wires should be arranged to ensure that strain is not applied to the hot junction when the sample is moved.

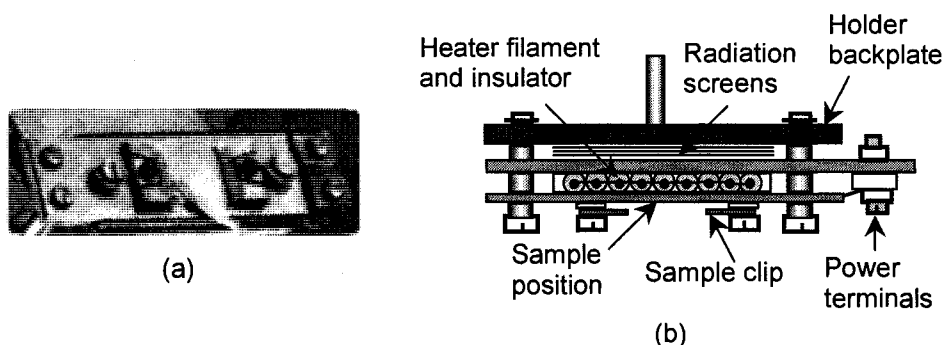


FIG. A.5. Resistive heater stage: (a) image of front part and (b) schematic diagram of the stage and its components.

A. 3.2.2. Powering the heater:

The heating filament requires a 90 W power supply limited to 3 A. The maximum duration at maximum current is limited to 20 min. For continuous heating, the maximum current is limited to 2.75 A, with a power consumption of about 80 W. Power should be applied to the heater under a vacuum of $\geq 10^{-4}$ Torr.

- The filament should be degassed when operating the heater for the first time. Degassing is obtained by raising the heater current gradually whilst monitoring the vacuum system pressure.
- **Bakeout:** All power supply leads and the thermocouple extension leads must be removed before bakeout.
- **Caution:** Avoid damaging the heating filament by directing the in situ electron beam or the focused laser beam on the heating elements in the vacuum chamber.

If the filament of the heater is consumed by time, it should be replaced and handled carefully.

A.4. Cleaning procedure of Si(100) surface

A procedure for surface cleaning of Si(100) samples to obtain clean reconstructed Si(100)-(2×1) surface prior to thin film deposition was attempted and followed successfully during the In/Si(100) work. This cleaning procedure is used to remove particulates in the micron and sub-micron size, organic materials, native oxides, and carbon contamination. Handle the Si samples with a tweezer, which is stainless steel, antiacide, and antimagnetic. The Si(100) surface cleaning steps were performed as follows:

I- Ex situ surface cleaning

A- Degreasing ultrasonic cleaning prior to chemical etching as follows:

- 1- Immerse the sample in acetone and use ultrasonic bath for 5 min.
- 2- Immerse the sample in ethyl alcohol and use ultrasonic bath for 5 min.
- 3- Use dry air or dry nitrogen to dry the sample.

B- Chemical etching prior to being loaded into the vacuum chamber as follows:

- 1- Dip the sample into a solution of H_2SO_4 (97 wt %): H_2O_2 (30 wt %) = 4:1 (by volume) for 10 min.
- 2- Rinse the sample with ultra pure water H_2O for 10 min.
- 3- Dip the sample into a solution of H_2O : HF (50 wt %) = 10:1 (by volume) for 1 min. Note that the diluted HF should be prepared in a plastic container or beaker.

- 4- Repeat the above three steps once again. Then install the sample into the substrate holder.

II- In situ heat cleaning under the UHV

- 1- Once the sample is loaded into the vacuum chamber, start pumping down the system and heat the sample to $\sim 200^\circ\text{C}$.
- 2- Wait for the pressure to go down to low 10^{-8} Torr and then start bakeout of the vacuum chamber and heat the sample to $\sim 400^\circ\text{C}$. The pressure will increase to $\sim \text{mid } 10^{-7}$ Torr.
- 3- The pressure should be monitored during heating the Si sample and during bakeout. A regulator power supply was used to heat the sample (maxi. 10 A and 20 V). In general, heating the Si sample was carried out by increasing the current in regular steps.
- 4- Bakeout the system (for 24 hours or more) as long as the pressure goes down to low 10^{-8} Torr.
- 5- After turning off baking of the system, heat the Si to 600°C for several hours.
- 6- Cool down the system and wait for the pressure to go down and then raise the sample temperature at a slow rate to 800°C . Monitor the pressure and wait until it goes down to 10^{-9} Torr range or low 10^{-8} Torr.
- 7- Rapidly flash-heat the sample to $\sim 1100^\circ\text{C}$ for $\sim 1\text{min}$ (watch the pressure), then cool down slowly to $< 400^\circ\text{C}$.
- 8- Flash-heating the sample may be repeated to obtain a contamination-free surface and the appearance of clear Si(100)-(2 \times 1) reconstruction.

- 9- Desorption of oxides and hydrocarbons can be monitored using the RGA. A live scan of spectrum lines will show changing in the partial pressures of different gaseous elements. The Si surface cleaning progress can be monitored using the in situ RHEED.

A.5. Residual gas analyzer (RGA)

The RGA (RGA 200-Stanford research systems) is a mass spectrometer of small physical dimensions that can be connected directly to a vacuum system to analyze the gases inside the vacuum chamber. It is mounted on one of 2.75" CF flange on the PLD vacuum chamber. It is installed to be away from the target and substrate holders locations to protect its head from evaporation sources that could coat the ionizer. Operating pressure range is 3×10^{-6} Torr to UHV and recommended bakeout temperature is 200 °C.

The RGA system consists of:

- 1- RGA quadrupole probe
- 2- Electronics control unit
- 3- RGA window software

The total probe equipment consists of the ionizer, the quadrupole mass filter, and the ion detector [2]. A stainless steel tube (with 2.75" CF flange ends) covers the probe assembly with the exception of the ionizer. Bombarding residual gas molecules with electrons emitted from a heated filament produces positive ions. The ions are then directed to the quadrupole filter where they are filtered according to their mass-to-charge ratios. Then the ions are focused towards an electron multiplier detector, which measures the electron current proportional to the ion current.

Running the RGA system:

- 1- Turn on the computer and start Microsoft Windows.
- 2- Start the RGA software. Double-click on the RGA icon “RGA Program.”
- 3- Connect to the RGA head as follows:
 - Select RS232 setup from the utilities menu.
 - Select the port to which the RGA head is connected (often COM2.)
 - Click on the connect button and then the RS232 button is highlighted.
- 4- Turn on the filament from the utilities menu or the toolbar’s filament button.
 - It takes a few seconds for the filament wire to warm up.
 - The filament button remains highlighted as the filament is emitting electrons.
 - A green status LED on the back panel of the electronics box indicates the emission status of the filament.
 - The filament emission can be toggled on/off at any time clicking on the filament button.
- 5- Perform an analog scan:
 - Analog mode is the spectrum analysis mode. The X-axis represents the mass range in the Mass Spec Parameters menu. The Y-axis represents the ion current amplitudes of every mass increment measured. The scan range defaults to 1 to 50 atomic mass unit (amu).
 - Select ‘Start’ from the scan menu. After a small delay, the analog scan data starts to display on the screen.

Figure A.6 shows the RGA unit and an example of using it in situ to monitor the residual gases in the vacuum chamber before and after heat cleaning a Si(100) sample.

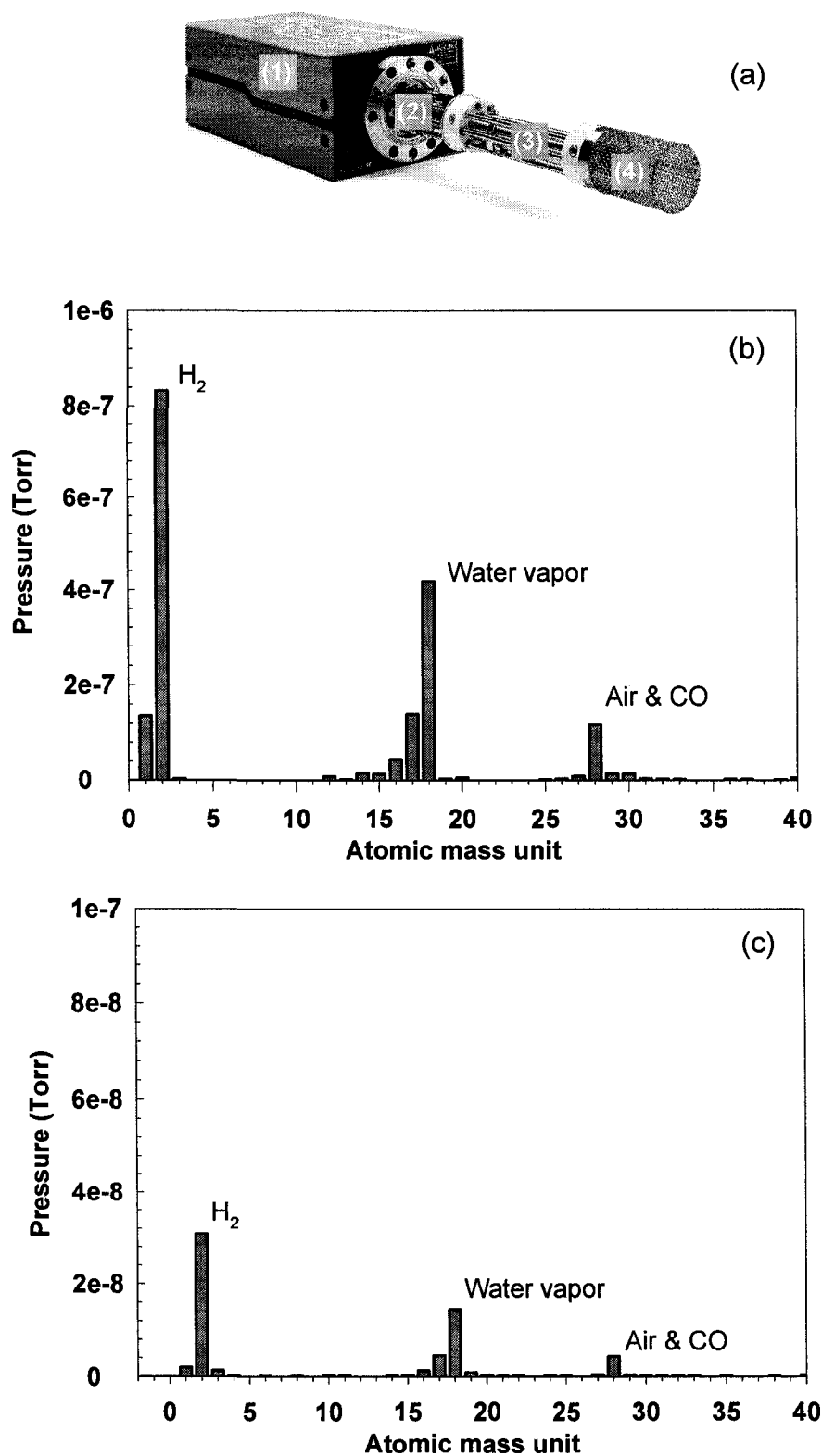


FIG. A.6. (a) RGA 200: (1) control unit; (2) ion detector; (3) quadrupole filter, and (4) ionizer. The RGA spectrum in (b) and (c) are taken before and after heat cleaning the Si(00) sample for preparation of PLD of In/Si(00) thin films.

A. 6. Ammonia cracker source

A thermal cracker source is built for dissociation of ammonia gas during preparing indium nitride thin films, Fig. A.7(a). The thermal cracker source consists of a tungsten filament inserted into a boron nitride tube and connected to tungsten wire terminals. Ceramic tubes are used around the tungsten wires. A stainless steel pipeline is used to flow the ammonia gas to the vacuum chamber. The ammonia is introduced to the chamber through an UHV leak valve. Then it becomes partially dissociated and the resultant atomic nitrogen is transported in a downward geometry close to the substrate.

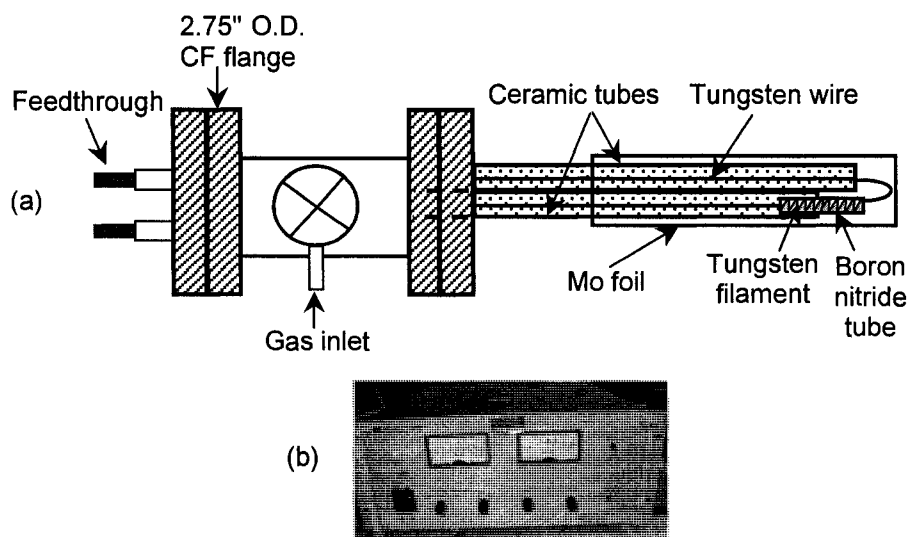


FIG. A.7. (a) Schematic diagram of ammonia cracker source. (b) Thermal cracker dc power supply (0-10 V and 0-50 A).

A. 6.1. Components and procedure:

- The tungsten filament is 4.75" long, 0.03" in diameter, and has 32 coils [3].
- The boron nitride tube is 100 mm long, 4 mm internal diameter, and 8 mm external diameter [4].
- The gas pipeline should be flushed out for the first time of installation and every three months to eliminate contamination. Flushing the gas pipeline is performed

by closing the UHV leak valve and filling out the pipeline with the gas while pumping down the vacuum chamber using the turbo pump. Then open the leak valve to flush out the gas. This step could be repeated a few times.

- The stainless steel pipeline should be baked out every four months. The pipeline is covered with an aluminum foil and wrapped with a thermal tape, which is covered with aluminum foil. The thermal tape is connected to a variac transformer. Bake the pipeline to $\sim 250^\circ\text{C}$ while leak valve is opened.
- During bake out the vacuum chamber, keep the filament current at 5 A. Degas the filament at 10 A for 1 hour.
- Before filling the pipeline with gas, pump down the system including the pipeline to low or less than 10^{-8} Torr. Then close the UHV leak valve and open the regulator of the gas cylinder to insert the gas to the pipeline.
- Keep the gas regulator pressure at 30 psi and check it regularly to make sure there is no leak or the gas cylinder is not empty.
- Power of 10-11.5 V and 15-20 A is used for the thermal cracker, Fig. A.7(b).
- To examine the efficiency of the cracker source, the RGA can be used to monitor the partial pressures during gas thermal cracking.

A. 6.2. Maintaining the UHV high precision valve

- Maintain a leak-tight seal by re-tightening the lock nut and control knob (two wheel knobs on same thread). The seal is created by elastically deforming a copper gasket against a knife-edge. Thus, it is recommended to reset seal the valve to the minimum torque level. This step may be readjusted every three months of operating the system.

- Lubricate the drive screw when the valve is subjected to long periods or high temperature bakeout, which cause relaxation of the compressive force. The thread should be carefully cleaned with a wire brush before applying lubricant.
- Minimize the possibilities of abrasive particles entering the valve. Particles embedded in the soft copper gasket can cause leaks in metal valves.
- The valve may be baked to 300 °C.

A.7. The vacuum system

A.7.1. Mechanical pump

The mechanical pump, Fig. A.8, is a rotary van type pump (Varian - model SD-301) working under the following conditions:

- To use the pump in optimum conditions, the oil level must be observed and checked regularly. This level is checked with pump switched off, hot, and on a horizontal plane. The oil lubricates mechanical components (bearings, seals, rotor, and vanes). It carries away the heat produced by the compressed gases. Ultimate pressure depends on the saturated vapor pressure of the oil, its viscosity and its ability to dissolve gases.
- An oil filter trap is connected between the inlet end fitting and the turbo pump to prevent oil from backstreaming into the pumped chamber and to prevent particles or condensed vapors from entering the pump.
- If the oil appears cloudy or discolored through the sight glass, run the pump and shut it off from the system at the inlet by a valve or a plug. Open the gas ballast (located next to the oil level glass) and allow the pump to operate for 30 min to 1

hour, or longer. This operation accelerates the temperature rise of the pump while eliminating residual vapors in the oil bath.

- The exhaust end of the pump is connected to the ventilation system.

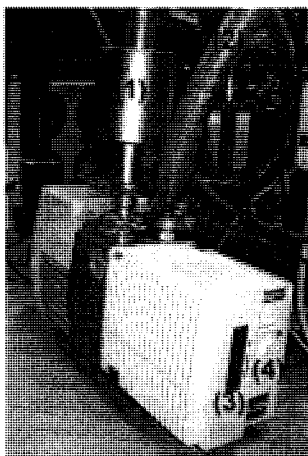


FIG. A.8. The mechanical pump: (1) forline trap; (2) exhaust line; (3) oil level, and (4) gas ballast.

A.7.2. Turbo pump

The turbo pump (Varian, turbo-V70) consists of a high frequency motor driving a turbine fitted with eleven bladed stages. The turbine rotates in an anticlockwise direction. The external body of the pump is fitted with fins, which allow the pump to function with natural convection air-cooling. A thermistor sensor is mounted near the upper bearing to prevent the pump from overheating. The turbo is characterized by the following:

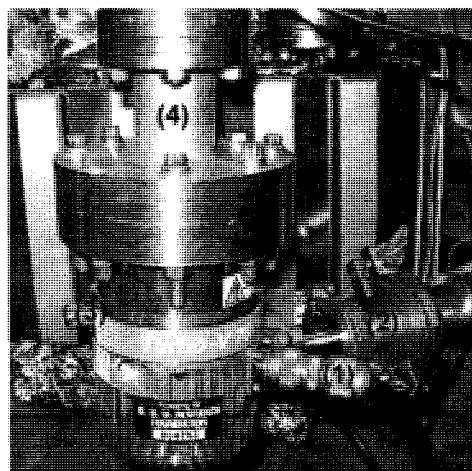
- Pumping speed is 70 l/s and rotational speed is 75000 RPM.
- The connection of the forevacuum on the side of the pump is a KF 16 NW flange.
- The inlet flange is CF 4.5" O.D. high vacuum.
- Start-up time is < 60 s.
- Cooling requires forced air, such as a fan, or water optional.

- Threaded plug screw enables a manual vent operation (Capable of replacement with an automatic vent device). Fig. A.9(a) shows the turbo pump connections.

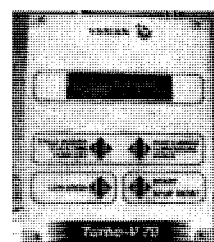
Turbo pump controller

The operation of the controller (Varian), Fig. A.9(b), is characterized by the following:

- The controller drives the turbo-V70 pump by controlling the voltage and current respect to the speed reached by the pump.
- Operating temperature is in the 0 - 40 °C range.
- The front panel has four keyboard pushbuttons to start/stop the turbo pump, to display the cycle number, cycle time, pump life, pump current, temperature, and power, and to select the low speed mode.
- If the pump has stopped automatically by a fault, the start/stop pushbutton must be pressed once to reset the controller and a second time to restart the pump.
- It is important to check the temperature of the turbo pump during pumping down operation by pushing the required button in the front panel of the controller.



(a)



(b)

FIG. A.9. (a) Turbo pump connections; (1) power line; (2) rough pump connection; (3) manual vent valve, and (4) connection to UHV valve. (b) Turbo pump controller.

A.7.3. Ion Pump

Ion pump (Perkin-Elmer TNB-X system) work by using an electrical, ionizing discharge, which is maintained under vacuum conditions, and chemically active metals, such as titanium. It consists of an anode structure suspended between a set of two cathode plates. A positive high voltage is established between the anode and the cathode plates. A magnetic field is parallel to the axis of the anode cells. The ion pump, Fig. A.10, is characterized by:

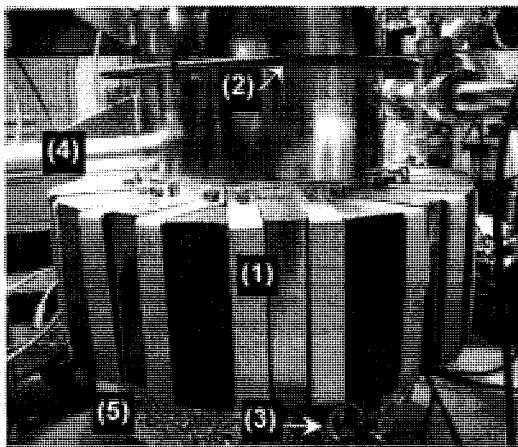
- Pumping speed is 220 l/s.
- Ultimate vacuum is 10^{-11} Torr range.
- Water vapor from atmosphere, adsorbed onto the surfaces of the ion pump and system, is normally the primary gas load encountered in starting the pump. Operators should take whatever measures to limit exposure the vacuum system to moisture air.
- Before opening the vacuum chamber, make sure that the gate valve of the ion pump is closed.
- It can normally be baked to 150 °C while operating with the magnets on, and to 450 °C with the magnets and cables removed.
- It is connected to a power supply using a high voltage cable. If the pressure in the chamber increased higher than 10^{-5} Torr, the power will disconnect automatically.

Titanium sublimation pump

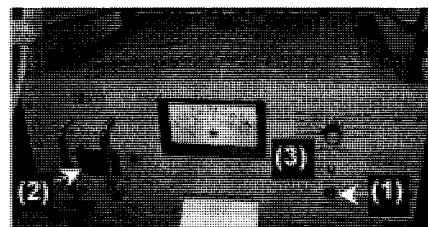
The titanium sublimation is used to accelerate overall pumping speed and capacity. Four titanium filaments are mounted on a holder that is located at the lower part

of the ion pump system and are shielded from the vacuum chamber and connected to power.

- The titanium filament is selected using the filament selector on the sublimation supply. The pump system has water terminals for cooling down after sublimation.
- Titanium should be outgassed:
 - After bakeout to achieve ultrahigh vacuum.
 - Before using titanium to assist ion pump operation.
- Filaments should be run between 50-55 A current
- Power settings below 50 A do not provide sublimation and should be used only to outgas titanium filaments.
- A sublimation period of only one or two minutes in 24 hours may be sufficient for a system maintaining ultrahigh vacuum.



(a)



(b)

FIG. A.10. (a) Ion pump components: (1) magnets; (2) bakeout line; (3) titanium filaments feedthrough; (4) manual gate valve, and (5) water cool line. (b) Ion pump control unit: (1) protect switch; (2) power switch, and (3) selector key to monitor pressure, voltage, and current.

A.8. Pumping down the PLD system

Before starting pumping down of the system verify the following:

- Make sure that the flanges are tightening well.
- Turn on the convector gauge power supply to monitor the pressure during pumping down the chamber from atmospheric to low 10^{-3} Torr.
- Make sure the turbo manual vent valve is closed.
- Connect the wires of the heating and thermocouple to the substrate manipulator.
- In case of low melting point targets, move and rotate the shutter to shield the target before starting substrate heating.

Then prepare the following steps:

- 1- Turn on the mechanical pump and the turbo pump. Monitor the pressure by the convector gauge and watch the speed of the turbo pump during starting up.
- 2- When the pressure reaches low 10^{-3} Torr, open the gate valve of the ion pump slowly and watch the pressure. The gate valve should be opened all the way.
- 3- If the pressure increases because of opening the ion gate valve, wait till it reaches low 10^{-3} Torr.
- 4- Turn on the ion gauge and then select the filament (there are two filaments). Press filament 1 or 2.
- 5- Leave the whole system to be pumped down by the turbo for 4-6 hours. In case of a substrate sample such as Si, preheat the sample to ~ 200 °C.
- 6- When the pressure is in the low of 10^{-6} Torr, close the right angle UHV valve followed by turning on the ion pump, while watching the pressure. It is better to turn on the ion pump at the lowest pressure.

- 7- Leave the turbo and mechanical pumps on until pumping the system by ion pump is operating normally. Next, shutdown the turbo pump and then shutdown the mechanical pump.
- 8- Observe the pressure and wait until it reaches the low 10^{-8} Torr range.
- 9- Prepare for bakeout of the PLD vacuum chamber. Use light bulbs around the vacuum chamber symmetrically and use aluminum foil to wrap the system. Thermal tapes can be used to bake the chamber. When baking starts, the pressure will increase to around mid 10^{-7} Torr. Heat the substrate sample to ~ 400 °C in case of using Si samples.
- 10- Degas filaments of the cracker sources during baking the system for about 3 hours.
- 11- Bakeout the system for 24-36 hours. Watch for the pressure and when it reaches low 10^{-8} Torr range, turn off the baking.

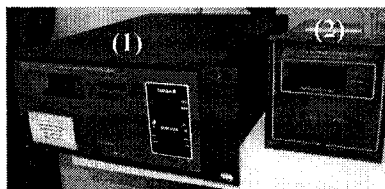


FIG. A.11. The pressure monitors of the ionization gauge (1) and the convector gauge (2) of the PLD system.

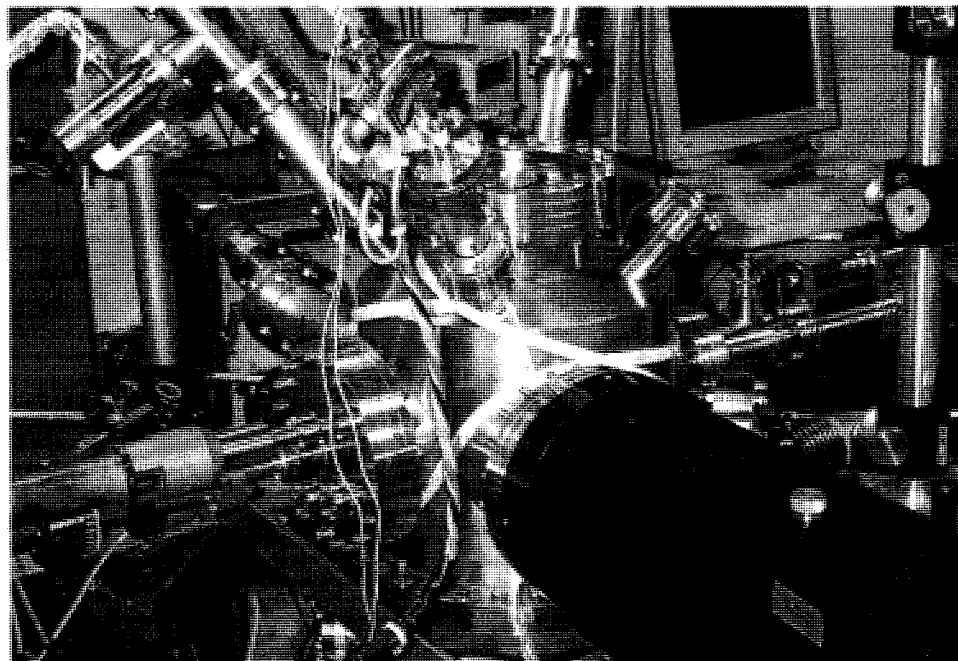


FIG. A.12. An overview of the PLD system.

A.9. References:

- [1] Thermo Vacuum Generators, operation instructions of resistive heater accessory HTS, UI 4212, (1998). Address: Thermo VG Scienta Inc., ARS Associates, 3440 Lehigh St., #250, Allentown, PA 18103. Phone: (610) 799-6197 and Fax: (610) 799-6194.
- [2] Stanford Research Systems Inc., operating manual and programming reference, model RGA 200 Residual Gas Analyzer. Address: Stanford Research Systems Inc., 1290-D Reamwood Avenue, Sunnyvale, CA 94089. Phone: (408) 744-9040 and Fax: (408) 744-9049.
- [3] R. D. Mathis Company. Address: P.O BOX 92916 Long beach, CA 90809-2916. Phone: (562) 426-7049 and Fax (562) 595-0907.
- [4] Carborandum, 168 Creekside, NY 14228. Phone: (716) 691-2051 and Fax: (716) 691-2090.

APPENDIX B

FEMTOSECOND LASER SYSTEM

The femtosecond laser system (spectra-physics) consists of four main units; diode-pumped continuous (cw) laser (Millennia Vs), mode-locked Ti:sapphire laser oscillator (Tsunami), multikilohertz intra-cavity doubled Nd:YLF laser (Merlin), and multikilohertz pulsed Ti:sapphire amplifier (Spitfire) [1].

B.1. Diode-pumped laser

The diode-pumped laser, Fig. B.1, comprises four basic components:

- Laser head: The laser head houses a sealed laser module and a shutter. The module contains the optical resonator, the neodymium yttrium vanadate (Nd:YVO₄) gain medium, the diode laser fiber delivery and telescope focusing systems, the lithium triborate (LBO) doubling crystal, and the output beam telescope system. The shutter provides a safe, mechanical means to block the output beam. The laser head is not subjected to the large heat load of a plasma tube nor required to support a heavy magnet assembly, only a simple resonator design is employed in the laser module.
- Power supply: The power supply houses two fiber-coupled, 20 W diode laser bars that pump the diode laser head. The power supply also contains the control logic and power modules for the system, as well as the refrigeration unit that cools the diodes. The power supply is air-cooled and requires no water or external cooling connections.

- Chiller: The chiller regulates the temperature of the Nd:YVO₄ crystal in the laser head with the cooling fluid temperature displayed on the chiller. The diode laser is a closed-loop system; it requires no facility water connections.
- Control module: The controller has a menu-driven program that provides control and monitoring the system.

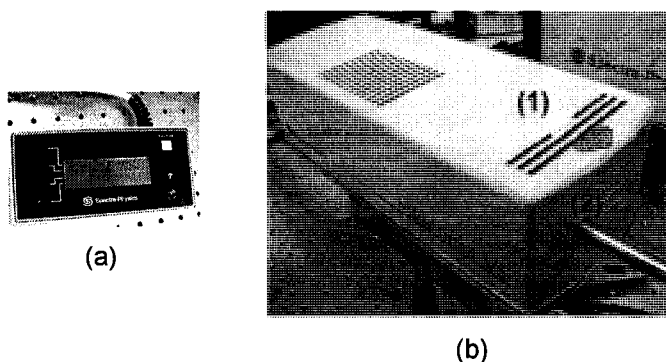


FIG. B.1. The diode laser. (a) Remote control module. (b) The laser head: (1) emission indicator and (2) output laser window connected to the laser oscillator.

B.2. Ti:sapphire laser oscillator

The mode-locked Ti:sapphire laser, Fig. B.2, is pumped by the diode laser. The Titanium-doped sapphire (Ti:sapphire) is a solid-state laser medium capable of tunable laser operation over a broad range of near infrared wavelengths. The Ti:sapphire laser oscillator comprises five main elements:

- Ti:sapphire laser head
- Electronics module
- Purge filter/regulator unit
- Chiller

The electronics module contains the heater and driver circuits for the mode locker. Acousto-optic modulator (AOM) ensures an 82 MHz nominal mode-locks operation at laser start-up. It also allows the laser to operate for extended periods without shutdowns associated with standard passive mode-locking systems. The AOM is at Brewster's angle and is driven by a regenerative-driven rf signal.

Wavelength tuning characteristics: Since the Ti:sapphire rod is birefringent, uninterrupted tuning is achieved when the c-axis of the rod is aligned coplanar with the polarization of the electric field within the cavity. Because the Ti:sapphire rod and prism surfaces are a total of ten Brewster's angle surfaces, the polarization within the cavity is largely determined by the orientation of these surfaces. Cavity losses are minimized and tuning is optimized when all these surfaces are accurately aligned at Brewster's angle.

Wavelength selection: The laser is tuned using a prism sequence and a slit, which provides a region in the cavity where the wavelengths are spatially spread. The output wavelength is tuned by changing the position of the slit in the vertical plane. The width of the slit can be changed so that the bandwidth (and hence the temporal width) of the output pulse can be varied.

Pulse width selection: The pulse width tuning is influenced by two factors: (1) inherent in the Ti:sapphire material itself and (2) cavity parameters. Therefore, the pulse width tuning can be modified through the net group velocity dispersion (GVD). The optical components in the laser cavity introduce positive GVD and cause pulse spreading. Further pulse spreading is caused by self-phase modulation in the laser rod, which results from the interaction of the short optical pulse width with the nonlinear refractive index. These effects are compensated with negative GVD using prism pairs. This allows the

system to produce < 80 fs near transform-limited pulses over most of the Tsunami wavelength regime.

Purging the laser head: Purging the laser cavity with drying nitrogen gas eliminates dust and contamination; in addition, it prevents tuning discontinuity caused by oxygen and water vapor.

Specification of the fs configurations: At standard λ of 790 nm, the pulsed width is < 80 fs, the tuning range with 6 W and TEM₀₀ pump is 735-840 nm, repetition rate is 82 MHz, spatial mode TEM₀₀, beam diameter at $1/e^2$ is < 2 mm, polarization is $> 500:1$ vertical. During experiments, the output spectrum can be verified using a monochromator and CCD detector.

Optical-mechanical controls:

- 1- High reflector is one of two-cavity end mirrors. Its vertical and horizontal adjustments allow alignment the laser cavity and to optimize output power and mode quality.
- 2- Prism dispersion compensation control is used to adjust prism-pair for overall cavity dispersion balance and shortest output pulse. It is used interactively with the nearby slit control.
- 3- Slit wavelength selector is used to select laser wavelength.
- 4- Output coupler is one of two-cavity end mirrors. Whereas the high reflector reflects all light back into the cavity, the output coupler allows a small percentage to pass through as the output beam. Its vertical and horizontal adjustments optimize output power and mode quality.

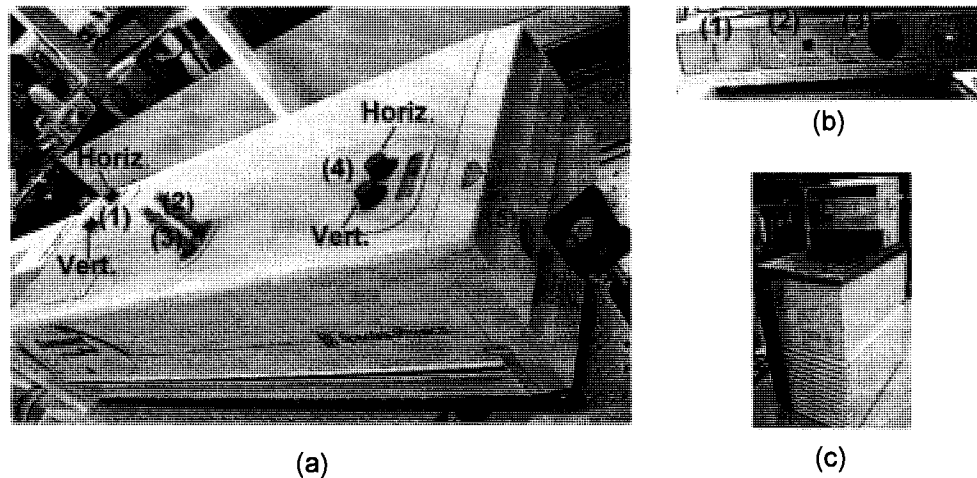


FIG. B.2. The Ti:sapphire laser oscillator system. (a) The laser head: (1) high reflector; (2) prism dispersion micrometer; (3) slit wavelength micrometer; (4) output coupler, and (5) output laser window. (b) Electronics module: (1) photodiode signal strength indicator; (2) pulsing and enable mode locker indicators showing if the system is mode locked, and (3) fine phase control to adjust the phase relationship between the AOM signal and the photodiode signal to provide a pulse-locking mechanism. (c) Chiller.

B.3. Nd:YLF pumped-laser

The Nd:YLF pumped-laser, Fig. B.3, consists of three main elements:

- Optical laser head assembly: The laser head assembly contains the Nd:YLF laser head, optical resonator, acousto-optical Q-switch, and the LBO frequency doubling crystal and temperature controller. The laser rod and the arc lamp are water cooled by an internal cooling system. The lasing crystal Nd:YLF rod and krypton arc lamp are located at the elliptical focal points of the reflector. The Q-switch is made of a high quality optical material to which an rf transducer is bonded. Fused silica material is cut and optically polished to be optically oriented at Brewster's angle for the "s" polarized intra-cavity laser radiation.

Approximately 25 W of rf power are delivered to the Q-switch, which is water-cooled, through BNC cable. The LBO crystal is located in a crystal housing which maintains its temperature at $\sim 320^{\circ}\text{F}$. At this temperature the crystal is non-critically phase matched for the intra-cavity 1053 nm radiation, ensuring high conversion efficiency to the second harmonic. The crystal should be permanently maintained at this temperature, even when the laser is not in use. The LBO crystal is anti-reflection coated for both 1053 nm and 527 nm. The temperature controller, a microprocessor-based device, is pre-programmed to maintain the crystal within 0.1 degree, which ensures stable operation of the laser.

- Power supply assembly: The power supply assembly includes the water-to-water heat exchanger and cooling system, Arc lamp power supply, and Q-switch driver/power supply. The lamp power supply capacity is 6 kW. The cooling system utilizes a water-to-water heat exchanger for cooling. Two to three gallons of de-ionized water is used in the primary cooling circuit to cool the laser head and the Q-switch. Standard city water is used in the secondary circuit to cool the de-ionized water. A combination de-ionization and particle filter is used in the primary circuit to prevent contamination and possible damage of components in the laser head and Q-switch. Remote interlock connector located on the rear panel enables the connection of an external interlock, such as switch on the laser room door, to terminate lasing if the interlock contacts are opened for safety purpose.
- Remote control box: This unit contains the electronics that control laser operation.

Maintenance of arc lamps: the flash lamps are required to be changed after certain operation hours within the manufacture specifications.

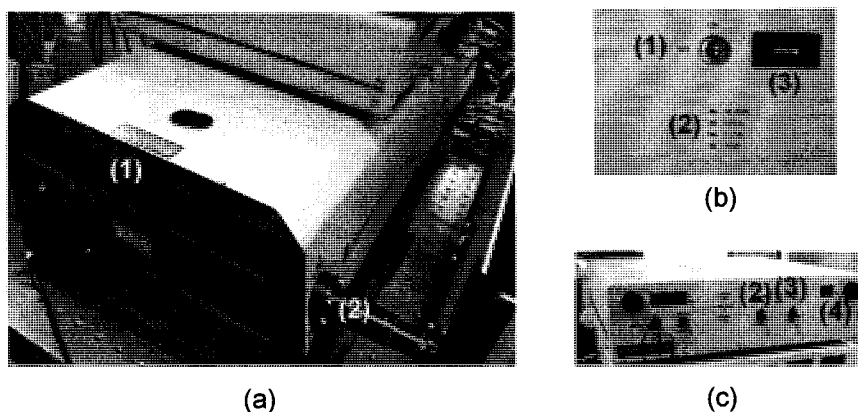


FIG. B.3. The Nd:YLF laser system. (a) The laser head: (1) emission indicators and (2) output laser window connected to the laser amplifier. (b) Power supply: (1) key switch; (2) indicators of power, water level and flow, and temperature, and (3) operation hour counter of the arc flash lamps. (c) Remote control box; (1) Q-Switch on/off; (2) shutter key; (3) lamp enable, and (4) lamp power control and display (in kW).

B.4. Ti:sapphire amplifier

The Ti:sapphire amplifier spitfire, Fig. B.4, comprises four main elements:

- Ti:sapphire amplification system
- Optical pulse stretcher
- Optical pulse compressor
- Timing electronics

The Ti:sapphire regenerative amplifier is designed to amplify single pulses from the mode-locked laser, at repetition rates from 1-5 kHz, to over 1 mJ energy. The amplification takes place as the optical pulse passes through a Ti:sapphire laser rod, which uses a pulsed, frequency doubled Nd:YLF laser as a pump source. The regenerative amplification technique enables the pulse to multipass the rod resulting in a

high overall gain. The spitfire laser amplifier contains the necessary elements to amplify ultrashort pulses to the millijoule level. Elements include a Faraday isolator, optical pulse stretcher, regenerative amplifier, optical pulse compressor. Chirped pulse amplification technique overcomes the limitation that comes from the tendency of bright beams to self focus destructively (a result of non-linearity in the index of refraction), which makes it necessary to limit the intensity present in amplifiers. In this technique, a very short duration pulse is initially generated. The next step is to stretch its pulse duration, thus considerably reducing its brightness (or peak power). This low brightness optical pulse is then amplified, with the probability of self-focusing induced damage significantly reduced. Following amplification, the pulse is recompressed to near its original duration. Pulse stretching and compression is achieved with the use of diffraction gratings. The gratings delays certain frequencies relative to others, which result in stretch a short pulse over a longer time, or alternatively, compress a long pulse into a shorter one. The role of regenerative amplification is to confine, by polarization, a single pulse (selected from a mode-locked train), amplifying it to an appropriate energy level, then cavity dump the output using two Pockels cells. The output beam is a near Gaussian profile and if poor beam occurs, it will be an indication of misalignment or optical damage. Beam uniformity can be checked by a visual inspection of burn patterns such as “burn paper.” Keep the burn paper in a transparent plastic bag to avoid getting residue on the optical surfaces and tilted downwards to have reflections go downwards.

The recommended diagnostic equipment for operation of the spitfire are:

- A power meter capable of measuring between 10 mW and 10 W average power.
- A fast oscilloscope at ≥ 300 MHz and a fast photodiode at ≥ 2 ns rise time.

- An infrared viewer.

The fs laser system starts with the continuous diode laser that provides 5 W of 532 nm output and pumps the Ti:sapphire oscillator, which delivers 800 nm and ~ 130 fs laser pulses (of few nJ). The amplification takes place as the optical pulse passes through a single Ti:sapphire rod, which has been optically excited by 532 nm laser pulses from the Nd:YLF pump laser. The amplified laser output has a pulse duration of ~ 130 fs and maximum energy of 2 mJ. The fs laser pulse width is measured by autocorrelation technique in which an incoming pulse is split into two pulses of equal intensity and an adjustable optical delay is imparted to one. The two beams are then recombined, using a lens, within a nonlinear crystal for second harmonic generation observed by an ultraviolet (UV) filter and a detector. The efficiency of UV generation depends on the degree of pulse overlap. Monitoring the UV intensity as a function of delay between the two pulses produce the autocorrelation function that related to the pulse width.

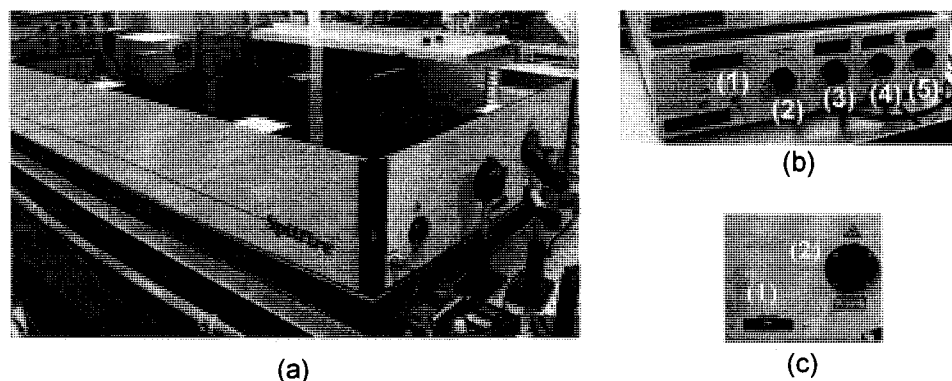


FIG. B.4. The Ti:sapphire amplifier system. (a) The amplifier laser head. (b) Synchronization and delay generator (SDG), which is used to control the precise timing necessary for a regenerative amplifier to operate: (1) laser output enable; (2) adjustable input divide to change the laser output frequency; (3) output 1 triggers the first Pockels cell driver used to set the timing of the input to the regenerative amplifier; (4) output 2 triggers the second Pockels cell driver used to set the timing of the output pulse from the regenerative amplifier, and (5) synchronization out. (c) Part of the front view of the laser amplifier: (1) LED indicator (Off if the SDG is in synchronization error) and (2) output laser window.

B.5. Laser operation procedure

Before operating the laser make sure that:

- 1- All warning signs are in place and safety glasses are available inside the lab.
- 2- Chilled water is opened and lines are connected.
- 3- Safety interlock system is activated.
- 4- Check that the diode laser power supply connectors and cables are plugged in.
- 5- Check to see if more distilled water is required by viewing the reservoir level on the rear of the Nd:YLF pumped-laser power supply.

B.5.1. Laser start-up

1- Diode-pumped laser (Millennia)

- Confirm the chiller is turned on and verify it is set to 18 °C (64.5 °F). Cooling water is always ON.
- Turn on the Millennia power supply switch.
- Press on the LASER POWER button of the remote control by holding the button for ~5 s until it begins the warm-up cycle. Let the laser warm up for 20 min.
- Confirm the Millennia SHUTTER is closed.
- If not already on, turn on the positive light of the SDG module.
- If not already on, turn on the model 3955 electronics module.
- After the warming up of the diode laser is completed, use the menu of the remote control and press the button that indicates, "LASER POWER." The laser power will increase gradually until it stabilized at the setting power (5 W).
- Open the SHUTTER of the Millennia by pressing the button on the remote control. In this step the diode laser will pump the Tsunami laser oscillator.

2- Mode-locked Ti:sapphire laser oscillator (Tsumani)

- Pulsing switch – ON (mode-locked)
- Make sure the two GREEN LEDs are ON (front of the laser amplifier). This can be maintained by keeping the two selectors of the prism dispersion compensation control and the slit wavelength and bandwidth at the optimum positions. These two controls are located at the top of the external laser head controls.
- Measure the output power to make sure that it is within anticipated power value.

3- Nd:YLF pumped-laser (Merlin)

- Verify the external cooling water supply is ON. Cooling water valve is should be always opened (City water, on the wall).
- Set the Merlin main power circuit breaker to the ON position (It is kept usually on under normal laser conditions).
- Turn the Merlin main power KEY to the ON position. The cooling system indicators on the remote box should be GREEN.
- Check to see if more distilled water is required by viewing the reservoir level on the rear of the Merlin power supply.
- Ensure that the interlock status lights on the Merlin remote box are all green.
- Lamp control box: Press the Merlin lamp start button upwards. The lamp will attempt to start – when it does, the “lamp on” indicator will light.
 - External reset – green (reset button is ON the wall)
 - Lamp enable “up” – ON
 - Shutter “up” – ON
- Turn on the Q-switch from the Synchronization box:

- Power “ON” (Back panel)
- Enable “UP” (Back panel, always up)
- Output enable “UP” (front panel)
- Verify that the repetition rate display on the remote box is indicating the correct repetition rate for this system.
- Check laser power output from Merlin.

B.5.2. Laser shutdown

1. Merlin (pump laser)

- Synchronization box:
 - . Output enable “DOWN” (Front).
 - . Power “OFF” (Back panel).
- Lamp control box (Q-switch):
 - . Shutter “DOWN” – OFF.
 - . Lamp enable “DOWN” – OFF.
 - . Wait for 10-20 min.
- Power supply key – OFF

2. Millennia (Diode-pump laser)

- “SHUTTER” – Press CLOSE (Remote control).
- “LASER POWER” – Press OFF (Remote control).

B.6. References:

- [1] Spectra-Physics Lasers user’s manuals and the manufacture, URL:
<http://www.spectra-physics.com>.

APPENDIX C

RHEED AND IMAGING SYSTEM

C.1. RHEED Electron gun

Inside the vacuum electrons are extracted from a filament that is heated by passing a current through it. The emitted electrons are focused and deflected in two orthogonal directions through the electron gun power supply, model Varian 981-3356, which consists of a two-chassis unit, 10 keV source and a control (Fig. C.1). The electron gun is mounted with tube of 4.5" CF ends (Fig. C.2).

C.1.1. Control parameters:

- 1- The filament current controls the temperature of the filament and therefore the maximum electron emission current. Care must be taken not to use such a high value that the filament is burned out. Longest filament life is achieved when operating below normal limit (~ 3.2 A).
- 2- The beam energy ranges from 0 to 10 keV and determines the kinetic energy, momentum, and wavelength of the electrons in the beam.
- 3- The objective knob adjusts focus of gun objective lens while the condenser knob adjusts the gun condenser lens. The extractor adjusts extractor voltage.
- 4- The stigmator, recessed screwdriver tuning potentiometer, is the electron beam spot shape adjustment.
- 5- The X and Y axes provide gun deflection plate voltage to control the beam position in horizontal and vertical planes, respectively.

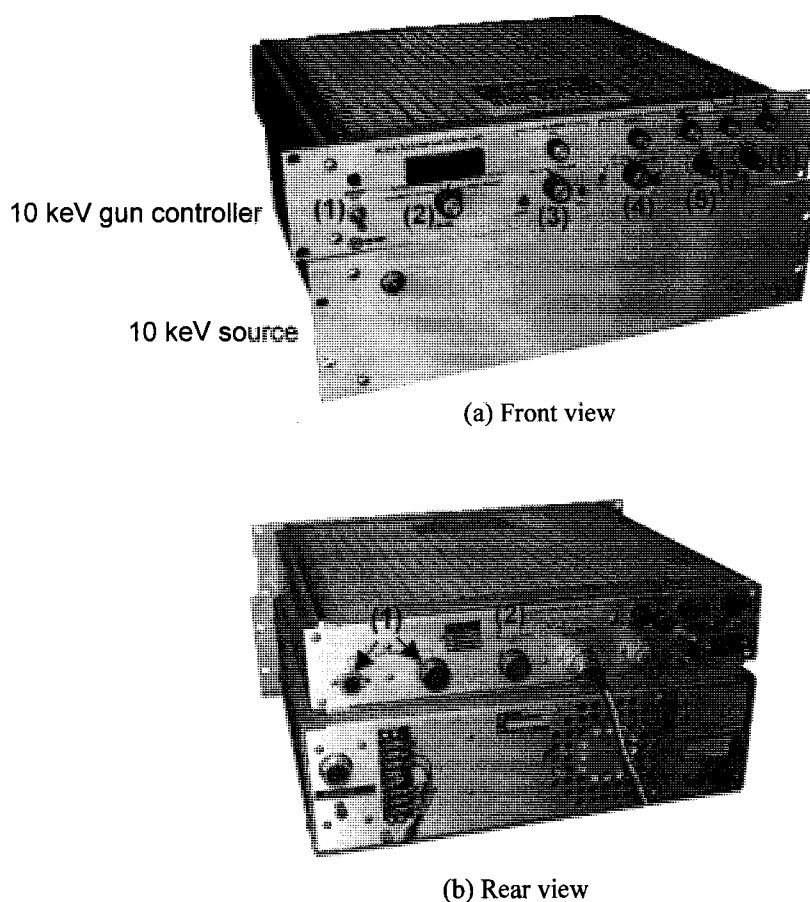


FIG. C.1. The electron gun power supply is two-chassis units, 10 keV source and a control. (a) Front view: (1) power; (2) meter switch; (3) filament control keys; (4) beam energy control keys; (5) x-axis deflector; (6) y-axis deflector; (7) stigmator, and (8) objective, condenser, and extractor keys. (b) Rear view: (1) electron gun cable and (2) high voltage input.

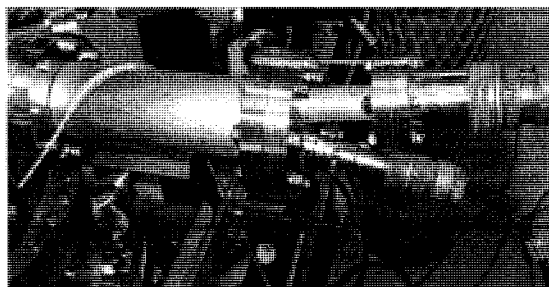


FIG. C.2. The electron gun source mounted on 4.5" CF on the vacuum chamber. It connected to the controller by two cables.

C.1.2. Operation of the power supply

Use the following procedure to begin operating the RHEED system to produce surface diffraction patterns.

- 1- Check the pressure in the vacuum chamber to make sure it is below 1×10^{-5} Torr.
If it is not, do not operate the electron gun.
- 2- Make sure the beam energy and filament current controls are both set to zero, and then turn on the main power supply.
- 3- Turn the meter function switch to the filament position and turn filament power on. The meter display, for this system, should indicate approximately 2.12 A.
- 4- Turn the meter function switch to the beam energy position and then turn beam energy switch to the 0-10 kV position. Using the adjustable knob to increase the beam energy to 5.0 keV over a span of about 20 seconds.
- 5- Slowly turn the filament current up to 2.30 A. Usually the system is kept working at these conditions for about ~10 minutes for purpose of beam stability.
- 6- Then increase the filament current slowly to operating value. The beam spot can be seen on the fluorescent screen.
- 7- Do not allow a well-focused beam to hit the screen directly for long times because localized heating can damage the screen's coating layer.
- 8- Increase the beam voltage to operating value.
- 9- Operating values of the filament current and beam energy are depending on observation and clarity of the RHEED pattern on the fluorescent screen.
- 10- To turn off the system, turn the filament current to zero, turn the beam energy to zero, turn the power supply off.

C.2. RHEED imaging and analysis

The kSA 400 is an integrated hardware and software system that used for both static and real time acquisition and analysis of RHEED patterns [1]. Charged coupled device (CCD) camera is controlled through kSA 400 software to capture the diffraction pattern with different acquisition modes.

C.2.1 kSA system

The kSA 400 system, version 4.16, is consists of the following:

1- kSA 400

- DT3152 framegrabber s/n 00503221.
- kSA 400 V4.16 software.

2- CCD Camera

- M2C Cooled CCD Detector s/n BP10096.
- CCD power bracket.
- EP306 and RG6 cables.

3- RHEED screen

- 8" O.D. CF mount.
- Viewport of 5.7" O.D screen of P43 phosphor.
- 1.73" uncoated region and Al backcoat.

The kSA system optics focuses the diffraction image from the phosphor screen onto the CCD detector, where the high linearity and high spatial resolution are important. The phosphor used for RHEED luminesces in a green tint. The system has the capability to upgrade.

C.2.2. Imaging procedure and acquisitions:

- 1- Start the computer and run the kSA 400 software.
- 2- Adjust the resolution of the CCD camera manually by using the telescope lens of the camera to adjust the focus and aperture opening. In addition, the camera can be moved back and forth on the mount track to find the best location to capture the diffraction patterns. From the header menu of the program select “acquire movie” mode. Choose a light source on the RHEED pattern and find the best focus and zoom.
- 3- Avoid over exposure the CCD detector by direct light sources.
- 4- Calibrate the pixels to cm of the RHEED image in both x and y directions. This step should be done if the focus or the camera location is changed. Check the calibration regularly, especially for quantitative RHEED analysis.
- 5- Select the acquisition mode to capture and record the RHEED data. The data acquisition modes are:
 - **Single image mode:** Acquires single images for quantitative static analysis and archiving.
 - **Multiple image mode:** Acquires a user-selected number of diffraction images sequentially for quantitative analysis and archiving. Images may be acquired in real-time to system RAM (up to the limit of physical memory) or may be stored directly to hard disk.
 - **Focus mode:** Displays the diffraction pattern simultaneously with line profiles during optics alignment and focusing, as well as for obtaining a symmetric RHEED diffraction pattern. The focus of the diffraction pattern

obtained by maximizing the intensity and minimizing the width of the streak profiles. If the integration time needs to be changed or select line profiles to plot, click on stop and enter the new parameters, and then click on start.

- **Scan mode:** Scan mode is a real-time acquisition and analysis feature. An arbitrary number of lines and windows of the incoming diffraction pattern are monitored simultaneously, yielding time-resolved, simultaneous intensity profiles, lattice spacing, and coherence length. Images stored with the kSA 400 include the image data and a record of exactly how the image was acquired. Double click on the image; the image properties (like exposure time, size, delay time, image type) will appear in a window.
 - **Movie mode:** Acquire complete image movies, with the capability to playback, analyze, and run scan mode on the movie. With acquired movies, the movie effectively becomes a built-in video recorder and acts as a second acquisition source (in addition to the camera).
 - **Interactive accumulation mode.** Allows continuous display of a real-time summed image, i.e. “interactive accumulation” mode. Useful for monitoring build-up of system noise, or monitoring pattern shifts with a single image.
- 6- Insert the input parameters to scan or capture RHEED patterns. For the scan mode the characteristics acquisition parameters are:
- Data can be acquired for a specific length of time (duration in sec) or for a specific number of images.

- Insert any multiple of $1/30$ s as the CCD exposure time. The shortest exposure time is $1/30$ s.
- The delay time parameter specifies the time in seconds and accurate to 1 millisecond, between image acquisitions.
- Tracking feature determines how the diffraction spot will track:
 Off: The window remains stationary, centered on the position as placed.
 Peak: The window tracks the peak intensity within the window.
 Centroid: The window tracks the centroid position of the window.
- Frame averaging is used to increase the signal-to-noise ratio of the RHEED image.

C.2.3. Analysis

- Intensities of the diffraction features in the RHEED image can be monitored by different plots (peak, average, centroid)
- FWHM/coherence analysis is used to determine the FWHM of a diffraction streak or profiles. Through instrument calibration parameters, the FWHM evolution is then converted to the average in-plane coherence length.
- Intensity oscillations operation allows plotting RHEED intensity oscillations from diffraction image. Enter the proper acquisition parameters in the scan mode dialog and commence the acquisition.
- Fast Fourier transform operation can be used to analyze 2D data plot displayed with the kSA 400 (for example, an intensity oscillations plot, line profile plot, FWHM plot). For oscillation data, the growth rates and overlayer thickness can be determined.

- Lattice spacing evolution can be obtained by using the pixel/d spacing analysis operation of the diffraction streaks. It is beneficial to zoom in to the diffraction image to create a large pixel distance between first order diffraction streaks for achieving high resolution.
- Line profile analysis routine interactively displays the line profile of a line overlaid on the currently active image window. The line may be moved by clicking and dragging the middle of the line anywhere on the image, or by clicking and dragging either end of the line to a new position.
- Image filters including background subtraction, inelastic background subtraction, contrast maximization, and high and low pass filters.
- 3D plot analysis allows 3-dimensional plotting of the diffraction image, static or dynamic. It can show simultaneous evolution of multiple features of the scan mode image, for example the intensity, spacing, coherence, and reconstruction as a function of growth time. For static images, 3D plotting can bring out weak features difficult to see in the 2-dimensional image, e.g. Kikuchi lines or anti-phase boundary diffraction features.

C.3. References:

- [1] k-Space Associates Inc., kSA manual of kSA 400 (Version 4.16), and the manufacture URL: <http://www.k-space.com>. Address: k-Space Associates Inc., 3626 West Liberty Rd., Ann Arbor, MI 48103. Phone: (734) 668-4644 and Fax: (734) 668-4663.

APPENDIX D

LIST OF MANUFACTURER CONTACTS

Equipment	Name & Address	Phone	Fax & E-mail
Vacuum components	MDC Vacuum Products, LLC 23842 Cabot Boulevard, Hayward, CA 94545.	800-443-8817 510-265-3500	510-887-0626 webtechsales@mdcvacuum.com
Vacuum components	Varian Inc. 121 Hartwell Avenue, Lexington, MA 02421.	800-882-7426 781-861-7200	781-860-5437 custserv@varianinc.com
Vacuum components	DUNIWAY Stockroom Corp. 1305 Space Park Way, Mountain View, CA 94043.	800-446-8811 650-969-8811	650-965-0764 info@duniway.com
Vacuum components	Kurt J. Lesker Company 3983 1st Street, Livermore, CA 94551.	800-245-1656 925-449-0104	925-449-5227 salesus@lesker.com
Instrumentation & software for surface science and thin film	k-Space Associates, Inc. 2182 Bishop Circle East, Dexter, MI 48130.	734-426-7977	734-426-7955 requestinfo@k-space.com
Indium Phosphite wafer	CRYSTACOMM, INC. 1599 North Shoreline Blvd., Mountain View, CA 94043.	650-961-4311	650-961-4364 info@crystacomm.com
Silicon wafers	Virginia Semiconductor, Inc. 1501 Powhatan Street, Fredericksburg, VA 22401.	540-373-2900	540-371-0371 sales@virginiasemi.com
Indium target	Kurt J. Lesker Company 1515 Worthington Avenue, Clairton, PA 15025.	800-245-1656	412-233-9705 materials@lesker.com
Optical components & assemblies	CVI Laser Corporation 200 Dorado South East, Albuquerque, NM 87123	505-296-9541	505-298-9908 optics@cvimellesgriot.com
Optical components & assemblies	Newport Corporation 1791 Deere Avenue Irvine, CA 92606.	800-222-6440 Spectra-Physics Lasers division at: 800-775 - 5273	949-253-1680 sales@newport.com
Optics, imaging, & photonic	Edmund Optics, Inc. 101 East Gloucester Pike, Barrington, NJ 08007.	800-363-1992	856-573-6295 sales@edmundoptics.com
Chemicals (Eathanol & Methanol) – Materials (Mo, In, Ti)	Alfa Aesar 26 Parkridge Road, Ward Hill, MA 01835.	800-343-0660 978-521-6300	800-322-4757 info@alfa.com
Indium nitride powder & sputtering targets	Plasmaterials, Inc. 2268 Research Drive, Livermore, CA 94550	925-447-4030	925-447-4031 info@plasmaterials.com
Sapphire substrates	Novotech Optical Semiconductor, Inc 3369 White Mountain Blvd, Lakeside, AZ 85929.	928-368-5013	928-368-6133
Sensors, thermocouples, electric heater, automation, & process control instruments	OMEGA Engineering, Inc. One Omega Drive, P.O. Box 4047, Stamford, CT 06907.	800-848-4286 203-359-1660	203-359-7700 cservice@omega.com info@omega.com

Electron microscopy supplies & instruments	Ted Pella, Inc. P.O. Box 492477, Redding, CA 96049.	800-237-3526 530-243-2200	530-243-3761 sales@tedpella.com
Scientific gases	Spectra gases, Inc. 3434 Route 22 West, Branchburg, NJ 08876.	800-932-0624 908-252-9300	908-252-0811 info@spectragases.com
AFM, SPM, cantilevers, probes, & tips	MikroMasch 111 N. Market Street, 6th Floor San Jose, CA 95113.	866-776-8477 919-636-3463	919-869-2443 usa@mikromasch.com
AFM probes	Nanoscience Instruments, Inc. 9831 South 51 st Street, Suite C119, Phoenix, AZ 85044	888-777-5573 480-940-3940	480-940-3941 info@nanoscience.com
Tubing, fitting, materials, & tools	Small Parts, Inc. 13980 N.W. 58 TH Court, P.O. Box 4650, Miami Lakes, FL 33014	800-220-4242	800-423-9009 smlparts@smallparts.com
Laboratory supplies	Fisher Scientific 2000 Park Lane Drive Pittsburgh, PA 15275.	800-766-7000	800-926-1166
Laboratory supplies	Lab safety supply PO Box 1368, Janesville, WI 53547.	800-356-0783	800-543-9910
Tools & supplies	Techni-Tool 1547 N. Trooper Rd., P.O. Box 1117, Worcester, PA 19490.	800-832-4866 610-941-2400	800-854-8665 support@techni-tool.com sales@techni-tool.com

VITA
For
MOHAMED ABD-ELSATTAR HAFEZ

Department of Electrical and Computer Engineering,
Old Dominion University,
Norfolk, VA 23529.
Email: mhafe001@odu.edu
mhafez8@yahoo.com

DEGREES:

Master of Science (Experimental Physics), Cairo University, Giza, Egypt, July 1998.

Bachelor of Science (Physics), Cairo University, Giza, Egypt, May 1991.

PROFESSIONAL CHRONOLOGY:

- Research Assistant (1998-2006 & 2007-2008), Old Dominion University, Applied Research Center, Jefferson Laboratory, Newport News, VA, USA.
- Engineer Intern (2006-2007), Siemens VDO Automotive Corporation, Newport News, VA, USA.
- Research Assistant (1994-1997), National Institute of Laser Enhanced Sciences, Cairo University, Giza, Egypt.
- Lecturer Assistant (2000-present), National Institute of Laser Enhanced Sciences, Cairo University, Giza, Egypt.

HONORS AND AWARDS:

- 1- Graduate Student Travel Grant Award, for American Vacuum Society Conference, Old Dominion University (2003).
- 2- Supplemental Dissertation Stipend Award, Old Dominion University (2005).
- 3- Internship at Siemens VDO Automotive Corporation (2006-2007).
- 4- Three articles selected to appear on American Physical Society's Virtual Journal of Ultrafast Science.

PUBLICATIONS

REFEREED JOURNAL

- 1- **M. A. Hafez** and H. E. Elsayed-Ali, "Low temperature growth of high-quality InN on Si(100) by femtosecond pulsed laser deposition," (in preparation).
- 2- **M. A. Hafez** and H. E. Elsayed-Ali, "Activation energy of surface diffusion and terrace width dynamics during the growth of In(4×3) on Si(100)-(2×1) by femtosecond pulsed laser deposition," *J. Appl. Phys.* **103**, 093510 (2008). [Selected to appear on the Virtual Journal of Ultrafast Science, Vol. 7, issue 6, June 2008].
- 3- **M. A. Hafez** and H. E. Elsayed-Ali, "Formation of In-(2×1) and In islands on Si(100)-(2×1) by femtosecond pulsed laser deposition," *J. Appl. Phys.* **101**, 113515 (2007). [Selected to appear on the Virtual Journal of Ultrafast Science, Vol. 6, issue 7, July 2007].
- 4- **M. A. Hafez** and H. E. Elsayed-Ali, "Femtosecond pulsed laser deposition of indium on Si(100)," *J. Laser Micro/Nanoengineering* **1**, 44-47 (2006).
- 5- **M. A. Hafez**, M. S. Hegazy, and H. E. Elsayed-Ali, "Indium growth on Si(100)-2×1 by femtosecond pulsed laser deposition," *J. Vac. Sci. Tech. A* **23**, 1681-1686 (2005). [Selected to appear on the Virtual Journal of Ultrafast Science, Vol. 4, issue 11, November 2005].
- 6- **M. A. Hafez**, K. A. Elamrawi, and H. E. Elsayed-Ali, "Pulsed laser deposition of InP thin films on Sapphire(1000) and GaAs(100)," *Appl. Surf. Sci.* **233**, 42-50 (2004).
- 7- **M. A. Hafez**, M. A. Khedr, F. F. Elaksher, and Y. E. Gamal, "Characteristics of Cu plasma produced by a laser interaction with a solid target," *Plasma sources Sci. Technol.* **12**, 185-198 (2003).
- 8- **M. A. Hafez** and H. E. Elsayed-Ali, "Atomic hydrogen cleaning of InP(100): electron yield and surface morphology of negative electron affinity activated surfaces," *J. Appl. Phys.* **91**, 1256-1264 (2002).
- 9- K. A. Elamrawi, **M. A. Hafez**, and H. E. Elsayed-Ali, "Atomic hydrogen cleaned GaAs(100) negative electron affinity photocathode: surface studies with reflection high-energy electron diffraction and quantum efficiency," *J. Vac. Sci. & Technol. A* **18**, 951-955 (2000).
- 10- K. A. Elamrawi, **M. A. Hafez**, and H. E. Elsayed-Ali, "Atomic hydrogen cleaning of InP(100) for preparation of a negative electron affinity photocathode," *J. Appl. Phys.* **84**, 4568-4572 (1998).

CONFERENCES

- 1- **M. A. Hafez** and H. E. Elsayed-Ali, "Low temperature growth of high-quality indium nitride on Si(100) by femtosecond pulsed laser deposition," *The American Vacuum Society 55th International symposium*, Boston, MA, October 19-24 (2008).

- 2- **M. A. Hafez** and H. E. Elsayed-Ali, "Morphology of Indium Nanoparticles on Si grown by Femtosecond Pulsed Laser Deposition," *Virginia Nanotech 2006*, Newport News, VA, June 11-13 (2006).
- 3- **M. A. Hafez** and H. E. Elsayed-Ali, "Indium nitride growth on Si(100) by femtosecond pulsed laser deposition," *American Physical Society (APS) meeting*, Baltimore, MD, March 13-17 (2006).
- 4- **M. A. Hafez** and H. E. Elsayed-Ali, "Femtosecond pulsed laser deposition of indium on Si(100)," *The 6TH International Symposium on Laser Precision Microfabrication*, Williamsburg, VA, April 4-8 (2005).
- 5- **M. A. Hafez**, M. S. Hegazy, and H. E. Elsayed-Ali, "Indium growth on Si(100) by femtosecond pulsed laser deposition," *American Physical Society (APS) meeting*, Palais des Congres de Montreal, Montreal, Quebec, Canada, March (2004).
- 6- **M. A. Hafez**, M. S. Hegazy, and H. E. Elsayed-Ali, "Growth of epitaxial two-dimensional layers of indium on Si(100) by femtosecond pulsed laser deposition," *The American Vacuum Society 50th International symposium*, Baltimore, MD, November 2-7 (2003).
- 7- **M. A. Hafez**, K. A. Elamrawi, H. E. Elsayed-Ali, "Preparation of InP(100) surface for negative electron affinity photocathode", [Conference Paper] *Conference Proceedings, The 12th International Conference on Indium Phosphide and Related Materials (Cat. No.00CH37107)*. IEEE, pp.197-200. Piscataway, NJ, USA (2000).
- 8- K. A. Elamrawi, **M. A. Hafez**, and H. E. Elsayed-Ali, "Pulsed laser deposition of thin film InP over GaAs(100)," *Bull. Amer. Phys. Soc.*, Vol. **44**, No. 1, Centennial Meeting, p. 1460 (1999).
- 9- **M. A. Hafez**, M. Atta, F. Elaksher, and Yosr E. E-D Gamal, "Investigation of the characteristics of laser produced copper plasma," *The 25th Anniversary IEEE, International Conference on Plasma Science*, Raleigh, NC, US, June 1-4 (1998).
- 10- K. A. Elamrawi, **M. A. Hafez**, and H. E. Elsayed-Ali, "Atomic Hydrogen Cleaning for InP Photocathode Surface Preparation," *The American Vacuum Society 45th International symposium*, Baltimore, MD, November 2-6 (1998).